University of Strathclyde

Department of Mechanical & Aerospace Engineering

Analytical Methods for Satellite Constellation Reconfiguration and Reconnaissance using Low-Thrust Manoeuvres

Ciara McGrath

Submitted to the Department of Mechanical and Aerospace Engineering in partial fulfillment of the degree of

Doctor of Philosophy (PhD) in Mechanical and Aerospace Engineering

2018

Declaration of author's rights

This thesis is the result of the author's original research. It has been composed by the author and has not been previously submitted for examination which has led to the award of a degree.

Ciara McGrath

August 24, 2018

To my Dad, who showed me the stars,

And my Mum, who taught me how to reach them.

Acknowledgements

First and foremost I would like to thank my supervisor, Prof Malcolm Macdonald, for all of his support during my time at the University for Strathclyde. You have always gone above and beyond what was required of you as a supervisor, not only to ensure the quality of my research, but also to help me develop as a young professional. Without your encouragement and guidance I would not be where I am today, and I can't thank you enough for everything that you have done.

I would like to thank Prof Paulo Lozano, Prof David Miller and Dr David Krejci of the Massachusetts Institute of Technology for welcoming me into their research groups and giving up their time to support me. My time at MIT was invaluable, personally and professionally, and their contributions have been instrumental in this work.

To my family, friends, and colleagues, it's difficult to convey how grateful I am to every single one of you; particularly for your understanding and kindness through what was a sometimes emotional journey. This dissertation has taken almost four years to complete and, whether you know it or not, every single one of you has contributed in some way to its outcome. In particular I'd like to thank: my parents, for their never-ending love and support, and for making me believe I can do anything I put my mind to; my brother, for checking my maths, helping with my work, and providing an infinite supply of much needed beer; Ross, for making sure I left the office at an (almost) reasonable hour, for believing in me when I'd all but lost faith in myself, and for making me smile even on the hardest days; and Ruaridh, for always being right there next to me every step of the way.

Finally, none of this work could have happened without the generous funding provided by the EPSRC, and the Fulbright-Schuman Award that supported me during my research visit to the USA.

Abstract

A fully-analytical general perturbation solution to a restricted low-thrust circular to circular Lambert rendezvous problem with tangential thrust and an optional coast arc is developed. The solution requires no iteration and is solved rapidly to generate a full range of possible manoeuvres to achieve the desired goal. The speed of the solution allows for large-scale problems involving numerous spacecraft and manoeuvres to be studied; this is demonstrated by applying the method to a range of mission scenarios. In the first scenario, a full range of manoeuvres providing rapid flyover of Los Angeles is generated, giving an insight to the trade-space and allowing the manoeuvre that best fulfils the mission priorities to be selected. Using a CubeSat equipped with electrospray propulsion, these manoeuvres can reduce the time to overflight by more than 85%, for less than 20 m/s velocity change, when compared with a non-manoeuvring satellite. The second scenario considers a constellation of 24 satellites that can manoeuvre to provide targeted coverage of a region of the Earth as required. A full set of manoeuvres for all satellites is generated for four sequential targets, allowing the most suitable manoeuvre strategy to be selected; regional improvements in coverage of more than ten times are shown to be achievable when compared to a static constellation. Finally, deploying a constellation of spacecraft by using low-thrust manoeuvres to achieve the desired configuration is studied. Deploying a constellation of 24 satellites using this technique could reduce launch costs by 75% compared with traditional methods. These cases demonstrate the advantages that manoeuvrable satellites can provide, but it is the analytical general perturbation solution, which allows for rapid exploration of these complex problems, that is the key contribution of this work.

Thesis Supervisor: Prof Malcolm Macdonald, University of Strathclyde

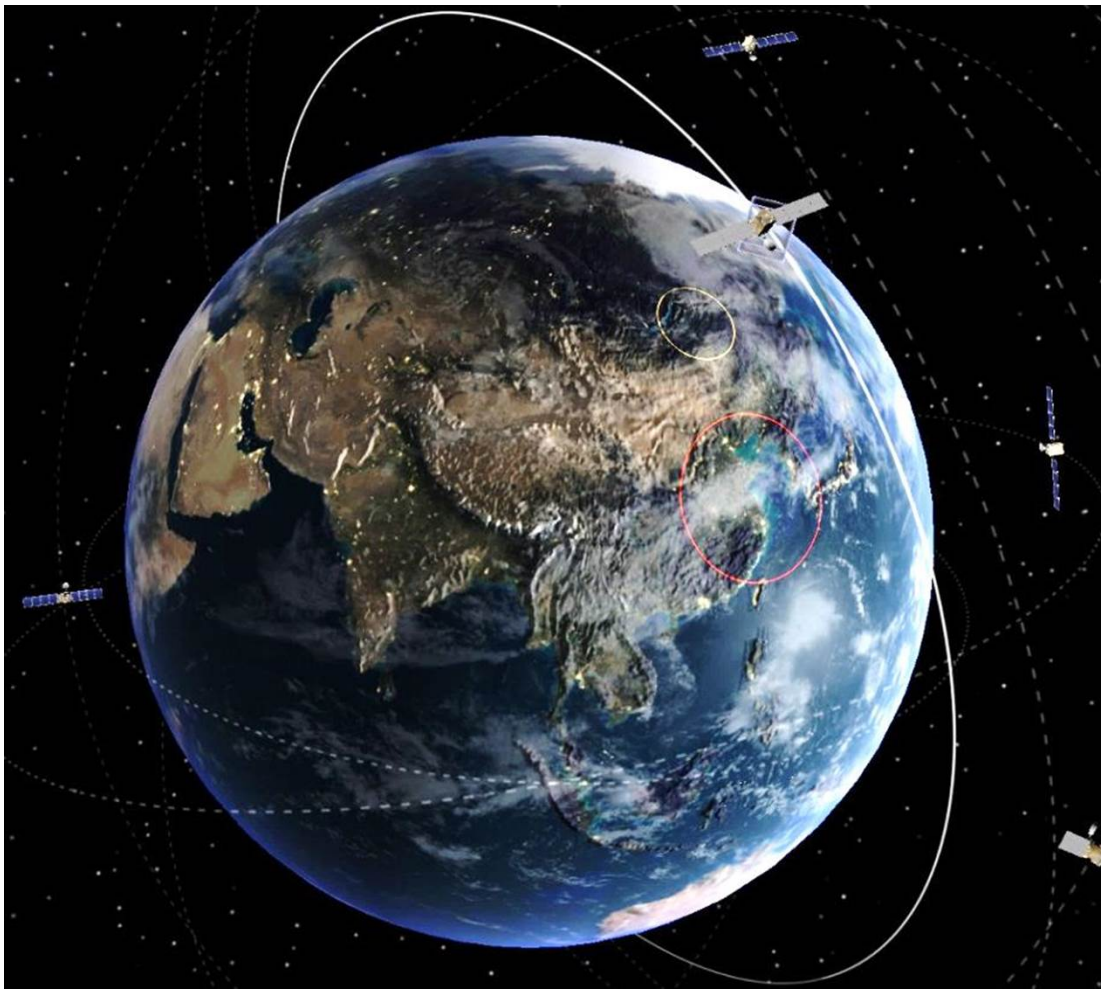

Image taken from a game produced by Glasgow School of Art Digital Design Studio as part of the Space for Art project. The game, based on the work presented in this dissertation, challenges players to manoeuvre satellites and provide targeted coverage to regions of the Earth, without exhausting the available propellant.

Contents

List of Figures

List of Tables

Nomenclature

Roman Symbols

A	=	acceleration, m/s^2
a	=	osculating semi-major axis, m
$\bar{a}$	=	mean semi-major axis, m
C_D	=	satellite coefficient of drag, -
d	=	great-circle distance, m
e	=	eccentricity, -
F	=	thrust, N
H	=	scale height of Earth's atmosphere, m
h	=	specific angular momentum, m^2/s
h_{ref}	=	reference altitude with respect to mean Earth radius, m
h_1	=	spacecraft altitude with respect to mean Earth radius, m
i	=	inclination, deg
J_2	=	coefficient of the Earth's gravitational zonal harmonic of the 2nd degree, -
k	=	utility function weighting factor, -
M	=	mean anomaly, deg
m	=	satellite total mass, kg
m_{dry}	=	satellite dry mass, kg
n	=	mean motion, deg
$\bar{n}$	=	perturbed mean motion, deg
P	=	average propellant mass, kg
P_{start}	=	propellant mass at launch, kg
P_{end}	=	propellant mass after deployment manoeuvres, kg

p = semi-latus rectum, m

R = disturbing function, m^2/s^2

R_e = mean Earth radius, m

r = orbit radius, m

s = swath width, m

t = time, s

U = utility function, -

u = argument of latitude, deg

v = satellite velocity, m/s

X = attribute of utility function, -

Greek Symbols

α = satellite effective cross-sectional area, m^2

Δu = change in argument of latitude, deg

ΔV = change in velocity, m/s

$\Delta\Omega$ = change in right ascension of the ascending node, deg

δ = latitude, deg

θ = true anomaly, deg

μ = standard gravitational parameter of Earth, m^3/s^2

ρ = atmospheric density, kg/m^3

Ψ = longitude, deg

Ω = right ascension of the ascending node, deg

Ω_{et0} = right ascension of Greenwich at epoch, deg

ω = argument of perigee, deg

ω_e = angular velocity of Earth, deg/s

Subscripts

0 = at epoch

1 = at end of phase 1

2 = at end of phase 2

3 = at end of phase 3

alt	=	total for altitude changing phases (i.e. phase 1 and phase 3)
atm	=	atmospheric drag
max	=	maximum
min	=	minimum
POI	=	point of interest
$prop$	=	propulsion system
R	=	in the radial direction
ref	=	reference value
S	=	in the transversal direction
SSP	=	sub-satellite point
$total$	=	total at manoeuvre end
W	=	in the direction normal to the orbit plane

Chapter 1

Introduction

Traditionally, satellites have been designed to operate in static parking orbits, in which they revolve around the Earth governed by natural orbit mechanics. Any on-board propulsion systems are, generally, only used for orbit insertion and maintenance. The exception to this are military reconnaissance satellites, such as the US *Keyhole* class satellites, which carried large amounts of propellant enabling them to lower their altitude and provide extremely high resolution images of their targets [1, 2]. The advantages provided by a responsive space system such as this are numerous, and are not limited to military operations. Satellites capable of frequent, agile manoeuvres could also enhance existing civil and commercial in-space capabilities by providing more frequent coverage of regions of interest, enabling on-demand overflight targeting, and offering bespoke look-angles and lighting conditions. They could also facilitate a wide range of missions that are of contemporary interest, but are yet to be realised, such as orbital debris removal and in-orbit servicing. However, the high propellant mass, and associated high launch cost, required to permit such agility has, to date, relegated these capabilities to the realm of the military, for whom financial considerations are of secondary concern to their requirements for increased resolution and rapid data delivery.

The dawn of "New Space" in recent years however, is changing the landscape of the space industry. In particular, the shift toward smaller satellites, requiring shorter development times and utilising off-the-shelf-components and standardised buses, has

driven down the cost of access to space. Alongside this, the miniaturisation of components has seen these small satellites reach a juncture in which they are capable of providing truly valuable scientific and commercial data [3–7]. Amongst these recent developments are propulsion systems for small satellites, both impulsive and electric, which could enable manoeuvrable small satellite missions in the very near future [8–11]. This class of mission has the advantage of being able to offset the increased risk and shorter mission life associated with manoeuvrable satellites against their relatively low mission cost.

The recent body of work undertaken by Co et al. [12–14] proposes the use of agile, manoeuvrable satellites as a means of enabling Operationally Responsive Space (ORS). ORS is a military concept that originally aimed to support the warfighter through the rapid launch of satellites, providing targeted support when and where it was needed [15]. This concept has since been extended to include in-orbit agility, in the form of agile instrument usage, frequent or rapid slewing, and active manoeuvring to change the satellite orbit [16–18]. Co et al. identify electric propulsion as an efficient, low-cost method of facilitating manoeuvrable satellites and providing a responsive in-orbit system. However, they note that all manoeuvres require a trade-off between the propellant used and the time taken to carry out the manoeuvre. As such, in order to assess the value of manoeuvrability, it is necessary to investigate this trade-off and consider the improvement in performance that can be enabled by manoeuvrability in the context of the associated cost. Quantifying this trade-off is difficult for a number of reasons. Firstly, the solution is highly dependent on the orbit parameters of the responding satellite, as well as the desired final satellite position; this makes it difficult to draw general conclusions about responsive capabilities without investigating a large number of disparate scenarios. Secondly, there is a wide range of possible trade-off criteria that may be of interest, depending on the mission priorities. Co et al. select a solution for their analyses by providing a compromise between propellant usage and manoeuvre time, however, the results will vary depending on the relative weighting given to each parameter. In addition, other potentially important parameters, such as look-angle to target and the local time at flyover, are not considered in the trade. Thus, the algorithm and the associated results presented can only be considered applicable to

missions that share their priorities with those assumed by Co et al.. Defining a general solution applicable to all possible mission goals is extremely challenging, and as such it would be beneficial to provide full knowledge of all possible responsive manoeuvres for a given scenario, alongside their associated parameters, allowing the mission designer or operator to quantify the resulting trade-off using their own unique criteria. Finally, Co et al. note that any scenario will have a range of discrete overflight opportunities, the number of which will increase as the allowable manoeuvre time increases, and each of these needs to be investigated in order to quantify the trade-off. Complicating matters further, each of these discrete opportunities will have a flyover window associated with it, within which varying the manoeuvre parameters can provide a different flyover time and a different look-angle to the target at flyover. This creates a discontinuous solution space that is not ideal for exploration by numerical optimisers, but which the user must navigate to formulate a reliable trade-off. The available literature to-date has not been able to provide a full overview of this solution space, meaning it is difficult to develop any insights or form any general conclusions about what this trade-space may look like. These findings have inspired the main thesis of this work:

"Manoeuvrable satellites can provide increased performance when compared to traditional static satellite missions, however there is an inherent, quantifiable trade-off between the achievable performance, the manoeuvre time and the propellant required, that can be presented as a full solution space, providing insight to this complex problem."

To investigate this trade-off it will be necessary to analyse a range of mission scenarios, each with thousands of possible manoeuvres to trade between. As such, a method of analysis that can be solved quickly, can be scaled across multiple satellites, and can be applied to a range of distinct missions is required. Further, a full overview of the solution space produced is needed to allow the engineer or operator to trade-off between the manoeuvre cost and time, and assess the corresponding benefit of the responsive system, if any. This is a key requirement of the proposed concept of operations for an ORS system [19]. This desire for a rapid, scalable solution enabling an insight into the capabilities of manoeuvrable satellites forms the basis of this dissertation.

1.1 Satellite Manoeuvrability

1.1.1 Lambert's Problem

At its most basic level, the problem of manoeuvring a satellite from one point to another can be considered as a specific presentation of *Lambert's Problem*. This posits the problem of determining an orbit given two position vectors and the time of flight between them. Originally presented as an orbit determination problem [20], it can also be used to describe an orbit transfer between two points [21]. This was originally posed considering impulsive transfers and numerous solutions have been proposed including the classic solutions by Gauss, Lambert and Euler [22]. These solutions are all geometric in nature but require iteration to find a solution. Bate's method uses universal variables to ease this iterative process [23]. Most recent work in this area has focused on increasing the efficiency of the available numerical solutions to Lambert's problem [24–26]. Breaking with this trend, a recent analytical solution has been developed for a single-impulse transfer that is extremely fast and non-iterative, making it ideal for preliminary trajectory design, or to provide an initial guess for the existing iterative methods [27].

The consideration of Lambert's problem as applied to low-thrust trajectories came much later than the impulsive transfer formulation. Inspired by missions such as SMART-1 [28], which pioneered solar-electric propulsion as an enabler for deep-space exploration, these solutions primarily focused on lunar and inter-planetary trajectories. These problems were mainly solved using either direct [29] or indirect numerical methods [30]. These both are highly dependent on the initial guesses provided and must be iterated to find a solution. As a result, quick, low-fidelity solutions have been developed as a method of providing accurate initial guesses. These predominantly take the form of shape-based solutions in which the trajectory is described by a geometrically defined spiral [31, 32] or a sequence of connected spirals or arcs [33]. These solutions are generally restricted to planar trajectories obtained using tangential thrust in order to form an analytical solution. Other approaches exist that attempt to combine the accuracy of numerical solutions with the speed of analytical expressions. One such solution is that presented in [34], which uses analytical formulations of the equations of motion

to create slightly modified Keplerian arcs and combines them in a finite elements approach to enable a numerical solution. Another method, presented by Avanzini et al., uses perturbative expansions of the equinoctial elements to formulate the low-thrust Lambert problem as a two-point boundary problem [35]. They divide the trajectory into a series of arcs and impose an arrival time boundary constraint to obtain a solution. This solution has the ability to consider large plane and eccentricity changes, and provides a compromise between accuracy and speed. However, it requires iteration to find a final solution and, as is stated, the efficiency of the method is thus highly dependent on the accuracy of the provided initial guess. In addition, many of these solutions are not applicable for low-thrust transfers in Earth orbit as they do not account for the perturbations caused by an oblate central body. Gao does consider the perturbing effect of an oblate central body in his solution in order to include Earth escape, using continuous tangential low-thrust, in the trajectory optimisation [36]. This is done by averaging the change in each of the orbit elements as a result of the perturbing forces over a single orbit and then integrating these with respect to the orbital energy until escape conditions are reached. While this allows for a relatively quick solution it does require incremental integration of the governing equations of motion [37].

1.1.2 Satellite Reconnaissance

Extending Lambert's problem to consider the ground track of the satellite, rather than its in-orbit position, produces the satellite reconnaissance problem. This requires a flyover of a target, or targets, on the surface of the central body. Passive satellite reconnaissance focuses on the design of a satellite orbit that can maximise coverage of a target, or targets, without the use of a propulsion system; instead, natural orbit perturbations are often exploited to produce a favourable ground track. This problem has received great attention in recent years and primarily focuses on the use of numerical methods, such as differential evolution, to identify the orbit parameters that can maximise the desired coverage metrics [38–40].

The availability of a propulsion system on-board a satellite could enable a greater degree of flexibility with regards to satellite reconnaissance, by allowing operators to re-task a satellite to flyover a newly identified target. In particular, electric propulsion,

which is highly efficient, could allow for the flyover of numerous successive targets throughout a satellite mission. This concept was apparently first proposed by Guelman and Kogan in 1999 [41]. Their work aimed to find a trajectory capable of passing over a set of targets in a given time, as well as determining the associated thrust profile that would minimise propellant consumption. They considered only quasi-circular orbits that are unperturbed except for applied tangential low-thrust manoeuvres, and were able to define the trajectory connecting two sequential targets as a two-point boundary problem that could be solved analytically. They determined the problem of scheduling sequential flyovers to be a discrete optimisation problem and thus used a simulated annealing method to identify the minimum propellant solution. Jean and de Lafontaine extended this work by incorporating the effects of the first zonal harmonic of an oblate central body, also known as J_2, and generalising the method to give an expression for the time to target flyby following in-plane, low-thrust circular to circular manoeuvres described by either cubic or quartic guidance laws [42]. They then incrementally search through the possible solutions to find a trajectory with an acceptable acceleration profile.

The use of high-thrust manoeuvres to provide overflight of a target has also been studied. Although less efficient than electric propulsion in terms of propellant usage, high-thrust, impulsive transfers can potentially offer a faster response than a low-thrust system that must gradually change the spacecraft orbit parameters over a period of time. Showalter et al. proposed the use of high-thrust responsive manoeuvres in a military context to increase the persistence of coverage available to a region, while simultaneously increasing the unpredictability of the satellite's motion [43]. They assumed the spacecraft experienced only two-body Keplerian forces and used particle swarm optimisation to identify single and multiple pass responsive targeting manoeuvres capable of meeting a set of criteria. This work identified interesting relationships between the time of flight and the distance to the target at flyover and concluded that this concept of responsive overflight targeting was an interesting premise for further investigation. Zhu et al. developed a solution using a circular to circular Hohmann transfer to achieve flyover of a given ground target [44]. Multiple objectives are considered, including maximising coverage time of the target and minimising the propellant

required for the orbit transfer. Combining these into a fitness function, Zhu et al. use particle swarm optimisation and differential evolution to select a satellite from an available set and to optimise the manoeuvre trajectory. However, they note that an optimal solution cannot be guaranteed. This is a weakness of all numerical techniques that have been used to tackle this problem to date, for both low- and high-thrust scenarios, as they do not provide a complete view of the solution space.

There have been some recent attempts to solve the reconnaissance problem analytically. Work by Zhang et al. provides approximate, semi-analytical solutions to the targeting problem for coplanar tranfers using high-thrust propulsion [45, 46]. This method, based on Kepler's equations and considering up to four impulsive manoeuvres, can be applied to both circular and elliptical orbits and allows for the minimum energy trajectory to be found. The results are found to be sub-optimal compared with a numerical solver, but Zhang et al. highlight that they could provide an initial guess for higher precision models and may be useful in cases where fast computational speed is desired. For low-thrust propulsion, Zhang and Cao propose a semi-analytical shape-based method using coplanar transfers to adjust the longitude of the spacecraft ground track relative to a non-manoeuvring reference [47]. However, this is only applicable to cases in which the final orbit is predefined, and requires iteration to determine the shape-function coefficients for a minimum energy solution. Co et al. have developed a control algorithm that allows a single satellite in a circular orbit to pass over a given target using low-thrust electric propulsion, considering both continuous thrust and thrust-coast manoeuvres [12–14]. Co et al. use the difference in time of flyover between the manoeuvring satellite and a non-manoeuvring reference satellite as a metric, and can solve for this using a single equation. This method requires that the reference satellite's position be numerically propagated for a given time using third-party software. Using the produced ground track, the method identifies all close passes to the target that occur within the propagation time. These close passes are then ordered in terms of the soonest encounter, if the fastest overflight solution is desired, or by order of closest pass if the minimum propellant solution is desired. Discarding those that are infeasible, the fastest, or minimum energy, feasible solution can be found. This work by Co et al. has a number of advantages; being based on a straightforward, analytical expression,

this solution allows an unprecedented insight into the problem, providing, for example, the possible reach of a manoeuvre of this type in a given time, and the impact of the initial orbit parameters on the manoeuvre efficiency. This work also includes a comparison of the effectiveness of in-plane and out-of-plane manoeuvres, concluding that out-of-plane manoeuvres can allow for fine adjustments to the target flyover time, but they are highly inefficient compared with in-plane manoeuvres. Co et al.'s method also has the advantage of providing a range of feasible solutions for each manoeuvre to be performed, allowing the operator to manually select the desired strategy. However, its accuracy is limited as it does not consider the effect of J_2 on the satellite mean motion; this introduces significant errors when directly considering the position of the satellite's ground track. The greatest limitation to this method however, is its reliance on the numerical propagation of the reference satellite as a starting point for the manoeuvres. This propagation can be time consuming and in order to accommodate this Co et al. limit their searches to just three days in the future, potentially missing lower propellant options available beyond this point. The propagation must also be repeated for each additional manoeuvre, as well as for any additional satellites, and so the applicability of this method for large scale constellations, or scenarios involving multiple targets and manoeuvres, is questionable.

1.1.3 Constellation Reconfiguration

Applying the solution to Lambert's problem across multiple satellites arranged in a constellation allows for so-called *constellation reconfiguration*, where reconfiguration is taken to mean the changing of a constellation from one formation to another through the manoeuvring of the constituent satellites. This could be used, for example, to re-establish even satellite spacing following a unit failure, to adapt an existing constellation to accommodate additional spacecraft, or to position satellites in a constellation following launch injection. Incorporating consideration of the satellite ground track, as in the case of satellite reconnaissance, could additionally allow the coverage provided by the constellation to be altered in response to changing mission requirements. The reconfiguration of satellite constellations is thus an appealing option to enable responsiveness and adaptability in orbit, as well as having the potential to reduce launch costs

and reduce risk associated with large scale missions by enabing staged deployment [48].

Crisp et al. considered the problem of deploying a constellation of satellites from a single launch injection point using nodal precession to achieve the desired spacing of the orbit planes through right ascension of the ascending node [49]. Their case studies considered satellites in circular orbits and used in-plane thrust to change the satellite altitude, resulting in a difference in the orbit period and nodal drift rate of the satellites; no inclination change is considered. They used a semi-analytical orbit propagator, which considered J_2 effects as well as atmospheric drag, and were able to accurately recreate the deployment of the FORMOSAT-3/COSMIC constellation [50, 51]. However, this method required that the initial and final orbit parameters of the constellation be known in advance, meaning it is not an ideal method for trade-space exploration. Baranov et al. proposes that reconfiguring a constellation could most efficiently be achieved through the use of an intermediate drift orbit [52]. They use linearised equations of motion to evaluate the propellant cost of achieving a desired satellite separation in argument of latitude, right ascension of the ascending node, inclination and altitude using two impulsive transfers to enter and exit the intermediate drift orbit. Baranov et al. investigate these effects for Earth, Mars and Lunar orbits and note that in each case the initial orbit parameters of the satellites influence the efficiency with which the manoeuvres can be achieved. They also highlight that increasing the time spent in the drift orbit tends to reduce the amount of propellant required. Leppinen also considered constellation deployment from a single launch injection point, but proposed the use of drag-augmentation devices to achieve a desired change in altitude and thus control the orbital precession of the satelites; no controlled change in inclination or eccentricity is considered [53]. The proposed method estimates the desired change in right ascension of the ascending node of a satellite using Gauss's equations and then uses a third-party orbit propagator to complete the simulation based on the provided initial guess. This method, however, is of limited accuracy as it estimates the relative change in right ascension of the ascending node that can be achieved between two satellites at constant altitudes, without considering the gradual change in relative drift that would occur as the satellites' altitudes change. In addition, its reliance on drag-augmentation devices means that satellites must initially be launched to a higher altitude than the mission

orbit requires; this can increase launch costs and also places an upper bound on the operational orbit of the satellites. Foster et al. recently published work on a novel method of satellite in-plane phasing using differential drag [54]. This method uses simulated annealing to sequentially solve the problems of assigning the satellites to the optimal orbit slots, as well as generating the optimal command profile to achieve this phasing in the shortest time. This method has been successfully used to deploy some of Planet's *Dove* satellites, though inaccuracies in predicting the ballistic coefficient of the satellites resulted in issues in on-orbit implementation [54].

Work by Davis focused on the expansion of a constellation through the addition of supplementary satellites, and proposed the use of Hohmann transfer manoeuvres for such a reconfiguration [55]. He approximated the solution to Lambert's problem using a 4th order polynomial and then used the auction algorithm proposed by De Weck et al. to assign the satellites to appropriate slots in the final constellation [56]. Ferringer et al. considered the opposite problem, of reconfiguring a satellite constellation after a loss of capacity has occurred. They simplify the problem to consider only satellites in circular orbits and use only in-plane phasing to reconfigure, due to the high propellant costs associated with plane change manoeuvres. They used a multi-objective evolutionary algorithm to solve the problem of both designing the new constellation and reassigning the satellites within it [57]. Appel et al. developed a method for constellation reconfiguration to enable expansion of an existing constellation through the addition of satellites using co-planar manoeuvres in both circular and eccentric orbits. They approached the problem by concurrently optimising the transfer trajectory of each spacecraft to minimise propellant usage, and the assignment of each satellite to a new orbit slot [58]. Appel et al. achieved this by providing a coupled set of terminal orbit parameters for the satellites and using an indirect method of numerical optimisation, based on the calculus of variations, to solve the resulting set of differential equations. Through combined optimisation of both trajectory and orbit slot assignment, this method avoids having to calculate all possible transfer trajectory combinations in order to find the optimal assignment. This method is presented asssuming two-body Keplerian dynamics only, though it is stated that perturbations could be incorporated into the solution. This work does not consider constellation design, instead assuming

that the final constellation configuration is known in advance. It also assumes that this final configuration can be defined in terms of the relative satellite positions in the final constellation. This is a fair assumption when considering expansion of constellations designed for global coverage, as Appel et al. do, but limits the applicability to other scenarios. For example, providing targeted coverage to a region relies not only on the relative positions of the satellites, but also on their position relative to the Earth and, as such, is dependent on the manoeuvre time; such a mission could not be considered by this method without extension of the work. Fakoor et al. use a similar approach to Appel et al., optimising the assignment of the satellites to the target orbits, and the orbital transfer in one step, but their work is not constrained to consider only coplanar transfers [59]; they use hybrid invasive weed optimisation/particle swarm optimisation to achieve this. Mushet and McInnes used coupled selection equations to allocate satellites in a constellation to targets on the Earth and design low-thrust manoeuvres using tangential thrust to shift their repeating ground tracks to pass over these targets [60]. They also applied an artificial potential field controller to generate the associated thrust profile. The model used excluded any orbit perturbations and is applicable only to circular orbits.

Consideration has also been given to how to design a constellation to enable efficient future reconfiguration. Legge considers constellations consisting of satellites that can transfer from their nominal orbits to repeating ground track orbits to obtain frequent flyovers of targets [61]. These manoeuvres are assumed to be performed using coplanar, circular to circular Hohmann transfers. Legge highlights that traditional constellation designs are non-optimal for reconfigurable missions and that when designing for reconfiguration, unusual constellation architectures can offer improved performance. In particular, Legge proposes asymmetrical constellation patterns that are shown to outperform traditional symmetric configurations. His work concludes that constellations capable of reconfiguration have a lifecycle cost, excluding operational costs, of 20–70% less than static constellations that provide similar levels of persistence of coverage. This clearly demonstrates the advantages these constellations can provide and motivates future work in the area. Legge's work however does not consider the option of using electric propulsion for reconfiguration, an area he suggests warrants further investiga-

tion. A significant constraint on the usability of Legge's work is that his design and optimisation tools were implemented on a 1024-processor cluster using parallel computing resources, restricting their use to those with access to high-performance facilities. Even with such high-powered computing, the run time for 85 cases was on the order of three months. Paek et al. have built on Legge's work by developing a tool that can run numerous reconfigurations and use a genetic algorithm to concurrently optimise satellite and constellation design [62]. However, this tool also requires long run times, and the authors highlight that the length of time required to propagate the satellite manoeuvres is a key limitation of the process.

1.2 Key Contributions

The preceding literature review has highlighted that there exists a gap in the research pertaining to manoeuvrable satellites. Much of the existing body of work has focused on applying optimisation techniques to both satellite reconnaissance and constellation reconfiguration. These offer techniques to solve specific reconnaissance and reconfiguration problems, and allow for optimal control and scheduling profiles to be identified. They can also consider a variety of manoeuvre profiles, including in- and out-of-plane thrusting, varying acceleration, and plane change manoeuvres, and can concurrently optimise the thrust profile and direction to minimise transfer time or fuel usage. However, these methods do not allow for a full overview of the solution space to be generated and thus restrict the insight available to the user. They also require long run times when multiple satellites or complex scenarios are considered. In addition, the research has overwhelmingly focused on impulsive manoeuvres, in spite of the notable advantages provided by low-thrust systems. Research by Co et al. stands alone as offering a straight-forward, analytical solution to the reconnaissance problem using low-thrust propulsion. It achieves this by restricting the problem to consider only circular orbits with a constant inclination. This reduces the generality of the solution, but offers benefits in terms of solution speed and the insights obtained. However, the need to numerically propagate the satellite orbit before applying the technique limits its scalability.

The work described in this dissertation aims to complement the existing research

by providing a solution to the satellite targeting problem that is fully-analytical, quick to solve, and scalable across multiple satellites and manoeuvres. It will also be general, allowing it to be applied to problems of rendezvous, as well as satellite reconnaissance, and scalable to the problem of constellation reconfiguration. To enable this, a general perturbation method based on the Gauss-Lagrange variation of parameters (VOP) equations is developed. These equations express the change in classical orbital elements over time as a function of applied accelerations or perturbations. Creation of a fully-analytical solution will require simplification of the problem; as such, this work will focus on a restricted Lambert rendezvous problem, considering only satellites in circular orbits, performing circular to circular, coplanar transfers using low-thrust tangential thrusting, with an optional coast arc. The accuracy of the developed solution will be investigated before being applied across a range of mission scenarios to demonstrate the applicability and scalability of the resulting solution.

The key contributions of this body of work are

1. A fully-analytical method that approximates the solution to the presented restricted Lambert rendezvous problem. This considers low-thrust circular to circular, coplanar transfers using tangential thrusting with an optional coast arc, and includes central body perturbations of the first zonal harmonic, J_2.

2. A fully-analytical solution to the satellite reconnaissance problem based on the developed solution to the restricted low-thrust Lambert problem. This allows for a manoeuvre selection trade-off to be performed by explicitly defining the distance to the target at flyover, equivalent to the target look-angle, in terms of the change in velocity required for the manoeuvre, and the time taken for the manoeuvre.

3. A quantification of the performance improvement provided by the responsive system versus the manoeuvre cost, in terms of change in velocity, for a range of responsive scenarios.

1.3 Relevant Publications

General perturbation method for satellite constellation reconfiguration using low-thrust maneuvers.

McGrath, C., Macdonald, M. Under review.

Applications of responsive small satellites with MIT TILE electrospray propulsion.

McGrath, C., Macdonald, M., Lozano, P., Miller, D., Krejci, D. Paper presented at 15th Reinventing Space Conference 2017, Glasgow, United Kingdom, 24/10/2017–26/10/2017. Paper BIS-RS-2017-28.

Analytical low-thrust satellite maneuvers for rapid ground target revisit.

McGrath, C., Macdonald, M. AIAA SPACE 2016 (p. 5294). DOI: 10.2514/6.2016-5294.

An analytical low-cost deployment strategy for satellite constellations.

McGrath, C., Kerr, E., Macdonald, M. Paper presented at 13th Reinventing Space Conference 2015, Oxford, United Kingdom, 9/11/15–12/11/15. Paper BIS-RS-2015-45.

Design of a reconfigurable satellite constellation.

McGrath, C., Macdonald, M. Paper presented at 66th International Astronautical Congress 2015, Jerusalem, Israel, 12/10/15–16/10/15. Paper IAC-15.C1.9.4.

Chapter 2

Method

A review of the existing literature, presented in Chapter 1, has highlighted the need for a solution to the satellite rendezvous problem that can be analysed quickly to obtain a full view of the solution space, and can be applied to diverse scenarios, including satellite reconnaissance and constellation reconfiguration. To address this, an analytical general perturbation solution to a restricted Lambert rendezvous problem will be developed using the Gauss-Lagrange variation of parameters (VOP) equations. General perturbation techniques were selected as they can be solved analytically over a certain time interval by introducing approximations to the governing equations of motion [63, 64].

The restricted problem addressed considers only circular to circular, coplanar transfers performed using low-thrust manoeuvres applied in the tangential direction, as previous research has shown out-of-plane thrusting to be highly inefficient compared with in-plane thrusting when a change in the satellite ground track is desired [14]. A single, optional coast arc is included in the manoeuvre as this has been shown to significantly reduce the amount of propellant required to achieve flyover of a target [12]. Note that in order to maintain a fully-analytical solution the orbit inclination is assumed to remain constant, and the satellite is assumed to maintain a constant altitude during the coast arc by thrusting to counteract the effect of atmospheric drag; this assumption is applied to all 'coasting phases' and 'coast arcs' throughout this work. The effect of atmospheric drag is neglected during the altitude change phases of the manoeuvre.

In addition, to allow the VOP equations to be integrated over the change in semi-major axis that occurs during the manoeuvre and obtain an analytical solution, it is assumed that the acceleration provided by the propulsion system is constant. This assumes that the propulsion system is not throttled during the manoeuvre, and that the spacecraft mass remains constant; this is a valid assumption when considering the use of low-thrust electric propulsion for which the propellant mass consumed will be very small compared to the spacecraft mass. The resulting satellite manoeuvre strategy is a 3-phase manoeuvre that consists of:

- *Phase 1*: An altitude change manoeuvre in which the satellite increases or decreases its altitude relative to its initial orbit. This is done using continuous low-thrust propulsion with a constant acceleration.
- *Phase 2*: A coast arc in which the satellite is assumed to maintain a constant altitude by thrusting to counteract the effect of atmospheric drag.
- *Phase 3*: A second altitude change phase in which the satellite moves to the desired final altitude; this may or may not be the same as the initial altitude at the beginning of phase 1. This manoeuvre is performed using continuous low-thrust propulsion with a constant acceleration of the same magnitude as in phase 1.

The 3-phase manoeuvre is shown in Figure 2.1. This use of three phases is similar to the three sequence transfer found by Cerf to offer the minimum propellant low-thrust transfer between circular orbits when the effects of J_2 are included [65]. Note that not all phases are required to be present for the solution to be valid; one or more of the phases can be excluded without fundamentally altering the solution presented.

The proposed manoeuvre strategy exploits the natural orbital motion of the satellite to achieve the desired change in the location of the satellite or sub-satellite point. Changing the satellite's altitude has a direct effect on the orbit period and can be used to change the satellite's true anomaly. In addition, the magnitude of the natural disturbances perturbing the satellite orbit are dependent on the satellite altitude. Thus, by changing the altitude of the satellite, these perturbations can be exploited to achieve the desired change in the satellite's orbital elements, and consequently its ground track.

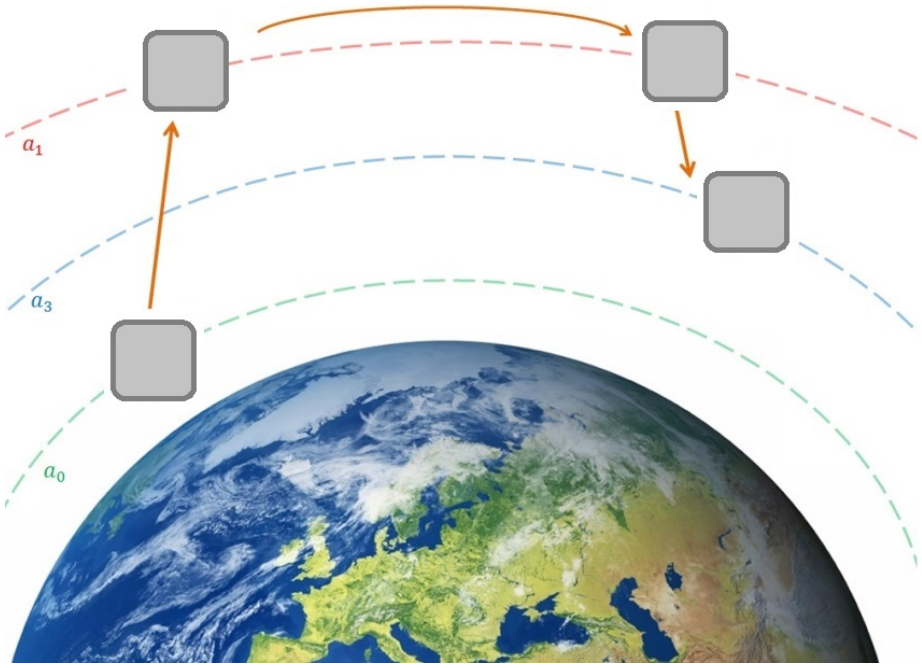

Figure 2.1: Schematic of 3-phase manoeuvre. Initial orbit (a_0), intermediate orbit (a_1), and final orbit (a_3) are marked by dashed lines.

Knowing this, an analytical expression can be created that defines the change in right ascension of the ascending node (RAAN) and argument of latitude (AoL) achieved during the 3-phase manoeuvre as a function of the total time taken and the total change in velocity (ΔV) required for the manoeuvre. This is then linked to the spacecraft ground track to determine the sub-satellite point location after the 3-phase manoeuvre has been performed.

To create a fully-analytical solution that can be rapidly solved, only secular perturbations of the orbit are considered in the developed solution. These are long-term, non-periodic perturbations, which, if left unaltered, will cause an ever increasing change in the orbital elements. This is distinct from long-periodic and short-periodic variations, which cause periodic variations in the orbital elements as a function of the orbit period, and the motion of the line of apsides or the line of nodes. It is necessary to carefully consider which secular perturbations should be included in the general perturbation solution, in order to maintain a balance between accuracy and solution speed. For a spacecraft in low Earth orbit (LEO), such as the Earth observation (EO) satellites considered in this dissertation, secular orbit perturbations come from four primary

sources: the non-spherical gravitational field of the Earth; the presence of additional gravitational fields; the effect of atmospheric drag (also called 'atmospheric friction'); and disturbances caused by solar radiation pressure [63, 64].

The perturbing effect of the non-spherical gravitational field of the Earth is dominated by the first zonal harmonic, also known as J_2, which is caused by the oblateness of the Earth about its polar axis. This is the most significant disturbance for LEO satellites and its effect is of key importance in accurately determining the position of the satellite post-manoeuvre. The next largest disturbing term due to the Earth's oblateness, J_3, is three orders of magnitude smaller than J_2. Due to the relatively small effect of the higher order disturbance terms of J_3 and beyond, it was decided not to include them in the developed general perturbation solution. However, it is of note that it would be straightforward to include their secular effects, were it deemed desirable, by incorporating them into the disturbing function used in the Langrange VOP equations in Section 2.1.

The Sun and the Moon are the two main external gravitational fields that will disturb the orbit of an Earth orbiting satellite, but their effect is generally much smaller than that of the central body for satellites at altitudes lower than geosynchronous orbit. Over long periods, on the order of years, these effects can become significant, but over the time scales considered herein their effect will remain small. As such it was deemed acceptable to exclude them from the solution.

The magnitude of the perturbing effect of atmospheric drag is highly dependent on the spacecraft properties, as well as the orbit altitude, but for a LEO satellite it is generally considered to be the most significant disturbance after central body oblateness. Atmospheric drag can have a notable impact on the satellite orbit, and its consideration for long-duration scenarios is vital. However, it was not possible to directly include its effects in the general perturbation solution whilst maintaining a fully-analytical solution. To tackle this, two simplifications are adopted. Firstly, it is assumed that the satellite thrusts to counteract the effects of atmospheric drag and maintain a constant altitude during phase 2, the coast arc, as well as during any other coast phases. Secondly the effect of atmospheric drag is not considered during the altitude change manoeuvre phases; this is deemed an acceptable simplification due to

the relatively short duration of these phases.

Solar radiation pressure effects are also highly dependent on spacecraft, and orbit, properties. For the cases considered herein, the spacecraft are assumed to operate at altitudes less than 800 km, in which regime the effect of solar radiation pressure is much smaller than that of atmospheric drag. As such, the effects of solar radiation pressure are not considered in the solution.

Based on the above discussion, the general perturbation solution describing the 3-phase satellite manoeuvre can be developed including only the secular effects of J_2, with the effects of atmospheric drag accounted for indirectly during the coast arc. The accuracy of this simplification will be explored in Chapter 4.

2.1 Fundamental Equations

The time rate of change of a satellite's orbital elements can be expressed as a sum of the conservative and non-conservative perturbing forces acting on the satellite [66]. The Lagrange VOP equations provide a convenient method to determine the effect of conservative forces acting on the satellite, while the Gauss VOP equations are more appropriate for the consideration of non-conservative perturbations, such as those caused by a constant applied thrust.

2.1.1 Lagrange Variation of Parameters Equations

The Lagrange VOP equations describe the time rate of change of the orbital elements as a result of a disturbing function, R. These are given by [67] and [63] as

$$\frac{da}{dt} = \frac{2}{na}\frac{\partial R}{\partial M_0} \tag{2.1}$$

$$\frac{de}{dt} = \frac{1-e^2}{na^2e}\frac{\partial R}{\partial M_0} - \frac{\sqrt{1-e^2}}{na^2e}\frac{\partial R}{\partial \omega} \tag{2.2}$$

$$\frac{di}{dt} = \frac{1}{na^2\sqrt{1-e^2}\sin(i)}\left(\cos(i)\frac{\partial R}{\partial \omega} - \frac{\partial R}{\partial \Omega}\right) \tag{2.3}$$

$$\frac{d\Omega}{dt} = \frac{1}{na^2\sqrt{1-e^2}\sin(i)}\frac{\partial R}{\partial i} \tag{2.4}$$

$$\frac{d\omega}{dt} = \frac{\sqrt{1-e^2}}{na^2e}\frac{\partial R}{\partial e} - \frac{\cot(i)}{na^2\sqrt{1-e^2}}\frac{\partial R}{\partial i} \tag{2.5}$$

$$\frac{dM_0}{dt} = -\frac{1-e^2}{na^2e}\frac{\partial R}{\partial e} - \frac{2}{na}\frac{\partial R}{\partial a} \tag{2.6}$$

where a is the semi-major axis, e is the eccentricity, i is the inclination, Ω is the right ascension of the ascending node, ω is the argument of perigee and t is time. M_0 is the initial value of the mean anomaly, with the final mean anomaly given by $M = M_0 + nt$ such that

$$\frac{dM}{dt} = n - \frac{1-e^2}{na^2e}\frac{\partial R}{\partial e} - \frac{2}{na}\frac{\partial R}{\partial a} \tag{2.7}$$

where n is the mean motion defined as $n = \sqrt{\mu/a^3}$, with μ being the standard gravitational parameter of Earth.

To consider only the secular effects of J_2, the relevant disturbing function can be averaged over one orbit period as in [67] and [63] to give

$$R_{avg} = -\frac{3}{2}n^2R_e^2J_2\left(\frac{1}{(1-e^2)^{3/2}}\right)\left(\frac{\sin^2(i)}{2} - \frac{1}{3}\right) \tag{2.8}$$

where R_e is the mean radius of the Earth, and J_2 is the coefficient of the second-order zonal harmonic of Earth. In an unperturbed system $\frac{dM}{dt} = n$ and is constant. However for an orbit perturbed by an oblate central body this is not the case, as is indicated by the presence of the disturbing function, R, in equation (2.7). To account for this, let $\frac{dM}{dt} = \bar{n}$, where $\bar{n}$ is the perturbed, or anomalistic, mean motion. Taking the partial derivatives as required and inserting the results into equation (2.7) gives an expression for the anomalistic mean motion as

$$\bar{n} = n\left[1 - \frac{3R_e^2J_2\sqrt{1-e^2}}{4p^2}\left(3\sin^2(i) - 2\right)\right] \tag{2.9}$$

where p is the semi-latus rectum defined as $p = a(1-e^2)$.

Continuing with the method described in [67], inserting the partial derivatives of (2.8) into equations (2.1)–(2.7), and using equation (2.9), gives the rate of change of the orbital elements of a satellite experiencing secular J_2 perturbations, as

$$\left(\frac{da}{dt}\right)_{J_2} = 0 \tag{2.10}$$

$$\left(\frac{de}{dt}\right)_{J_2} = 0 \tag{2.11}$$

$$\left(\frac{di}{dt}\right)_{J_2} = 0 \tag{2.12}$$

$$\left(\frac{d\Omega}{dt}\right)_{J_2} = -\frac{3\bar{n}R_e^2 J_2}{2p^2}\cos(i) \tag{2.13}$$

$$\left(\frac{d\omega}{dt}\right)_{J_2} = \frac{3\bar{n}R_e^2 J_2}{4p^2}\left(4 - 5\sin^2(i)\right) \tag{2.14}$$

$$\left(\frac{dM}{dt}\right)_{J_2} = \bar{n} = n\left[1 - \frac{3R_e^2 J_2\sqrt{1-e^2}}{4p^2}\left(3\sin^2(i) - 2\right)\right]. \tag{2.15}$$

For a circular orbit, $e = 0$ and $p = a$, which is equal to the orbit radius. This further reduces equations (2.13), (2.14), and (2.15) to

$$\left(\frac{d\Omega}{dt}\right)_{J_2} = -\frac{3\bar{n}R_e^2 J_2}{2a^2}\cos(i) \tag{2.16}$$

$$\left(\frac{d\omega}{dt}\right)_{J_2} = \frac{3\bar{n}R_e^2 J_2}{4a^2}\left(4 - 5\sin^2(i)\right) \tag{2.17}$$

$$\left(\frac{dM}{dt}\right)_{J_2} = \bar{n} = n\left[1 - \frac{3R_e^2 J_2}{4a^2}\left(3\sin^2(i) - 2\right)\right]. \tag{2.18}$$

2.1.2 Gauss Variation of Parameters Equations

The Gaussian form of the VOP equations provides a description of the time rate of change of the orbital elements as a result of perturbations that are expressed as disturbing accelerations or specific forces. The standard form of the Gauss VOP equations are given by [63] and [68] as

$$\frac{da}{dt} = \frac{2}{n\sqrt{1-e^2}}\left(e\sin(\theta)A_R + \frac{p}{r}A_S\right) \tag{2.19}$$

$$\frac{de}{dt} = \frac{\sqrt{1-e^2}}{na}\left(\sin(\theta)A_R + \left[\cos(\theta) + \frac{e+\cos(\theta)}{1+e\cos(\theta)}\right]A_S\right) \tag{2.20}$$

$$\frac{di}{dt} = \frac{r\cos(u)}{na^2\sqrt{1-e^2}} A_W \tag{2.21}$$

$$\frac{d\Omega}{dt} = \frac{r\sin(u)}{na^2\sqrt{1-e^2}\sin(i)} A_W \tag{2.22}$$

$$\frac{d\omega}{dt} = \frac{\sqrt{1-e^2}}{nae}\left(-\cos(\theta) A_R + \sin(\theta)\left[1+\frac{r}{p}\right] A_S\right) - \frac{r\cot(i)\sin(u)}{h} A_W \tag{2.23}$$

$$\frac{dM_0}{dt} = \frac{1}{na^2 e}\left(\left[p\cos(\theta) - 2er\right] A_R - \left[p+r\right]\sin(\theta) A_S\right) \tag{2.24}$$

where the specific angular momentum $h = \sqrt{\mu p}$, θ is the true anomaly, r is the orbit radius and u is the argument of latitude. A_S, A_R and A_W are the acceleration components of the disturbing force in the transversal direction, radial direction and normal to the orbital plane respectively.

The only non-conservative force being directly considered is the spacecraft propulsion system acceleration; atmospheric drag does produce a non-conservative force, but it is assumed to be compensated for during any coast arcs, and it is neglected during the altitude change phases. During the altitude change phases, the propulsion system acceleration will be continually applied in the tangential direction, corresponding to the A_S acceleration component as all orbits are assumed to be circular. As this force is small, the orbit can be assumed to remain circular throughout the manoeuvre. Considering this non-conservative force only (i.e. $A_R = A_W = 0$) equations (2.19) to (2.24) reduce to

$$\left(\frac{da}{dt}\right)_{thrust} = \frac{2}{n\sqrt{1-e^2}}\left(\frac{p}{r} A_S\right) \tag{2.25}$$

$$\left(\frac{de}{dt}\right)_{thrust} = \frac{\sqrt{1-e^2}}{na}\left(\left[\cos(\theta) + \frac{e+\cos(\theta)}{1+e\cos(\theta)}\right] A_S\right) \tag{2.26}$$

$$\left(\frac{di}{dt}\right)_{thrust} = 0 \tag{2.27}$$

$$\left(\frac{d\Omega}{dt}\right)_{thrust} = 0 \tag{2.28}$$

$$\left(\frac{d\omega}{dt}\right)_{thrust} = \frac{\sqrt{1-e^2}}{nae}\left(\sin(\theta)\left[1+\frac{r}{p}\right] A_S\right) \tag{2.29}$$

$$\left(\frac{dM_0}{dt}\right)_{thrust} = \frac{1}{na^2 e}\left(-\left[p+r\right]\sin(\theta) A_S\right). \tag{2.30}$$

With the assumption that a circular orbit is maintained, $e = 0$, $p = r = a$ and $\left(\frac{de}{dt}\right)_{thrust} = 0$. As the propulsion acceleration is assumed to be constant throughout the altitude change phases, all periodic terms (i.e. those that are a function of the true anomaly, θ) can be ignored as the resulting perturbations will be zero when averaged over a single orbit period. The resulting equations are then

$$\left(\frac{da}{dt}\right)_{thrust} = \frac{2}{n} A_{prop} \tag{2.31}$$

$$\left(\frac{de}{dt}\right)_{thrust} = 0 \tag{2.32}$$

$$\left(\frac{di}{dt}\right)_{thrust} = 0 \tag{2.33}$$

$$\left(\frac{d\Omega}{dt}\right)_{thrust} = 0 \tag{2.34}$$

$$\left(\frac{d\omega}{dt}\right)_{thrust} = 0 \tag{2.35}$$

$$\left(\frac{dM_0}{dt}\right)_{thrust} = 0 \tag{2.36}$$

where A_{prop} is the propulsion system acceleration.

2.1.3 Combined Lagrange and Gauss Equations

Summing the equations from Sections 2.1.1 and 2.1.2, and using equation (2.9) to account for the change in mean motion as a result of J_2, gives full expressions for the time rate of change of the orbital elements under the influence of J_2 and with constant applied thrust. These are

$$\frac{da}{dt} = \left(\frac{da}{dt}\right)_{J_2} + \left(\frac{da}{dt}\right)_{thrust} = \frac{2}{\bar{n}} A_{prop} \tag{2.37}$$

$$\frac{de}{dt} = \left(\frac{de}{dt}\right)_{J_2} + \left(\frac{de}{dt}\right)_{thrust} = 0 \tag{2.38}$$

$$\frac{di}{dt} = \left(\frac{di}{dt}\right)_{J_2} + \left(\frac{di}{dt}\right)_{thrust} = 0 \tag{2.39}$$

$$\frac{d\Omega}{dt} = \left(\frac{d\Omega}{dt}\right)_{J_2} + \left(\frac{d\Omega}{dt}\right)_{thrust} = -\frac{3\bar{n}R_e^2 J_2}{2a^2}\cos(i) \tag{2.40}$$

$$\frac{d\omega}{dt} = \left(\frac{d\omega}{dt}\right)_{J_2} + \left(\frac{d\omega}{dt}\right)_{thrust} = \frac{3\bar{n}R_e^2 J_2}{4a^2}\left(4 - 5\sin^2(i)\right) \tag{2.41}$$

$$\frac{dM}{dt} = \left(\frac{dM}{dt}\right)_{J_2} + \left(\frac{dM}{dt}\right)_{thrust} = n\left[1 - \frac{3R_e^2 J_2}{4a^2}\left(3\sin^2(i) - 2\right)\right] = \bar{n}. \tag{2.42}$$

As the argument of perigee is undefined for circular orbits, it is helpful to instead consider the change in argument of latitude, u, defined as $u = \theta + \omega$. For a circular orbit, $\theta = M$ and as such the rate of change of the argument of latitude can be defined as

$$\frac{du}{dt} = \frac{dM}{dt} + \frac{d\omega}{dt} = \bar{n} + \frac{3\bar{n}R_e^2 J_2}{4a^2}\left(4 - 5\sin^2(i)\right). \tag{2.43}$$

2.2 Conversion to Mean Orbital Elements

The solution of the equations described in Section 2.1 includes thrust and secular perturbations resulting from the first zonal harmonic, J_2; no periodic contributions are considered due to the averaging of the disturbing function [67]. The resulting orbital elements calculated using these expressions are thus *mean elements*, as the short-periodic and long-periodic contributions have been ignored. Hence, for a consistent solution, mean elements should be used in the calculation of these expressions. There are many accepted methods to calculate mean orbital elements; for the analysis presented herein, Brouwer's definition of mean orbital elements is used [69]. The use of a different mean element set will impact the results obtained, however the practical issues of converting from osculating to mean elements and vice-versa do not affect the fundamental method presented [66, 70].

Of particular note is the conversion from osculating to mean semi-major axis. Brouwer's conversion from mean to osculating semi-major as presented by Jean and de Lafontaine [42] is

$$a = \bar{a} + \frac{3J_2 R_e^2}{2\bar{a}}\sin^2(i)\cos(2\bar{u}) \tag{2.44}$$

where $\bar{a}$ is the mean semi-major axis and $\bar{u}$ is the mean argument of latitude. From this, a calculation of the mean semi-major axis from the osculating can be approximated as

$$\bar{a} = a - \frac{3J_2R_e^2}{2a}\sin^2(i)\cos(2u)\,. \tag{2.45}$$

As will be discussed in Section 2.3, forming a fully-analytical solution describing the 3-phase transfer requires that the altitude change manoeuvres be integrated over the semi-major axis, rather than over time. As such, this conversion from osculating to mean semi-major axis can be implemented into the solution in two different ways, either by integrating over the mean semi-major axis or by integrating over the osculating semi-major axis.

2.2.1 Integration over Mean Semi-Major Axis

The most straightforward implementation of the method is to integrate over the mean semi-major axis. In this case, the mean semi-major axis should first be calculated using equation (2.45) and the numerical value then used in the equations of motion. This gives the governing equations as

$$\frac{d\bar{a}}{dt} = \frac{2}{\bar{n}}A_{prop} \tag{2.46}$$

$$\frac{de}{dt} = 0 \tag{2.47}$$

$$\frac{di}{dt} = 0 \tag{2.48}$$

$$\frac{d\Omega}{dt} = -\frac{3\bar{n}R_e^2J_2}{2\bar{a}^2}\cos(i) \tag{2.49}$$

$$\frac{du}{dt} = \bar{n} + \frac{3\bar{n}R_e^2J_2}{4\bar{a}^2}\left(4 - 5\sin^2(i)\right) \tag{2.50}$$

where

$$\bar{n} = n\left[1 - \frac{3R_e^2J_2}{4\bar{a}^2}\left(3\sin^2(i) - 2\right)\right]. \tag{2.51}$$

When integrated, these equations will be integrated over the mean semi-major axis, $\bar{a}$.

2.2.2 Integration over Osculating Semi-Major Axis

An alternate method of implementation is to integrate over the osculating semi-major axis. This is achieved by including the conversion from osculating to mean semi-major axis as part of the equations of motion. However, incorporating the conversion from osculating to mean semi-major axis directly into the equations of motion prevents a fully-analytical solution being obtained due to the complex functions produced during integration. To avoid this issue, the osculating semi-major axis value can be used in the equation for the rate of change of the semi-major axis with minimal impact on the solution accuracy. This gives the governing equations of motion as

$$\frac{da}{dt} = \frac{2}{\bar{n}'} A_{prop} \tag{2.52}$$

$$\frac{de}{dt} = 0 \tag{2.53}$$

$$\frac{di}{dt} = 0 \tag{2.54}$$

$$\frac{d\Omega}{dt} = -\frac{3\bar{n}R_e^2 J_2}{2\bar{a}^2}\cos(i) \tag{2.55}$$

$$\frac{du}{dt} = \bar{n} + \frac{3\bar{n}R_e^2 J_2}{4\bar{a}^2}\left(4 - 5\sin^2(i)\right) \tag{2.56}$$

where $\bar{n}$ is as given by equation (2.51), $\bar{a}$ is as given by equation (2.45) and

$$\bar{n}' = n\left[1 - \frac{3R_e^2 J_2}{4a^2}\left(3\sin^2(i) - 2\right)\right]. \tag{2.57}$$

Both the solution integrating over the mean semi-major axis and the solution integrating over the osculating semi-major axis have a similar level of accuracy, however there are certain considerations when integrating over the osculating semi-major axis that will be discussed in Section 3.2. For speed and simplicity, the solution has been integrated over the mean semi-major axis for all analyses in Chapters 3 and 4, except where otherwise stated. For ease of comparison with numerical solutions, the solution has been integrated over the osculating semi-major axis for the analyses in Chapters 5 and 6.

2.3 Change in Right Ascension of the Ascending Node and Argument of Latitude

2.3.1 Integration over Mean Semi-Major Axis

The rate of change of RAAN and AoL of the satellite when integrating over the mean semi-major axis are described by equations (2.49) and (2.50) respectively. During the coast arc the semi-major axis can be assumed to remain constant and equations (2.49) and (2.50) can be integrated over time to produce expressions for the change in RAAN and AoL during this phase such that

$$\Delta\Omega_2 = \int_{t_1}^{t_2} \frac{d\Omega}{dt} dt \tag{2.58}$$

and

$$\Delta u_2 = \int_{t_1}^{t_2} \frac{du}{dt} dt \tag{2.59}$$

where $\Delta\Omega_2$ and Δu_2 are the changes in RAAN and AoL in phase 2, and t_1 and t_2 are the time at the beginning and end of phase 2 respectively.

During the altitude change phases, the semi-major axis is not constant and varies according to equation (2.46). As a result, equations (2.49) and (2.50) cannot be directly integrated over time. By combining equations (2.46) and (2.49), an expression for the change in RAAN as a function of the mean semi-major axis can be produced in the form of

$$\frac{d\Omega}{d\bar{a}} = -\frac{3\bar{n}^2 R_e^2 J_2}{4\bar{a}^2 A_{prop}} \cos(i) \,. \tag{2.60}$$

Assuming inclination and acceleration remain constant throughout the altitude change manoeuvre, equation (2.60) can be integrated with respect to the mean semi-major axis to give the change in RAAN over the course of the altitude change manoeuvre as

$$\Delta\Omega_1 = \int_{\bar{a}_0}^{\bar{a}_1} \frac{d\Omega}{d\bar{a}} d\bar{a} \tag{2.61}$$

and

$$\Delta\Omega_3 = \int_{\bar{a}_2}^{\bar{a}_3} \frac{d\Omega}{d\bar{a}} d\bar{a} \tag{2.62}$$

where $\Delta\Omega_1$ and $\Delta\Omega_3$ are the change in RAAN in phase 1 and phase 3 respectively, $\bar{a}_0$ and $\bar{a}_1$ are the mean semi-major axis at the beginning and end of phase 1 respectively, and $\bar{a}_2$ and $\bar{a}_3$ are the mean semi-major axis at the beginning and end of phase 3 respectively.

Similarly, combining equation (2.46) and equation (2.50) gives an expression for the change in AoL as a function of the mean semi-major axis as

$$\frac{du}{d\bar{a}} = \frac{\bar{n}^2}{2A_{prop}} \left(1 + \frac{3R_e^2 J_2}{4\bar{a}^2} \left(4 - 5\sin^2(i)\right)\right). \tag{2.63}$$

This can be integrated with respect to the mean semi-major axis to give the change in AoL over the course of the altitude change manoeuvres as

$$\Delta u_1 = \int_{\bar{a}_0}^{\bar{a}_1} \frac{du}{d\bar{a}} d\bar{a} \tag{2.64}$$

and

$$\Delta u_3 = \int_{\bar{a}_2}^{\bar{a}_3} \frac{du}{d\bar{a}} d\bar{a} \tag{2.65}$$

where Δu_1 and Δu_3 are the change in AoL in phase 1 and phase 3 respectively.

2.3.2 Integration over Osculating Semi-Major Axis

When integrating over the osculating semi-major axis, the rate of change of RAAN and AoL of the satellite are described by equations (2.55) and (2.56). These can be integrated over time to produce expressions for the change in RAAN and AoL during phase 2 as given by equations (2.58) and (2.59).

The rate of change of the osculating semi-major axis of the satellite is as given by equation (2.52) for the case in which the equations are integrated over the osculating semi-major axis. In this case, the expressions for the change in RAAN and AoL during the altitude change phases as a function of the change in osculating semi-major axis become

$$\frac{d\Omega}{da} = -\frac{3\bar{n}\bar{n}' R_e^2 J_2}{4\bar{a}^2 A_{prop}} \cos(i) \tag{2.66}$$

and

$$\frac{du}{da} = \frac{\bar{n}\bar{n}'}{2A_{prop}} \left(1 + \frac{3R_e^2 J_2}{4\bar{a}^2} \left(4 - 5\sin^2(i)\right)\right) \tag{2.67}$$

respectively, where $\bar{a}$ is as given by equation (2.45). Integrating these with respect to the osculating semi-major axis gives the change in RAAN and AoL over the course of the altitude change manoeuvres as

$$\Delta\Omega_1 = \int_{a_0}^{a_1} \frac{d\Omega}{da} da \tag{2.68}$$

$$\Delta\Omega_3 = \int_{a_2}^{a_3} \frac{d\Omega}{da} da \tag{2.69}$$

$$\Delta u_1 = \int_{a_0}^{a_1} \frac{du}{da} da \tag{2.70}$$

and

$$\Delta u_3 = \int_{a_2}^{a_3} \frac{du}{da} da \tag{2.71}$$

where a_0 and a_1 are the osculating semi-major axis at the beginning and end of phase 1 respectively, and a_2 and a_3 are the osculating semi-major axis at the beginning and end of phase 3.

2.4 Full Analytical Description of 3-Phase Manoeuvre

Combining the equations derived in Section 2.3 to account for all three phases of the manoeuvre gives fully-analytical expressions for the RAAN and AoL of the satellite after the manoeuvre is complete. That is,

$$\Omega_{total} = \Omega_0 + \Delta\Omega_1 + \Delta\Omega_2 + \Delta\Omega_3 \tag{2.72}$$

and

$$u_{total} = u_0 + \Delta u_1 + \Delta u_2 + \Delta u_3 \tag{2.73}$$

where $\Delta\Omega_j$ and Δu_j are the change in RAAN and AoL in the jth phase respectively. These expressions, while complete, express the final RAAN and AoL in terms of the semi-major axis at the end of phase 1 and the time required for the coast arc. For the purposes of this work it is more useful to express these changes in terms of the total manoeuvre time, t_{total}, and the required change in velocity.

2.4.1 Integration over Mean Semi-Major Axis

In order to express equations (2.72) and (2.73) in terms of the total manoeuvre time, the coast time is expressed as

$$t_2 = t_{total} - t_1 - t_3 \tag{2.74}$$

where t_1 and t_3 are the time taken for the phase 1 and phase 3 manoeuvres respectively. Integrating equation (2.46) with respect to time for phases 1 and 3 independently and rearranging gives an expression for t_1 as

$$t_1 = \frac{\sqrt{\mu}\left(\bar{a}_0^{5/2}\left\{20\bar{a}_1^2 + 3J_2R_e^2\left[2 - 3\sin^2(i)\right]\right\} + 3\bar{a}_1^{5/2}J_2R_e^2\left[3\sin^2(i) - 2\right] - 20\bar{a}_1^{5/2}\bar{a}_0^2\right)}{20\bar{a}_0^{5/2}\bar{a}_1^{5/2}A_{prop}} \tag{2.75}$$

with t_3 being calculated using the same expression but with $\bar{a}_2$ in place of $\bar{a}_0$, and $\bar{a}_3$ in place of $\bar{a}_1$. Substituting these into equation (2.74), with the assumption that $\bar{a}_2 = \bar{a}_1$, and then into equations (2.72) and (2.73) allows the final RAAN and AoL of the satellite at the end of the 3-phase manoeuvre to be expressed in terms of the total time required for the manoeuvre, t_{total}, and the mean semi-major axis of the satellite at the end of phase 1, $\bar{a}_1$.

It is then possible to express the mean semi-major axis of the satellite at the end of phase 1 in terms of the change in velocity required to change the altitude of the satellite over the full manoeuvre, ΔV_{alt}. Assuming a small propellant mass flow rate

and a small propellant mass fraction [71], the change in velocity required to change the satellite altitude in phase 1 can be approximated as

$$\Delta V_1 = \left| \sqrt{\frac{\mu}{\bar{a}_1}} - \sqrt{\frac{\mu}{\bar{a}_0}} \right| \tag{2.76}$$

with ΔV_3 calculated using a similar expression but with $\bar{a}_3$ in place of $\bar{a}_0$. From this, an expression for the mean semi-major axis at the end of phase 1 as a function of the total ΔV required for altitude change manoeuvres, ΔV_{alt}, can be derived as

$$\bar{a}_1 = \frac{4\mu\bar{a}_0}{\mu + \bar{a}_0 \left(\sqrt{\frac{\mu}{\bar{a}_3}} \pm \Delta V_{alt}\right)\left(2\sqrt{\frac{\mu}{\bar{a}_0}} + \sqrt{\frac{\mu}{\bar{a}_3}} \pm \Delta V_{alt}\right)} \tag{2.77}$$

where $\Delta V_{alt} = \Delta V_1 + \Delta V_3$. Note this does not include the change in velocity required for atmospheric drag compensation during the coast arc, ΔV_2; this is discussed in Section 2.5. In equation (2.77), a '+' should be used in place of '$\pm$' in the case where the satellite decreases its altitude in phase 1 and increases it in phase 3, whilst a '$-$' should be used in place of '$\pm$' in the case where a satellite raises its altitude in phase 1 and lowers it in phase 3. Using this definition of $\bar{a}_1$ in equations (2.72) and (2.73), and assuming that the initial and final altitude of the satellite are known, fully-analytical expressions are produced for the RAAN and AoL at the end of the 3-phase manoeuvre as a function of the total time required for the manoeuvre and the ΔV used to change the satellite altitude. Full expressions for $\Delta\Omega_1$, $\Delta\Omega_2$, $\Delta\Omega_3$, Ω_{total} and Δu_1, Δu_2, Δu_3 and u_{total} as a function of ΔV_{alt} and t_{total} are given in Appendix A for the case in which integration is performed over the mean semi-major axis. Note that the equations are derived in such a way that only a single propulsive acceleration value for A_{prop} is required; in the case that the satellite raises its altitude in phase 1 a positive value should be used, whilst if the satellite lowers its altitude in phase 1 a negative value should be used.

2.4.2 Integration over Osculating Semi-Major Axis

For the method in which the equations of motion are to be integrated over the osculating semi-major axis, the expression for t_1 is obtained by integrating equation (2.52) with respect to time giving

$$t_1 = \frac{\sqrt{\mu}\left(a_0^{5/2}\left\{20a_1^2 + 3J_2R_e^2\left[2 - 3\sin^2(i)\right]\right\} + 3a_1^{5/2}J_2R_e^2\left[3\sin^2(i) - 2\right] - 20a_1^{5/2}a_0^2\right)}{20a_0^{5/2}a_1^{5/2}A_{prop}} \tag{2.78}$$

with t_3 being calculated using the same expression but with a_2 in place of a_0, and a_3 in place of a_1. Substituting into equation (2.74), with the assumption that $a_2 = a_1$, and then into equations (2.72) and (2.73) allows the final RAAN and AoL of the satellite at the end of the 3-phase manoeuvre to be expressed in terms of the total time required for the manoeuvre, t_{total}, and the osculating semi-major axis of the satellite at the end of phase 1, a_1.

The osculating semi-major axis of the satellite at the end of phase 1 can then be expressed in terms of the change in velocity required to change the altitude of the satellite over the full manoeuvre. The ΔV required to change the altitude of the satellite in phase 1 is approximated as

$$\Delta V_1 = \left|\sqrt{\frac{\mu}{a_1}} - \sqrt{\frac{\mu}{a_0}}\right|. \tag{2.79}$$

with ΔV_3 calculated using a similar expression but with a_3 in place of a_0. From this, an expression for the osculating semi-major axis at the end of phase 1 can be derived as

$$a_1 = \frac{4\mu a_0}{\mu + a_0\left(\sqrt{\frac{\mu}{a_3}} \pm \Delta V_{alt}\right)\left(2\sqrt{\frac{\mu}{a_0}} + \sqrt{\frac{\mu}{a_3}} \pm \Delta V_{alt}\right)}. \tag{2.80}$$

Using this definition of a_1 in equations (2.72) and (2.73) gives fully-analytical expressions for the RAAN and AoL at the end of the 3-phase manoeuvre for the case in which the equations are to be integrated over the osculating semi-major axis. Full expressions for $\Delta\Omega_1$, $\Delta\Omega_2$, $\Delta\Omega_3$, Ω_{total} and Δu_1, Δu_2, Δu_3 and u_{total} as a function of ΔV_{alt} and t_{total} are given in Appendix B for the case in which integration is performed over the osculating semi-major axis.

2.5 Atmospheric Drag Compensation during Coast Arc

The acceleration caused by the force of atmospheric drag can be approximated by

$$\vec{A}_{atm} = -\frac{1}{2}\frac{C_D\alpha}{m}\rho v_{rel}^2\frac{\vec{v_{rel}}}{|\vec{v_{rel}}|} \tag{2.81}$$

where v_{rel} is the relative velocity between the spacecraft and the atmosphere, C_D is the spacecraft coefficient of drag, α is the spacecraft effective area, m is the spacecraft mass and ρ is the atmospheric density at the spacecraft altitude. Making the assumption that the atmosphere is static, and that the atmospheric drag force acts only in the negative transversal direction gives

$$A_{atm} = -\frac{1}{2}\frac{C_D\alpha}{m}\rho v^2 \tag{2.82}$$

where v is the satellite velocity, which, for a circular orbit, can be expressed as

$$v = \sqrt{\frac{\mu}{\bar{a}}}. \tag{2.83}$$

The atmospheric density can be approximated using an exponential density model [72] as

$$\rho = \rho_{ref}\exp\left[-\frac{h_{ref}-h_1}{H}\right]. \tag{2.84}$$

where h_{ref} is the reference altitude, ρ_{ref} is atmospheric density at the reference altitude, h_1 is the spacecraft altitude and H is the scale height of the atmosphere. For all cases considered in this dissertation, this exponential model is implemented in the general perturbation method using the CIRA-72 atmospheric model for 25–500 km, and CIRA-72 with exospheric temperature $T_\infty = 1000$ K for 500–1000 km, as presented in [72].

Once the acceleration caused by atmospheric drag has been calculated for the given coast arc altitude using equation (2.82) the necessary ΔV to counteract this acceleration can be calculated as the required acceleration multiplied by the time of the coast phase,

$$\Delta V_2 = A_{atm}t_2. \tag{2.85}$$

This atmospheric drag compensation ΔV_2 is added to the ΔV required for altitude change, ΔV_{alt}, to give the total change in velocity as

$$\Delta V_{total} = \Delta V_{alt} + \Delta V_2. \tag{2.86}$$

It is of note that because the atmospheric model used is divided into altitude bands for the calculation of atmospheric density, it is not possible to express Ω_{total} and u_{total} in terms of ΔV_{total} whilst maintaining a fully-analytical solution. As such, the possible manoeuvre options are first calculated as a function of ΔV_{alt}, and ΔV_2 is then calculated and added to this to be included in the manoeuvre selection trade-off.

2.6 Analytical Description of Relative Satellite Motion

If the goal of a manoeuvre is to position the satellite relative to another satellite, it is necessary to account for the continued motion of the other satellite, herein referred to as the reference satellite, throughout the manoeuvre. The difference in RAAN between the manoeuvring satellite and the reference satellite can be calculated as

$$\Omega_{dif} = \Omega_{total} - \Omega_{ref} \tag{2.87}$$

where Ω_{total} is as given by equation (2.72) and, assuming the reference satellite performs no manoeuvres, Ω_{ref} can be calculated using equation (2.49) for the change in RAAN of a non-manoeuvring satellite, or equation (2.55) if integrating over the osculating semi-major axis.

The difference in AoL between the manoeuvring satellite and the reference satellite can be similarly calculated as

$$u_{dif} = u_{total} - u_{ref} \tag{2.88}$$

where u_{total} is as given by equation (2.73) and u_{ref} is calculated using equation (2.50), or equation (2.56) if integrating over the osculating semi-major axis. The full integrated solutions to these equations are given in Appendix A for the method in which the equations are integrated over the mean semi-major axis. Due to the size of the equations

for Ω_{dif} and u_{dif} produced by the method in which the equations are integrated over the osculating semi-major axis, these full expressions are not given; instead equations for Ω_{ref} and u_{ref} are given in Appendix B, alongside the equations for Ω_{total} and u_{total}.

2.7 Analytical Description of Ground Track Motion

If the aim of the manoeuvre is to target a specific point of interest (POI) on the ground, it is necessary to link the RAAN and AoL of the satellite post-manoeuvre to changes in the satellite ground track. Using spherical geometry, the geocentric latitude of the satellite's sub-satellite point (SSP), δ_{SSP}, at a given time can be calculated from the orbital elements by

$$\delta_{SSP} = \sin^{-1}\left(\sin i \sin u_{total}\right) \tag{2.89}$$

with the corresponding geocentric longitude of the SSP, Ψ_{SSP}, given as

$$\Psi_{SSP} = \tan^{-1}\left(\frac{\cos i \sin u_{total}}{\cos u_{total}}\right) - \omega_e t + \Omega_{total} - \Omega_{et0} \tag{2.90}$$

where Ω_{et0} is the right ascension of Greenwich at epoch (i.e. at $t = t_0$), and ω_e is the angular rate of rotation of the Earth [73]. It is necessary to include the inverse tangent function in this form to allow for the quadrant of the angle to be correctly determined.

The haversine formula given by

$$d = 2R_e \sin^{-1}\left[\sqrt{\sin^2\left(\frac{\delta_{SSP} - \delta_{POI}}{2}\right) + \cos\left(\delta_{SSP}\right)\cos\left(\delta_{POI}\right)\sin^2\left(\frac{\Psi_{SSP} - \Psi_{POI}}{2}\right)}\right] \tag{2.91}$$

can be used to calculate the great-circle distance between the sub-satellite point and the point of interest on the ground after the manoeuvre, assuming the geocentric latitude, δ_{POI}, and longitude, Ψ_{POI}, of the point of interest are known [74]. Note that the use of geocentric latitude and longitude values in equation (2.91) assumes a spherical Earth for the calculation of the distance between the satellite SSP and POI; due to the short distances being considered any errors arising from this will be small [75].

Using equations (2.89) and (2.90), the haversine distance, d, can be expressed in

terms of the orbital elements, and thus, using equations (2.72) and (2.73), as a function of the manoeuvre time, t_{total}, and the change in velocity required for the altitude change manoeuvre, ΔV_{alt}.

The partial derivative of equation (2.91) with respect to time, $\frac{\partial d}{\partial t_{total}}$ can be found analytically. By identifying the values of t_{total} for which $\frac{\partial d}{\partial t_{total}} = 0$, the extrema of the distance function, d, for a given ΔV_{alt} can be identified. Throughout this work, this is implemented using the 'EventLocator' method available in Wolfram Mathematica, which uses numerical methods to locate the roots of the function [76]. The second partial derivative, $\frac{\partial^2 d}{\partial t_{total}^2}$, can also be found analytically. Evaluating this at the locations of the extrema of d enables the minima of the function to be distinguished from the maxima. Any of these minima that have a value less than half the swath width of the satellite can be identified as manoeuvres that will finish with the point of interest in view of the satellite, assuming the satellite payload has a conical field of view. This full set of possible manoeuvres can then be evaluated by the user, providing them a full view of the solution space and the ability to select the manoeuvre that best meets their mission criteria. Each of these solutions will have a corresponding ΔV cost, manoeuvre time and distance to target associated with it; this is in contrast to the classical presentation of Lambert's problem in which the manoeuvre time is given. While it is possible to calculate manoeuvres requiring a given time using the derived method, due to the restrictions placed on the manoeuvres (i.e. only circular to circular, coplanar manoeuvres are considered), a rendezvous or target flyover requiring a given manoeuvre time cannot be guaranteed. Throughout this work, this method derived herein will be referred to as the 'general perturbation method'.

Chapter 3

Analysis

The method of satellite manoeuvring outlined in Chapter 2 requires that satellites be manoeuvred to different altitudes to achieve a change in their relative positioning or ground track. This can be done by either raising or lowering the satellite's altitude relative to its initial position. An example of the full solution space that can be produced using the fully-analytical general perturbation method derived in Chapter 2 is shown in Figure 3.1 as a 3-dimensional plot, and in Figure 3.2 as a contour plot. These show the distance from the point of interest to the sub-satellite point plotted for manoeuvre times up to one day, for an altitude-lowering manoeuvre using a range of ΔV_{alt} values from 0–120 m/s. The POI in this case is Los Angeles and the orbital constants and orbit parameters used are given in Tables 3.1 and 3.2. The manoeuvre durations that will finish with the POI in view for a given ΔV_{alt} can be found by locating the minima of the solution, as described in Section 2.7, and identifying those that fall within view of the satellite; these solutions are shown as red dots in Figure 3.2. Some of the solutions found will be infeasible as the required ΔV_{alt} cannot be produced in the allotted time using the defined propulsion system acceleration; these solutions can be readily discarded.

Figure 3.3 shows the same surface as Figure 3.1 plotted over a smaller region. The black contours are drawn along paths of constant manoeuvre time. These contours can be seen to cross the troughs and peaks of the surface, demonstrating how the function can vary with ΔV_{alt}. A single contour for a manoeuvre time of 121.25 hours is shown

in Figure 3.4. It is clear that the function varies smoothly with ΔV_{alt}, and that for a given manoeuvre time and ΔV_{alt} range there will be a minimum distance to the target corresponding to a single ΔV_{alt} value. Identifying these minima for which the target is in view gives the list of possible solutions for the specified time and ΔV_{alt} range.

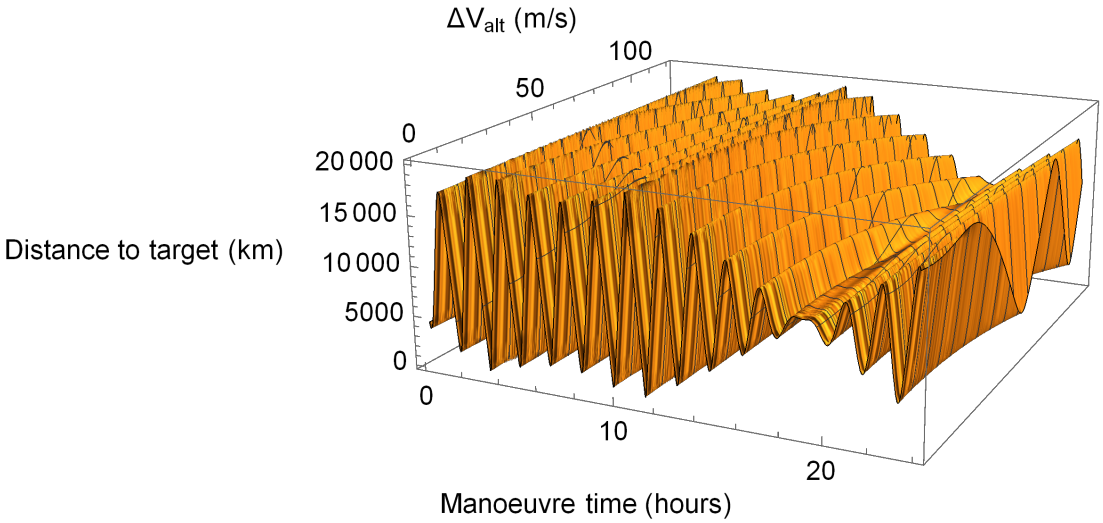

Figure 3.1: Distance to point of interest plotted as a function of total time and ΔV_{alt} required for the manoeuvre.

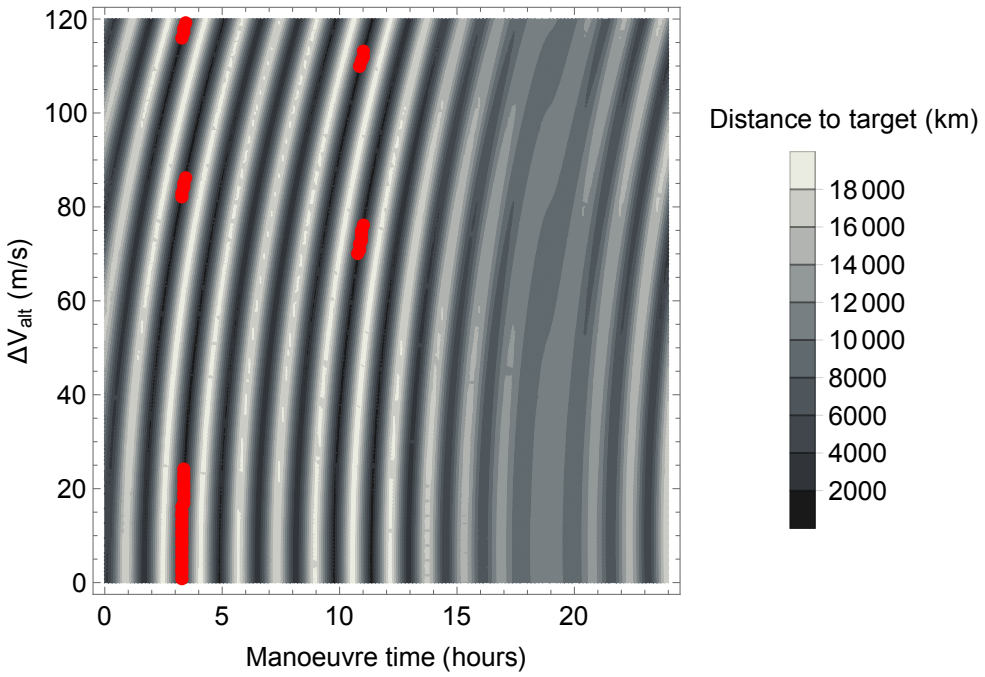

Figure 3.2: Distance to point of interest plotted as a function of total time and ΔV_{alt} required for the manoeuvre. Red dots indicate manoeuvres that end with the target in view of the satellite.

Table 3.1: Orbital constants.

Parameter	Symbol	Value	Units
Gravitational Parameter	μ	3.986×10^{14}	m^3/s^2
Radius of Earth	R_e	6.371×10^3	km
Coefficient of J_2 for Earth	J_2	1.0827×10^{-3}	—
Angular velocity of Earth	ω_e	7.2921×10^{-5}	rad/s

Table 3.2: Orbit parameters.

Parameter	Symbol	Value	Units
Propulsion acceleration	A_{prop}	$\pm 1.1667 \times 10^{-4}$	m/s^2
Inclination	i	51.64	deg
Initial/final osculating semi-major axis	a_0, a_3	6773	km
Initial/final mean semi-major axis	$\bar{a}_0$, $\bar{a}_3$	6767	km
Initial AoL	u_0	0	deg
Initial RAAN	Ω_0	0	deg
Latitude of POI	δ_{target}	34.05	deg
Longitude of POI	Ψ_{target}	-118.24	deg
Epoch	—	01 Jan 1990 00:00:00	—
Right ascension of Greenwich at epoch	Ω_{et0}	100.39	deg
Swath width	s	200	km

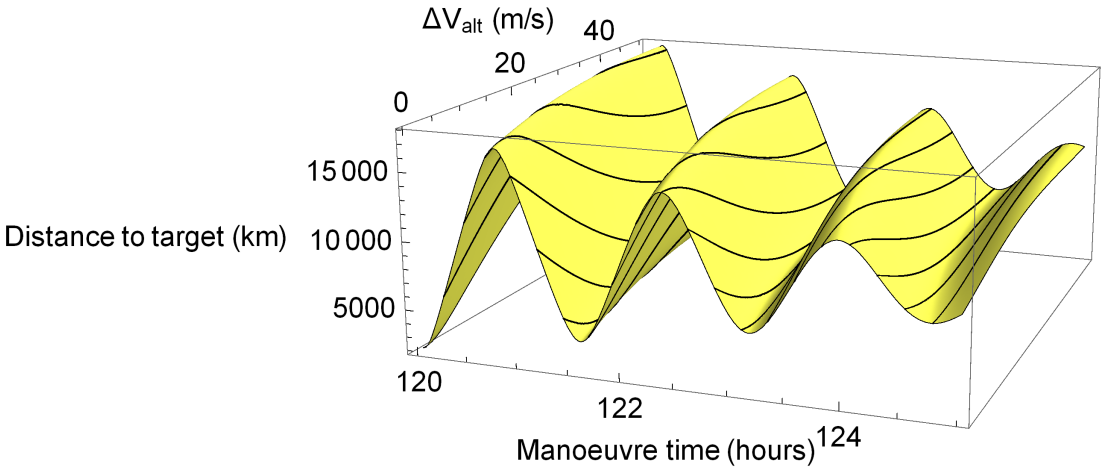

Figure 3.3: Zoomed graph of distance from sub-satellite point to point of interest plotted as a function of total time and ΔV_{alt}. Contours drawn at constant manoeuvre time.

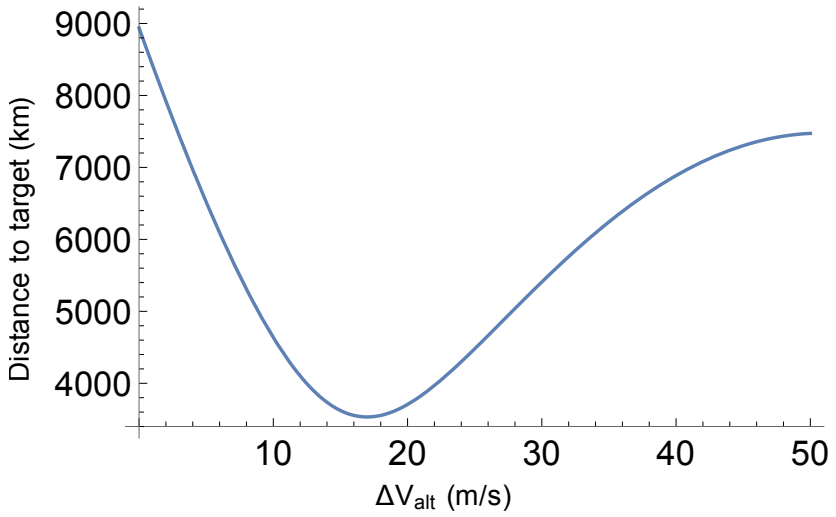

Figure 3.4: Graph of distance from sub-satellite point to point of interest plotted as a function of ΔV_{alt} for a manoeuvre time of 121.25 hours.

3.1 Comparison of Satellite-Lowering and -Raising Manoeuvres

This section will compare the RAAN and AoL change achievable using both satellite-lowering and satellite-raising manoeuvres. The parameters given in Tables 3.1 and 3.3 are used for this investigation. In all cases the results presented show the change in RAAN, Ω_{dif}, and AoL, u_{dif}, that can be achieved when compared with a non-manoeuvring reference satellite. It is assumed for this investigation that the satellite begins and ends its manoeuvres at the same altitude.

Table 3.3: Analysis mission parameters.

Parameter	Symbol	Value	Units
Propulsion acceleration	A_{prop}	$\pm 1.1667 \times 10^{-4}$	m/s^2
Inclination	i	45	deg
Initial/final osculating semi-major axis	a_0,a_3	6971	km
Initial/final mean semi-major axis	$\bar{a}_0$,$\bar{a}_3$	6965	km
Initial AoL	u_0	0	deg
Initial RAAN	Ω_0	0	deg
ΔV for altitude change	ΔV_{alt}	30	m/s
Manoeuvre time	t_{total}	7	days

3.1.1 Changing Right Ascension of the Ascending Node

Figure 3.5 shows contours of desired RAAN change and the corresponding manoeuvre time and ΔV_{alt} for both satellite-lowering and -raising manoeuvres. This graph shows that for a given desired change in RAAN, a lowering manoeuvre requires less time than a raising manoeuvre using the same ΔV_{alt}. The relative difference between the two increases as the desired RAAN separation increases. For example, it is possible to achieve a separation of 45 deg in RAAN in 100.5 days with a ΔV_{alt} of 200 m/s using a satellite-lowering manoeuvre. For the satellite-raising manoeuvre, a separation of 45 deg can be achieved with a ΔV_{alt} of 200 m/s in 107.9 days; a difference of more than seven days. A separation of 90 deg in RAAN is achievable in 191.0 days with a ΔV_{alt} of 200 m/s using a satellite-lowering manoeuvre. For the satellite-raising manoeuvre, a separation of 90 deg can be achieved with a ΔV_{alt} of 200 m/s in 206.1 days; a difference of 15 days. These results indicate that if the primary goal is separation of satellites through RAAN, the satellite-lowering manoeuvre is more efficient. This is as would be expected; considering equation (2.49) shows that the rate of change of RAAN is proportional to $1/\bar{a}^{7/2}$ and as such the relative difference in the rate of change in RAAN of two satellites separated by altitude will increase as their altitudes decrease.

3.1.2 Changing Argument of Latitude

Figure 3.6 shows contours of AoL change and the corresponding manoeuvre time and ΔV_{alt} for both the satellite-lowering and -raising manoeuvres. As was the case for RAAN, a satellite-lowering manoeuvre requires less time than a satellite-raising manoeuvre to achieve the desired AoL change using the same ΔV_{alt}, and the relative difference between the two increases as the desired AoL separation increases. As before, these results indicate that if the primary goal is separation of satellites, the satellite-lowering manoeuvre is more efficient. This is also expected, as considering equation (2.50) shows that the rate of change of AoL is proportional to $(1 + \bar{a}^2)/\bar{a}^{7/2}$, meaning that the relative difference in the rate of change of AoL of satellites separated by altitude will increase as their altitude decreases. It is of note that the same effect will also be seen considering smaller changes in AoL less than one revolution, but these values are used for illustrative purposes.

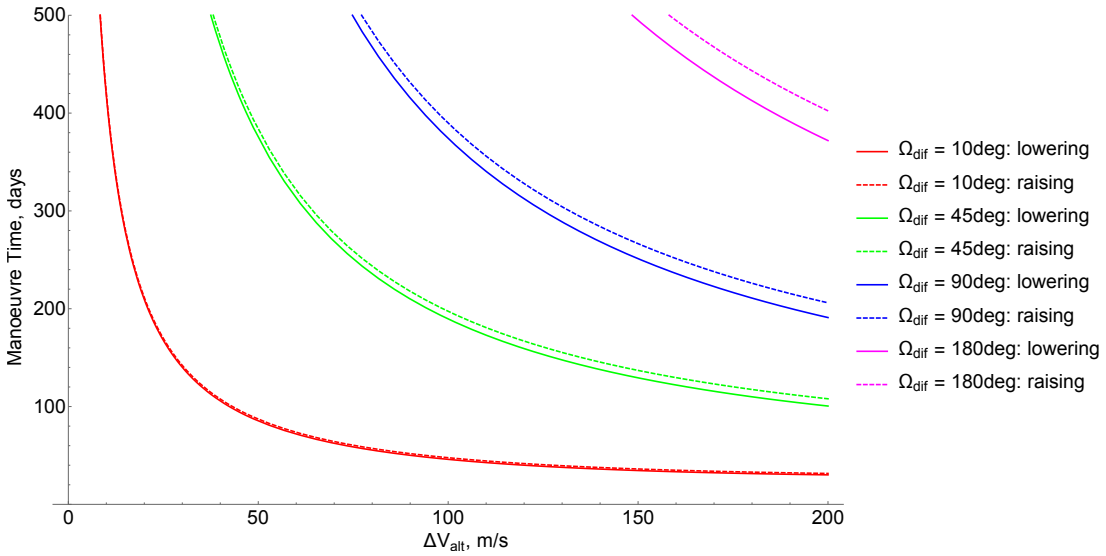

Figure 3.5: Comparison of manoeuvre time necessary to achieve a desired change in RAAN as a function of ΔV_{alt} for satellite-lowering and -raising manoeuvres.

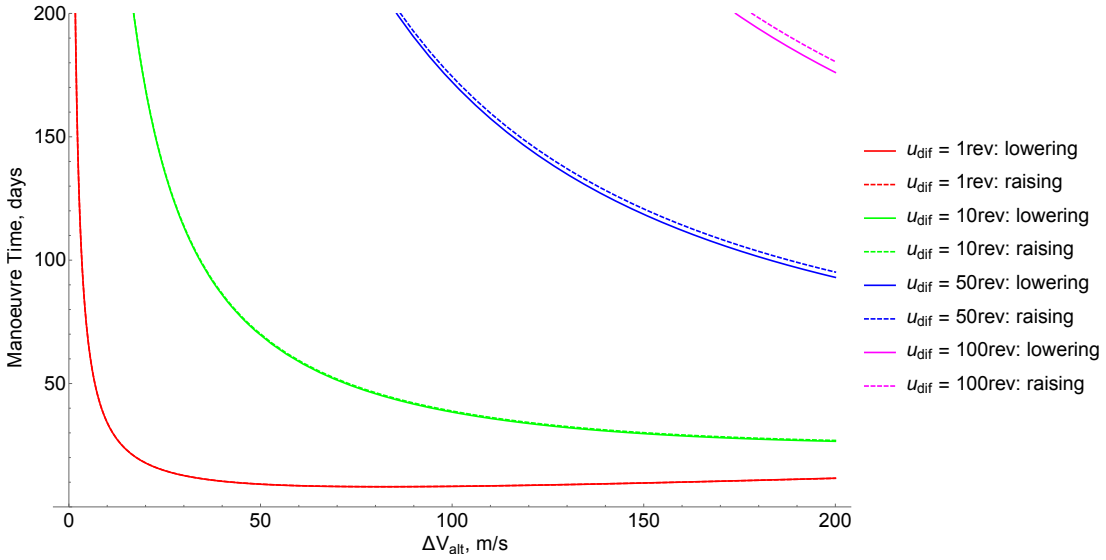

Figure 3.6: Comparison of manoeuvre time necessary to achieve a desired change in AoL as a function of ΔV_{alt} for satellite-lowering and -raising manoeuvres.

3.2 Investigation of Effect of Orbit Parameters

The initial orbit parameters of the satellite will have an impact on the effectiveness of the manoeuvres. It is useful to quantify this dependence on initial orbit conditions to determine preferable orbits for manoeuvrable satellites to occupy. The analytical nature of the solution is beneficial in this investigation as it allows the change in RAAN and AoL to be easily calculated as functions of the variable, or variables, of interest. These can be plotted as continuous functions giving a full overview of the solution and providing a deeper insight into the method.

An investigation into the effect of initial orbit parameters is carried out for the 3-phase manoeuvre with the parameters given in Tables 3.1 and 3.3 used, excluding the parameter being investigated. Unless otherwise stated, a 30 m/s ΔV_{alt} and a manoeuvre time of seven days is used for the investigation. The results presented show the change in RAAN, Ω_{dif}, and AoL, u_{dif}, that can be achieved when compared with a non-manoeuvring reference satellite as calculated using equations (2.87) and (2.88).

3.2.1 Varying Inclination

Change in right ascension of the ascending node

The effect of varying inclination on the achievable change in RAAN is shown in Figure 3.7 (a) for an altitude-lowering manoeuvre, and in Figure 3.7 (b) for an altitude-raising manoeuvre. These graphs provide the intuitive result that as the orbit inclination approaches 90 deg, the achievable RAAN separation approaches zero. This is because the rate of change of RAAN due to J_2 is zero at 90 deg inclination, as expressed by equation (2.16). Also clear is that when using an altitude-lowering manoeuvre, for prograde orbits (i.e. orbit inclination is less than 90 deg) the relative RAAN change will be negative while for retrograde orbits (i.e. orbit inclination is 90–180 deg) the change in RAAN will be positive. The opposite is true for the satellite-raising manoeuvre.

Figure 3.8 shows the same analysis as Figure 3.7, but is integrated over the osculating semi-major axis, using the equations as described in Appendix B. It can be seen that when using this method the solution becomes unstable for certain inclination values. This is due to the existence of the $\sin^2(i)$ term in the conversion from the os-

culating to mean semi-major axis as shown in equation (2.45) that causes the solution to tend to infinity as the inclination approaches zero and 180 deg.

The minimum inclination for which the solution is valid when integrating over the osculating semi-major axis was investigated by plotting a seventh order polynomial curve fit to the solution for a satellite-lowering manoeuvre, as shown in Figure 3.9. Taking the difference between the solution and the curve fit gives the deviation in change in RAAN from the expected trend. The curved surface distance between the resulting sub-satellite point as calculated using the general perturbation solution and the RAAN as given by the expected trend gives the results shown in Figure 3.10; this is done for an AoL of 0 deg as this gives the largest deviation due to the presence of the $\cos(2u)$ term in the conversion from osculating to mean semi-major axis as given by equation (2.45). Further examination of these results reveals the maximum deviation from the trend in kilometres for different inclination ranges, as shown in Table 3.4. This shows that for inclination values between 15–165 deg, the maximum deviation is less than 6 km for the case considered. For inclination values between 10–170 deg, the maximum deviation increases to more than 500 km. As a result of this, it is recommended that the method integrating over the osculating semi-major axis should not be used for inclinations less than 15 deg or greater than 165 deg.

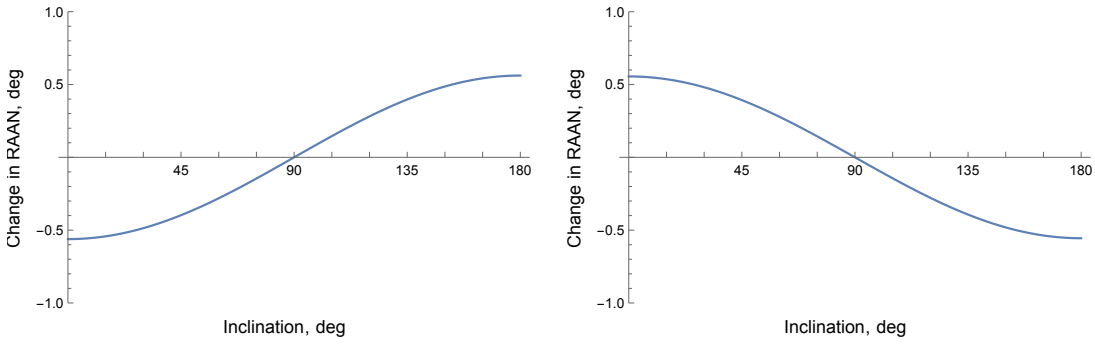

Figure 3.7: Achievable change in RAAN as a function of inclination for (a) an altitude-lowering manoeuvre, (b) an altitude-raising manoeuvre using 30 m/s ΔV_{alt} and with a manoeuvre time of 7 days.

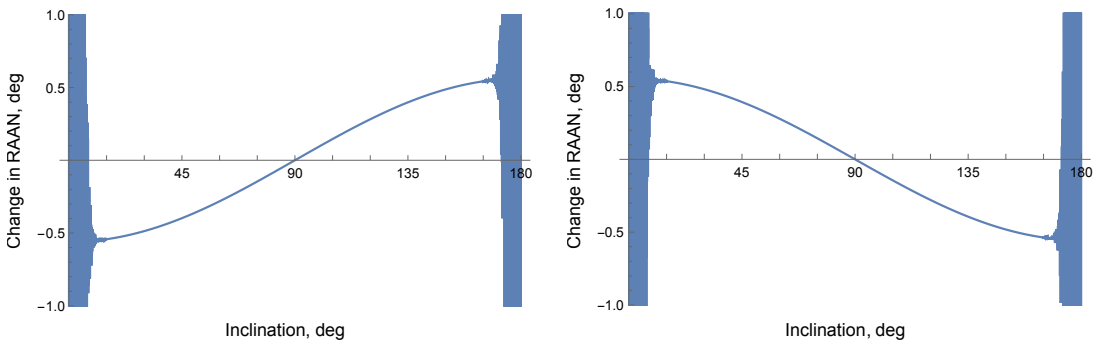

Figure 3.8: Achievable change in RAAN as a function of inclination integrating over the osculating semi-major axis for (a) an altitude-lowering manoeuvre, (b) an altitude-raising manoeuvre using 30 m/s ΔV_{alt} and with a manoeuvre time of 7 days.

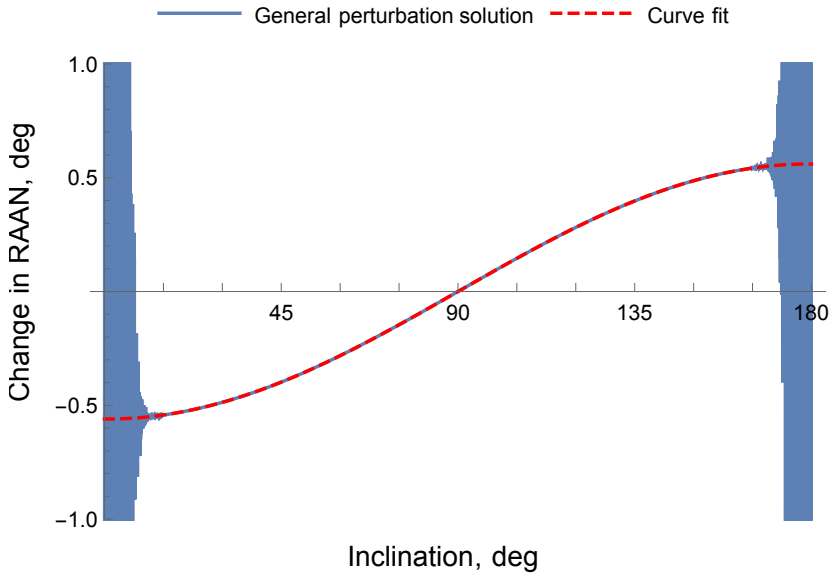

Figure 3.9: Curve fit to general perturbation solution integrating over the osculating semi-major axis for change in RAAN over a range of inclinations.

Table 3.4: Maximum difference between sub-satellite point location as calculated by the general perturbation solution integrated over the osculating semi-major axis and the expected trend for change in RAAN for ranges of inclination.

Inclination range, deg	50–130	20–160	15–165	10–170	5–175	0–180
Maximum deviation, km	0.2	1.4	5.7	541.9	20014.5	20014.5

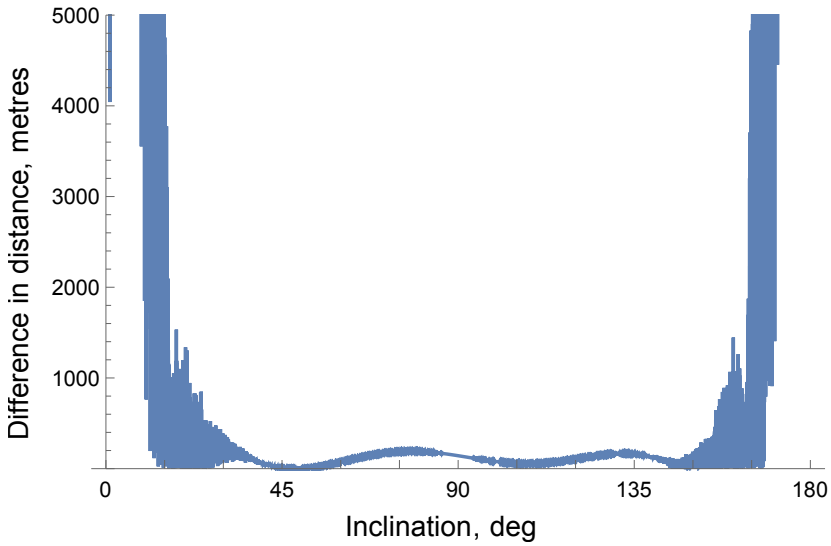

Figure 3.10: Difference between sub-satellite point location as calculated by the general perturbation solution integrated over the osculating semi-major axis and the expected trend.

Change in argument of latitude

The effect of varying inclination on the achievable change in AoL is shown in Figure 3.11 (a) for an altitude-lowering manoeuvre, and in Figure 3.11 (b) for an altitude-raising manoeuvre. These graphs show that the AoL separation achievable decreases as the inclination of the satellite approaches 90 deg, with a difference of approximately 2 deg between the maximum and minimum possible separation. This is a very small difference compared to the magnitude of the separation, which is just less than 180 deg, demonstrating that the inclination of the responsive satellite is of small consequence if the goal is to achieve separation in AoL. Contrary to the RAAN, the AoL change will be positive for both prograde and retrograde orbits for an altitude-lowering manoeuvre; for an altitude-raising manoeuvre, the change in AoL will be negative for all inclinations.

Figure 3.12 shows the same analysis as Figure 3.11, but is calculated by integrating over the osculating semi-major axis. The instability of the solution identified when considering the effect of inclination on the change in RAAN is also visible here. As was done for the RAAN investigation, a seventh order polynomial curve fit is performed, and the resultant deviation in the position of the sub-satellite point compared to the expected trend is calculated for a reference AoL of 0 deg. These results are given in Table 3.5. In this case, for inclination values between 15–165 deg, the maximum

deviation is approximately 25 km; this is almost 20 km greater than in the RAAN case, but is of a similar magnitude to other error sources, as will be seen in Chapter 4. For inclination values between 10–170 deg, the maximum deviation increases to more than 1000 km. This remains consistent with the prior recommendation that for inclinations less than 15 deg or greater than 165 deg, the method that is integrated over the osculating semi-major axis should not be used.

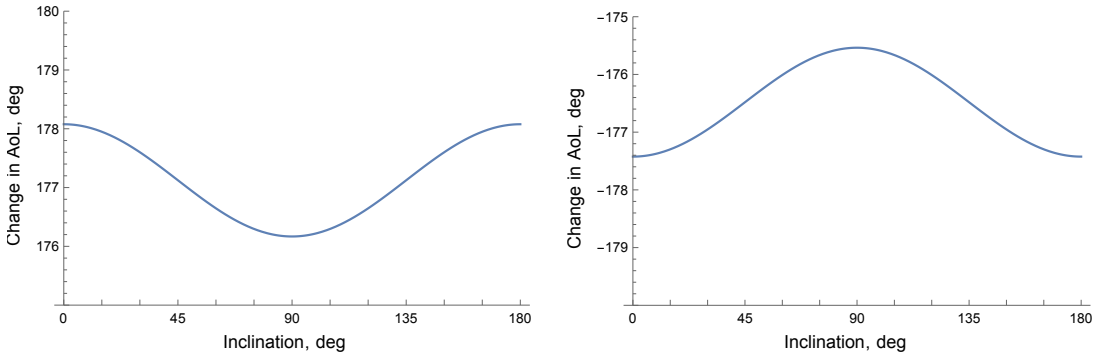

(a) (b)

Figure 3.11: Achievable change in AoL as a function of inclination for (a) an altitude-lowering manoeuvre, (b) an altitude-raising manoeuvre using 30 m/s ΔV_{alt} and with a manoeuvre time of 7 days.

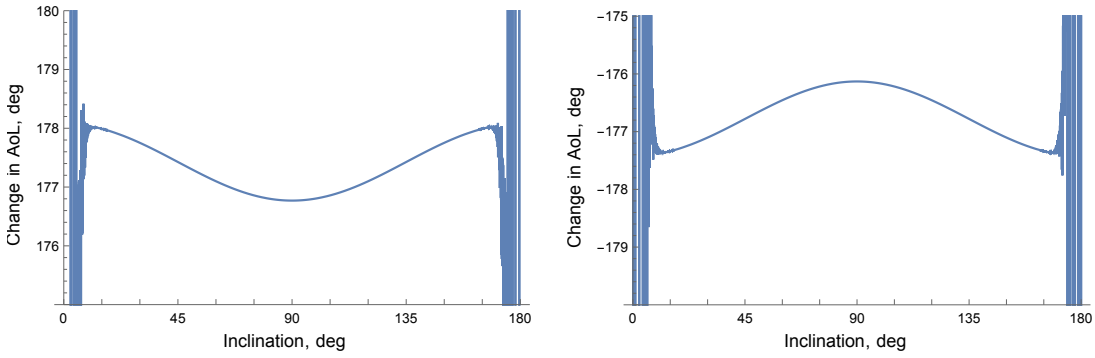

(a) (b)

Figure 3.12: Achievable change in AoL as a function of inclination integrating over the osculating semi-major axis for (a) an altitude-lowering manoeuvre, (b) an altitude-raising manoeuvre using 30 m/s ΔV_{alt} and with a manoeuvre time of 7 days.

Table 3.5: Maximum difference between sub-satellite point location as calculated by the general perturbation solution integrated over the osculating semi-major axis and the expected trend for change in AoL for ranges of inclination.

Inclination range, deg	50–130	20–160	15–165	10–170	5–175	0–180
Maximum deviation, km	2.9	10.1	25.2	1049.3	19370.0	19842.3

Displacement of sub-satellite point

If the reason for manoeuvring a spacecraft is to achieve a change in the position of the sub-satellite point, then the manoeuvre effectiveness can be quantified in terms of the curved surface distance between the manoeuvred satellite's sub-satellite point, as compared with that of a non-manoeuvring reference satellite. The effect of varying inclination on the achievable distance is shown in Figure 3.13 (a) for an altitude-lowering manoeuvre, and in Figure 3.13 (b) for an altitude-raising manoeuvre. These graphs show that the distance achievable decreases as the inclination of the satellite approaches 90 deg, with a difference of approximately 100 km between the maximum and minimum achievable distance. This is very small compared to the total distance achieved which is just less than 20,000 km. This is because the change in AoL is the primary contributor to the displacement of the sub-satellite point, as demonstrated by the similar trend seen in Figures 3.11 and 3.13. This indicates that the inclination of the satellite orbit will have relatively little impact on the maximum distance achievable.

Also evident from Figure 3.13 is that a satellite-lowering manoeuvre produces a greater change in the location of the sub-satellite point than an altitude-raising manoeuvre, though the difference, which is approximately 100 km, is very small compared to the total distance. This is consistent with the findings from Section 3.1 that an altitude-lowering manoeuvre is a more efficient means of changing the RAAN and AoL of a satellite. Note that the distance shown in both Figures 3.13 (a) and 3.13 (b) is positive, as only the magnitude of the distance is considered here and not the direction.

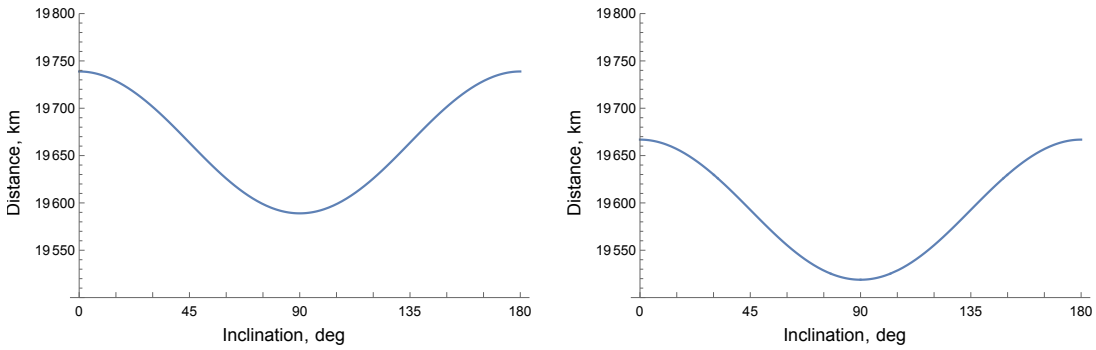

Figure 3.13: Displacement of sub-satellite point as a function of inclination for (a) an altitude-lowering manoeuvre, (b) an altitude-raising manoeuvre using 30 m/s ΔV_{alt} and a manoeuvre time of 7 days.

3.2.2 Varying Initial Altitude

This section investigates the effect of varying the satellite initial altitude on the manoeuvre effectiveness. To maintain consistency, it is decided that the satellite should always return to its initial altitude at the manoeuvre end (i.e. $\bar{a}_3 = \bar{a}_0$), and as such both the initial and final altitude of the satellite are varied.

Change in right ascension of the ascending node

The achievable change in RAAN as a function of the satellite initial altitude is shown in Figure 3.14 (a) for an altitude-lowering manoeuvre, and in Figure 3.14 (b) for an altitude-raising manoeuvre. From this it can be seen that the achievable RAAN separation increases with decreasing altitude. This is as expected, due to the nature of J_2, as discussed in Section 3.1. For an altitude-lowering manoeuvre, the relative RAAN change will be negative for all initial altitudes while for an altitude-raising manoeuvre the change in RAAN will be positive.

Change in argument of latitude

The achievable change in AoL as a function of the satellite initial altitude is shown in Figure 3.15 (a) for an altitude-lowering manoeuvre, and in Figure 3.15 (b) for an altitude-raising manoeuvre. As with RAAN, the achievable AoL separation increases with decreasing altitude. Here, for an altitude-lowering manoeuvre, the relative AoL

change will be positive for all initial altitudes while for an altitude-raising manoeuvre the change in AoL will be negative.

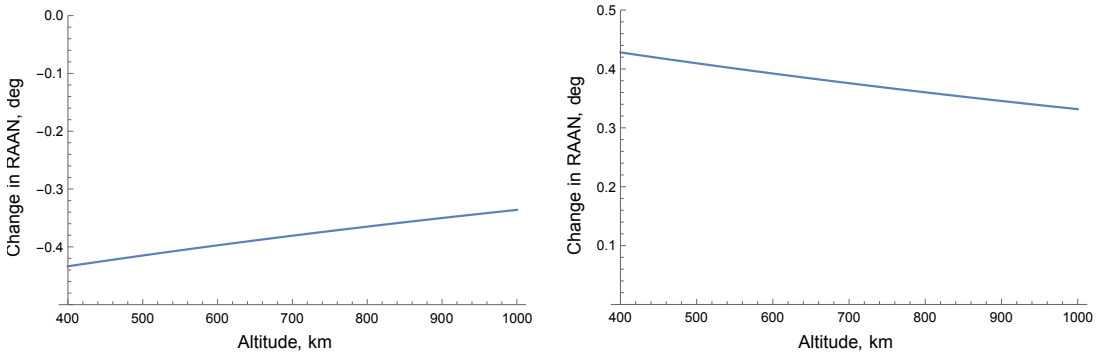

(a) (b)

Figure 3.14: Achievable change in RAAN as a function of initial altitude for (a) an altitude-lowering manoeuvre, (b) an altitude-raising manoeuvre using 30 m/s ΔV_{alt} and with a manoeuvre time of 7 days.

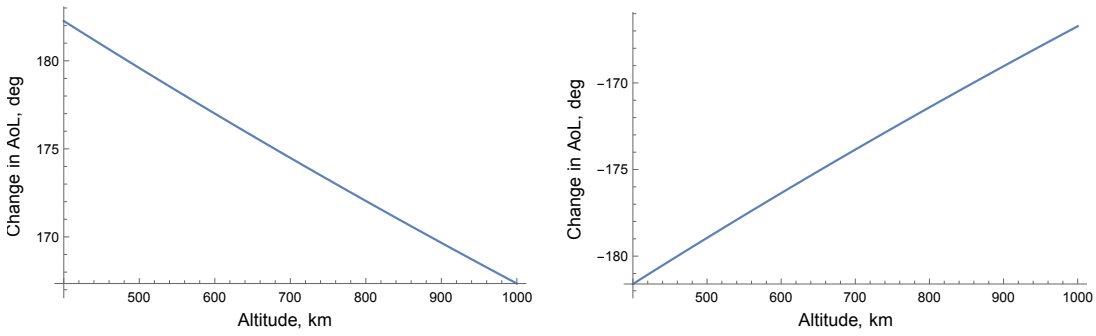

(a) (b)

Figure 3.15: Achievable change in AoL as a function of initial altitude for (a) an altitude-lowering manoeuvre, (b) an altitude-raising manoeuvre using 30 m/s ΔV_{alt} and with a manoeuvre time of 7 days.

Displacement of sub-satellite point

The displacement of the sub-satellite point as a function of the satellite initial altitude is shown in Figure 3.16 (a) for an altitude-lowering manoeuvre, and in Figure 3.16 (b) for an altitude-raising manoeuvre. These graphs show that the displacement, in general, increases as the initial altitude of the satellite decreases. The reason for the apparent decrease in distance below approximately 500 km altitude is that at this point the sub-satellite point has been displaced by more than half the circumference of the Earth

and thus the absolute distance between the sub-satellite points of the manoeuvred and reference satellites begins to decrease. The oscillation seen in the distance near the maximum is likely due to difficulties in the calculation of the haversine distance as the longitude difference approaches 180 deg. This instability is a well documented issue with this method of calculating the curved surface distance between two points [74].

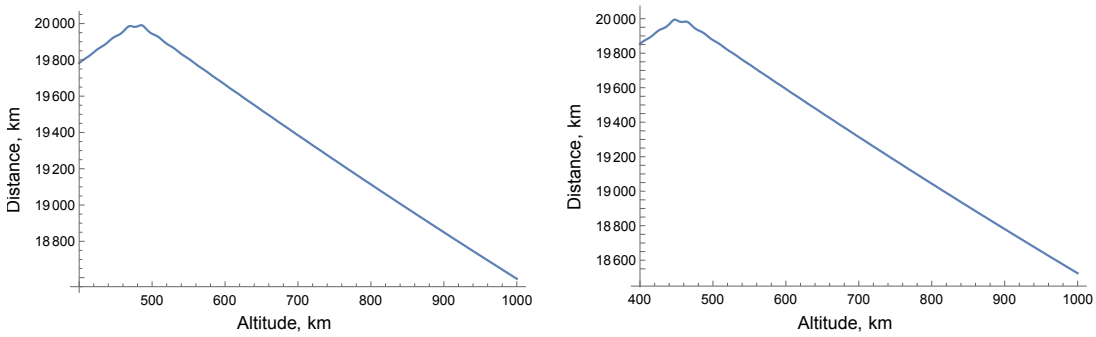

Figure 3.16: Displacement of sub-satellite point as a function of initial altitude for (a) an altitude-lowering manoeuvre, (b) an altitude-raising manoeuvre using 30 m/s ΔV_{alt} and with a manoeuvre time of 7 days.

3.2.3 Varying Manoeuvre Time and ΔV

Change in right ascension of the ascending node

The crucial variables for control of the satellite manoeuvre are the manoeuvre time and the ΔV_{alt} used. The achievable change in RAAN is shown in Figure 3.17 (a) as a function of these parameters for an altitude-lowering manoeuvre, and in Figure 3.17 (b) for an altitude-raising manoeuvre. In both graphs the solution is only plotted for cases in which the manoeuvre time is sufficient to achieve the corresponding ΔV_{alt}. As would be expected, the achievable RAAN separation increases with increased manoeuvre time and increased ΔV_{alt}. However this relationship is non-linear.

Considering the change in RAAN as a function of time only for a ΔV_{alt} of 30 m/s using an altitude-lowering manoeuvre gives the results in Figure 3.18 (a) from which it is clear that for a given ΔV_{alt} the change in RAAN achievable increases almost linearly with time. A similar result is obtained using an altitude-raising manoeuvre as shown in Figure 3.18 (b). Note that a minimum manoeuvre time of 3 days is required to achieve

a ΔV_{alt} of 30 m/s. This sets the lower limit of the presented graphs.

For a constant manoeuvre time of 30 days, the results in Figure 3.19 (a) are obtained for an altitude-lowering manoeuvre. From this it can be seen that whilst the change in RAAN achievable increases with increasing ΔV_{alt}, the relative increase lessens as the amount of ΔV_{alt} increases. Figure 3.19 (b) shows a similar result for an altitude-raising manoeuvre.

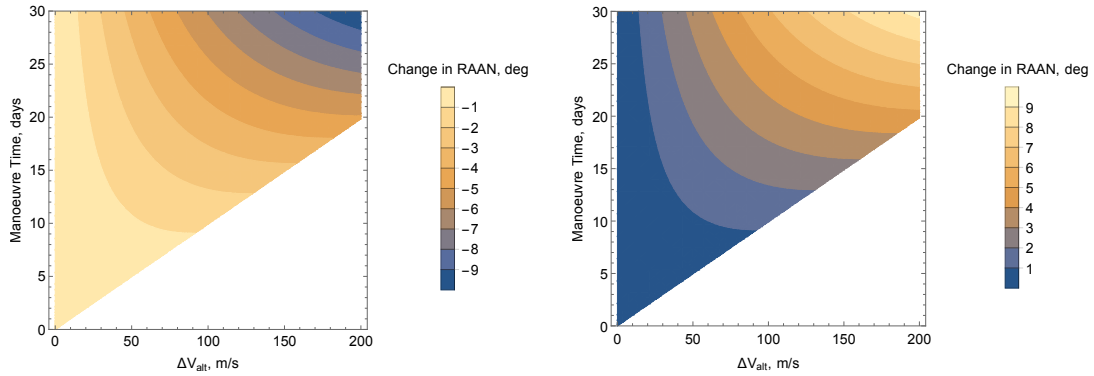

(a) (b)

Figure 3.17: Achievable change in RAAN as a function of manoeuvre time and ΔV_{alt} for (a) an altitude-lowering manoeuvre, (b) an altitude-raising manoeuvre.

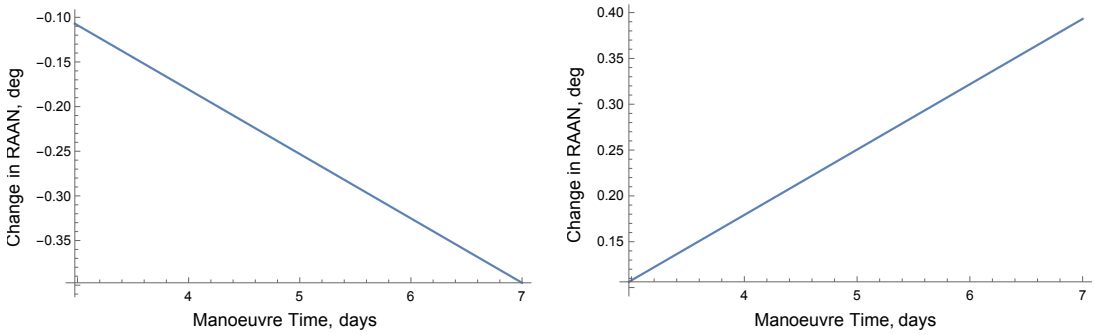

(a) (b)

Figure 3.18: Achievable change in RAAN as a function of manoeuvre time for (a) an altitude-lowering manoeuvre, (b) an altitude-raising manoeuvre using 30 m/s ΔV_{alt}.

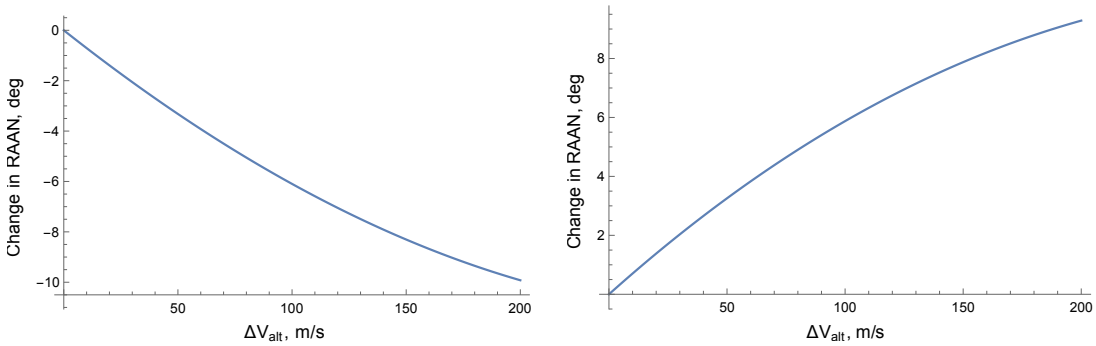

(a) (b)

Figure 3.19: Achievable change in RAAN as a function of ΔV_{alt} for (a) an altitude-lowering manoeuvre, (b) an altitude-raising manoeuvre with a manoeuvre time of 30 days.

Change in argument of latitude

The achievable change in AoL as a function of manoeuvre time and ΔV_{alt} is shown in Figure 3.20 (a) for an altitude-lowering manoeuvre, and in Figure 3.20 (b) for an altitude-raising manoeuvre. These solutions are only plotted for cases in which the manoeuvre time is sufficient to achieve the corresponding ΔV_{alt}. The negative number of revolutions achieved using the altitude-raising manoeuvre indicates that the manoeuvred satellite will lag the reference satellite. As would be expected, the achievable AoL separation increases with increased manoeuvre time and increased ΔV_{alt}.

Considering the change in AoL as a function of time only for an altitude-lowering manoeuvre using a ΔV_{alt} of 30 m/s, gives the results in Figure 3.21 (a) from which it is clear that for a given ΔV_{alt} the change in AoL achievable increases almost linearly with time. A similar result is obtained for an altitude-raising manoeuvre as shown in Figure 3.21 (b).

For a constant manoeuvre time of 30 days the results in Figure 3.22 (a) are obtained for an altitude-lowering manoeuvre. From this it can be seen that the change in AoL as a function of ΔV_{alt} follows the same trend as the change in RAAN; the change in AoL achievable increases with increasing ΔV_{alt}, but the relative increase lessens as the amount of ΔV_{alt} increases. Figure 3.22 (b) shows a similar result for an altitude-raising manoeuvre.

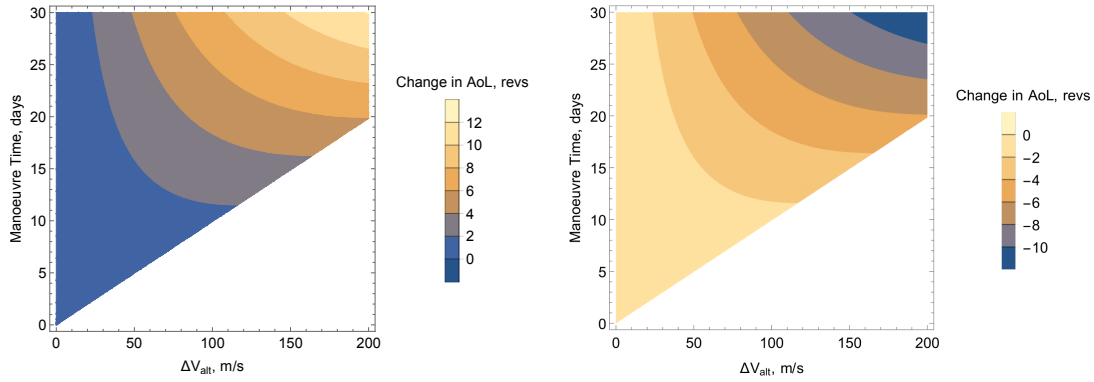

(a) (b)

Figure 3.20: Achievable change in argument of latitude as a function of manoeuvre time and ΔV_{alt} for (a) an altitude-lowering manoeuvre, (b) an altitude-raising manoeuvre.

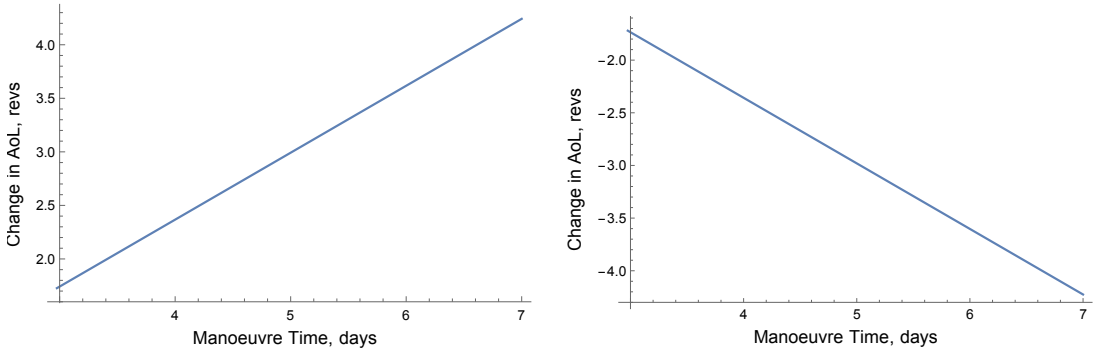

(a) (b)

Figure 3.21: Achievable change in argument of latitude as a function of manoeuvre time for (a) an altitude-lowering manoeuvre, (b) an altitude-raising manoeuvre using 30 m/s ΔV_{alt}.

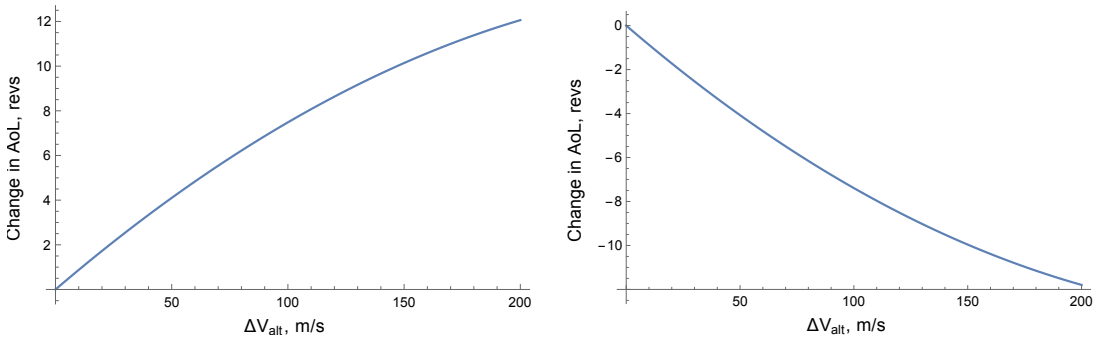

(a) (b)

Figure 3.22: Achievable change in argument of latitude as a function of ΔV_{alt} for (a) an altitude-lowering manoeuvre, (b) an altitude-raising manoeuvre with a manoeuvre time of 30 days.

Displacement of sub-satellite point

The displacement of the sub-satellite point as a function of manoeuvre time and ΔV_{alt} is shown in Figure 3.23 (a) for an altitude-lowering manoeuvre, and in Figure 3.23 (b) for an altitude-raising manoeuvre. In both graphs the solution is only plotted for cases in which the manoeuvre time is sufficient to achieve the corresponding ΔV_{alt}.

Considering the displacement of the sub-satellite point as a function of time only for an altitude-lowering manoeuvre using a ΔV_{alt} of 30 m/s gives the results in Figure 3.24 (a) from which it is clear that for a given ΔV_{alt} the displacement of the sub-satellite point increases almost linearly with time. A similar result is obtained using an altitude-raising manoeuvre as shown in Figure 3.24 (b).

For an altitude-lowering manoeuvre with a constant manoeuvre time of one day, the results in Figure 3.25 (a) are obtained. From this it can be seen that the displacement of the sub-satellite point as a function of ΔV_{alt} increases with increasing ΔV_{alt} but, as with RAAN and AoL, the relative increase lessens as the amount of ΔV_{alt} increases. Figure 3.25 (b) shows a similar result for an altitude-raising manoeuvre.

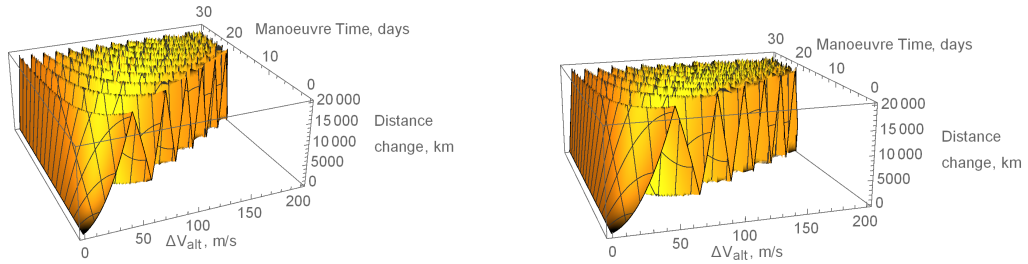

Figure 3.23: Displacement of sub-satellite point as a function of manoeuvre time and ΔV_{alt} for (a) an altitude-lowering manoeuvre, (b) an altitude-raising manoeuvre.

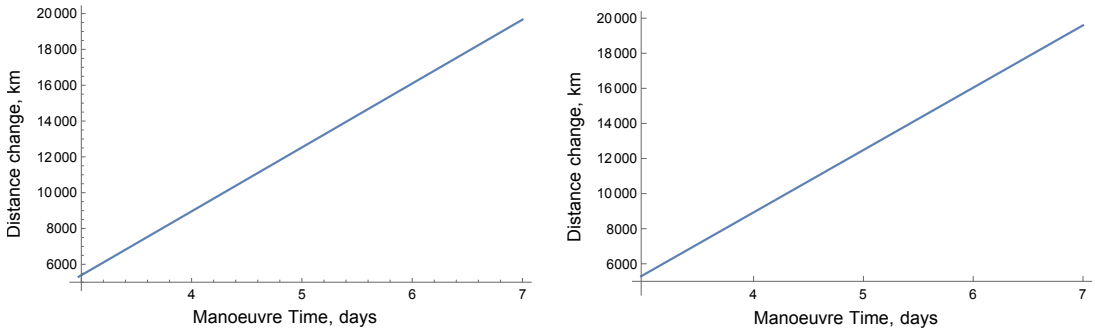

(a) (b)

Figure 3.24: Displacement of sub-satellite point as a function of manoeuvre time for (a) an altitude-lowering manoeuvre, (b) an altitude-raising manoeuvre using 30 m/s ΔV_{alt}.

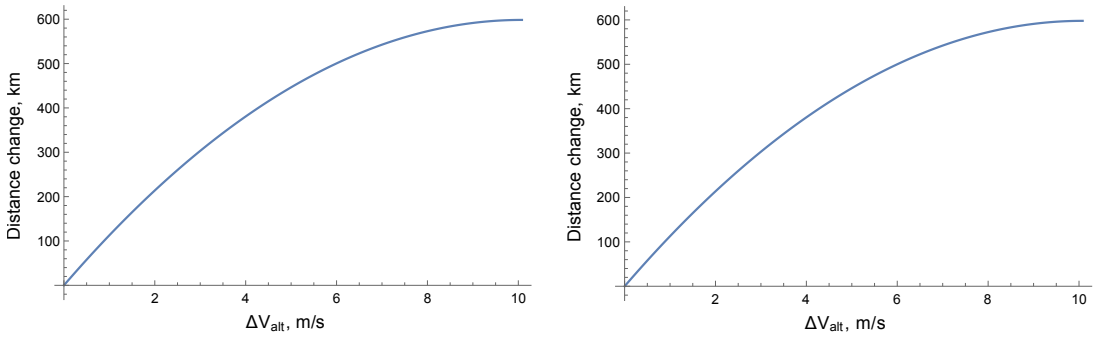

(a) (b)

Figure 3.25: Displacement of sub-satellite point as a function of ΔV_{alt} for (a) an altitude-lowering manoeuvre, (b) an altitude-raising manoeuvre with a manoeuvre time of 1 day.

Chapter 4

Validation: Rapid Flyover

In this chapter, the developed general perturbation method will be applied to a simple scenario to quantify its accuracy and to illustrate the applicability of the method before applying it to more complex scenarios in Chapters 5 and 6.

4.1 Validation Case Description

The scenario investigated in this chapter considers a satellite in the same orbit as the International Space Station (ISS). The goal of the proposed mission is to reduce the revisit time of the satellite over Los Angeles, California. This kind of operation could be desirable, for example, in response to an earthquake in the region. The orbital constants used for the analysis are given in Table 4.1, the initial satellite orbit parameters are given in Table 4.2, and the spacecraft properties are given in Table 4.3. The ground track of the satellite as plotted over a single day is shown in Figure 4.1 with the location of the target also indicated.

The satellite propulsion system acceleration is calculated assuming a 3 kg satellite (e.g. a 3U CubeSat [77, 78]), equipped with the TILE electrospray propulsion system, developed by the Space Propulsion Laboratory of the Massachusetts Institute of Technology (MIT), that produces a nominal thrust of 350 μN and has a specific impulse of 760 seconds [8, 79–82]. For a 3 kg 3U Cubesat carrying 50 g of propellant, this equates to a maximum ΔV of 120 m/s, assuming a constant nominal thrust and a constant acceleration. This is a valid assumption as the propellant accounts for just 1.6% of the

spacecraft wet mass and would see a change in acceleration of just 0.00264 mm/s^2 if the full propellant mass were used, a change of less than 2.5%.

Table 4.1: Orbital constants.

Parameter	Symbol	Value	Units
Gravitational Parameter	μ	3.986×10^{14}	m^3/s^2
Radius of Earth	R_e	6.371×10^3	km
Coefficient of J_2 for Earth	J_2	1.0827×10^{-3}	—
Angular velocity of Earth	ω_e	7.2921×10^{-5}	rad/s

Table 4.2: Orbit parameters.

Parameter	Symbol	Value	Units
Propulsion acceleration	A_{prop}	$\pm 1.1667 \times 10^{-4}$	m/s^2
Inclination	i	51.64	deg
Initial/final osculating semi-major axis	a_0, a_3	6773	km
Initial/final mean semi-major axis	$\bar{a}_0$, $\bar{a}_3$	6767	km
Initial AoL	u_0	0	deg
Initial RAAN	Ω_0	0	deg
Latitude of POI	δ_{target}	34.05	deg
Longitude of POI	Ψ_{target}	-118.24	deg
Epoch	—	01 Jan 1990 00:00:00	—
Right ascension of Greenwich at epoch	Ω_{et0}	100.39	deg
Swath width	s	200	km

Table 4.3: Spacecraft parameters.

Parameter	Symbol	Value	Units
Coefficient of drag	C_D	2.2	—
Satellite mass	m	3	kg
Satellite cross-sectional area	α	0.03	m^2

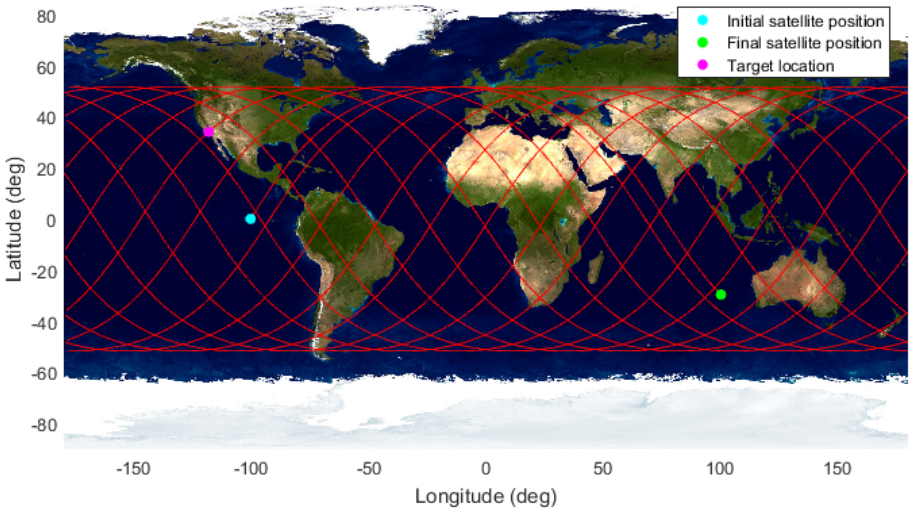

Figure 4.1: Ground-track of non-manoeuvring satellite plotted over a one-day period.

4.2 Comparison with Numerical Simulation

The results produced by the general perturbation solution are compared with the results produced by a numerical simulation, to quantify its accuracy. The results presented here are for the general perturbation method integrated over the mean semi-major axis; the results for the general perturbation method integrated over the osculating semi-major axis are given in Appendix C. A comparison will be made against three numerical simulations, incorporating different perturbations; the first will include central body perturbations up to J_2 only, the second will include central body perturbations to J_2 and atmospheric drag, and the third simulation will include central body perturbations modelled using an 18th order tesseral model as well as atmospheric drag. The numerical simulator propagates the position of the spacecraft using a set of modified equinoctial elements [83], and is implemented using MatLab's 'ode45' function [84] that uses an explicit variable step size Runge Kutta (4,5) formula, the Dormand-Prince pair [85]. A relative and absolute error tolerance of 1×10^{-8} are used for all solutions. The solution refinement factor, which specifies the number of output points for each solution step, is set to 30. Atmospheric drag is modelled in the numerical simulator using the U.S. Standard 1976 atmosphere model [86]; this is a more recent, and more detailed, atmospheric model than that employed in the general perturbation solution.

4.2.1 Non-manoeuvring Satellite

For a non-manoeuvring satellite (i.e. $\Delta V_{alt} = 0$ m/s) the distance from the sub-satellite point to Los Angeles is shown in Figure 4.2 for a 16-day period as calculated by the analytical general perturbation method. The horizontal line is drawn at half the swath width, taken to be 100 km, indicating the distance at which the POI will be visible to the satellite, assuming a conical field of view. This solution assumes that the satellite maintains a constant altitude over the time considered by performing atmospheric drag compensation manoeuvres. This was calculated to require 3.22 m/s ΔV. The times of each of the target flyovers and the distance of the SSP from the POI at that time as calculated by the general perturbation solution are given in Tables 4.4 – 4.6.

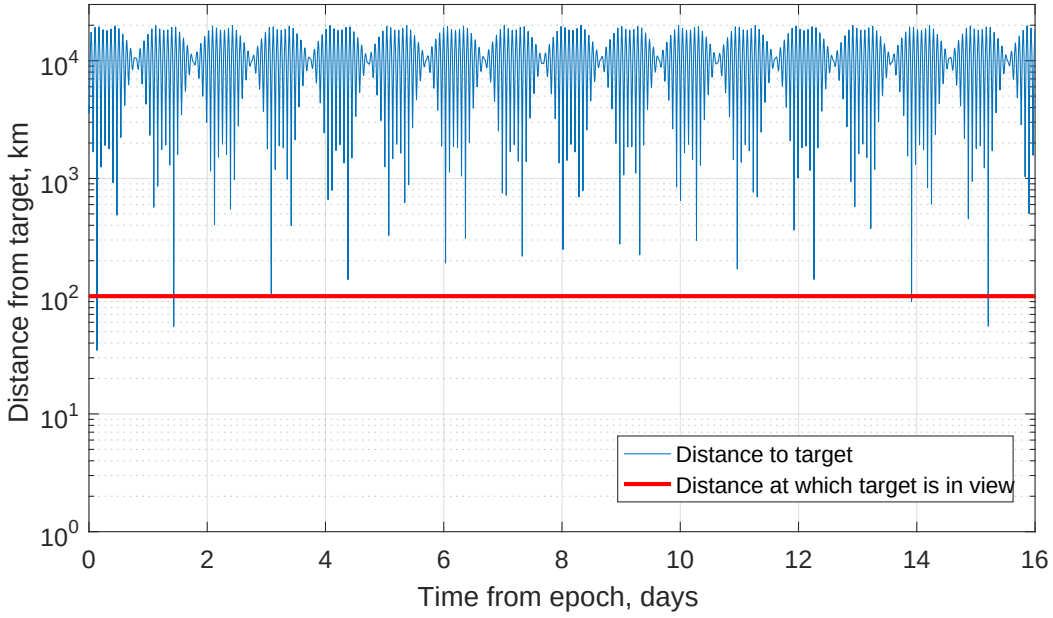

Figure 4.2: Distance from sub-satellite point to point of interest plotted as a function of total time for a non-manoeuvring satellite as calculated by the general perturbation method.

A comparison is first made to a numerical simulation considering a non-manoeuvring satellite subject to the effects of J_2 only; the effects of atmospheric drag, higher order central body effects and all other perturbations are ignored. By propagating the numerical simulator over 16 days, the times at which the POI is predicted to be in view can be found. These times are given in Table 4.4 with the corresponding distance to the POI at that time.

A second comparison is made against the same numerical simulator but with the

inclusion of atmospheric drag. To model the atmospheric drag compensation thrust, the thrust is set to be equal to the transversal component of the atmospheric drag perturbation throughout the simulation. The times at which the POI is found to be in view for this case are given in Table 4.5 with the corresponding distance to target at flyover. The total ΔV required for atmospheric drag compensation over the 16 days was found to be 2.53 m/s. This value is 20% less than the amount calculated using the general perturbation method; this discrepancy is likely due to the use of the more detailed atmospheric model in the numerical method.

A final comparison is made against the numerical simulator including an 18th order tesseral model of the central body perturbations, as well as atmospheric drag. The times at which the POI is found to be in view in this simulation are given in Table 4.6 with the corresponding distance to the target. The total ΔV required for atmospheric drag compensation over the 16-day period was found to be 2.52 m/s.

Tables 4.4, 4.5 and 4.6 show a close correlation between the general perturbation and numerical methods. The greatest difference in flyover time identified between the general perturbation and numerical models is less than 5 seconds and the largest difference in distance to target at flyover is approximately 16 km. It is of note that the general perturbation method misses a pass at 3.083 days identified by the three numerical solutions. This pass is at a distance of approximately 95 km from the POI and so this is likely due to errors in the accuracy of the general perturbation method. In addition, the general perturbation method identifies a pass at 13.91 days that is not identified by the three numerical simulations. This implies that in this case the general perturbation method has under-estimated the distance to the target and identified a pass that would not occur in reality.

Table 4.4: Comparison of flyover times for non-manoeuvring satellite calculated using the general perturbation method versus numerically including only central body effects to J_2.

	Gen. perturbation		Numerical		Difference	
Viewing Instance	Time from epoch, days	Distance to target, km	Time from epoch, days	Distance to target, km	Time from epoch, sec	Distance to target, km
1	0.136	20.52	0.136	29.11	4.76	-8.59
2	1.433	55.24	1.433	67.61	-0.47	-12.37
3	—	—	3.083	94.84	—	—
4	13.912	86.67	—	—	—	—
5	15.209	52.53	15.209	49.68	-1.77	2.86

Table 4.5: Comparison of flyover times for non-manoeuvring satellite calculated using the general perturbation method versus numerically with the inclusion of central body effects to J_2 and atmospheric drag.

	Gen. perturbation		Numerical		Difference	
Viewing Instance	Time from epoch, days	Distance to target, km	Time from epoch, days	Distance to target, km	Time from epoch, sec	Distance to target, km
1	0.136	20.52	0.136	29.11	4.76	-8.59
2	1.433	55.24	1.433	67.57	-0.48	-12.34
3	—	—	3.083	94.97	—	—
4	13.912	86.67	—	—	—	—
5	15.209	52.53	15.209	47.97	-3.69	4.56

Table 4.6: Comparison of flyover times for non-manoeuvring satellite calculated using the general perturbation method versus numerically with the inclusion of perturbations due to atmospheric drag and an 18th order tesseral model.

	Gen. perturbation		Numerical		Difference	
Viewing Instance	Time from epoch, days	Distance to target, km	Time from epoch, days	Distance to target, km	Time from epoch, sec	Distance to target, km
1	0.136	20.52	0.136	10.53	1.47	9.98
2	1.433	55.24	1.433	70.85	1.35	-16.2
3	—	—	3.083	95.93	—	—
4	13.912	86.67	—	—	—	—
5	15.209	52.53	15.209	47.22	3.22	5.31

Figures 4.3, 4.4, and 4.5 show the haversine distance between the sub-satellite points as calculated by the general perturbation method and the three numerical solutions over the same 16-day period as in Figure 4.2. From these results it is clear that the distance between the calculated SSPs oscillates over time. This is due to the short periodic variations in the orbital elements caused by J_2 that are not included in the general perturbation solution. This is a key consideration when using this method, and indeed all general perturbation methods, as due to the averaging of the disturbances over the orbit, these short periodic changes cannot be captured by the solution and thus the results produced will be at their most accurate after an integer number of orbit revolutions. Due to these oscillating differences, it is useful to consider the maximum difference and mean difference between the general perturbation and numerical methods. These are shown in Figures 4.3, 4.4, and 4.5 where the mean and maximum values are calculated over a one-day period in each case. These results show a general increase in the maximum difference over 16 days when comparing with the numerical simulation including J_2, as well as with J_2 and atmospheric drag. When comparing with the

numerical simulation including the 18th order tesseral model, the maximum difference first decreases before increasing, suggesting that the long periodic effects caused by the oblate central body are responsible for some of these differences. The largest maximum difference in the 16-day period is approximately 32 km. The mean difference increases slowly from 14–17 km in all cases. These results indicate that for an analysis up to 16 days, an error bound of 30–35 km can be applied to the calculated distance to the target. It should be noted that this error bound is defined based on the specific case considered herein; cases with different orbit and satellite parameters may be subject to greater or lesser errors. Passes three and four from Table 4.4, which were not identified by the general perturbation solution and numerical solutions respectively, are just 5 km and 15 km from the edge of the swath respectively and thus fall within the proposed error bound.

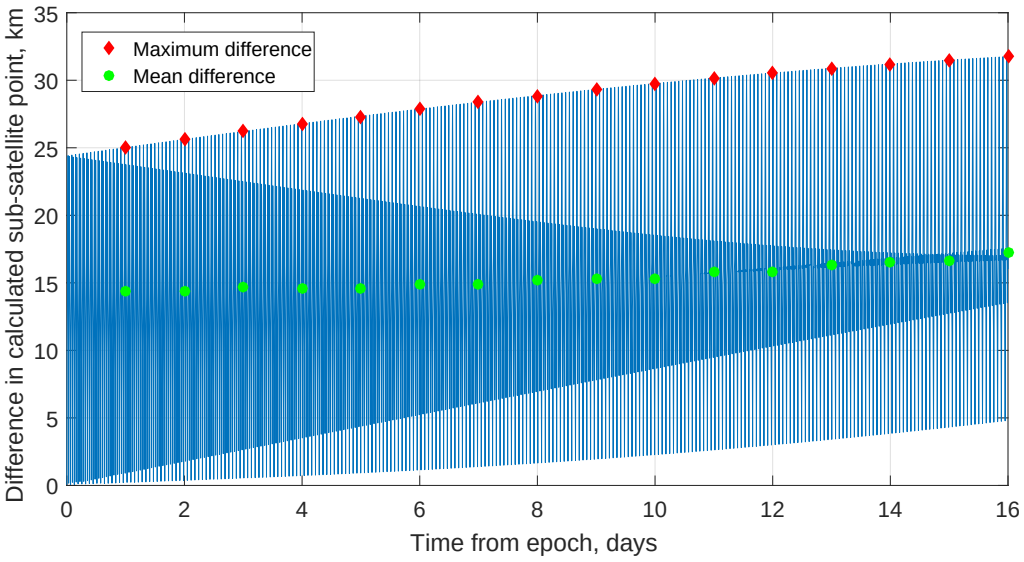

Figure 4.3: Haversine distance between sub-satellite points as calculated by general perturbation and numerical solution including J_2 for a non-manoeuvring satellite.

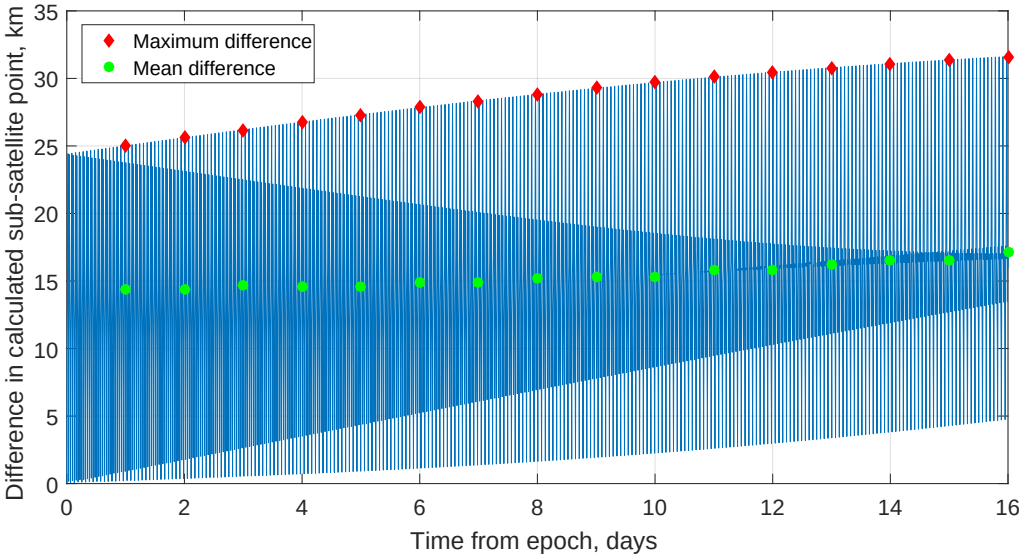

Figure 4.4: Haversine distance between sub-satellite points as calculated by general perturbation and numerical solution including J_2 and atmospheric drag for a non-manoeuvring satellite.

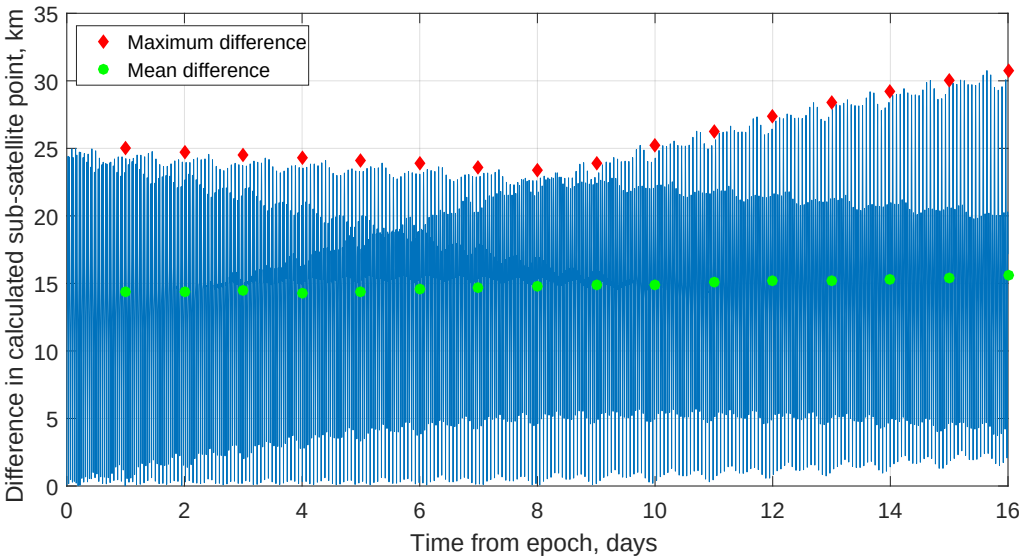

Figure 4.5: Haversine distance between sub-satellite points as calculated by general perturbation and numerical solution including atmospheric drag and 18th order tesseral model for a non-manoeuvring satellite.

4.2.2 Manoeuvring Satellite

The general perturbation method is now used to calculate the time required to flyover the target when the satellite is manoeuvred using a given ΔV_{alt}. Considering the results from Section 4.2.1, it was decided that the manoeuvre should begin 1.433 days from epoch, at the time of the second viewing instance as calculated by the general perturbation method and given in Tables 4.4 – 4.6, with the aim of reducing the subsequent flyover time of the POI from the 13.8 day gap that would otherwise exist; this assumes that the pass at 3.083 days, found by the numerical simulations, would be too short and too close to the edge of the swath width to be of value, and that the pass at 13.91 days identified by the analytical solution is not a valid pass. In order to compare with the numerical simulations, only a single manoeuvre is analysed; the results for a range of ΔV_{alt} values will be investigated in Section 4.3. A 3-phase altitude-lowering manoeuvre, using 30 m/s ΔV_{alt} is arbitrarily selected for this purpose. At the end of the manoeuvre, the satellite will return to its initial altitude, as would likely be necessary to ensure consistent observation conditions. Using 30 m/s ΔV_{alt}, the general perturbation method identifies three possible manoeuvres in a 13-day period, with different coast arc durations, that would end with the satellite in view of the target. These are shown in Table 4.7 with the corresponding distance from the SSP to the POI at closest approach. The shortest possible flyover time using 30 m/s ΔV_{alt} is found to be 5.06 days from epoch, shortening the time of flyover by more than ten days when compared with the non-manoeuvring case.

Table 4.7: Flyover times for manoeuvring satellite with 30 m/s ΔV_{alt} calculated using the general perturbation method.

Possible Flyover Instance	Time from epoch, days	Manoeuvre time, days	Distance from SSP to POI, km
1	5.06	3.62	54.50
2	8.32	6.88	28.81
3	11.94	10.50	57.19

The numerical simulations described in Section 4.2.1 are now used to investigate the solution for a manoeuvring satellite found using the general perturbation method. In order to simulate the entire mission, the satellite is first propagated 1.433 days from epoch in its initial orbit to reach viewing instance two from Tables 4.4 – 4.6 as calculated by the general perturbation method. At this point the 3-phase manoeuvre is carried out, based on the solution found using the general perturbation method for the first achievable flyover. This consists of an initial altitude change manoeuvre using 15 m/s ΔV to lower the orbit, lasting 35.71 hours, followed by a 15.54 hour coasting phase. Finally a 35.71 hour altitude change manoeuvre, using another 15 m/s ΔV, raises the orbit back to its initial altitude. For the simulations including atmospheric drag, the satellite is assumed to perform atmospheric drag compensation during phase 2, the coast arc, as well as before and after the manoeuvre. Figure 4.6 shows the ground track of the manoeuvring satellite over the five-day manoeuvre period. Figure 4.7 is a smaller region of the same plot, showing the position of the satellite relative to the target at the end of the manoeuvre.

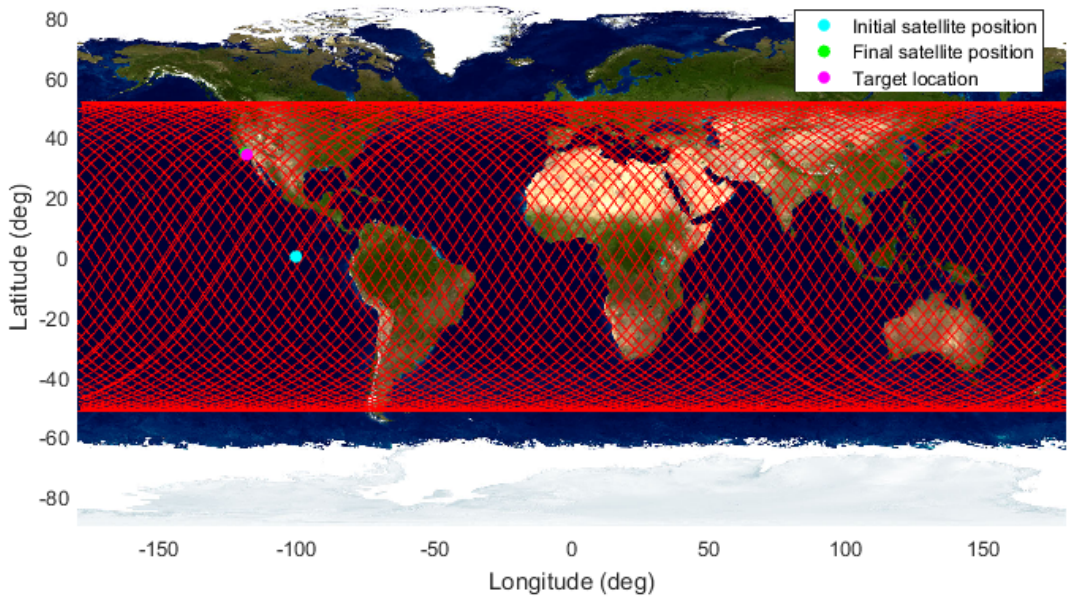

Figure 4.6: Ground-track of manoeuvring satellite plotted over the 5.06 day period from epoch to manoeuvre end.

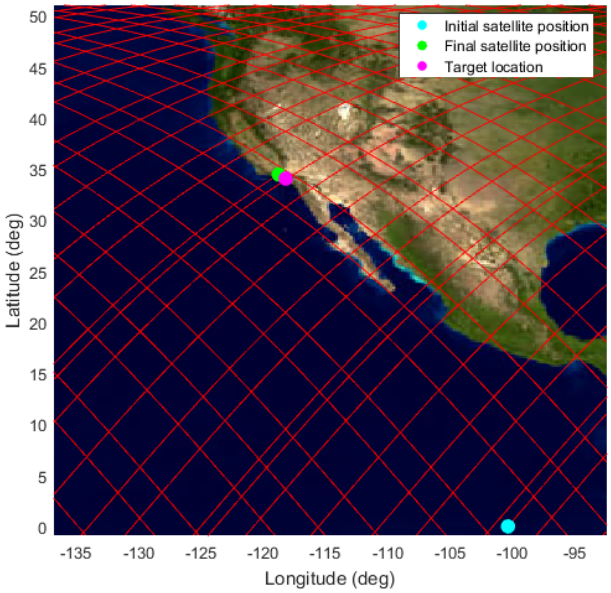

Figure 4.7: Section of Figure 4.6 showing satellite position relative to target at end of manoeuvre.

Figures 4.8, 4.9 and 4.10 show the distance from the sub-satellite point to the target as calculated using the haversine formula at each time step throughout the mission for the three numerical cases. The horizontal line indicates the distance at which the POI will be visible to the satellite, and the vertical dotted line indicates the time at which the manoeuvre starts. The first two peaks in these figures correspond to viewing instances one and two, which occur before the manoeuvre begins. The third peak, seen in all cases, corresponds to the pass that occurs at the end of the manoeuvre, as predicted by the general perturbation method, providing a flyover of the target at 5.06 days from epoch. The exact time of the closest pass found by each of the numerical simulations is given in Table 4.8 along with the distance to the target at that time.

The closest pass found by the numerical solution including only J_2 occurs just 1.19 seconds earlier than predicted by the general perturbation method, and the distance from the SSP to the POI at this time is found to be 67.17 km, which is a difference of 12.67 km. This falls within the expected error range as found in Section 4.2.1. After the manoeuvre is completed the satellite will remain in its orbit and the numerical solution predicts additional flyovers of the target at 6.35, 8.00, and 9.30 days from epoch.

The numerical simulation including atmospheric drag as well as J_2 identifies the closest pass as occurring 39 seconds earlier than predicted by the general perturbation

solution. The distance from the SSP to the target at this time is found to be 57.67 km, which is a difference of 3.18 km. This difference in predicted time of flyover is due to the effect of atmospheric drag during the altitude-lowering and -raising manoeuvres, when no atmospheric drag compensation is assumed to take place. If atmospheric drag compensation is performed during phase 1 and phase 3 in addition to the coast phases, the predicted flyover occurs just 1.2 seconds earlier than it is predicted by the general perturbation solution, at a distance of 67.15 km from the POI, giving a difference of 12.65 km when compared with the general perturbation method.

The numerical simulation with an 18th order tesseral model and atmospheric drag predicts the closest pass to be 41 seconds earlier than predicted by the general perturbation solution. The distance from the SSP to the target at this time is found to be 56.34 km; a difference of 1.85 km. If atmospheric drag compensation is performed during the lowering and raising manoeuvres in addition to the coasting phases, the predicted flyover occurs just 2 seconds earlier than it is predicted by the general perturbation solution, at a distance of 65.98 km from the POI, giving a difference of 11.5 km when compared with the general perturbation method.

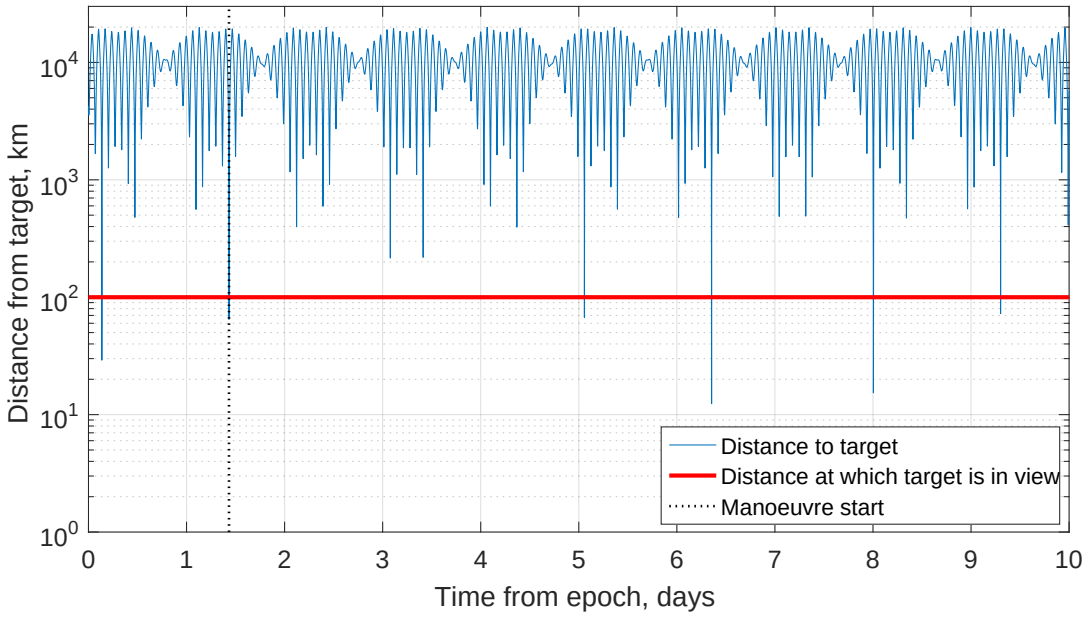

Figure 4.8: Distance from sub-satellite point to target throughout mission for numerical simulation including only J_2 perturbations. Manoeuvre begins at 1.433 days following the solution given by the general perturbation method.

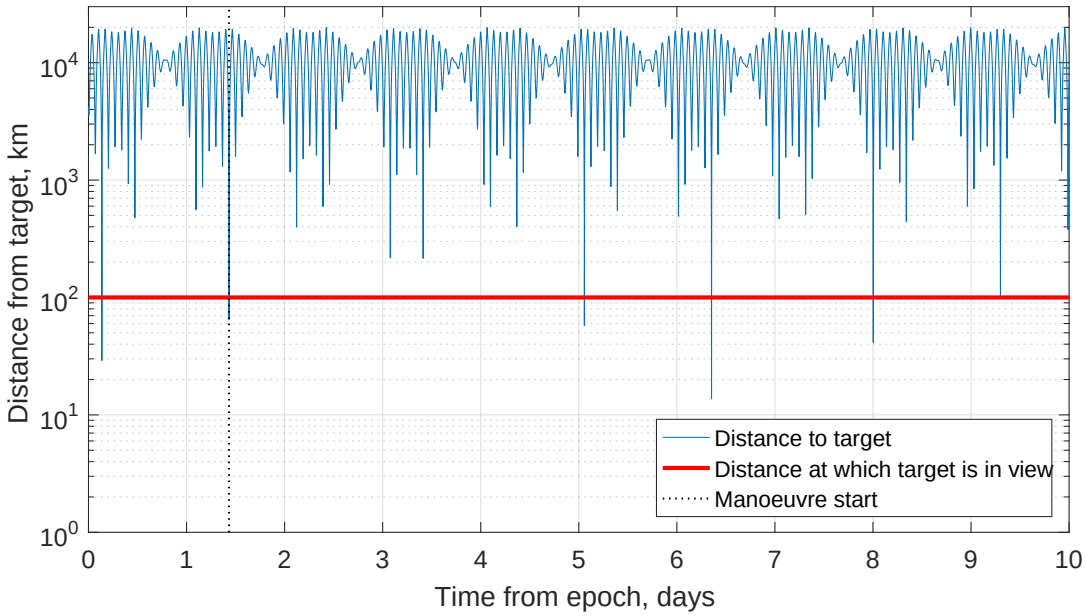

Figure 4.9: Distance from sub-satellite point to target throughout mission for numerical simulation including J_2 and atmospheric drag. Manoeuvre begins at 1.433 days following the solution given by the general perturbation method.

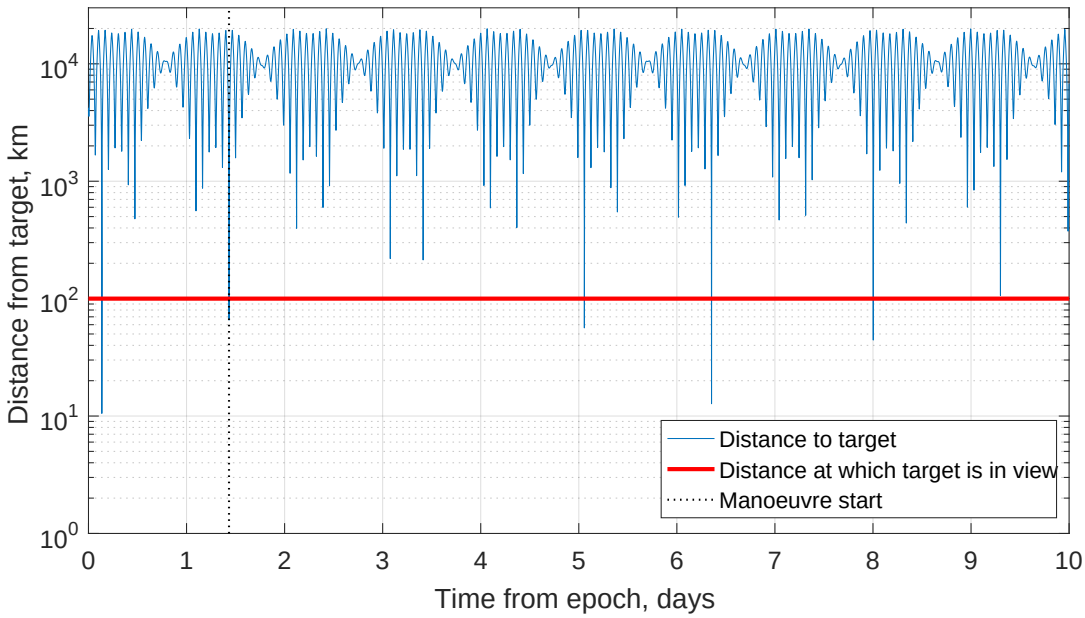

Figure 4.10: Distance from sub-satellite point to target throughout mission for numerical simulation including atmospheric drag and an 18th order tesseral model. Manoeuvre begins at 1.433 days following the solution given by the general perturbation method.

Table 4.8: Comparison of flyover times for manoeuvring satellite calculated using the general perturbation method versus numerically.

	Time from epoch, days	Distance to target, km	Difference in time, sec	Difference in distance, km
General perturbation method	5.06	54.50	—	—
Numerical: J_2	5.06	67.17	1.19	12.67
Numerical: J_2 and atmospheric drag	5.06	57.67	39.36	3.18
Numerical: J_2 and atmospheric drag w/ compensation during altitude change	5.06	67.15	1.20	12.65
Numerical: 18th order tesseral and atmospheric drag	5.06	56.34	41.17	1.85
Numerical: 18th order tesseral and atmospheric drag w/ compensation during altitude change	5.06	65.98	2.33	11.5

The results of this analysis imply that the effects of atmospheric drag are the largest contributor to the discrepancy in the time of flyover as predicted by the general perturbation method, however the largest difference is very small at less than one minute over a five-day simulation. The difference in the distance to the target at flyover does not show consistent improvement with the addition of atmospheric drag compensation during phase 1 and phase 3, suggesting that the periodic effects of the central body perturbations, particularly J_2, have the largest impact on this variation, within the time period considered.

4.3 Rapid Flyover Mission Results

As shown in Section 4.2, if no manoeuvres are performed there is a 13.8 day gap between flyovers of Los Angeles after its second viewing at 1.433 days from epoch. It has been shown that an altitude-lowering manoeuvre using 30 m/s ΔV_{alt} can reduce the time between flyovers from 13.8 days to 3.6 days. The same scenario is investigated here for a range of ΔV_{alt} values from 0–120 m/s in increments of 1 m/s, for both altitude-lowering and altitude-raising manoeuvres. Using the general perturbation method, the shortest possible time in which a pass can be made over Los Angeles is calculated for each ΔV_{alt} value. The corresponding atmospheric drag compensation ΔV for each manoeuvre is then calculated using equation (2.85) and added to give the change in velocity required for the full manoeuvre, ΔV_{total}. For all solutions the atmospheric drag compensation

ΔV required was found to be less than 3.1 m/s, with those manoeuvres requiring a longer coast time at a low altitude the most affected. All possible manoeuvres are shown in Figure 4.11 where the circles indicate altitude-lowering manoeuvres, and the squares show altitude-raising manoeuvres. Note that the time shown is the time taken for the manoeuvre, not the time from epoch. These results show that the minimum achievable flyover time for a ΔV_{total} less than 120 m/s is 1.65 days, or 39.61 hours, achieved with a ΔV_{total} of just 1.34 m/s using an altitude-raising manoeuvre. This gives a decrease in flyover time of more than 12 days when compared with the non-manoeuvring case.

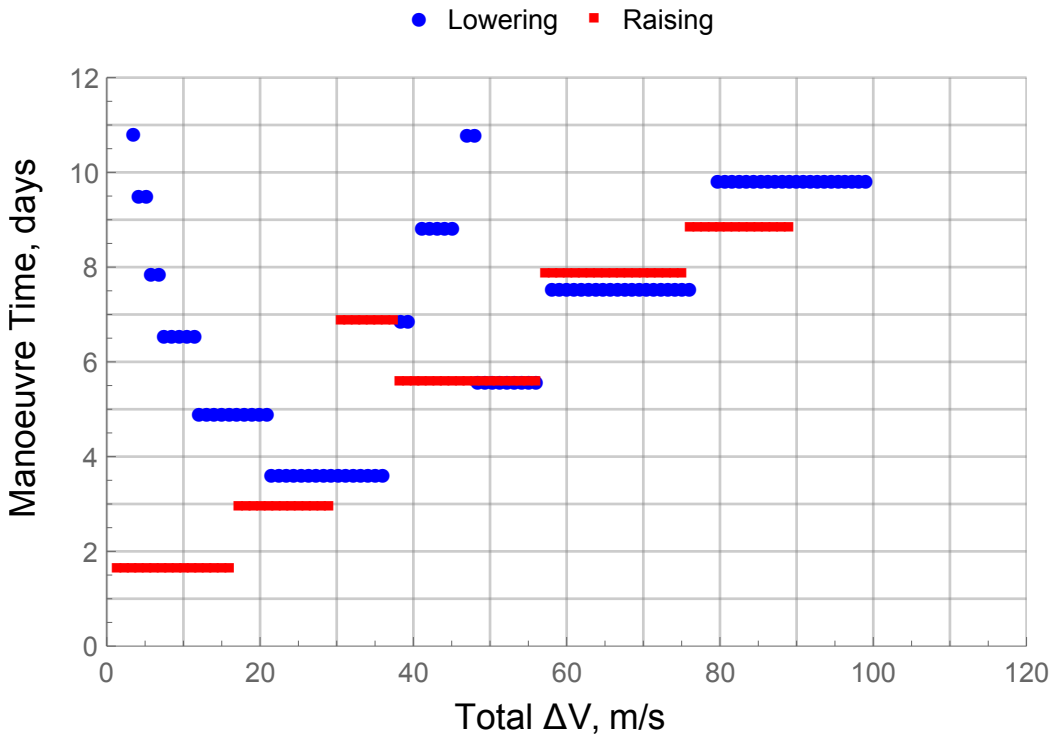

Figure 4.11: Shortest possible time to flyover for a given ΔV_{total} as calculated by the general perturbation method.

Each manoeuvre option in Figure 4.11 will have a corresponding minimum distance to the target at flyover, which will define the payload look-angle. This is shown in Figure 4.12 for the solutions requiring a manoeuvre time of approximately 1.6 days and a ΔV_{alt} of 0–17 m/s; these are all altitude-raising manoeuvres. Figure 4.12 shows that for a ΔV_{alt} of 1 m/s the minimum distance to the target will be more than 90 km at flyover. Increasing ΔV_{alt} increases the required manoeuvre time but also reduces the minimum distance to the target at flyover; however this trend gives diminishing

returns as ΔV_{alt} is increased further. These insights obtained from the solution space can be extremely valuable to an operator, allowing for an informed trade-off between mission goals, and are difficult to gain through numerical methods alone.

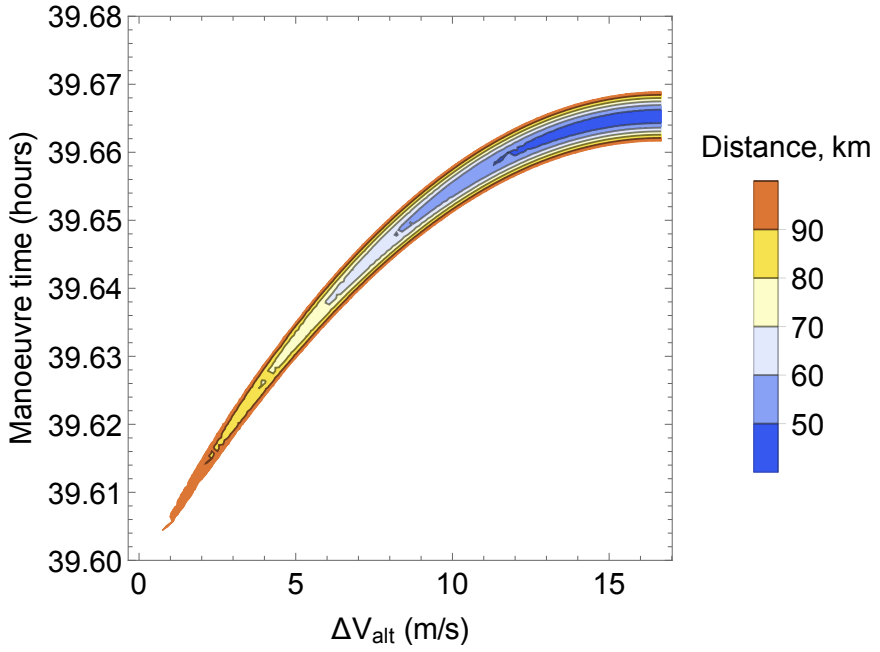

Figure 4.12: Minimum distance to target for selected solutions as a function of manoeuvre time and required ΔV_{alt} as calculated by the general perturbation method.

A 12.09 m/s manoeuvre, predicting a distance to target at flyover of 48 km and requiring a manoeuvre time of 39.66 hours, is selected as a compromise between ΔV, flyover time and look-angle at flyover. This predicts a flyover time of 3.06 days from epoch. The manoeuvre is analysed using the numerical propagator described in Section 4.2 including atmospheric drag and an 18th order tesseral model. The satellite is first propagated 1.433 days from epoch in its initial orbit and the 3-phase altitude-raising manoeuvre is then carried out. Atmospheric drag compensation is assumed to be performed during the phase 2 coast arc, as well as before and after the manoeuvre, but not during the altitude-raising and -lowering phases. Figure 4.13 shows the distance from the sub-satellite point to the target as calculated using the haversine formula at each time step throughout this simulation. The horizontal line indicates the point at which the target will be in view of the satellite, and the vertical dotted line marks the time at which the manoeuvre begins. A peak can be seen in this figure corresponding to a pass that occurs at 3.06 days from epoch. This pass occurs just 7 seconds earlier

than predicted by the general perturbation solution with the distance from the SSP to the target at this time found to be 38 km; this is 10 km closer than that predicted by the general perturbation solution. The total ΔV required is found to be 12.07 m/s including that required for atmospheric drag compensation, a difference of just 0.02 m/s when compared with the general perturbation solution.

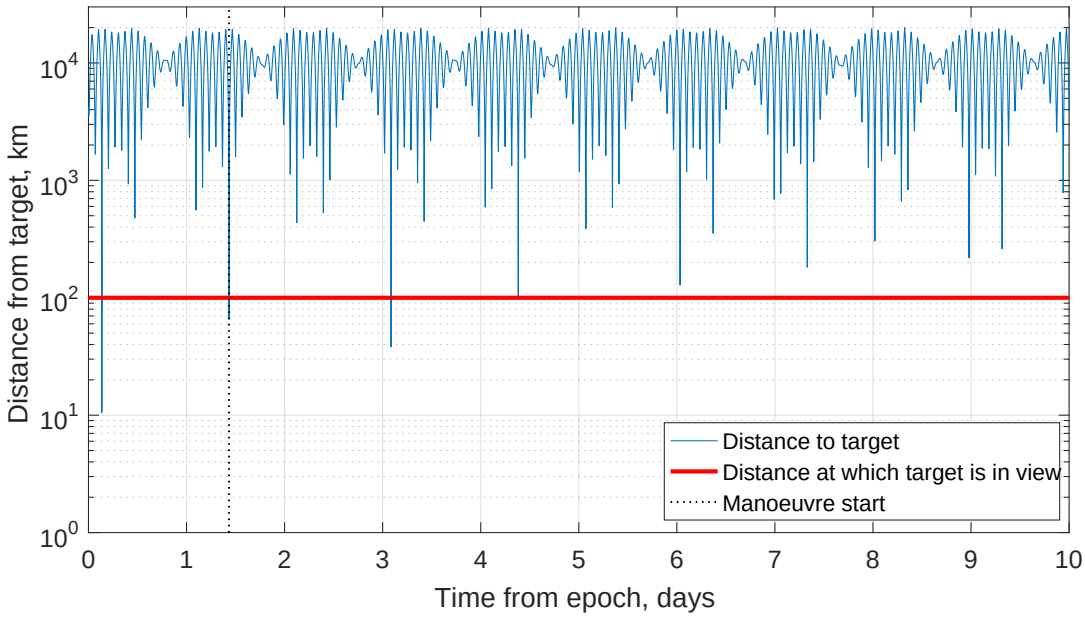

Figure 4.13: Distance from sub-satellite point to target throughout mission for the numerical simulation including atmospheric drag and an 18th order tesseral model. Altitude-raising manoeuvre begins at 1.433 days following the solution given by the general perturbation method.

It is of interest to note that the solution shown in Figure 4.13, requiring 12.09 m/s ΔV and a manoeuvre time of 39.66 hours, only has one possible subsequent flyover of the target, at approximately 4.3 days from epoch, and this will be close to the edge of the swath and of poor quality. Thus, if subsequent flyovers are desired, further manoeuvres will be required. Revisiting the results seen in Figures 4.8, 4.9 and 4.10, it can be seen that although the initial manoeuvre takes longer and requires 30 m/s ΔV_{alt}, there are numerous subsequent natural flyovers in the following days. This is an interesting observation that implies that, depending on the mission goals, it may be useful to look ahead at future natural flyovers for each manoeuvre option and include these as trade-off criteria. This would be possible using the general perturbation solution with minor adaptations.

Chapter 5

Constellation Reconfiguration

The general perturbation solution to the satellite overflight targeting problem developed in Chapter 2, and validated in Chapter 4, is now applied to a constellation reconfiguration scenario to demonstrate the ease with which intricate problems can be examined and valuable insights gained. The scenario to be analysed considers a constellation of 24 satellites tasked with fire detection and subsequent manoeuvring to provide targeted coverage of fire outbreaks.

The proposed fire response mission is based on a modified version of the nano-satellite constellation proposed by the Universitat Politécnica de Catalunya for global fire detection [87]. They identify a need for near-real-time, global fire monitoring capability and suggest a constellation of CubeSats equipped with a high resolution optical system could provide such a service. They state that a minimum six hour revisit time is required for all regions of interest, but a one hour revisit is desirable. They propose a constellation at 600 km altitude with four orbit planes inclined at 55 deg and six satellites per plane, for 24 total satellites. A similar constellation is under development by the Spanish company AISTECH who envision a 100 nano-satellite constellation, with the first due for launch in 2018 [88].

The ability of a responsive constellation comprising manoeuvrable satellites to provide the desired coverage will be compared with the performance of a traditional, static constellation. For the responsive constellation, the "ReCon" concept proposed by the Massachusetts Institute of Technology will be used [61, 89, 90]. In this concept, the

Earth observing constellation has two operational modes that it can manoeuvre between. The first is a global observation mode (GOM) in which the satellites are spread out to provide even coverage of the observation region. The second mode is regional observation mode (ROM) in which some of the satellites are moved into repeating ground track (RGT) orbits over a specific point of interest to provide improved coverage of the region. For the proposed mission, the constellation in GOM would be used to detect the outbreak of fire, and then would transition to ROM to provide more frequent revisits of the affected area. Once targeted coverage is no longer required, the constellation would return to GOM and continue global observations. This strategy is visualised in Figure 5.1 [61].

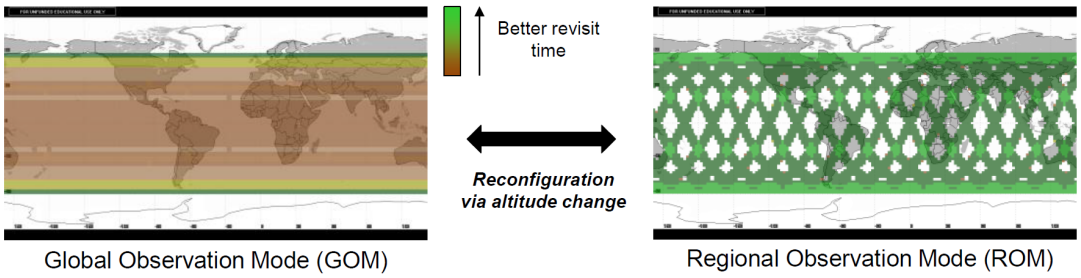

Figure 5.1: Visualisation of the ReCon concept [61].

Sequential fire outbreaks in four different locations are considered to assess the ability of a responsive constellation to provide increased coverage across a range of latitudes. The areas considered are the Cairngorms National Park, Scotland; Yosemite National Park, California; Agulhas National Park, South Africa; and the Lagunas de Montebello National Park, Mexico. These areas were selected due to their historical, or predicted future, propensity for fire outbreaks. Cairngorms National Park is a region of spectacular beauty in Scotland that is of high conservation importance due to its unique flora and fauna, however it is at increasing risk of fire outbreak [91, 92]. Yosemite National Park is the third most visited national park in the world with almost 4 million visitors annually but it has a very high fire risk in the drier months [93–95]. Agulhas National Park is situated approximately 210 km from Cape Town and surrounds the southern-most tip of Africa. On December 26th 2009, the Agulhas National Park was devastated by a fire that burnt over 60% of the park [96, 97]. Lagunas de Montebello National Park, Mexico is a small protected area on the border of Guatemala that was

subject to extensive fires in 1998 [98] and the entire Chiapas region is highlighted as one of the highest risk areas for wildfires [99]. The park itself is experiencing extreme damage and degradation due to deforestation and as such many efforts are currently being put in place to further protect the region [100].

The constellation proposed for this study is based on the constellation proposed by the Universitat Politécnica de Catalunya for fire monitoring [87], but with an inclination of 60 deg to incorporate mainland UK wholly in the observable region. This constellation is composed of 24 satellites in four evenly spaced orbit planes. For an orbit inclined at 60 deg, a repeat ground track of 15 orbits per day requires a mean altitude of 513.087 km as calculated for a circular orbit using the method described in [61] and [101]. The initial mean altitude of the GOM constellation is arbitrarily selected as 542.857 km. From this altitude a satellite requires a minimum 17 m/s ΔV to reach the ROM orbit altitude. The parameters of the constellation are given in Table 5.1 and the initial position of the satellites are given in Appendix G. The proposed swath width of 50 km is based on the mission design of the Universitat Politécnica de Catalunya [87]. Although the swath width would in fact vary due to the difference in constellation altitude, the proposed payload is a theoretical, early-stage design and so the use of a 50 km swath is deemed appropriate for the purpose of this investigation. For this study, the use of 3U CubeSats equipped with electrospray propulsion is assumed and the constants given in Table 3.1 and the spacecraft parameters in Table 4.3 are used.

In order to transition between GOM and ROM, two satellites per plane will be manoeuvred into repeating ground track orbits (i.e. eight satellites in total), with one satellite per plane providing coverage of the target region on the upwards pass, and the other providing coverage on the downwards pass. Moving additional satellites provides limited benefit as there are only two positions in each RGT orbit plane that provide a flyover of the target. Thus the manoeuvring of more satellites would result in multiple satellites positioned very close together, providing overlapping coverage and limited increased utility. The satellites remaining in the GOM orbit are not re-phased to provide even coverage from this altitude, however they will still provide incidental coverage of the target. These satellites could be re-phased but that would incur an additional ΔV cost.

Table 5.1: Fire response constellation mission parameters.

Parameter	Value	Units
Propulsion acceleration	$\pm 1.1667 \times 10^{-4}$	m/s^2
Inclination	60	deg
GOM osculating/mean altitude	550 / 542.857	km
ROM osculating/mean altitude	520.261 / 513.087	km
Number of orbit planes	4	—
Number of satellites per plane	6	—
RAAN spacing between orbit planes	90	deg
In plane spacing between satellites	60	deg
Phasing between satellites in adjacent planes	0	deg
Epoch	01 Jan 1990 00:00:00	—
Right ascension of Greenwich at epoch	100.39	deg
Instrument swath	50	km

For all targets, the region of interest is assumed to be a rectangle encompassing the national park with the parameters given in Table 5.2 and shown in Appendix D. The test scenario considered is selected arbitrarily, but is designed to consider locations across a range of latitudes and incorporate different reconfiguration scenarios. In the scenario the fire outbreaks occur sequentially in each region as follows: 1. Cairngorms, 2. Yosemite, 3. Agulhas, 4. Lagunas de Montebello. For each outbreak, the constellation will manoeuvre to ROM and then remain in ROM for seven days before transitioning back to GOM. The constellation then remains in GOM for seven days before the next fire is detected. The exception to this is the transition between targeting Yosemite and Agulhas; in this case the fire in Agulhas is assumed to be detected while the constellation is still targeting Yosemite and so a direct transition from ROM to ROM occurs. This time-line is shown in Figure 5.2, where each arrow indicates a reconfiguration of the constellation.

Table 5.2: National park locations.

Point of Interest	Minimum Latitude, deg	Maximum Latitude, deg	Minimum Longitude, deg	Maximum Longitude, deg
Cairngorms	56.58	57.66	-4.64	-2.65
Yosemite	37.49	38.18	-119.89	-119.20
Agulhas	-34.83	-34.68	19.63	20.02
Lagunas de Montebello	16.07	16.12	-91.74	-91.63

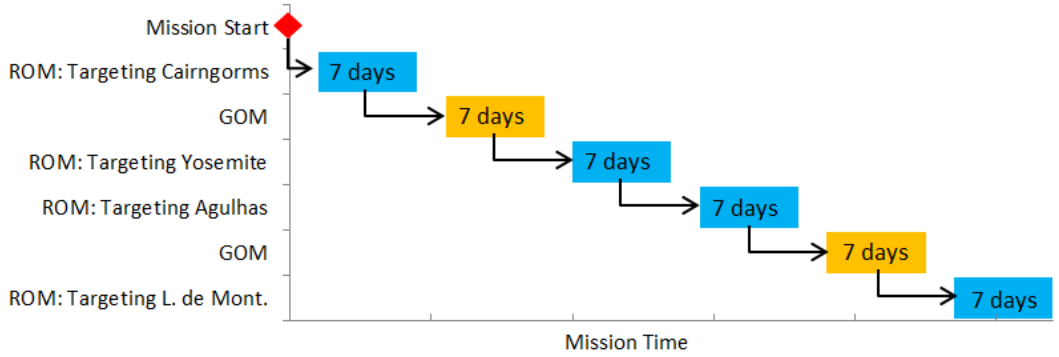

Figure 5.2: Fire response mission scenario.

5.1 Method

In order to decide which satellites should be manoeuvred during each reconfiguration, and what form these manoeuvres should take, each satellite is analysed using the general perturbation method described in Chapter 2, producing a list of all possible manoeuvres that each satellite could perform that would conclude with the satellite over the target region and in a repeating ground track orbit. This is done for a ΔV_{alt} range of 17–120 m/s in steps of 1 m/s, for up to 10 days total manoeuvre time, and considers both altitude-raising and altitude-lowering manoeuvres. In addition to the ΔV_{total} required for the manoeuvre, the satellites are assumed to perform atmospheric drag compensation at all times when not manoeuvring; this applies to the satellites in GOM and ROM. As this ΔV is dependent on the length of the manoeuvres selected, it cannot be included in the trade space while maintaining a fully-analytical solution, and so it is instead calculated after the mission scenario has been defined. Compared to the ΔV required for manoeuvring, these values are extremely small and relatively consistent across all satellites in either ROM or GOM, and as such their exclusion from the trade space is deemed acceptable.

The full set of possible manoeuvres for all satellites to target the Cairngorms are shown in Figure 5.3, where the colour is scaled to the z-axis showing the distance to the target at the end of each possible manoeuvre. The results in the foreground of the graph have been discarded as the time allocated for these manoeuvres would be less than that required to achieve the necessary ΔV. This leaves 1979 possible manoeuvres, each of

which will have a corresponding manoeuvre time and ΔV associated with it. For all solutions shown the satellite SSP will pass within the region of interest, however it can be seen that the distance from the SSP to the centre of the POI will vary depending on the manoeuvre selected. This full overview of the solution space allows the operator to identify all possible solutions and then select those that best meet their mission criteria, whether that be to minimise time to first viewing, minimise propellant usage, minimise distance to target at flyover, or a compromise between all three.

In order to select the 'best' manoeuvres from the full solution set, the solutions are grouped first by orbit plane and then by whether they will view the target on an upwards or downwards pass. A simple additive multi-attribute utility function is then applied to produce a single utility score for each solution [102, 103]. The solution in each grouping with the highest utility function is then selected. In some cases where the difference in utility function between satellites was small, a judgement was made to select the preferred solution; this was done to bring the desired outcome in-line with what a mission operator would likely select, while avoiding the need to fine-tune the utility function, which is outside the scope of this work.

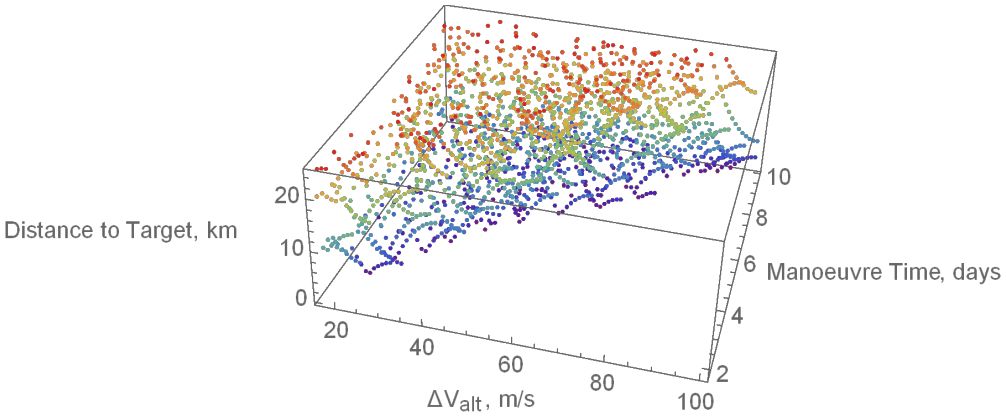

Figure 5.3: Full set of solutions for Cairngorms flyover.

A simple additive multi-attribute utility function can be described by

$$U(X) = \sum_{n=1}^{N} k_n U_n(X_n) \tag{5.1}$$

where X_n is a single attribute, $U_n(X_n)$ is the utility function of a single attribute, k_n is a weighting factor for a single attribute, and $U(X)$ is the multi-attribute utility function.

The weighting factors determine the relative weighting to be given to each attribute considered. The attributes considered are ΔV_{total}, manoeuvre time, and distance to the centre of the region of interest at the end of the manoeuvre. Each of these is normalised against the range of possible values of the attribute to give a utility between 0 and 1. That is,

$$U_n = \frac{X_{worst} - X_n}{X_{worst} - X_{ideal}} \tag{5.2}$$

where X_{worst} is the worst possible value of the attribute and X_{ideal} is the best possible value. For ΔV, the worst possibility is the maximum possible ΔV so $X_{worst} = 120$ m/s, while the ideal case is the minimum possible ΔV so $X_{ideal} = 17$ m/s. For manoeuvre time the worst option is the maximum time possible so $X_{worst} = 10$ days, while $X_{ideal} = 0$ days. For distance to the centre of the region of interest at the end of the manoeuvre the worst possible value is half the swath width, so in this case $X_{worst} = 25$ km, while $X_{ideal} = 0$ km.

5.1.1 Return to Global Monitoring Constellation

Once the fire has been dealt with, it is assumed that the constellation would return to GOM mode to continue global observation. This is considered a non-urgent manoeuvre, and so the minimum ΔV possible is used, with the required satellite in-plane phasing being achieved by the satellite remaining in the RGT orbit for as long as is necessary before manoeuvring. In this case, there is essentially no phase 1 manoeuvre, and instead the satellite coasts as in phase 2 before raising its altitude to return to the GOM constellation. To calculate the required manoeuvre time for each satellite, a simplified version of the general perturbation method is used in which the time and ΔV for phase 1 are both set to zero.

Taking any satellite in the same plane and at the GOM altitude as a reference, the desired difference in the final AoLs of the manoeuvring satellite and the reference satellite can be specified, as described in Section 2.6, and thus the total required manoeuvre time calculated to achieve the desired spacing using the minimum ΔV of 17 m/s. All possible solutions are investigated for each plane and the solutions selected to give the shortest total manoeuvre time for each plane. It is of note that on return

to GOM using this method, the satellite spacing within each orbit plane will return to 60 deg, however the RAAN of the manoeuvred satellites will have a slight variation from the other satellites. This could be readjusted by raising the altitude of these satellites above the GOM altitude and allowing them to drift in RAAN before re-phasing. For this study the orbit planes were not adjusted and the largest difference in RAAN between two satellites in the same plane was less than 2 deg at the end of the mission.

5.1.2 Direct Manoeuvre from ROM to ROM

When manoeuvring to target Agulhas National Park the constellation is assumed to begin manoeuvring directly from observing Yosemite with no transition to GOM, as indicated in Figure 5.2. The general perturbation method is used, as normal, to select the satellites to manoeuvre. Any satellites remaining in RGT orbits over Yosemite are returned to GOM using the minimum possible ΔV of 17 m/s, with the required satellite in-plane phasing being achieved by the satellite remaining in the RGT orbit for as long as required. This is similar to the standard return to GOM manoeuvre but due to additional satellites moving from GOM to ROM there is a wider range of orbital slots available to return to, increasing the complexity of the analysis.

5.2 Comparison of Non-Weighted and Weighted Utility Functions

Before analysing the full mission, a comparison will be made between the results obtained using a non-weighted and a weighted utility function, considering only the first reconfiguration to target the Cairngorms. For the non-weighted utility function each variable is given equal weight, while the weighted utility function is adjusted to prioritise minimising manoeuvre time, while reducing the importance of the distance to the target at flyover. The ΔV_{total} required is taken as the normal value, so $k_{\Delta V} = 1$ and relative weightings are given to the manoeuvre time and distance to target respectively as $k_{time} = 3$ and $k_{distance} = 0.5$.

To select the 'best' solutions for each plane, the solutions are grouped by orbit plane and then according to the pass type: up or down. Each solution is then assigned

a utility function. Figure 5.4 (a) shows the utility calculated with the non-weighted function for all solutions for orbit plane 1 that result in an upwards pass over the Cairngorms; Figure 5.4 (b) shows the corresponding solution using the weighted utility function. Figure 5.5 (a) shows the non-weighted utility for the orbit plane 1 solutions that result in a downwards pass over the target. Figure 5.5 (b) shows the same results for the weighted utility function. The blue dots are those manoeuvres in which the altitude is lowered in phase 1 and the orange dots are those in which the altitude is raised in phase 1. Similar results are obtained for all other orbit planes and are given in Appendix E.

From these results, those manoeuvres with the highest utility in each plane, and for each pass type, are selected as the final solution. These are presented in Table 5.3 for the non-weighted utility function and in Table 5.4 for the weighted utility function. From this is it is clear that the utility function selected, or correspondingly the user's priorities, can have a significant impact on the solution that is determined to be the 'best'. For orbit planes 1–3, the same satellites are selected to manoeuvre by both utility functions but there are differences in the ΔV_{total} and manoeuvre time, and hence the distance to the target at flyover. In the case of plane 4, the two satellites selected to manoeuvre are entirely different depending on the utility function used.

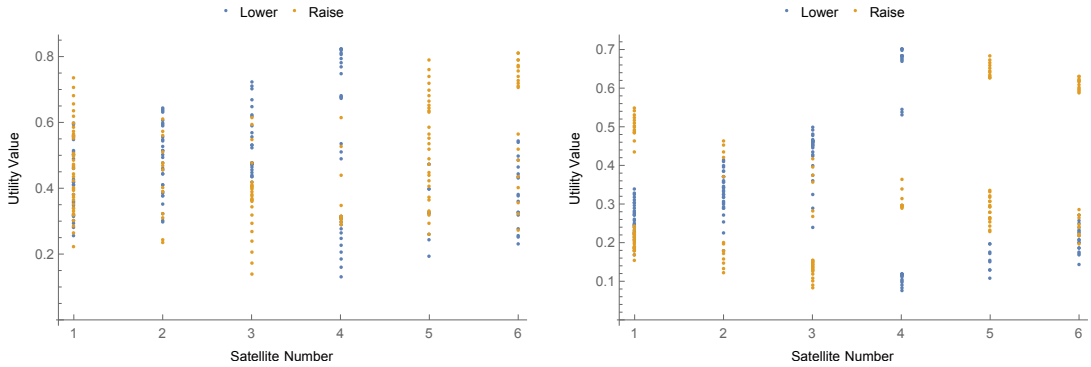

Figure 5.4: Utility of manoeuvre versus satellite number for orbit plane 1 for upwards pass over the Cairngorms for (a) the non-weighted case, (b) the weighted case.

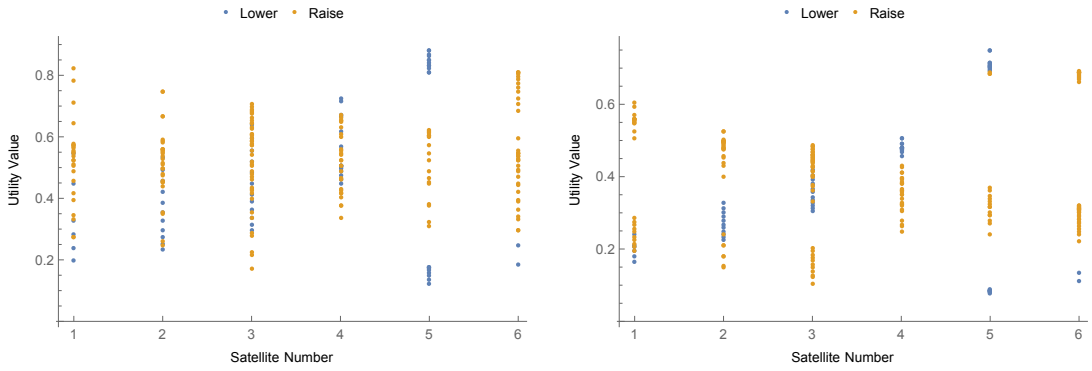

(a) (b)

Figure 5.5: Utility of manoeuvre versus satellite number for orbit plane 1 for downwards pass over the Cairngorms for (a) the non-weighted case, (b) the weighted case.

Table 5.3: Selected satellite manoeuvres to target the Cairngorms using unweighted utility function.

	Satellite	ΔV_{total}, m/s	Time, days	Distance, km	Pass type	Manoeuvre Type
Plane 1	4	29.00	3.02	2.85	Downwards	Lower
	5	22.02	2.87	0.59	Upwards	Lower
Plane 2	7	20.00	2.13	8.45	Upwards	Raise
	12	17.01	2.28	8.07	Downwards	Raise
Plane 3	13	26.03	3.51	3.71	Downwards	Lower
	14	23.00	2.38	5.09	Upwards	Lower
Plane 4	20	34.05	4.74	0.18	Downwards	Lower
	23	26.02	3.61	0.16	Upwards	Raise

Table 5.4: Selected satellite manoeuvres to target the Cairngorms using weighted utility function.

	Satellite	ΔV_{total}, m/s	Time, days	Distance, km	Pass type	Manoeuvre Type
Plane 1	4	18.01	2.03	18.80	Downwards	Lower
	5	17.01	1.88	9.64	Upwards	Lower
Plane 2	7	19.00	2.13	8.79	Upwards	Raise
	12	17.00	2.28	8.07	Downwards	Raise
Plane 3	13	23.01	2.52	13.07	Downwards	Lower
	14	21.01	2.38	5.75	Upwards	Lower
Plane 4	21	17.00	1.78	19.92	Downwards	Raise
	22	17.02	2.62	18.08	Upwards	Raise

5.2.1 Coverage Results for Non-Weighted and Weighted Utility Functions

In order to quantify the effect that utility function selection can have on the results, the coverage of the Cairngorms region available from the constellation is considered over a one-week period after the manoeuvres have been performed (i.e. in ROM mode) for both the non-weighted and weighted utility function solutions. The coverage analysis is performed using an orbit propagator that considers only the secular effects of J_2 and considers the Earth to be spherical for the purposes of determining the latitude and longitude of the sub-satellite point. Comparison with the coverage available from a non-manoeuvred static constellation, as well as coverage of the other regions of interest, will be investigated in Section 5.4, after the utility function has been selected.

Figure 5.6 shows the total time in the one-week period analysed that a region of the Cairngorms has been viewed after the constellation reconfiguration has been carried out following (a) the unweighted solution, and (b) the weighted solution. After the manoeuvres have been carried out following the unweighted solution, the average coverage time is 4.5 minutes, with the best viewed regions receiving 8.8 minutes total coverage. For the weighted solution the average coverage time is 5.1 minutes, with the best viewed regions receiving 8.4 minutes of coverage in the one-week period.

Figure 5.7 shows the maximum time between viewings for regions of the Cairngorms in the one-week period analysed after the constellation reconfiguration has been carried out following (a) the unweighted solution, and (b) the weighted solution. For the unweighted case, a one-week analysis shows the average revisit time for any point in the Cairngorms is 4.1 hours, with the most frequently viewed point having an average revisit of 2.0 hours. The longest time that any individual region in the Cairngorms is not viewed is 43.5 hours, and the longest time for which the entire Cairngorms area is not viewed is 3.1 hours. For the weighted case, a one-week analysis shows the average revisit time for any point in the Cairngorms is 3.4 hours, with the most frequently viewed point having an average revisit of 1.9 hours. The longest time that any individual region in the Cairngorms is not viewed is 17.7 hours, and the longest time for which the entire Cairngorms area is not viewed is 3.1 hours.

The results obtained show that the weighted solution gives slightly worse coverage

than the unweighted solution, but requires a much shorter transfer time; it requires just 2.62 days for complete reconfiguration, while the unweighted solution requires 4.74 days. The weighted solution also performed better in terms of maximum revisit time, with the longest gap in coverage for a localised region of just 17.7 hours, compared with 43.5 hours in the unweighted case. This high revisit gap in the unweighted case is due to the distance to target parameter being ranked equally with the other parameters and causing the coverage to be focused on the centre of the target region. For this fire response case study in which speed is of high importance, and regular coverage of the entire region of interest is desired, the weighted solution will be taken as the 'best' option and this utility function will be used for all future solution selection. The results of this investigation highlight that the weighting of the trade-off criteria will have an impact on the final coverage available. However, the speed of the general perturbation solution means that the impact of a variety of utility functions can rapidly be analysed, in order to fine-tune the selection criteria.

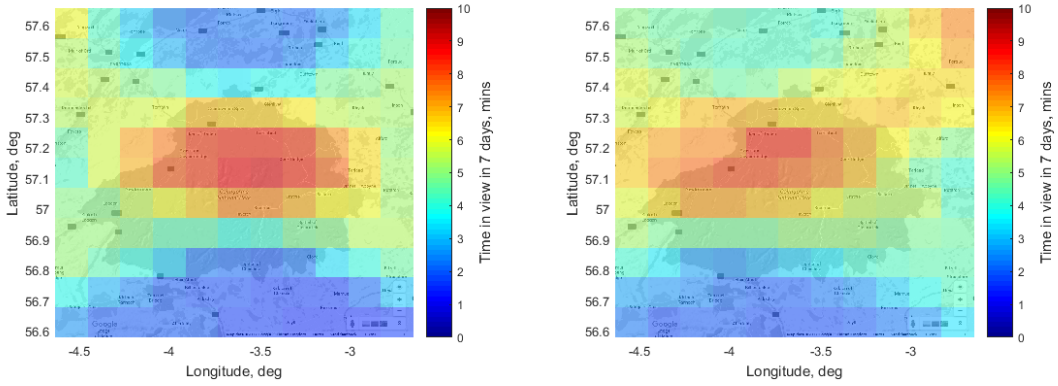

(a) (b)

Figure 5.6: Total time that a region of the Cairngorms has been in view over 1 week after manoeuvring following (a) the unweighted solution and (b) the weighted solution [104].

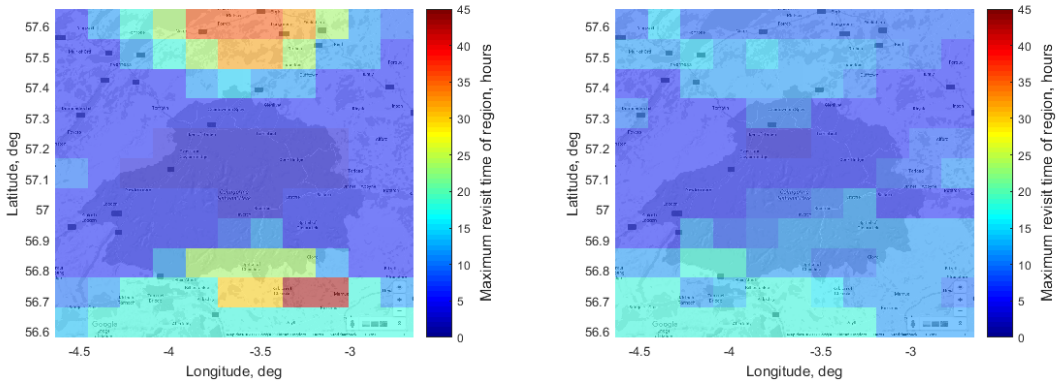

(a) (b)

Figure 5.7: Maximum time that a region of the Cairngorms has not been seen over 1 week after manoeuvring following (a) the unweighted solution and (b) the weighted solution [104].

5.3 Comparison against Numerical Simulation

The same numerical simulator used in Chapter 4 to compare with the general perturbation method, including atmospheric drag and an 18th order tesseral central body perturbation model, is used to analyse the accuracy of the proposed manoeuvres for the fire response constellation for the weighted case to target the Cairngorms, as described in Section 5.2. All satellites to be manoeuvred, with manoeuvre descriptions given in Table 5.4, are considered separately and are analysed for one week from manoeuvre start.

Figures 5.8 and 5.9 show the distance between the sub-satellite point and the centre of the Cairngorms for the manoeuvred satellites in orbit plane 1 (i.e. Satellites 4 and 5) over the one-week period. Similar graphs for the other orbit planes are given in Appendix F. The horizontal line is drawn at half the swath width and indicates the distance at which the centre of the Cairngorms will be visible to the satellite. In all cases, close approaches can be seen at the expected times of flyover, with daily close approaches thereafter indicating that the satellite has finished in, or close to, the repeating ground track orbit as desired. The errors in the final altitude are caused by the manoeuvres taking place over a non-integer number of orbits, leading to differences in the expected final altitude due to the short-term periodic perturbation effects of the central body.

The time of the flyover at the end of each satellite's manoeuvre and the corresponding distance at this time as calculated by the numerical simulator and the general perturbation method are given in Table 5.5. Comparing the two sets of results, they agree well; the largest error in flyover time is just 5 seconds and the largest error in the distance to the target is 23 km. This falls within the maximum expected errors as a result of excluding periodic J_2 effects as discussed in Chapter 4.

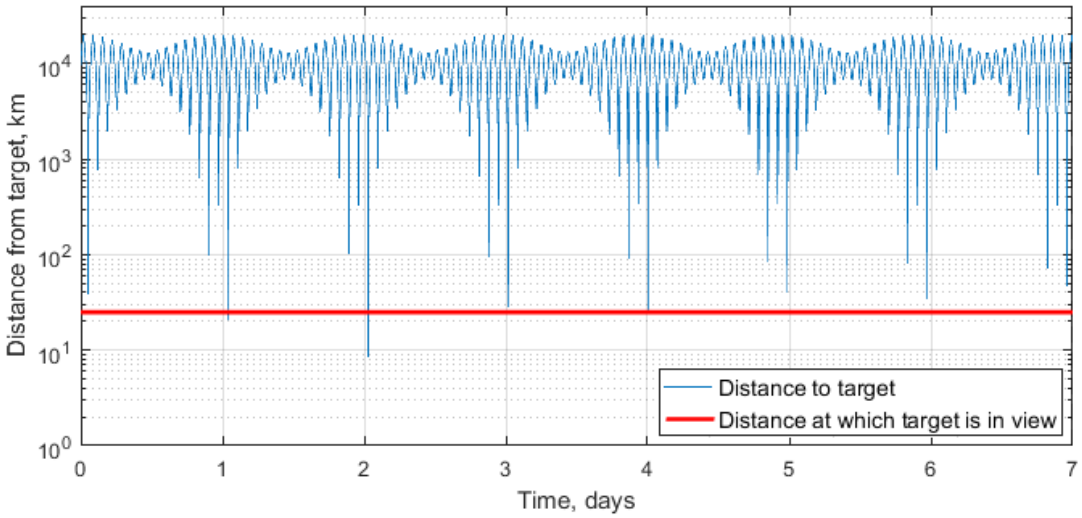

Figure 5.8: Distance from sub-satellite point to centre of the Cairngorms plotted as a function of total time for Satellite 4 using numerical solution.

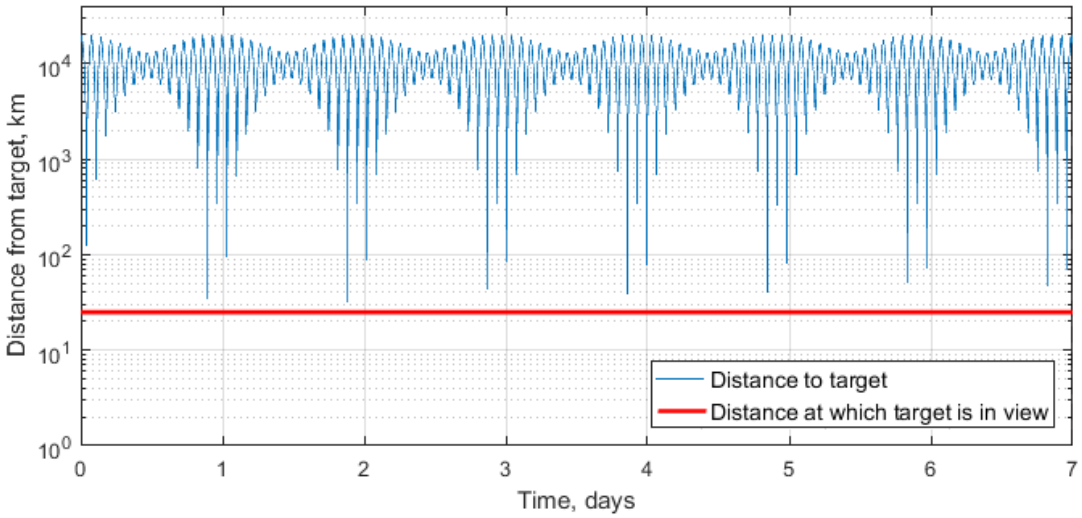

Figure 5.9: Distance from sub-satellite point to centre of the Cairngorms plotted as a function of total time for Satellite 5 using numerical solution.

Table 5.5: Comparison of flyover times for manoeuvred satellites calculated using general perturbation method versus numerical method.

	Gen. Perturbation		Numerical		Absolute Difference	
Satellite	Manoeuvre Time, days	Distance to target, km	Manoeuvre Time, days	Distance to target, km	Time, sec	Distance to target, km
4	2.03	18.80	2.03	16.87	<0.5	1.93
5	1.88	9.64	1.88	32.63	<1	22.99
7	2.12	8.79	2.12	8.56	<0.5	0.23
12	2.28	8.07	2.28	9.89	<0.5	1.82
13	2.52	13.07	2.52	3.59	5	9.49
14	2.38	5.75	2.38	24.30	3	18.55
21	1.78	19.92	1.78	36.45	3	16.53
22	2.62	18.08	2.62	36.83	2	18.75

5.4 Results

5.4.1 Mission Overview

Having defined the utility function to be used and ensured the accuracy of the method by comparison with a numerical simulator, the general perturbation method is used to define the full sequence of manoeuvres required to provide coverage of all four target regions as defined in Section 5.1. These manoeuvres and the corresponding orbital elements at the beginning and end of each reconfiguration are given in Appendix G.

Table 5.6 summarises the entire mission. The mission takes just less than 83 days, assuming seven days for each GOM and ROM phase, and requires 1011.23 m/s total ΔV, including that required for atmospheric drag compensation throughout. This is just 35% of the total available across the constellation. Satellite 10 uses the largest proportion of propellant, requiring a ΔV of almost 99 m/s. Satellite 3 and Satellite 11 perform no altitude changing manoeuvres throughout the mission and require just 1.6 m/s ΔV for atmospheric drag compensation. The average ΔV used across all satellites is 42 m/s, thus it is likely that the constellation could perform numerous further reconfigurations before all propellant would be depleted. The standard deviation of the propellant usage across all satellites is 20.19 m/s.

It is possible to balance propellant usage by individual satellites, to help ensure that no satellite runs out of propellant prematurely. This was done by including each satellite's remaining propellant in the manoeuvre selection utility function. To do this,

an additional attribute term, U_{fb}, was added to the utility function to account for the propellant remaining on board each satellite. This was included in equation (5.1) with a weighting $k_{fb} = 2$. In this case X_{worst} is the minimum possible remaining ΔV, 0 m/s, X_{ideal} is the maximum possible ΔV, 120 m/s, and X_n is the actual remaining ΔV. In this scenario, the first two reconfigurations to target the Cairngorms and Yosemite are the same as for the case with no propellant balancing. However, beyond this point the scenario changes due to the new utility function. The full mission summary is given in Table 5.7. The mission takes 10 days longer than the previous case, and uses approximately 80 m/s more ΔV across the constellation; this is 38% of the total available constellation, giving an increase of just 3% when compared with using no propellant balancing. However, the total ΔV used by each individual satellite across the constellation is reduced. The standard deviation of the propellant usage across all satellites is reduced to 16.8 m/s, with only Satellite 23 having not manoeuvred, and the largest amount of ΔV used by a single satellite being 79.18 m/s used by Satellite 19.

The total cumulative ΔV used over time for the cases with and without propellant balancing is shown in Figure 5.10. From this it can be seen that the total propellant used across the constellation is higher when propellant balancing is considered. This is because less favourable manoeuvres must be selected to avoid the repeated use of the same satellites and hence a greater depletion of their individual propellant. The effect of this is shown in Figure 5.11 which shows the maximum ΔV used by an individual satellite during each targeting manoeuvre. It is clear that when considering propellant balancing, satellites are required to perform higher ΔV manoeuvres at the later stages of the mission, to avoid repeated use of those satellites that have already manoeuvred. Figure 5.12 shows the total ΔV used by each satellite to complete the mission for both cases. Here it can be seen that although the inclusion of propellant balancing uses a greater ΔV overall, it does reduce the maximum ΔV used by the individual satellites. This assessment of the impact of a change in mission priorities is a valuable insight that is facilitated by the use of the general perturbation solution, as its speed allows for the impact of such decisions to be quickly analysed and compared.

Table 5.6: Fire response mission ΔV and time for each section.

Section	**Section time, days**	**Total time, days**	**Section ΔV, m/s**	**Total ΔV, m/s**
Start	0.00	0.00	0	0
Manoeuvre to target Cairngorms	2.62	2.62	149.98	149.98
Observing Cairngorms in ROM	7.00	9.62	3.93	153.91
Return to GOM	12.32	21.94	141.94	295.85
Time in GOM	7.00	28.94	3.28	299.12
Manoeuvre to target Yosemite	4.84	33.78	180.05	479.18
Observing Yosemite in ROM	7.00	40.78	3.93	483.11
Manoeuvre to target Agulhas	7.97	48.76	191.02	674.12
Observing Agulhas in ROM	7.00	55.76	3.93	678.06
Return to GOM	9.21	64.97	140.48	818.54
Time in GOM	7.00	71.97	3.28	821.81
Manoeuvre to target L. de Mont.	3.79	75.76	185.49	1007.30
Observing L. de Mont. in ROM	7.00	82.76	3.93	1011.23

Table 5.7: Fire response mission with propellant balancing; ΔV and time for each section.

Section	**Section time, days**	**Total time, days**	**Section ΔV, m/s**	**Total ΔV, m/s**
Start	0.00	0.00	0	0
Manoeuvre to target Cairngorms	2.62	2.62	149.98	149.98
Observing Cairngorms in ROM	7.00	9.62	3.93	153.91
Return to GOM	12.32	21.94	141.94	295.85
Time in GOM	7.00	28.94	3.28	299.12
Manoeuvre to target Yosemite	4.84	33.78	180.05	479.18
Observing Yosemite in ROM	7.00	40.78	3.93	483.11
Manoeuvre to target Agulhas	10.68	51.46	236.55	719.66
Observing Agulhas in ROM	7.00	58.46	3.93	723.59
Return to GOM	14.05	72.51	143.01	866.60
Time in GOM	7.00	79.51	3.28	869.88
Manoeuvre to target L. de Mont.	6.31	85.82	217.83	1087.70
Observing L. de Mont. in ROM	7.00	92.82	3.72	1091.42

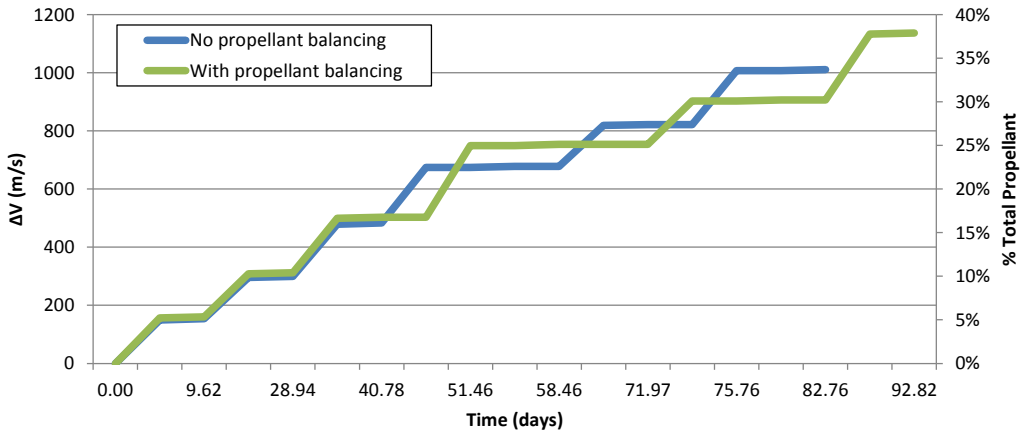

Figure 5.10: Total ΔV used over time for the fire response mission with and without propellant balancing.

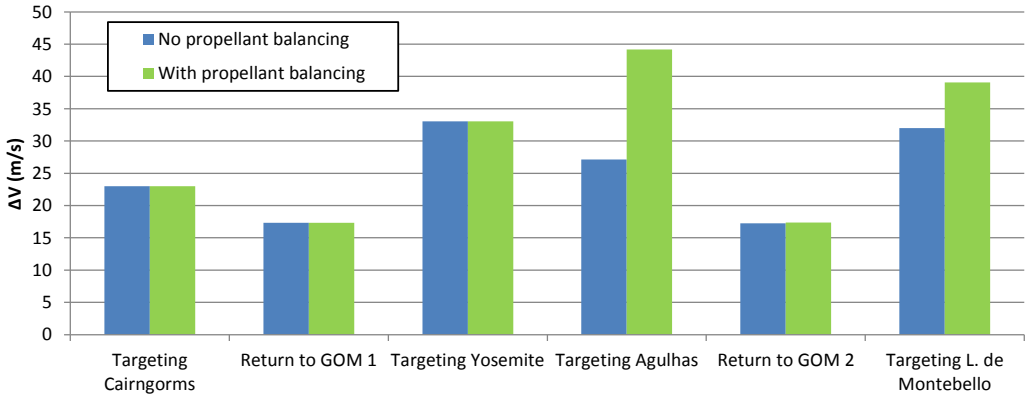

Figure 5.11: Maximum ΔV used by any satellite for each manoeuvre in the fire response mission with and without propellant balancing.

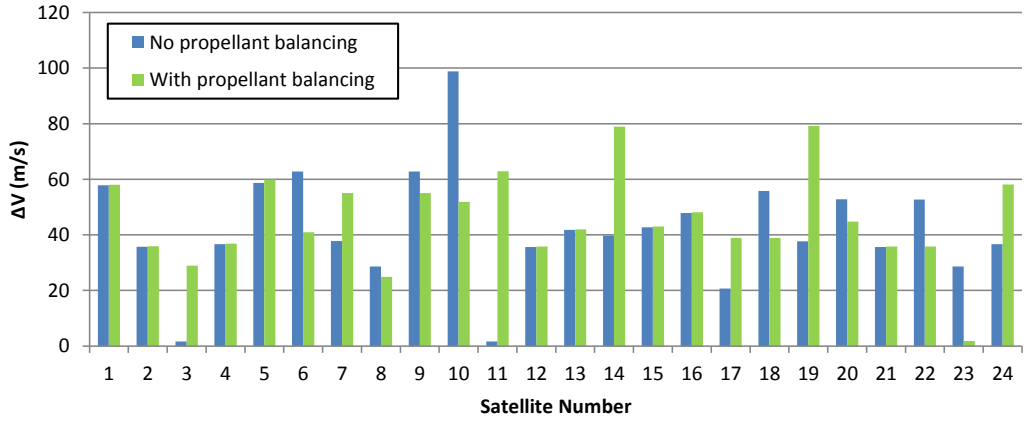

Figure 5.12: ΔV used by each satellite in the fire response mission with and without propellant balancing.

5.4.2 Coverage of Targets

In order to assess the improvement in coverage and revisit time that could be achieved through the use of the proposed responsive constellation, a comparison is made with a static constellation of 24 satellites inclined at 60 deg and at a mean altitude of 542.9 km; this is the same as the initial GOM constellation with no manoeuvres performed. The coverage available from both the static constellation and the responsive constellation is analysed for each region over a one-week period using an orbit propagator that considers only the secular effects of J_2 and considers the Earth to be spherical for the purposes of determining the latitude and longitude of the sub-satellite point. A summary of these results is given in Table 5.8, where the average coverage and revisit time refers to the

mean value across the entire region of interest. Peak coverage refers to the maximum coverage available to any single location within the region of interest. Maximum local revisit time refers to the maximum time that any single location within the region is not viewed.

Figure 5.13 to Figure 5.16 visually depict the total time in a one-week period that the region has been viewed by the responsive constellation and the static constellation. From these results it is clear that in all cases, manoeuvring the constellation improves the average coverage provided across the target region. A more significant increase is seen in those targets at lower latitudes as the coverage available to them from the static constellation is lower when compared to targets at the upper latitudes of the satellites' visible region. For example, the Cairngorms see an improvement in average regional coverage of approximately 1.8 times after manoeuvring, while the Yosemite region sees an improvement of more than 6 times.

Figure 5.17 to Figure 5.20 show the average revisit of each region from both the static and responsive constellations. For all regions there is a reduction in the average revisit time when using the responsive constellation, with the reduction in revisit time most significant at the lower latitudes where the revisit time of the static constellation is higher. Also of note is that the revisit time provided by the responsive constellation is consistent for all latitudes, with a revisit time of between 2.5–3.5 hours for all regions considered; this is expected as the predominance of coverage is provided by the eight satellites in evenly spaced RGT orbits, with additional incidental coverage from the satellites in GOM. This is in contrast to the static constellation, which will provide more frequent revisits at higher latitudes.

The results presented in this section demonstrate that the proposed responsive constellation can improve the revisit time from the six hours proposed by the Universitat Politécnica de Catalunya [87] to approximately three hours. However it cannot reach the one hour capability desired; this could theoretically be achieved with 24 satellites if they were spread across 12 orbit planes, but all satellites would be required to partake in each targeting manoeuvre, and this would decrease the number of reconfigurations possible before all propellant was depleted. The consistent revisit time provided to the target regions from ROM is an additional advantage when comparing with a static

constellation that must be designed for coverage of the lower latitudes, providing an excess of coverage elsewhere. These results demonstrate the insights that can be rapidly obtained through the application of the general perturbation solution to complex reconfiguration problems with thousands of possible solutions.

Table 5.8: Coverage of target regions over 7 days for both static and responsive constellations.

	Cairngorms		Yosemite		Agulhas		L. de Montebello	
	Static	Responsive	Static	Responsive	Static	Responsive	Static	Responsive
Average coverage of region (mins)	2.8	5.1	1.0	5.5	1.0	6.7	0.64	6.7
Peak local coverage (mins)	3.2	8.4	1.1	8.4	1.1	7.5	0.7	6.96
Average revisit time (hrs)	5.6	3.4	16.1	3.15	16.7	2.7	23.8	2.7
Maximum local revisit time (hrs)	15.5	17.7	56.8	11.86	62.3	5.9	48.6	5.9

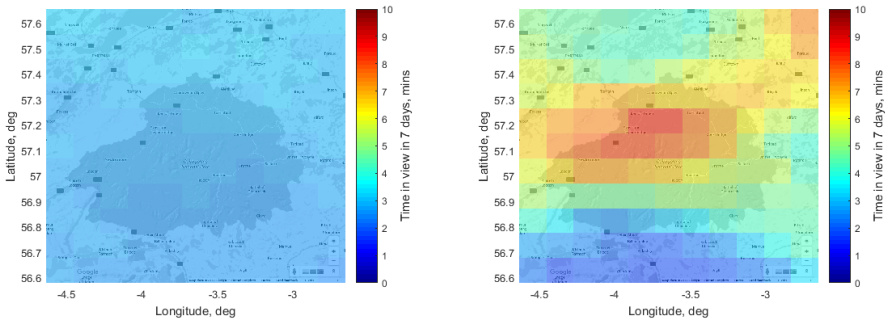

(a) (b)

Figure 5.13: (a) Total time that a region of the Cairngorms has been seen in a 1-week period for (a) the static constellation, (b) the responsive constellation [104].

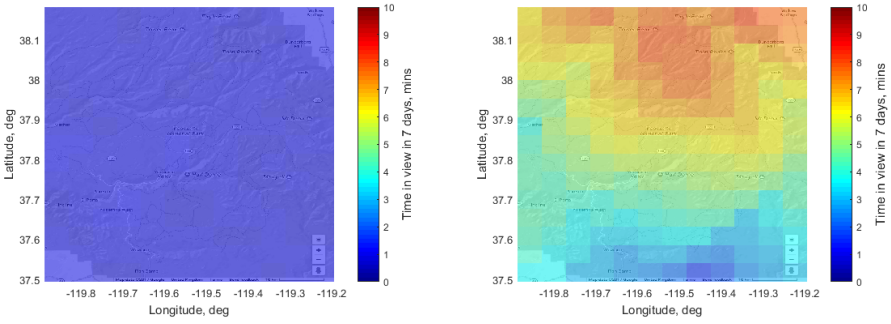

(a) (b)

Figure 5.14: (a) Total time that a region of Yosemite has been seen in a 1-week period for (a) the static constellation, (b) the responsive constellation [104].

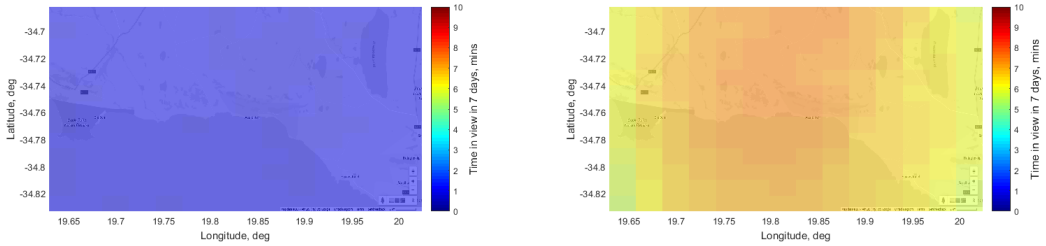

(a) (b)

Figure 5.15: (a) Total time that a region of the Agulhas has been seen in a 1-week period for (a) the static constellation, (b) the responsive constellation [104].

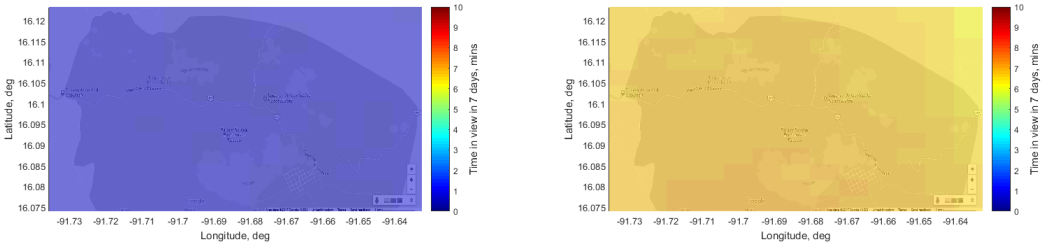

(a) (b)

Figure 5.16: (a) Total time that a region of Lagunas de Montebello has been seen in a 1-week period for (a) the static constellation, (b) the responsive constellation [104].

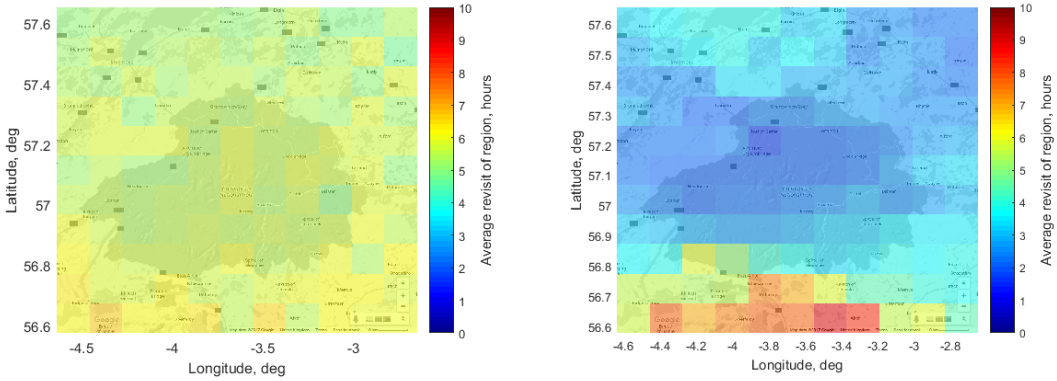

(a) (b)

Figure 5.17: (a) Average revisit time of the Cairngorms in a 1-week period for (a) the static constellation, (b) the responsive constellation [104].

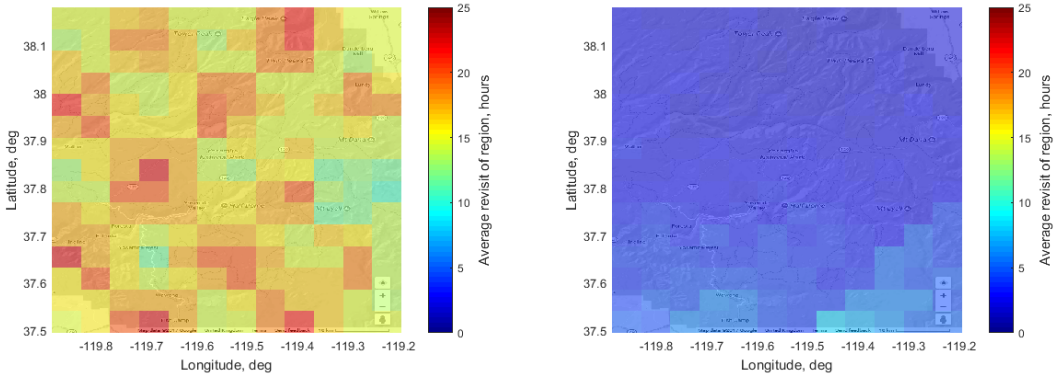

(a) (b)

Figure 5.18: (a) Average revisit time of Yosemite in a 1-week period for (a) the static constellation, (b) the responsive constellation [104].

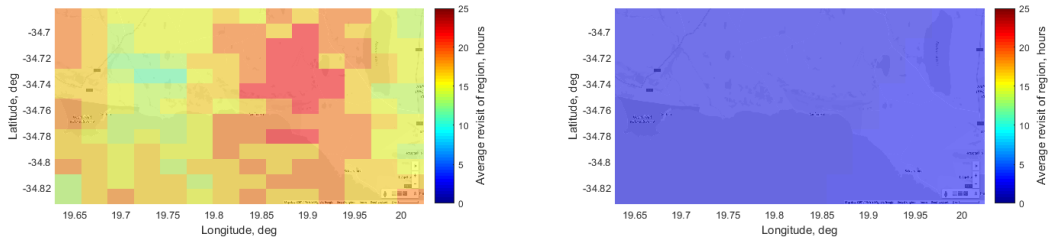

(a) (b)

Figure 5.19: Average revisit time of the Agulhas in a 1-week period for (a) the static constellation, (b) the responsive constellation [104].

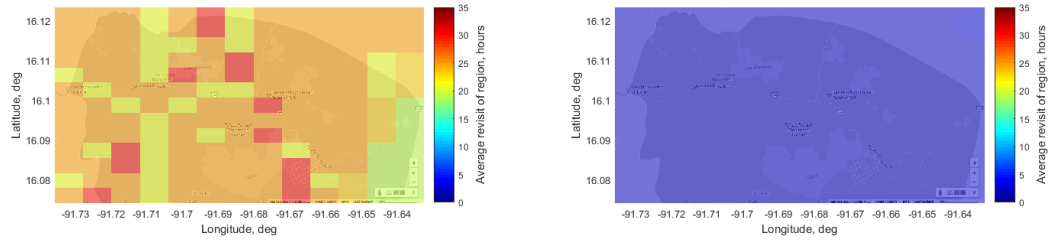

(a) (b)

Figure 5.20: Average revisit time of Lagunas de Montebello in a 1-week period for (a) the static constellation, (b) the responsive constellation [104].

Chapter 6

Constellation Deployment

Traditionally, the launching of satellite constellations has been extremely costly, with a different launch required for each orbit plane to be populated. This can stifle and even prohibit some missions requiring numerous orbit planes as the launch cost increases beyond what can be justified for the mission. An alternative deployment strategy, patented in 1993, proposed launching all satellites into a single orbit plane and then manoeuvring them to different altitudes, utilising the Earth's natural perturbing effects to achieve the desired separation of right ascension of the ascending node [105]. This was successfully demonstrated by the FORMOSAT-3/COSMIC mission in 2006 [50, 51], and is proposed for the upcoming FORMOSAT-7/COSMIC-2 mission [106, 107]. The FORMOSAT-3/COSMIC satellites were deployed by launching them into a low altitude orbit and exploiting the natural perturbations of the Earth's J_2 effect to produce the desired RAAN change. They were then raised to their desired final orbit altitude using low-thrust propulsion, with the manoeuvres timed appropriately to obtain the desired orbit plane spacing between the satellites. This method requires a relatively small amount of propellant compared with traditional, high-thrust plane-change manoeuvres, but this comes at the expense of requiring a long deployment time. However if the deployment could be done alongside the satellite commissioning phase, the lost mission time could be reduced. It may also be possible to provide a partial service during the remaining deployment time, depending on the mission requirements.

This chapter applies the general perturbation method developed in Chapter 2 to

the challenge of constellation deployment, to investigate the possible cost savings that could be made by using this deployment strategy in place of traditional launch methods. The key complexity of this deployment strategy comes from the fact that although the relative orbit plane spacing is defined, for the cases considered herein, the absolute position of the orbit planes is not defined. As such, the solution space is extremely large, and the manoeuvre selected for one satellite will impact the solutions available to the others. The analytical nature of the general perturbation solution offers an advantage in this case, compared to numerical optimisers, as it allows for the full solution space to be explored and insights gained into the interplay between the manoeuvre selection for each satellite. In order to validate the general perturbation method's applicability to the satellite deployment problem, the actual deployment of the FORMOSAT-3/COSMIC constellation will be analysed, and the possible reduction in deployment times that could be achieved using the 3-phase manoeuvre are examined. Following this, the method will be applied to the fire monitoring constellation described in Chapter 5 to gain insights into the technique and investigate the possible reduction in launch costs that could be achieved.

6.1 FORMOSAT-3/COSMIC Constellation Deployment

FORMOSAT-3/COSMIC is a Global Positioning System (GPS) radio occultation mission that performs global atmospheric measurements contributing to climate monitoring and weather forecasting [50, 51]. The constellation consists of six satellites, dubbed FM1 – FM6, that were initially launched to a 516 km altitude circular parking orbit at 72 deg inclination. These satellites were then raised to an altitude of 800 km, with the timing of the manoeuvres phased so as to achieve a 30 deg RAAN separation between the satellites. The order of manoeuvring was as follows: 1. FM5, 2. FM2, 3. FM6, 4. FM4, 5. FM3, 6. FM1. The six satellite manoeuvres were carried out over an 18 month period in 2006 and 2007. One of the satellites, FM3, experienced a solar array deployment failure and could not complete the orbit-raising manoeuvre. The other five satellites all reached the required final altitude and achieved the desired RAAN separation [51].

6.1.1 Deployment Time Calculated using General Perturbation Method

The FM5 satellite was the first of the FORMOSAT-3/COSMIC satellites to be raised to the final altitude. Using this as a reference satellite for all other manoeuvres, equation (2.87) for the relative change in RAAN of two satellites, given as

$$\Omega_{dif} = \Omega_{total} - \Omega_{ref} \tag{6.1}$$

can be used to express the desired RAAN of all other satellites relative to FM5 as a function of time, the ΔV required to change the satellite altitude, the given orbital parameters and the propulsion system acceleration, A_{prop}.

The FORMOSAT-3/COSMIC satellites are equipped with a blow-down mono-propellant hydrazine propulsion system that produces a thrust between 1.1 N (at beginning of life) and 0.2 N (at end of life). This gradual change in thrust and spacecraft mass over time will result in a varying acceleration profile. As the general perturbation method assumes a constant acceleration, an average acceleration will be estimated for the satellites and taken as the acceleration value. With a satellite dry mass of 54 kg and an average propellant usage across all manoeuvred satellites of 4.65 kg of an available 6.65 kg [51], this average acceleration can be estimated as

$$A_{prop} = \frac{F_{max} + F_{min}}{2(m_{dry} + P)} \tag{6.2}$$

where F_{max} and F_{min} are the maximum and minimum available thrusts respectively, m_{dry} is the satellite dry mass and P is the average mass of the on-board propellant during the manoeuvre, calculated as

$$P = \frac{P_{start} + P_{end}}{2} \tag{6.3}$$

where P_{start} is the maximum available propellent mass and P_{end} is the average propellant mass remaining at the end of the manoeuvre. In this case, P_{end} is 2 kg giving an average acceleration, A_{prop}, of ± 0.0111 m/s^2.

Assuming circular orbits are maintained throughout the manoeuvre, the ΔV re-

quired to raise the satellites' altitudes from the initial parking orbit to the desired final orbit can be calculated using equation (2.76) as 151.7 m/s. This allows the achievable RAAN separation to be described as a function of time only. Solving this for the desired satellite separations gives the results shown in Figure 6.1 and Table 6.1, where the epoch (i.e. $t = 0$) is assumed to occur at the time that FM5 reaches the desired 800 km altitude. The total times shown here consist of the time spent in the initial orbit as well as the time required to complete the orbit-raising manoeuvre.

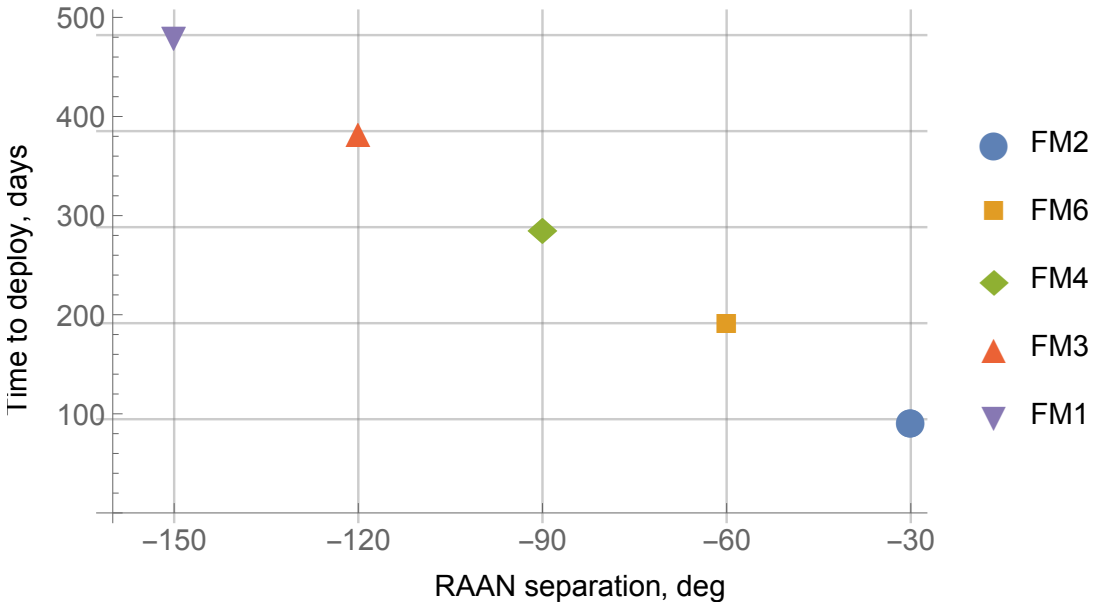

Figure 6.1: Required time to deploy FORMOSAT-3/COSMIC satellites as calculated using the general perturbation method.

6.1.2 Comparison with Two-Line Element Data

Using the two-line element (TLE) data of the FORMOSAT-3/COSMIC satellites, it is possible to track the satellites through their actual deployment manoeuvres, as shown in Figure 6.2, and thus to determine the true time required to achieve the desired RAAN separation. Note that the epoch in Figure 6.2 is taken as the time at which FM5 reaches the desired final altitude. The satellite positions derived from the TLE data are in the true equator mean equinox (TEME) coordinate system and, as such, there will be inherent discrepancies between the TLE values and the values calculated

using the general perturbation method, however it is considered sufficiently accurate for the purposes of this comparison. These results are shown in Table 6.1. Note that as the RAAN separation is calculated in reference to FM5, the time shown is the time from when FM5 reaches its final orbit. These results show that for FM6, FM4 and FM1 the general perturbation method accurately predicts the time required to achieve the given RAAN separation with less than 2% error for FM4 and FM1 and less than 6% error for FM6. FM3 cannot be used for comparison as it never reached the desired final orbit altitude, and the error in the prediction of the time for FM2 can be explained by the approximately 40 day pause at 700 km altitude during its manoeuvre. This was due to a change in the mission parameters that originally called for a 24 deg RAAN separation between orbit planes. There is also a noticeable change in the gradient of the TLE data after this pause that would affect the results; this may have been due to the need to fine-tune the deployment after the change in mission requirements. While the consideration of atmospheric drag and other influences would likely give improved results, the current solution is considered to be sufficiently accurate to predict the required time for constellation deployment.

Table 6.1: Time required to achieve desired RAAN separation; calculated values versus two-line element data. Spacecraft marked with an asterix (*) cannot be used for comparison due to issues that occurred during their deployment.

Spacecraft	Desired RAAN separation w.r.t. FM5, deg	Calculated manoeuvre time, days	TLE manoeuvre time, days	Difference in time, days
FM5	0	0	0	—
FM2*	-30	95	157	62
FM6	-60	191	202	11
FM4	-90	288	291	3
FM3*	-120	385	—	—
FM1	-150	482	476	6

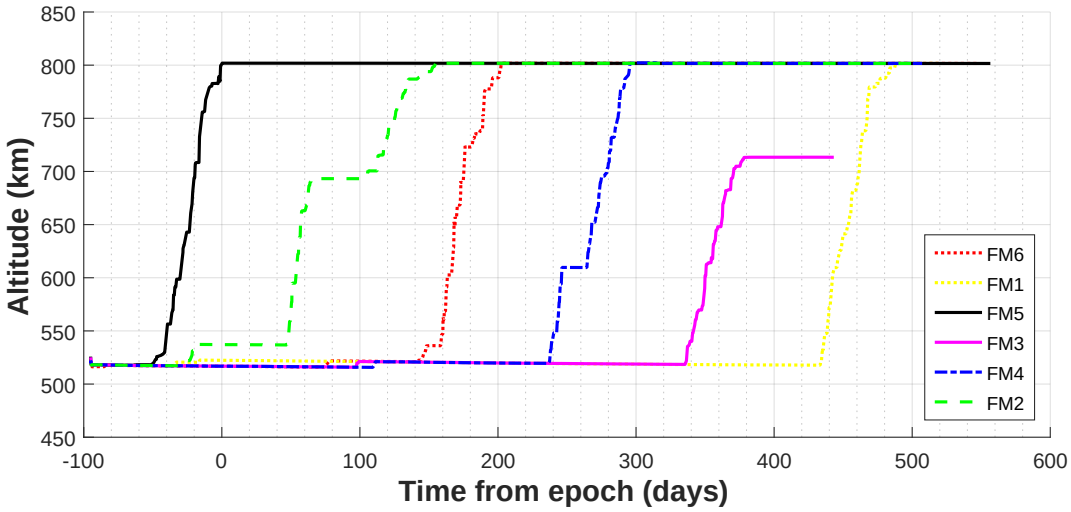

Figure 6.2: Two line element data from FORMOSAT-3/COSMIC constellation showing constellation deployment manoeuvres.

6.1.3 Using 3-Phase Manoeuvre to Reduce Deployment Time

The actual deployment strategy for the FORMOSAT-3/COSMIC constellation as described in Section 6.1.2 uses the minimum possible ΔV for the manoeuvre; the satellite coasts at the initial altitude until the required phasing time has passed and then manoeuvres to the final altitude. This manoeuvre uses just over 66% of the available propellant. Using the additional propellant to initially lower the satellite altitude could reduce the deployment time of the individual satellites and the overall constellation.

Assuming that 4.65 kg of propellant can provide 151.7 m/s ΔV, linear extrapolation predicts that the full 6.65 kg of propellant could provide 217 m/s ΔV. This is likely an under-estimation as the 4.65 kg of propellant must also have provided thrust for atmospheric drag compensation before and after the altitude-raising manoeuvre; however it is considered a valid estimate for this illustrative example. The average propulsion system acceleration will change due to the use of the additional on-board propellant. Taking the case in which all on-board propellant is used, the average acceleration as calculated using equations (6.2) and (6.3) is ± 0.0113 m/s^2.

Knowing the maximum available ΔV and the desired satellite spacing, the general perturbation method can be used to calculate the deployment time for each satellite as a function of the ΔV used, including that required for atmospheric drag compensation

during the coasting phase and after the manoeuvre is completed. For consistency, the ΔV required for atmospheric drag compensation for all satellites is calculated to 500 days from epoch; beyond this time all satellites will have reached the desired final orbit and so any additional ΔV required for atmospheric drag compensation beyond this time will be consistent across all spacecraft. The results of this are shown in Figure 6.3. The point markers indicate the minimum ΔV solutions used by the constellation for the actual deployment, with the inclusion of the ΔV that would have been required for atmospheric drag compensation throughout the manoeuvres and up to 500 days from epoch.

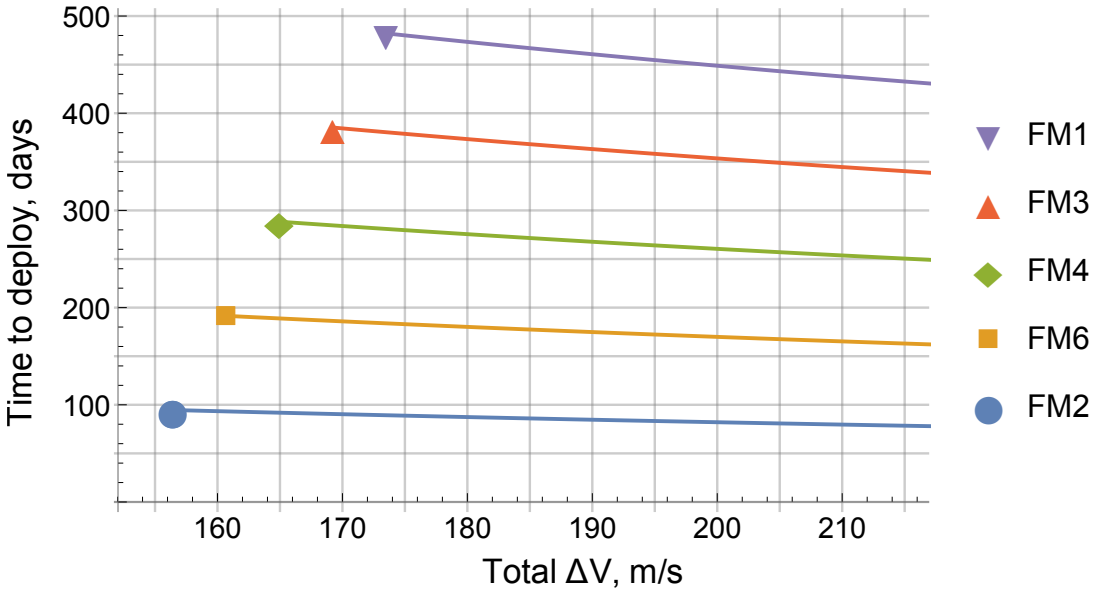

Figure 6.3: Required time to deploy FORMOSAT-3/COSMIC satellites using 3-phase manoeuvre as calculated using the general perturbation method for a range of ΔV.

Table 6.2 shows the possible reduction in deployment time for each satellite if the maximum ΔV of 217 m/s is used. For FM2, the satellite with the shortest deployment time, there is a possible 17.9% reduction in deployment time when the full available on-board propellant is used. However, the possible percentage reduction in deployment time decreases as the deployment time increases. This is because for longer deployments a higher proportion of the available propellant is required for atmospheric drag compensation, reducing the amount available to change the satellite altitude. Consid-

ering FM1, which has the longest deployment time, using the maximum available ΔV reduces the time required to deploy from 482 days to 431 days. This is more than the deployment time required by FM3 using the minimum ΔV, and so the time to full constellation deployment could be reduced by more than 50 days just by increasing the amount of propellant used by FM1. The minimum altitude that would be reached if all satellites used the maximum available ΔV is 473 km by FM2.

Table 6.2: Time required to achieve desired RAAN separation using 3-phase manoeuvre.

	Desired RAAN separation w.r.t. FM5, deg	Manoeuvre time for minimum ΔV, days	Manoeuvre time for maximum ΔV, days	Possible reduction in deployment time
FM5	0	0	0	—
FM2	-30	95	78	17.9%
FM6	-60	191	162	15.2%
FM4	-90	288	249	13.5%
FM3	-120	385	339	11.9%
FM1	-150	482	431	10.6%

6.2 Deployment of Fire Monitoring Constellation

The fire monitoring constellation proposed and investigated in Chapter 5 consists of 24 satellites in four evenly spaced orbit planes. Using traditional constellation deployment strategies, this would require four individual launches, one per plane, each carrying six 3 kg satellites. This could be extremely costly compared to the development and manufacturing costs of the satellites. As such, it is of interest to consider alternate deployment strategies such as that used by the FORMOSAT-3/COSMIC constellation discussed in Section 6.1. For the analysis below it is assumed that the mission will last a total of eight years from launch; any time spent to deploy the constellation is assumed to result in a reduction in useful mission time, though it is possible that a partial service could be provided during deployment. An end-of-life de-orbit strategy, and any associated ΔV requirements, is not considered herein.

6.2.1 Decoupling of RAAN and AoL Change

Full deployment of this constellation will require that the satellites are placed in the desired orbit planes, corresponding to a change in RAAN, as well as spaced correctly within the orbit planes, corresponding to a change in AoL. As both the RAAN and the AoL separation manoeuvres are performed by varying the satellite's altitude, it is impossible to vary one without affecting the other. However, due to the relatively short time required to change the satellite's AoL compared with its RAAN, as can be seen by comparing Figures 3.5 and 3.6 in Section 3.1, it is assumed that the RAAN change can be performed first, and that the AoL change can be completed in the desired orbit plane with minimal effect on the satellite RAAN.

To investigate this, the resultant RAAN change is calculated for the case in which the argument of latitude is changed by a full revolution of 360 deg. The fire monitoring constellation orbit parameters as given in Table 5.1, and the constants and parameters given in Tables 3.1 and 4.3 are used. The general perturbation solution, in the form given by equation (2.88), can be solved to find the manoeuvre time required to achieve a change in AoL, u_{dif}, of 360 deg compared to a non-manoeuvring reference satellite as a function of the ΔV required for the altitude change manoeuvres. The change in RAAN of the satellite with respect to a non-manoeuvring reference, Ω_{dif}, as given by equation (2.87), can be used to determine the resultant change in RAAN that would occur as the AoL is changed by 360 deg. This is calculated by replacing the manoeuvre time in equation (2.87) with the expression for the time required to achieve the desired 360 deg AoL change. These results are shown in Figure 6.4. From this it can be seen that the maximum change in RAAN that would occur as the AoL is changed by 360 deg will be less than -0.6 deg for all ΔV_{alt} values considered. This interdependence between the two parameters is a valuable insight that is uniquely enabled by the analytical nature of the presented general perturbation method.

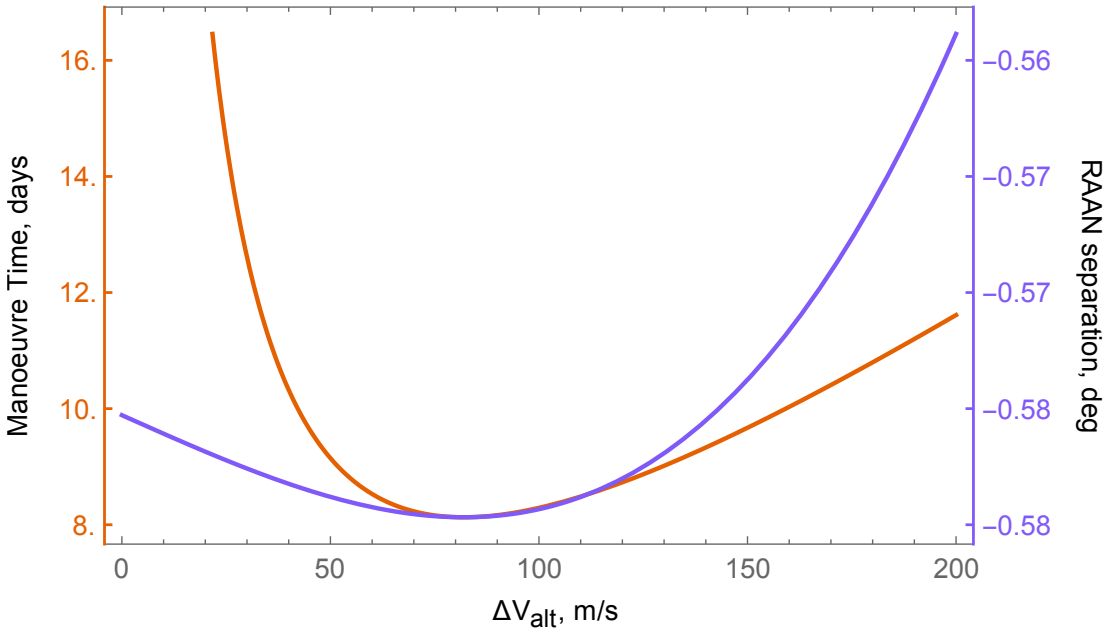

Figure 6.4: Manoeuvre time and corresponding RAAN separation as a function of ΔV required for altitude change, for a change in AoL of 360 deg.

6.2.2 Satellite Distribution

The desired spacing of the satellites in the fire monitoring constellation relative to each other is described in Tables 5.1 and G.1. However, for deployment, it is also necessary to define the position of each satellite with respect to the launch injection point. As shown in Chapter 3, achieving a desired change in RAAN or AoL can be done more efficiently in one direction than in the other, by the use of either an altitude-lowering or altitude-raising manoeuvre. This means that evenly distributing the satellites in both directions from the launch injection point is unlikely to be the most efficient deployment method.

The constellation being considered consists of four orbit planes evenly distributed through 360 deg (i.e. 90 deg separation between each plane). Recall that in Chapter 3 it was determined that an altitude-lowering manoeuvre will always be more efficient than an altitude-raising manoeuvre if the goal is to achieve a desired satellite separation through RAAN or AoL. As such, there are two possibilities to deploy the satellites into the desired planes. The first option is that all satellites can lower their altitudes and

move in the 'same direction', achieving a negative change in RAAN, hereafter referred to as a *co-directional* manoeuvre; this is illustrated in Figure 6.5 (a). In this case the shortest deployment time will occur when the satellites in one plane immediately use a minimum ΔV manoeuvre to reach the desired final altitude; all other planes can then be phased relative to this plane to achieve the desired configuration. The other option is that some satellites can lower their altitudes, giving a negative change in RAAN, while others raise their altitudes, giving a positive change in RAAN, with the satellites then moving in 'opposite directions'; this will be referred to as a *contra-directional manoeuvre* and is illustrated in Figure 6.5 (b).

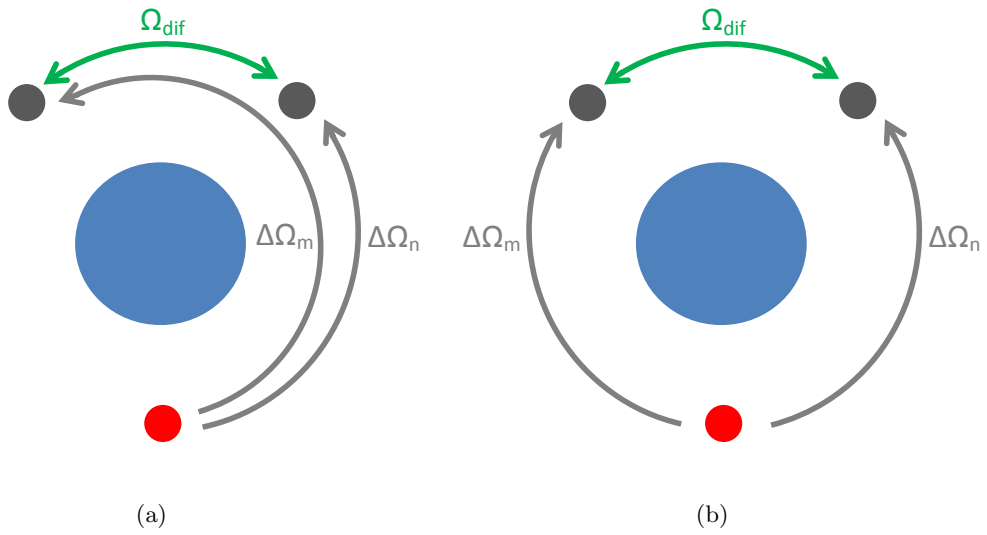

Figure 6.5: (a) A co-directional manoeuvre and (b) a contra-directional manoeuvre. Red dots represent launch injection points, grey dots represent orbit planes being deployed.

In order to determine whether a contra-directional or co-directional manoeuvre will be more efficient for a given scenario, the time required to deploy the two orbit planes furthest from the launch injection point, plane n and plane m, can be considered. To do this, the desired separation between the two orbit planes, Ω_{dif}, is defined, and a requirement is set that the satellites in both planes must reach their desired orbit at the same time; this will provide the shortest possible deployment time for these planes. In the case of either a contra-directional or co-directional manoeuvre, the RAAN separation between planes n and m after the manoeuvre is given by

$$\Omega_{dif} = \Delta\Omega_n - \Delta\Omega_m. \tag{6.4}$$

Having defined Ω_{dif}, equation (6.4) can be solved to find the deployment time for planes n and m as a function of the ΔV used for the manoeuvres.

Spacing the satellites through AoL within the plane can be similarly considered. As described in Section 6.2.1, the assumption is made that the AoL phasing manoeuvres occur after the satellites have achieved the desired orbit plane spacing. As such, all satellites will start and finish this manoeuvre at the final desired orbit altitude. For this case then, if a co-directional manoeuvre is to be used, one satellite per plane can perform no manoeuvres and act as a reference satellite for the manoeuvring satellites.

6.2.3 Costing

Launch costs are a difficult attribute to define with confidence. They are often mission specific and prices are rarely publicly available. However, the recent development of smaller launch vehicles aimed at the small satellite market has made strides towards not only cost reduction, but also accessibility and openness [108, 109]. One such vehicle is the *Electron*, developed by Rocket Lab Ltd, which had its first successful launch on May 25th 2017, and on January 21st 2018 successfully deployed CubeSats into orbit for its customers Planet and Spire Global [110]. As of writing, Rocket Lab Ltd are offering flights to 500 km sun-synchronous orbit (SSO) with a nominal payload of 150 kg, and are looking to expand their orbit offerings in the coming years [111]. They are currently quoting a price of $240,000 per 3U CubeSat for rideshare launches, with a fairing capable of holding up to 24 3U CubeSats [112]. Dedicated launches are also available with prices upon request. This system will be used as a baseline for comparing the different constellation deployment strategies.

The fire monitoring constellation has a 60 deg inclination and as such is not compatible with the current *Electron* launch offerings to SSO. For the traditional launch method, in which a dedicated launch is required for each orbit plane, it is assumed that a dedicated launch to the desired 60 deg inclination, 543 km altitude orbit could be procured at the same cost as the currently available launch to SSO (i.e. $240,000 per 3U CubeSat). It is also assumed that the vehicle launching to this orbit would have

the same maximum capacity of 24 3U CubeSats. For the single launch with in-orbit deployment, it is assumed that the *Electron* will launch to a 500 km altitude orbit inclined at 60 deg inclination. This is assumed to require the same cost of $240,000 per 3U CubeSat and have the same maximum capacity of 24 3U CubeSats.

6.2.4 Traditional Launch

Traditional launch methods require a dedicated launch for each orbit plane to be populated. For the proposed constellation, this would require four dedicated launches to 543 km altitude, each carrying six 3U CubeSats, for a total mass of 18 kg per launch. Assuming that a dedicated launch would be necessary due to the specific orbit requirements (i.e. rideshare would not be an option), the cost per launch is taken to be the cost of launching the *Electron* launch vehicle at the full capacity of 24 3U CubeSats, even though only six would actually be on board each vehicle. Based on the launch cost of $240,000 per 3U CubeSat, this is estimated to cost $5.76 million per launch, for a total launch cost of $23 million for all four planes. It is possible that the remaining slots on-board the vehicle could be sold to other parties as rideshare opportunities, reducing this cost, but, as this is challenging to predict, for the purposes of this work the maximum cost of $5.76 million per launch is assumed.

Assuming one launch per quarter, in line with Rocket Lab's current launch schedule, the constellation could be fully deployed within a year. The amount of ΔV required for atmospheric drag compensation for an eight year mission in the case of direct injection to 543 km altitude is calculated as 51 m/s, noting that those satellites launched later would require slightly less ΔV for this purpose. This value of 51 m/s will be taken as the baseline, minimum atmospheric drag compensation ΔV, and all other cases will be benchmarked against this value.

After injection the satellites will need to be distributed within the orbit plane. This would be done in the same manner as in the case of a single launch with in-orbit deployment and is discussed in Section 6.2.5.

6.2.5 Single Launch and In-Orbit Deployment

A single *Electron* launch to 500 km altitude at 60 deg inclination is assumed to be capable of carrying 24 3U CubeSats. Thus it would be possible to deploy the full fire monitoring constellation at 500 km altitude on a single launch vehicle at a cost of $5,760,000.

Manoeuvre type selection

Using the method described in Section 6.2.2, the time required to manoeuvre the satellites into the two orbit planes furthest from the launch injection point is investigated for both a co-directional manoeuvre and a contra-directional manoeuvre. With four evenly spaced orbit planes, the desired separation between these furthest planes will be 270 deg. Knowing this, equation (6.4) can be solved to find the deployment time for these two planes as a function of the ΔV used. The results of this are shown in Figure 6.6, where the ΔV shown is only that required for the altitude change manoeuvre; any ΔV required for atmospheric drag compensation is not included. It is assumed that in the contra-directional case the satellites in the two orbit planes being manoeuvred use the same amount of ΔV, and the ΔV shown in Figure 6.6 is the total required for one satellite in each of the two orbit planes being considered to complete the manoeuvre. For the co-directional case, it is assumed that the satellites in one plane use the minimum required ΔV to reach the final orbit altitude and the satellites in the other orbit plane manoeuvre relative to this; again the ΔV shown in Figure 6.6 is the total required for one satellite from each of the two orbit planes to complete the manoeuvre. The minimum ΔV required for each satellite to reach the final desired altitude is found to be 27.6 m/s; as Figure 6.6 shows the combined ΔV required for two satellites to deploy, it is plotted for values ranging from twice this, 55.2 m/s, to 200 m/s.

The results from Figure 6.6 show that for a given total ΔV_{alt} a co-directional manoeuvre will always be faster than a contra-directional manoeuvre for the ranges considered. This is shown more clearly in Figure 6.7 (a), which shows a smaller portion of the same graph. Of note is that a turning point is found at approximately 1020 m/s ΔV_{alt}, as shown in Figure 6.7 (b). For values of ΔV_{alt} greater than this, a contra-directional manoeuvre will be faster; however, these values are unrealistic for the case considered.

It is of note that there may be operational reasons, such as a desire to balance propellant usage across the constellation, that would favour the use of a contra-directional manoeuvre; however for the work herein only the deployment time is considered.

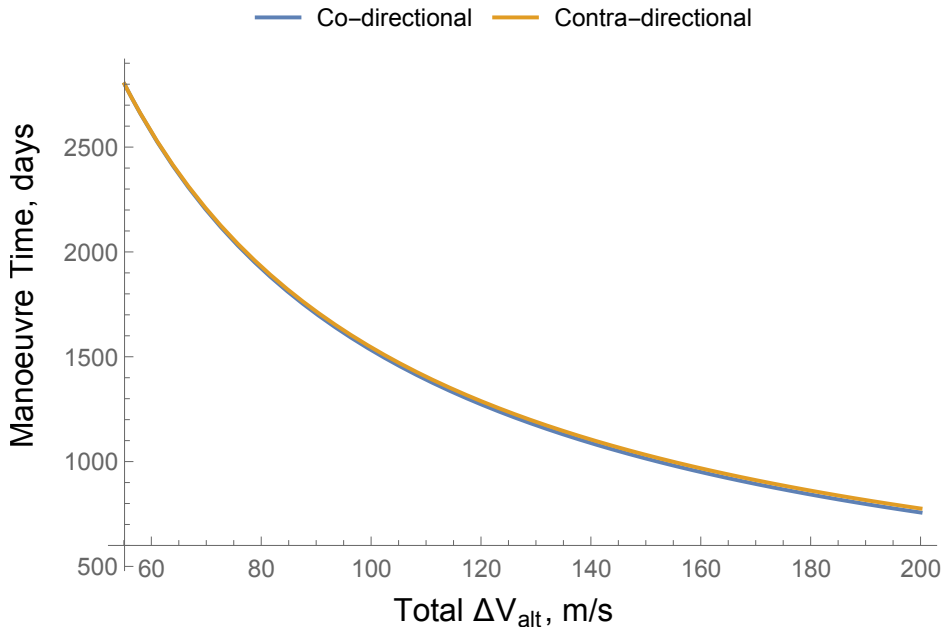

Figure 6.6: Manoeuvre time and corresponding ΔV_{alt} to reach furthest two orbit planes for both co-directional and contra-directional manoeuvres for deployment from a dedicated *Electron* launch to a 500 km altitude, 60 deg inclined orbit. The ΔV_{alt} shown includes the ΔV required for one satellite from each of the two orbit planes to be deployed.

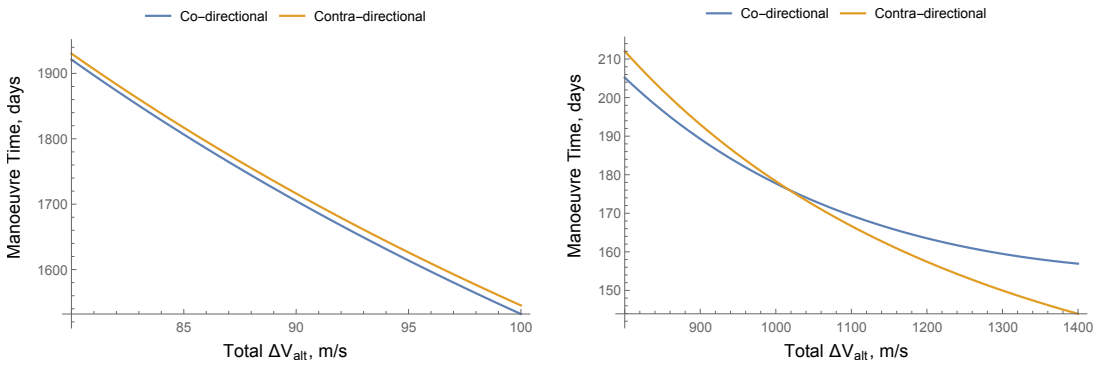

Figure 6.7: Manoeuvre time and ΔV_{alt} to reach furthest two orbit planes for co- and contra-directional manoeuvres after deployment from a dedicated *Electron* launch. (a) shows a zoomed portion of Figure 6.6, and (b) shows a turning point in the data at a high ΔV range.

Orbit plane placement

Having established that a co-directional manoeuvre will be more efficient than a contra-directional manoeuvre for the ΔV range of interest, the time and ΔV required to place all four orbit planes can be analysed. It is assumed that the satellites in plane 4 will immediately manoeuvre to reach the desired final orbit altitude using the minimum possible ΔV, and all other planes will be positioned relative to this, with plane 3 to be separated from plane 4 by -90 deg, plane 2 by -180 deg, and plane 1 by -270 deg.

The time and ΔV required to deploy one satellite in each of the four orbit planes is shown in Figure 6.8, where the time and ΔV required by the satellite in plane 4 is fixed and indicated by the red dot. In order to directly compare with a traditional launch, the *deployment* ΔV shown in Figure 6.8 is calculated as

$$\Delta V_{deploy} = \Delta V_{total} + \Delta V_{atm} - \Delta V_{base} \tag{6.5}$$

where ΔV_{total} is the ΔV required for the deployment manoeuvre, ΔV_{atm} is that required for atmospheric drag compensation for the eight-year mission and ΔV_{base} is the baseline value of 51 m/s that was found in Section 6.2.4 to be required for atmospheric drag compensation throughout the eight-year mission if traditional launch methods were used. This is plotted for ΔV values up to a maximum of 200 m/s per satellite.

The dashed horizontal line on Figure 6.8 indicates the time that would be required to deploy plane 1, if the satellites in this plane were to use the maximum available ΔV of 200 m/s each; this is the minimum time in which the full constellation can be deployed for this maximum ΔV. If the goal is to minimise time to total constellation deployment, then the ΔV used by the satellites in the other planes can be reduced while still ensuring that they reach their desired orbit at the same time as the satellites in plane 1. This is indicated by the intersection of the dashed line with the orange curve in Figure 6.8 for the satellites in plane 2. There is no intersection of the dashed line and the green curve as, even using the minimum possible ΔV, the satellites in plane 3 will reach their final orbit more quickly than the satellites in plane 1. This solution gives a minimum constellation deployment time while also minimising the total ΔV used across the constellation. The corresponding times and ΔV values for this minimum

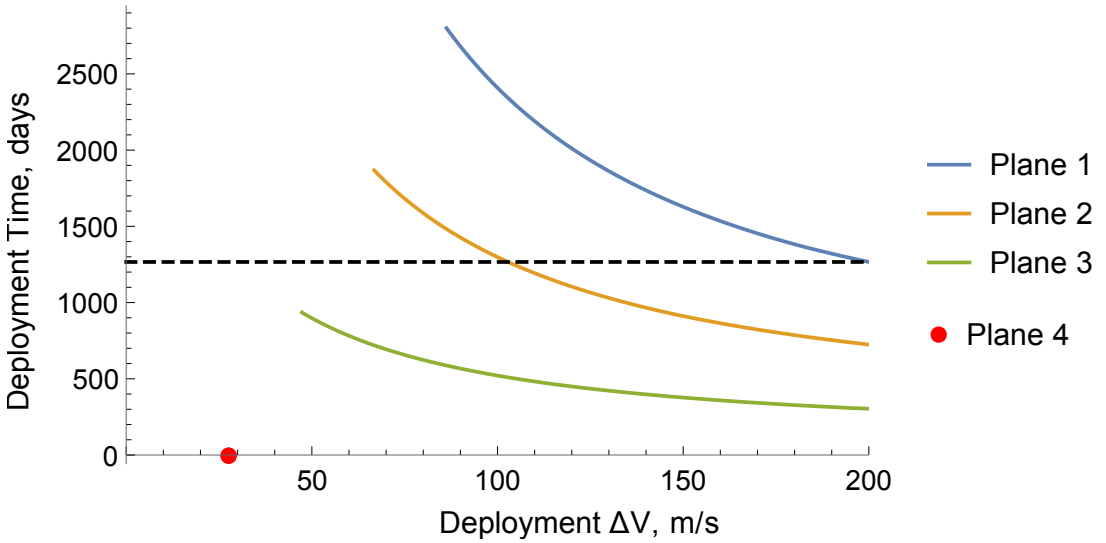

Figure 6.8: Manoeuvre time and ΔV to deploy all four orbit planes from a dedicated *Electron* launch to a 500 km altitude, 60 deg inclined orbit. Dashed line indicates minimum time for full constellation deployment for a maximum ΔV of 200 m/s. The ΔV_{deploy} shown is that required to deploy a single satellite in each orbit plane.

time / minimum ΔV constellation deployment are given in Table 6.3.

Also shown in Table 6.3 are the deployment times that would be required for each orbit plane if all satellites used the minimum possible ΔV to reach the final orbit and were to remain at the injection orbit altitude, compensating for atmospheric drag effects, until the desired orbit spacing was achieved. Note that in this case the deployment ΔV required includes both the 27.6 m/s required to raise the altitude, as well as the additional ΔV required for atmospheric drag compensation at this lower coasting altitude, beyond the baseline 51 m/s that would be required for satellites in the final, higher altitude, orbit for the same duration. Also given is the deployment time for each plane if all satellites were to minimise their deployment time by using the maximum ΔV of 200 m/s; the exception to this is the satellites in plane 4 that use the minimum possible ΔV to immediately manoeuvre to the desired orbit altitude. The lowest altitude reached for a manoeuvre requiring 200 m/s ΔV is 398 km.

Table 6.3: Manoeuvre time and ΔV for constellation deployment from a dedicated *Electron* launch for a range of scenarios. The ΔV given is that required to deploy a single satellite in each orbit plane.

		Min. time/ΔV deployment	Min. ΔV deployment	Min. time deployment
Plane 1	Time, days	1266	2800	1266
	Deployment ΔV, m/s	200	86	200
Plane 2	Time, days	1266	1868	724
	Deployment ΔV, m/s	103	67	200
Plane 3	Time, days	935	935	304
	Deployment ΔV, m/s	47	47	200
Plane 4	Time, days	3	3	3
	Deployment ΔV, m/s	28	28	28

Satellite placement within the orbit plane

Distributing the satellites through AoL within the orbit plane is assessed in a similar manner to the orbit plane placement. With six satellites per plane, the desired separation between the furthest two satellites will be 300 deg. The comparison between a co-directional and contra-directional manoeuvre to place these furthest satellites is shown in Figure 6.9 where it is assumed for the contra-directional manoeuvre that both satellites use the same ΔV. In the co-directional case it assumed that one satellite remains in place while all other satellites move relative to it. As before, atmospheric drag compensation ΔV is neglected for this comparison. For the range of ΔV_{alt} values considered it can be seen that a contra-directional manoeuvre will always be faster for the same total ΔV. It is also clear that for both manoeuvre types there is a ΔV value that will give a minimum time manoeuvre. For the contra-directional manoeuvre this minimum time is found to be 5.26 days and requires 106 m/s ΔV, i.e. 53 m/s for each of the two manoeuvring satellites.

It is of note that the region around the minimum time solution is very flat, and so an operator may accept an increased manoeuvre time in order to significantly reduce the amount of ΔV required. For example, reducing the amount of ΔV used to 50 m/s (i.e. 25 m/s per satellite) requires just 6.81 days deployment time, which is just 1.5 days more than the minimum time solution. This is especially true as, compared to the time to phase the satellites through RAAN, the manoeuvre times required to space the satellites through AoL are relatively short. In particular, for those planes that are

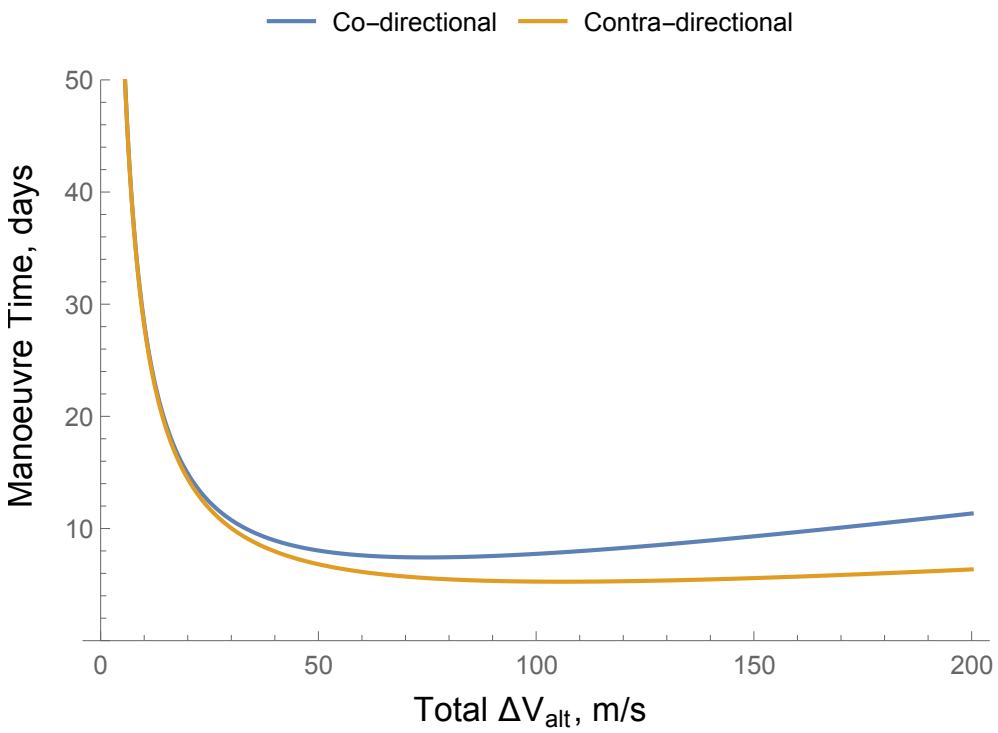

Figure 6.9: Manoeuvre time and corresponding ΔV_{alt} to reach furthest two satellite positions within an orbit plane for both co-directional and contra-directional manoeuvres.

deployed first (e.g. planes 3, and 4 from Figure 6.8 and Table 6.3) it may be possible to use a very small amount of ΔV and still achieve the desired AoL spacing before the satellites in plane 1 reach their final orbit. For example, using just 1 m/s ΔV, the time to space the satellites through AoL is 279 days, which would still allow the satellites in plane 3 and 4 to be positioned before the satellites in planes 1 and 2 have reached their final orbit plane. Due to the steepness of the solution at the lower ΔV range, increasing the ΔV used to just 5 m/s significantly reduces the deployment time to 56 days. The full view of the solution space is extremely valuable in this case as it allows the operator to thoroughly investigate the deployment options available. As this distribution in AoL occurs in the final orbit, the results will be the same for all deployment strategies considered.

Note that for the contra-directional manoeuvre the position of both the furthest satellites to be placed will be dependent on the ΔV selected for their manoeuvres; this is in contrast to the co-directional manoeuvre in which the position of one satellite is determined in advance. Once the desired manoeuvre ΔV for the two furthest satellites

has been selected, the other satellites can be placed relative to these positions. As this selection will be dependent on the mission priorities, and as the solution will be same for all deployment strategies, the ΔV required to phase the satellites through AoL is not included in the total deployment ΔV presented in the results in Section 6.2.7.

6.2.6 Deployment from the International Space Station

Launching from the International Space Station is an alternative option opted for by many small satellite operators. Launches from the ISS provide an orbit with an apogee of 380 – 420 km and inclination of 51.6 deg, with just 100 – 250 days of operation expected before the satellite will deorbit [109]. However, constellations of satellites with propulsive capability could use this as an initial parking orbit to obtain the desired orbit plane spacing before transitioning to the final mission orbit. It is of note that as only in-plane manoeuvres are to be used for deployment, the final constellation achieved from this launch would have an inclination of 51.6 deg, rather than the desired 60 deg.

The cost of launching a CubeSat to the ISS was not publicly available at the time of writing. However it is assumed to be similar or lower cost per 3U CubeSat as the cost of an *Electron* launch as discussed in Section 6.2.3. As such, a cost of $240,000 per 3U CubeSat is assumed for this case.

Manoeuvre type selection

A comparison of the co-directional and contra-directional manoeuvres for orbit plane separation after deployment from the ISS is shown in Figure 6.10. The ΔV shown on the graph is the total for one satellite from each of the two orbit planes being considered to complete the manoeuvre, and it is assumed that in the contra-directional case the manoeuvring satellites in both planes use equal amounts of ΔV. The ΔV required for atmospheric drag compensation is not included in this comparison. The minimum ΔV required for each satellite to reach the final desired altitude from the injection orbit, assumed to be a 402 km altitude circular orbit, is found to be 82.5 m/s, which is much higher than that required for the dedicated *Electron* launch. As with the dedicated launch, for the ranges considered, a co-directional manoeuvre will always be faster than a contra-directional manoeuvre for the same total ΔV.

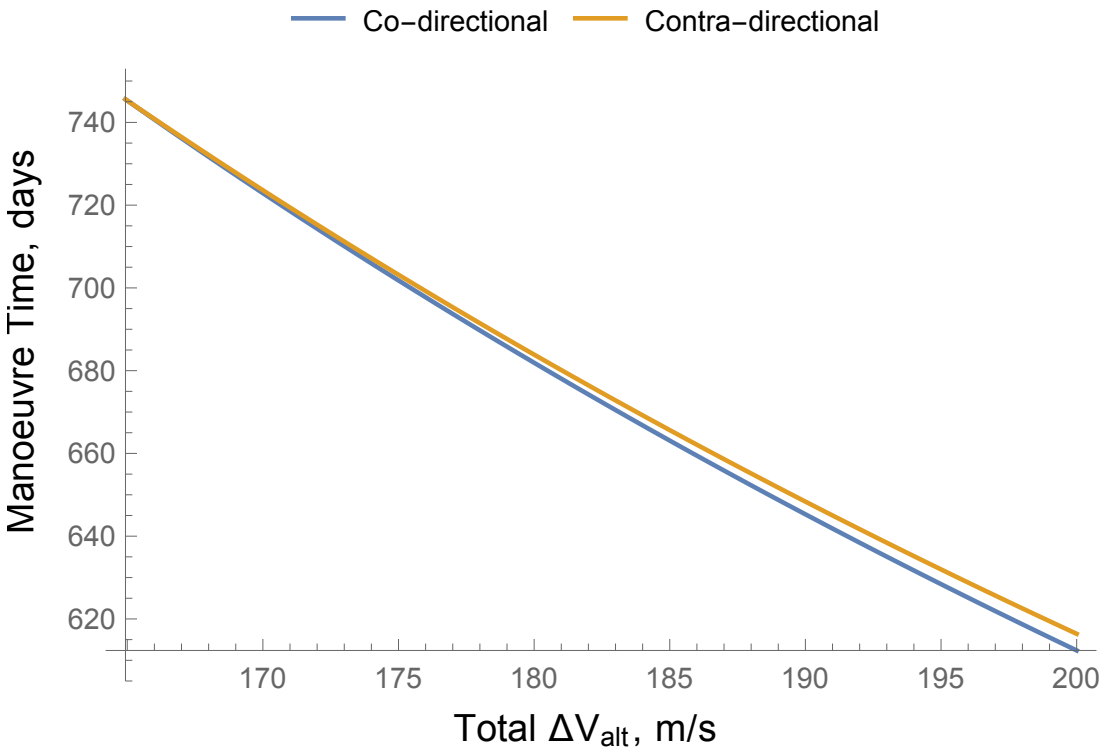

Figure 6.10: Manoeuvre time and corresponding ΔV_{alt} to reach furthest two orbit planes for both co-directional and contra-directional manoeuvres after deployment from the ISS. The ΔV_{alt} shown includes the ΔV required for one satellite from each of the two orbit planes to be deployed.

Orbit plane placement

The time and ΔV required to deploy one satellite in each orbit plane using co-directional manoeuvres from an ISS launch is shown in Figure 6.11; this is the additional deployment ΔV required, ΔV_{deploy}, as given by equation (6.5). Solutions for ΔV values up to 300 m/s are shown, as no solutions exist for plane 1 using less than 200 m/s. The minimum time / minimum ΔV solution for complete constellation deployment is given in Table 6.4, assuming that the satellites in plane 1 use the minimum possible ΔV of 219 m/s to deploy. Also given are the results for the minimum ΔV deployment manoeuvres, and minimum time manoeuvres in which all satellites use 200 m/s ΔV, with the exception of plane 1, which is assumed to use the minimum possible in all cases. The lowest altitude that would be reached by any satellite using the maximum allowable ΔV is 365 km.

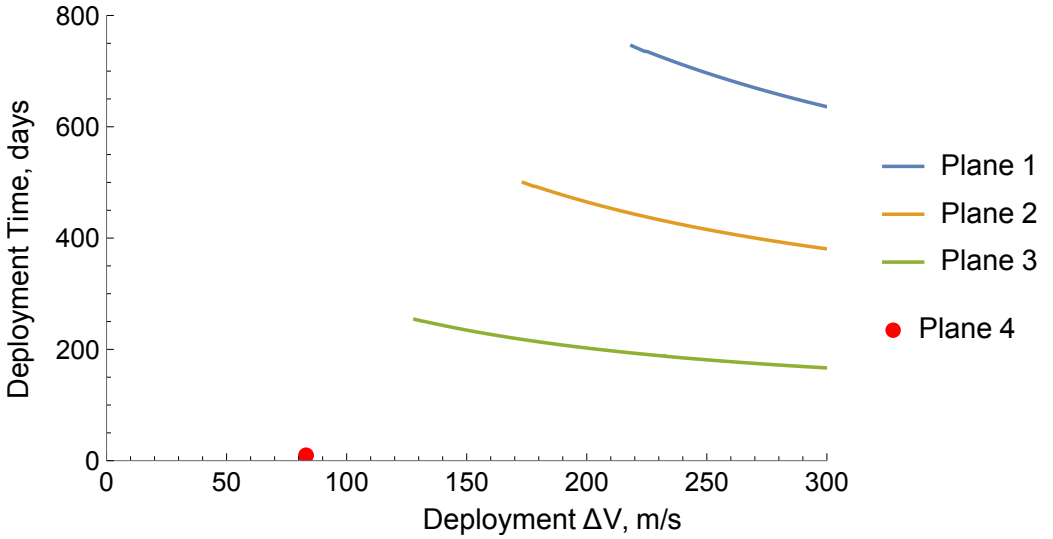

Figure 6.11: Manoeuvre time and ΔV to deploy all four orbit planes from the ISS. The ΔV_{deploy} shown is that required to deploy a single satellite in each orbit plane.

Table 6.4: Manoeuvre time and ΔV for constellation deployment from the ISS for a range of scenarios. The ΔV shown is that required to deploy a single satellite in each orbit plane.

		Min. time/ΔV deployment	Min. ΔV deployment	Min. time deployment
Plane 1	Time, days	746	746	746
	Deployment ΔV, m/s	219	219	219
Plane 2	Time, days	500	500	465
	Deployment ΔV, m/s	174	174	200
Plane 3	Time, days	254	254	202
	Deployment ΔV, m/s	128	128	200
Plane 4	Time, days	8	8	8
	Deployment ΔV, m/s	83	83	83

6.2.7 Results

A comparison of all three methods for the deployment of the 24 satellite fire monitoring constellation is given in Table 6.5. Also given are the results for a deployment scenario using two *Electron* launches. All results are for the strategy resulting in minimum time to full constellation deployment with minimum ΔV; this corresponds to the first column in Tables 6.3 and 6.4. Note that these results show the deployment ΔV, ΔV_{deploy}, and as such exclude the baseline 51 m/s that would be required for atmospheric drag compensation over the eight-year mission in the case of direct injection into the desired final orbit. It also does not include any ΔV required for in-plane phasing as the

amount used will be at the discretion of the operator. The results in Table 6.5 show that deployment from a single launch, whether using the *Electron* launch vehicle or from the ISS, can offer a theoretical reduction in launch costs of 75% when compared with traditional launch methods. However, this comes at the cost of an increased deployment time of 2–3.5 times that of a traditional launch.

Table 6.5: Summary of deployment times, costs and required ΔV for each deployment method.

Deployment Method	Time to deploy, years	Deployment ΔV for all satellites, m/s	Cost, $
Traditional Launch	1	0	23,040,000
Single Launch: *Electron*	3.5	2268	5,760,000
Single Launch: ISS	2	3624	5,760,000
Two Launches: *Electron*	1.1	2220	11,520,000

Comparing a launch aboard Rocket Lab's *Electron* launch vehicle with a launch from the ISS, the launch from the ISS offers the clear advantage of a shorter deployment time, requiring just two years to fully deploy. However, deployment from the ISS requires a ΔV of more than 200 m/s for the satellites in plane 1, and requires more than 1300 m/s extra deployment ΔV across the constellation when compared with a single *Electron* launch. The *Electron* launch requires 3.5 years to fully deploy, but requires 40% less ΔV across the constellation than the ISS launch. In addition, deployment from the ISS would result in a constellation in which the orbit planes are inclined at 51.6 deg, rather than the desired 60 deg. This would restrict the field of coverage of the constellation to between $\pm$ 51.6 deg latitude and would clearly impact the mission performance.

An alternative launch strategy to reduce the constellation deployment time could be to use two *Electron* launches, each carrying 12 satellites to be deployed into two orbit planes. As shown in Table 6.3, the time required to deploy two planes separated by 90 deg (i.e. plane 3 and plane 4) is just 304 days if a ΔV of 200 m/s is used by the satellites in plane 3; this corresponds to the far-right column of Table 6.3. Assuming that two sequential *Electron* launches could be procured three months apart, the total time to constellation deployment could be reduced to just 395 days, or 1.1 years if the satellites in the second plane of the second launch were to use the maximum ΔV of 200 m/s to deploy. The satellites in the second plane of the first launch would require 142 m/s ΔV to reach their final orbit in 394 days, completing their manoeuvres at the

same time as the satellites on the second launch. This gives a total deployment ΔV of just 2220 m/s. However, this would double the launch costs to \$11,520,000. These results are summarised in Table 6.5.

Having identified the possible deployment options, it will be up to the mission designer to trade-off all competing parameters and select the launch that provides the best solution for their specific mission, noting that a lower injection altitude, and lower inclination, corresponds to a shorter deployment time. However, satellites at lower altitudes will also be required to use a greater proportion of their propellant for atmospheric drag compensation during coasting phases. For this reason, comparison of different launch injection altitudes and inclinations is not straightforward, and a full exploration of the solution space would be required for an informed trade-off to be possible. The speed and flexibility of the general perturbation method would enable such a trade to be rapidly performed across a wide range of injection altitudes and final orbits, providing an unprecedented insight into the problem of constellation deployment. The analytical nature of the method also allows for the interplay between the satellite deployment manoeuvres to be examined and the impact that the manoeuvres used for one orbit plane can have on the other orbit planes assessed. Such techniques will become increasingly valuable as the size of the constellations being launched continues to increase. It is notable that the general perturbation method in its current form, while capable of highlighting trends and supporting trade-offs, is restricted to considering circular to circular, coplanar manoeuvres and, as such, the results produced may be sub-optimal. However, the insights provided could be used by an experienced operator or designer to better inform their decisions and rapidly explore alternative deployment strategies.

Chapter 7

Conclusions and Future Work

The main thesis of this work proposed in the introduction was:

"Manoeuvrable satellites can provide increased performance when compared to traditional static satellite missions, however there is an inherent, quantifiable trade-off between the achievable performance, the manoeuvre time and the propellant required, that can be presented as a full solution space, providing insight to this complex problem."

In order to investigate this theory, a fully-analytical solution to a restricted low-thrust Lambert rendezvous problem was derived from general perturbation methods, to provide a fast, flexible method of analysing satellite manoeuvres across a range of scenarios. This restricted problem considers circular to circular, coplanar transfers using tangential low-thrust. The conclusions drawn from the subsequent investigations using this method are presented in the following section, followed by a short discussion of possible further extensions of this work.

7.1 Conclusions

A fully-analytical solution developed from general perturbation methods can be used to solve the restricted, circular to circular, coplanar, low-thrust Lambert rendezvous problem and gain an insight into the capabilities of a manoeuvrable satellite, or satellites, that would be difficult to achieve using numerical methods alone. This solution can be applied to a range of scenarios, such as identifying suitable manoeuvres to achieve

a desired orbit position relative to a non-manoeuvring reference satellite, obtaining a desired spacing between multiple manoeuvring satellites, and can be extended to include the satellite's ground track to directly allow overflight targeting of a location on the surface of the Earth. The full solution space for these problems can be generated almost instantaneously and used to gain insight into the complex and non-intuitive trade-space. The speed of the solution means it is scalable across numerous satellites, allowing multifaceted scenarios with thousands of possible manoeuvres to be analysed extremely quickly.

If the goal of a mission is to achieve a desired separation in either right ascension of the ascending node or argument of latitude between a manoeuvring satellite and a non-manoeuvring reference, then a 3-phase manoeuvre in which the satellite altitude is lowered in phase 1 using a constant acceleration, coasts at a constant altitude in phase 2, and then raises its altitude in phase 3 using a constant acceleration, is more efficient than a similar manoeuvre in which the satellite altitude is raised in phase 1 and lowered in phase 3. Initial orbit parameters have an impact on the efficiency with which manoeuvres can be carried out; satellites at low inclinations and low altitudes can be manoeuvred more efficiently to achieve a desired change in right ascension of the ascending node and argument of latitude. As such, orbit and constellation design for responsive missions should be done with future manoeuvrability taken into consideration from the outset. Increasing the change in velocity used for a manoeuvre will reduce the time required to achieve a desired change in right ascension of the ascending node or argument of latitude, but this effect gives diminishing returns as the change in velocity is increased. If flyover of a given target is required, increasing the change in velocity used for the manoeuvre will not necessarily reduce the time required to achieve flyover.

The assumptions and simplifications necessary to obtain a fully-analytical solution – such as the assumption that atmospheric drag compensation manoeuvres are performed throughout all coasting phases but not throughout the altitude changing manoeuvres, and the omission of higher order central body perturbations – do have an impact on the accuracy of the solution, but comparison with a numerical simulation including atmospheric drag and an 18th order tesseral model shows that the general perturbation

method is sufficiently accurate to plan overflight targeting manoeuvres up to at least two weeks in the future. The omission of atmospheric drag effects during the altitude changing phases of the manoeuvre is the largest contributor to inaccuracies in the predicted time of flyover when performing an overflight targeting manoeuvre. However, it is the periodic oscillation caused by the first zonal harmonic of the central body that is the largest contributor to the error in the predicted position of the sub-satellite point. The exclusion of this periodic oscillation from the solution is due to the averaging of the central body disturbance function over the orbit period; this simplification is fundamental to all general perturbation methods and thus to increase the accuracy of the predicted sub-satellite point location would require that a semi-analytical, or fully numerical, method be used that could incorporate these effects.

How to best select the manoeuvre, or manoeuvres, to perform from the full range of possible solutions for any scenario will depend on the specific mission requirements. This selection may not be straightforward as there are multiple trade-off criteria to be considered. A different set of mission priorities will lead the operator to select a different manoeuvre, or set of manoeuvres, as the ideal solution. Detailed investigation of these criteria is outside the scope of this work, but the speed and ease with which the proposed method of manoeuvre design can be solved means that the effect of different priorities, and the introduction of additional trade-off criteria, can be rapidly assessed and compared.

Responsive missions, using manoeuvres defined by the general perturbation method and carried out by satellites equipped with existing propulsion technology, can provide a significant reduction in flyover time of a target when compared with a non-manoeuvrable spacecraft. The time reduction possible will be highly dependent on the case being studied but in any case a minimum time solution will exist. There is an inherent trade-off between the time to flyover, the change in velocity required for the manoeuvre, and the look angle to the target at closest approach. The relationship between these competing parameters forms a discontinuous solution space, making it an ideal problem for the general perturbation method as numerical optimisers may struggle to explore such a solution set.

A responsive constellation of small satellites can provide significant improvements

in the volume and frequency of data collection when compared with a static constellation. The improvement in coverage available is dependent on the target latitude, as a static constellation will naturally provide better coverage to latitudes at the upper and lower ranges of its region of coverage; in contrast, a responsive constellation in which the satellites can manoeuvre into repeating ground track orbits over the region of interest can provide relatively consistent coverage, and a consistent revisit time, to all regions targeted, irrespective of their latitude. This makes such a system particularly attractive for scenarios in which targets may lie across a range of latitudes, or for a mission in which the targets are primarily close to the equator, but there is an additional requirement to have coverage available at higher and lower latitudes, for example to provide ground station access. Analysis of such a scenario is challenging as the large number of satellites available to manoeuvre results in thousands of possible outcomes for each reconfiguration, all of which must be analysed and compared to identify the best solution to meet the mission goals. The rapid solution provided by the general perturbation method makes such a detailed analysis possible, allowing for an in-depth consideration of the solution space and an informed trade-off between the many competing options.

The proposed solution to the restricted low-thrust Lambert problem can be used to define the manoeuvres required to deploy a satellite constellation through right ascension of the ascending node and argument of latitude from a single launch injection point. It is possible to identify, for a given scenario, whether a co-directional manoeuvre, in which all satellites phase their right ascension of the ascending node or argument of latitude in the same direction (either positive or negative), or a contra-directional manoeuvre, in which the satellites phase their parameters in opposite directions (one positive and one negative), will be more efficient. A clear turning point is identifiable as a function of the change in velocity and time required for the manoeuvre, beyond which one technique will be more efficient than the other. A minimum constellation deployment time exists for a given maximum change in velocity, though the time to deploy some satellites can be shorter, and that minimum time is defined by the satellites manoeuvring to the furthest orbit plane. As such, the most efficient deployment strategy may be one in which the satellites in each plane use a different amount of

propellant. This deployment technique can reduce launch costs significantly, and although the deployment manoeuvre time can be lengthy, the time to total constellation deployment can be comparable with traditional launch methods due to the possible wait time between subsequent launches.

The presented general perturbation method can be used to quickly analyse a range of complex scenarios requiring responsive spacecraft manoeuvring. It can be scaled to consider large constellations whilst maintaining its solution speed and can produce a full overview of the solution space in question, avoiding the need to limit the search space prematurely, or rely on optimisers that may overlook valuable solutions. The analytical nature of the method also allows for unique insights to be obtained without requiring the solution to be numerically evaluated at multiple points. Based on these observations the core thesis of this work can be deemed to be confirmed.

7.2 Future Work

Future work to improve the accuracy of the developed method, whilst maintaining its speed, would be extremely valuable. Atmospheric drag has been shown to be a key source of inaccuracy. The inclusion of this perturbation in the developed general perturbation method would not only improve accuracy, but could also remove the need to assume that atmospheric drag compensation is performed throughout the coasting phases. For some manoeuvres, this may in fact be advantageous as the effects of atmospheric drag could be used to naturally lower the satellite altitude, reducing the amount of propellent needed to manoeuvre. However, including this perturbation while still maintaining a fully-analytical solution may not be possible; instead a semi-analytical method may be required to include perturbations due to atmospheric drag and improve the accuracy of the solution. Inclusion of other disturbing forces such as higher order central body effects, solar radiation pressure and third body effects would also improve the accuracy of the solution, but their impact is predicted to be much less than from the inclusion of atmospheric drag. Additional improvements in accuracy could be achieved by developing the method to calculate the position of the sub-satellite point considering an oblate Earth, rather than a spherical Earth. Extension of the work to elliptical orbits would also be a valuable development. This would

require a complete reworking of the governing equations of motion and it is likely to be challenging to obtain a fully-analytical solution. To enable these advances, the general perturbation method could be used as an initial estimate, with a semi-analytical or fully numerical analysis used to fine-tune the results and provide an optimal control profile for the manoeuvre.

Further constraints could be added to the manoeuvre to bound arrival time and ensure specific lighting conditions at flyover, or to achieve desired look angles during target passes. The relationship between the time of sequential flyovers by satellites in a constellation could also be constrained, to provide simultaneous coverage of a target, or provide repeated passes in quick succession. Manoeuvres could be used to target not only regions of interest, but also ground stations, to expedite data downlink and reduce the overall time from target identification to data delivery. This would require consideration of the overflight targeting of both the region of interest and the ground station in tandem, as using a less favourable manoeuvre to flyover the target may make it easier to subsequently target the ground station and complete the data delivery. In a similar way, it may be of interest to consider the long-term impact of the manoeuvres in the trade-space. For example, the manoeuvre that provides the fastest, or most propellant efficient, solution may only provide one flyover followed by a long gap; another manoeuvre that is less favourable for the initial flyover however, could provide repeated flyovers in a short period, making it more favourable in the long-term, if continued coverage is desired.

The breadth of scenarios considered could also be extended. Staged deployment of constellations, or reconfiguration of constellations following the addition or loss of satellites, has not been addressed in this body of work. It was highlighted in the literature review that this scenario has been looked at in some detail in the past, primarily using numerical optimisers; however, the use of the general perturbation method could provide further insight into this challenge, and may provide alternative solutions that have previously not been considered. Another area that could be of interest for future studies is the application of the technique to non-standard constellation architectures, such as asymmetric constellations, or pseudo-random constellations that can arise as a result of using rideshare launches. Active debris removal, or spacecraft servicing, are

other scenarios to which the method could be applied, to determine optimal trajectories to visit the greatest number of targets, for example. The method could also be applied to obtain close-approach passes for satellites with inter-satellite communication capabilities. In addition, the method could theoretically be extended to applications beyond Earth orbit to analyse inter-planetary trajectories, or to design rendezvous missions to multiple bodies, such as asteroids or comets.

One factor that emerged during this body of work, but was not explored, is the effect of performing multiple sequential manoeuvres. In this work, each manoeuvre, or set of manoeuvres, was considered individually and the 'best' manoeuvres chosen from the available options by considering their individual properties. However, each manoeuvre choice will impact the next phase of an extended scenario, and thus impact the future manoeuvre choices that are available. This creates an expanding decision tree, with potentially thousands of manoeuvre choices available at each branch. For multiple sequential manoeuvres, this decision tree becomes extremely large and considering all possible scenario outcomes becomes challenging. Due to the extremely fast solution speed of the general perturbation method, it may be possible to explore large numbers of solutions extremely quickly and offer some insight into the expansive decision tree. Coupling the method with an optimiser could allow for even larger and more complex scenarios to be quickly explored and a range of possible solutions found.

Appendix A

Full Analytical Equations for Change in Right Ascension of the Ascending Node and Argument of Latitude as Integrated Over Mean Semi-Major Axis

Right Ascension of the Ascending Node Equations

$$\Delta\Omega_1 = \frac{3\beta^8 J_2 R_e^2 \cos(i)}{134217728 a_0^{16} A_{prop} \mu^7} \left\{ \frac{32768 a_0^8 \mu^4 \left(a_0^4 - \frac{256 a_0^4 \mu^4}{\beta^4}\right)}{\beta^4} \right.$$
$$\left. + 9 J_2^2 R_e^4 (3\cos(2i)+1)^2 \left(a_0^8 - \frac{65536 a_0^8 \mu^8}{\beta^8}\right) + \frac{1024 a_0^4 J_2 \mu^2 R_e^2 (3\cos(2i)+1)\left(a_0^6 - \frac{4096 a_0^6 \mu^6}{\beta^6}\right)}{\beta^2} \right\}$$

$$\Delta\Omega_2 = -\frac{3\beta^2 J_2 R_e^2 \cos(i)}{256 a_0^2 \mu^2} \sqrt{\frac{\beta^3}{a_0^3 \mu^2}} \left(\frac{3\beta^2 J_2 R_e^2 \left(1 - \frac{3\sin^2(i)}{2}\right)}{32 a_0^2 \mu^2} + 1 \right)$$
$$\times \left\{ \frac{\sqrt{\mu}\left(-640 a_0^2 \left(\frac{a_0\mu}{\beta}\right)^{5/2} + a_0^{5/2}\left(\frac{320 a_0^2\mu^2}{\beta^2} + 3 J_2 R_e^2 \left(2 - 3\sin^2(i)\right)\right) + 96 J_2 R_e^2 \left(3\sin^2(i) - 2\right)\left(\frac{a_0\mu}{\beta}\right)^{5/2}\right)}{640 a_0^{5/2} A_{prop} \left(\frac{a_0\mu}{\beta}\right)^{5/2}} \right.$$
$$\left. - \frac{\sqrt{\mu}\left(-\frac{320 a_0^2 a_3^{5/2}\mu^2}{\beta^2} + 32\left(\frac{a_0\mu}{\beta}\right)^{5/2}\left(20 a_3^2 + 3 J_2 R_e^2 \left(2 - 3\sin^2(i)\right)\right) + 3 a_3^{5/2} J_2 R_e^2 \left(3\sin^2(i) - 2\right)\right)}{640 a_3^{5/2} A_{prop} \left(\frac{a_0\mu}{\beta}\right)^{5/2}} + t_t \right\}$$

$$\Delta\Omega_3 = -\frac{3\beta^8 J_2 R_e^2 \cos(i)}{134217728 a_0^8 a_3^8 A_{prop} \mu^7} \left\{ \frac{32768 a_0^4 a_3^4 \mu^4 \left(\frac{256 a_0^4 \mu^4}{\beta^4} - a_3^4\right)}{\beta^4} \right.$$

$$+9J_2^2R_e^4(3\cos(2i)+1)^2\left(\frac{65536a_0^8\mu^8}{\beta^8}-a_3^8\right)+\frac{1024a_0^2a_3^2J_2\mu^2R_e^2(3\cos(2i)+1)\left(\frac{4096a_0^6\mu^6}{\beta^6}-a_3^6\right)}{\beta^2}\Bigg\}$$

$$\begin{aligned}
\Omega_{total} =&\frac{3\beta^8J_2R_e^2\cos(i)}{134217728a_0^{16}A_{prop}\mu^7}\left\{\frac{32768a_0^8\mu^4\left(a_0^4-\frac{256a_0^4\mu^4}{\beta^4}\right)}{\beta^4}\right.\\
&\left.+9J_2^2R_e^4(3\cos(2i)+1)^2\left(a_0^8-\frac{65536a_0^8\mu^8}{\beta^8}\right)+\frac{1024a_0^4J_2\mu^2R_e^2(3\cos(2i)+1)\left(a_0^6-\frac{4096a_0^6\mu^6}{\beta^6}\right)}{\beta^2}\right\}\\
&-\frac{3\beta^8J_2R_e^2\cos(i)}{134217728a_0^8a_3^8A_{prop}\mu^7}\left\{\frac{32768a_0^4a_3^4\mu^4\left(\frac{256a_0^4\mu^4}{\beta^4}-a_3^4\right)}{\beta^4}\right.\\
&\left.+9J_2^2R_e^4(3\cos(2i)+1)^2\left(\frac{65536a_0^8\mu^8}{\beta^8}-a_3^8\right)+\frac{1024a_0^2a_3^2J_2\mu^2R_e^2(3\cos(2i)+1)\left(\frac{4096a_0^6\mu^6}{\beta^6}-a_3^6\right)}{\beta^2}\right\}\\
&-\frac{3\beta^2J_2R_e^2\cos(i)}{256a_0^2\mu^2}\sqrt{\frac{\beta^3}{a_0^3\mu^2}}\left(\frac{3\beta^2J_2R_e^2\left(1-\frac{3\sin^2(i)}{2}\right)}{32a_0^2\mu^2}+1\right)\\
&\times\left\{\frac{\sqrt{\mu}\left(-640a_0^2\left(\frac{a_0\mu}{\beta}\right)^{5/2}+a_0^{5/2}\left(\frac{320a_0^2\mu^2}{\beta^2}+3J_2R_e^2\left(2-3\sin^2(i)\right)\right)+96J_2R_e^2\left(3\sin^2(i)-2\right)\left(\frac{a_0\mu}{\beta}\right)^{5/2}\right)}{640a_0^{5/2}A_{prop}\left(\frac{a_0\mu}{\beta}\right)^{5/2}}\right.\\
&\left.-\frac{\sqrt{\mu}\left(-\frac{320a_0^2a_3^{5/2}\mu^2}{\beta^2}+32\left(\frac{a_0\mu}{\beta}\right)^{5/2}\left(20a_3^2+3J_2R_e^2\left(2-3\sin^2(i)\right)\right)+3a_3^{5/2}J_2R_e^2\left(3\sin^2(i)-2\right)\right)}{640a_3^{5/2}A_{prop}\left(\frac{a_0\mu}{\beta}\right)^{5/2}}+t_t\right\}
\end{aligned}$$

$$
\begin{aligned}
\Omega_{dif} =& \frac{3\beta^8 J_2 R_e^2 \cos(i)}{134217728 a_0^{16} A_{prop} \mu^7} \left\{ \frac{32768 a_0^8 \mu^4 \left(a_0^4 - \frac{256 a_0^4 \mu^4}{\beta^4}\right)}{\beta^4} \right. \\
& \left. + 9 J_2^2 R_e^4 (3\cos(2i)+1)^2 \left(a_0^8 - \frac{65536 a_0^8 \mu^8}{\beta^8}\right) + \frac{1024 a_0^4 J_2 \mu^2 R_e^2 (3\cos(2i)+1)\left(a_0^6 - \frac{4096 a_0^6 \mu^6}{\beta^6}\right)}{\beta^2} \right\} \\
& - \frac{3\beta^8 J_2 R_e^2 \cos(i)}{134217728 a_0^8 a_3^8 A_{prop} \mu^7} \left\{ \frac{32768 a_0^4 a_3^4 \mu^4 \left(\frac{256 a_0^4 \mu^4}{\beta^4} - a_3^4\right)}{\beta^4} \right. \\
& \left. + 9 J_2^2 R_e^4 (3\cos(2i)+1)^2 \left(\frac{65536 a_0^8 \mu^8}{\beta^8} - a_3^8\right) + \frac{1024 a_0^2 a_3^2 J_2 \mu^2 R_e^2 (3\cos(2i)+1)\left(\frac{4096 a_0^6 \mu^6}{\beta^6} - a_3^6\right)}{\beta^2} \right\} \\
& - \frac{3\beta^2 J_2 R_e^2 \cos(i)}{256 a_0^2 \mu^2} \sqrt{\frac{\beta^3}{a_0^3 \mu^2}} \left(\frac{3\beta^2 J_2 R_e^2 \left(1 - \frac{3\sin^2(i)}{2}\right)}{32 a_0^2 \mu^2} + 1 \right) \\
& \times \left\{ \frac{\sqrt{\mu}\left(-640 a_0^2 \left(\frac{a_0 \mu}{\beta}\right)^{5/2} + a_0^{5/2}\left(\frac{320 a_0^2 \mu^2}{\beta^2} + 3 J_2 R_e^2 \left(2 - 3\sin^2(i)\right)\right) + 96 J_2 R_e^2 \left(3\sin^2(i) - 2\right)\left(\frac{a_0 \mu}{\beta}\right)^{5/2}\right)}{640 a_0^{5/2} A_{prop} \left(\frac{a_0 \mu}{\beta}\right)^{5/2}} \right. \\
& \left. - \frac{\sqrt{\mu}\left(-\frac{320 a_0^2 a_3^{5/2} \mu^2}{\beta^2} + 32\left(\frac{a_0 \mu}{\beta}\right)^{5/2}\left(20 a_3^2 + 3 J_2 R_e^2 \left(2 - 3\sin^2(i)\right)\right) + 3 a_3^{5/2} J_2 R_e^2 \left(3\sin^2(i) - 2\right)\right)}{640 a_3^{5/2} A_{prop} \left(\frac{a_0 \mu}{\beta}\right)^{5/2}} + t_t \right\} \\
& + \frac{3 J_2 t_t R_e^2 \cos(i) \sqrt{\frac{\mu}{a_{\text{ref}}^3}} \left(\frac{3 J_2 R_e^2 \left(1 - \frac{3\sin^2(i)}{2}\right)}{2 a_{\text{ref}}^2} + 1 \right)}{2 a_{\text{ref}}^2}
\end{aligned}
$$

where for the case where the satellite altitude is lowered in phase 1,

$$\beta = a_0 \left(\sqrt{\frac{\mu}{a_3}} + \Delta \mathrm{V}_{alt} \right) \left(2\sqrt{\frac{\mu}{a_0}} + \sqrt{\frac{\mu}{a_3}} + \Delta \mathrm{V}_{alt} \right) + \mu$$

while for the case in which the satellite altitude is raised in phase 1

$$\beta = a_0 \left(\sqrt{\frac{\mu}{a_3}} - \Delta \mathrm{V}_{alt} \right) \left(2\sqrt{\frac{\mu}{a_0}} + \sqrt{\frac{\mu}{a_3}} - \Delta \mathrm{V}_{alt} \right) + \mu.$$

Argument of Latitude Equations

$$\Delta u_1 = -\frac{\beta^8}{536870912 a_0^{16} A_{prop} \mu^7}\left\{\frac{8388608 a_0^{12}\mu^6\left(a_0^2-\frac{16a_0^2\mu^2}{\beta^2}\right)}{\beta^6}+27J_2^3R_e^6(3\cos(2i)+1)^2(5\cos(2i)+3)\left(a_0^8-\frac{65536a_0^8\mu^8}{\beta^8}\right)\right.$$
$$\left.+\frac{98304a_0^8J_2\mu^4R_e^2(11\cos(2i)+5)\left(a_0^4-\frac{256a_0^4\mu^4}{\beta^4}\right)}{\beta^4}+\frac{768a_0^4J_2^2\mu^2R_e^4(68\cos(2i)+39\cos(4i)+53)\left(a_0^6-\frac{4096a_0^6\mu^6}{\beta^6}\right)}{\beta^2}\right\}$$

$$\Delta u_2 = \left\{\frac{3\beta^2J_2R_e^2}{256a_0^2\mu^2}\left(2-\frac{5\sin^2(i)}{2}\right)\sqrt{\frac{\beta^3}{a_0^3\mu^2}}\left(\frac{3\beta^2J_2R_e^2\left(1-\frac{3\sin^2(i)}{2}\right)}{32a_0^2\mu^2}+1\right)\right.$$
$$\left.+\frac{1}{8}\sqrt{\frac{\beta^3}{a_0^3\mu^2}}\left(\frac{3\beta^2J_2R_e^2\left(1-\frac{3\sin^2(i)}{2}\right)}{32a_0^2\mu^2}+1\right)\right\}$$
$$\times\left\{-\frac{1}{2A_{prop}}\left(\frac{-\sqrt{\mu}}{\sqrt{\frac{a_0\mu}{\beta}}}+\frac{9J_2\sqrt{\mu}R_e^2\sin^2(i)}{320\left(\frac{a_0\mu}{\beta}\right)^{5/2}}-\frac{9J_2\sqrt{\mu}R_e^2\sin^2(i)}{10a_0^{5/2}}-\frac{3J_2\sqrt{\mu}R_e^2}{160\left(\frac{a_0\mu}{\beta}\right)^{5/2}}+\frac{3J_2\sqrt{\mu}R_e^2}{5a_0^{5/2}}+\frac{2\sqrt{\mu}}{\sqrt{a_0}}\right)\right.$$
$$\left.+\frac{1}{2A_{prop}}\left(\frac{\sqrt{\mu}}{\sqrt{\frac{a_0\mu}{\beta}}}-\frac{9J_2\sqrt{\mu}R_e^2\sin^2(i)}{320\left(\frac{a_0\mu}{\beta}\right)^{5/2}}+\frac{9J_2\sqrt{\mu}R_e^2\sin^2(i)}{10a_3^{5/2}}+\frac{3J_2\sqrt{\mu}R_e^2}{160\left(\frac{a_0\mu}{\beta}\right)^{5/2}}-\frac{3J_2\sqrt{\mu}R_e^2}{5a_3^{5/2}}-\frac{2\sqrt{\mu}}{\sqrt{a_3}}\right)+t_t\right\}$$

$$\Delta u_3 = \frac{\beta^8}{536870912 a_0^8 a_3^8 A_{prop} \mu^7} \left\{ \frac{8388608 a_0^6 a_3^6 \mu^6 \left(\frac{16 a_0^2 \mu^2}{\beta^2} - a_3^2 \right)}{\beta^6} + 27 J_2^3 R_e^6 (3\cos(2i)+1)^2 (5\cos(2i)+3) \left(\frac{65536 a_0^8 \mu^8}{\beta^8} - a_3^8 \right) \right.$$
$$\left. + \frac{98304 a_0^4 a_3^4 J_2 \mu^4 R_e^2 (11\cos(2i)+5) \left(\frac{256 a_0^4 \mu^4}{\beta^4} - a_3^4 \right)}{\beta^4} + \frac{768 a_0^2 a_3^2 J_2^2 \mu^2 R_e^4 (68\cos(2i)+39\cos(4i)+53) \left(\frac{4096 a_0^6 \mu^6}{\beta^6} - a_3^6 \right)}{\beta^2} \right\}$$

$$u_{total} = \frac{1}{536870912 A_{prop} \mu^7 a_0^8 a_3^8} \left\{ \frac{8388608 \mu^6 a_0^6 \left(\frac{16 \mu^2 a_0^2}{\beta^2} - a_3^2 \right) a_3^6}{\beta^6} + \frac{98304 \mu^4 (11\cos(2i)+5) a_0^4 \left(\frac{256 \mu^4 a_0^4}{\beta^4} - a_3^4 \right) J_2 R_e^2 a_3^4}{\beta^4} \right.$$
$$+ \frac{768 \mu^2 (68\cos(2i)+39\cos(4i)+53) a_0^2 \left(\frac{4096 \mu^6 a_0^6}{\beta^6} - a_3^6 \right) J_2^2 R_e^4 a_3^2}{\beta^2}$$
$$\left. + 27 (3\cos(2i)+1)^2 (5\cos(2i)+3) \left(\frac{65536 \mu^8 a_0^8}{\beta^8} - a_3^8 \right) J_2^3 R_e^6 \right\} \beta^8$$
$$- \frac{1}{536870912 A_{prop} \mu^7 a_0^{16}} \left\{ \frac{8388608 \left(a_0^2 - \frac{16 \mu^2 a_0^2}{\beta^2} \right) \mu^6 a_0^{12}}{\beta^6} + \frac{98304 \left(a_0^4 - \frac{256 \mu^4 a_0^4}{\beta^4} \right) \mu^4 (11\cos(2i)+5) J_2 R_e^2 a_0^8}{\beta^4} \right.$$
$$+ \frac{768 \left(a_0^6 - \frac{4096 \mu^6 a_0^6}{\beta^6} \right) \mu^2 (68\cos(2i)+39\cos(4i)+53) J_2^2 R_e^4 a_0^4}{\beta^2}$$
$$\left. + 27 \left(a_0^8 - \frac{65536 \mu^8 a_0^8}{\beta^8} \right) (3\cos(2i)+1)^2 (5\cos(2i)+3) J_2^3 R_e^6 \right\} \beta^8$$

$$+\left\{\frac{3J_2R_e^2}{256\mu^2a_0^2}\left(2-\frac{5\sin^2(i)}{2}\right)\beta^2\sqrt{\frac{\beta^3}{\mu^2a_0^3}}\left(\frac{3\left(1-\frac{3\sin^2(i)}{2}\right)\beta^2J_2R_e^2}{32\mu^2a_0^2}+1\right)\right.$$
$$\left.+\frac{1}{8}\sqrt{\frac{\beta^3}{\mu^2a_0^3}}\left(\frac{3\left(1-\frac{3\sin^2(i)}{2}\right)\beta^2J_2R_e^2}{32\mu^2a_0^2}+1\right)\right\}\left\{-\frac{1}{2A_{prop}}\left(\frac{9\sin^2(i)\sqrt{\mu}J_2R_e^2}{320\left(\frac{\mu a_0}{\beta}\right)^{5/2}}+\frac{3\sqrt{\mu}J_2R_e^2}{5a_0^{5/2}}\right.\right.$$
$$-\frac{3\sqrt{\mu}J_2R_e^2}{160\left(\frac{\mu a_0}{\beta}\right)^{5/2}}-\frac{9\sqrt{\mu}\sin^2(i)J_2R_e^2}{10a_0^{5/2}}-\frac{\sqrt{\mu}}{\sqrt{\frac{\mu a_0}{\beta}}}+\frac{2\sqrt{\mu}}{\sqrt{a_0}}\Bigg)+\frac{1}{2A_{prop}}\left(\frac{3\sqrt{\mu}J_2R_e^2}{160\left(\frac{\mu a_0}{\beta}\right)^{5/2}}+\frac{9\sin^2(i)\sqrt{\mu}J_2R_e^2}{10a_3^{5/2}}\right.$$
$$\left.\left.-\frac{9\sqrt{\mu}\sin^2(i)J_2R_e^2}{320\left(\frac{\mu a_0}{\beta}\right)^{5/2}}-\frac{3\sqrt{\mu}J_2R_e^2}{5a_3^{5/2}}+\frac{\sqrt{\mu}}{\sqrt{\frac{\mu a_0}{\beta}}}-\frac{2\sqrt{\mu}}{\sqrt{a_3}}\right)+t_t\right\}$$

$$u_{dif}=\frac{1}{536870912A_{prop}\mu^7a_0^8a_3^8}\left(\frac{8388608\mu^6a_0^6\left(\frac{16\mu^2a_0^2}{\beta^2}-a_3^2\right)a_3^6}{\beta^6}+\frac{98304\mu^4(11\cos(2i)+5)a_0^4\left(\frac{256\mu^4a_0^4}{\beta^4}-a_3^4\right)J_2R_e^2a_3^4}{\beta^4}\right.$$
$$+\frac{768\mu^2(68\cos(2i)+39\cos(4i)+53)a_0^2\left(\frac{4096\mu^6a_0^6}{\beta^6}-a_3^6\right)J_2^2R_e^4a_3^2}{\beta^2}$$
$$\left.+27(3\cos(2i)+1)^2(5\cos(2i)+3)\left(\frac{65536\mu^8a_0^8}{\beta^8}-a_3^8\right)J_2^3R_e^6\right)\beta^8$$
$$-\frac{1}{536870912A_{prop}\mu^7a_0^{16}}\left\{\frac{8388608\left(a_0^2-\frac{16\mu^2a_0^2}{\beta^2}\right)\mu^6a_0^{12}}{\beta^6}+\frac{98304\left(a_0^4-\frac{256\mu^4a_0^4}{\beta^4}\right)\mu^4(11\cos(2i)+5)J_2R_e^2a_0^8}{\beta^4}\right.$$
$$\left.+\frac{768\left(a_0^6-\frac{4096\mu^6a_0^6}{\beta^6}\right)\mu^2(68\cos(2i)+39\cos(4i)+53)J_2^2R_e^4a_0^4}{\beta^2}\right.$$

$$
\begin{aligned}
&+27\left(a_0^8-\frac{65536\mu^8a_0^8}{\beta^8}\right)(3\cos(2i)+1)^2(5\cos(2i)+3)J_2^3R_e^6\Bigg\}\beta^8\\
&-\Bigg\{\frac{3J_2R_e^2}{2a_{\text{ref}}^2}\left[\left(2-\frac{5\sin^2(i)}{2}\right)\sqrt{\frac{\mu}{a_{\text{ref}}^3}}\left[\frac{3J_2R_e^2}{2a_{\text{ref}}^2}\left(1-\frac{3\sin^2(i)}{2}\right)+1\right]\right]\\
&+\sqrt{\frac{\mu}{a_{\text{ref}}^3}}\left[\frac{3J_2R_e^2}{2a_{\text{ref}}^2}\left(1-\frac{3\sin^2(i)}{2}\right)+1\right]\Bigg\}t_t\\
&+\Bigg\{\frac{3J_2R_e^2}{256\mu^2a_0^2}\left(2-\frac{5\sin^2(i)}{2}\right)\beta^2\sqrt{\frac{\beta^3}{\mu^2a_0^3}}\left(\frac{3\left(1-\frac{3\sin^2(i)}{2}\right)\beta^2J_2R_e^2}{32\mu^2a_0^2}+1\right)\\
&+\frac{1}{8}\sqrt{\frac{\beta^3}{\mu^2a_0^3}}\left(\frac{3\left(1-\frac{3\sin^2(i)}{2}\right)\beta^2J_2R_e^2}{32\mu^2a_0^2}+1\right)\Bigg\}\Bigg\{-\frac{1}{2A_{prop}}\left(\frac{9\sin^2(i)\sqrt{\mu}J_2R_e^2}{320\left(\frac{\mu a_0}{\beta}\right)^{5/2}}+\frac{3\sqrt{\mu}J_2R_e^2}{5a_0^{5/2}}\right.\\
&-\frac{3\sqrt{\mu}J_2R_e^2}{160\left(\frac{\mu a_0}{\beta}\right)^{5/2}}-\frac{9\sqrt{\mu}\sin^2(i)J_2R_e^2}{10a_0^{5/2}}-\frac{\sqrt{\mu}}{\sqrt{\frac{\mu a_0}{\beta}}}+\left.\frac{2\sqrt{\mu}}{\sqrt{a_0}}\right)+\frac{1}{2A_{prop}}\left(\frac{3\sqrt{\mu}J_2R_e^2}{160\left(\frac{\mu a_0}{\beta}\right)^{5/2}}+\frac{9\sin^2(i)\sqrt{\mu}J_2R_e^2}{10a_3^{5/2}}\right.\\
&-\left.\frac{9\sqrt{\mu}\sin^2(i)J_2R_e^2}{320\left(\frac{\mu a_0}{\beta}\right)^{5/2}}-\frac{3\sqrt{\mu}J_2R_e^2}{5a_3^{5/2}}+\frac{\sqrt{\mu}}{\sqrt{\frac{\mu a_0}{\beta}}}-\left.\frac{2\sqrt{\mu}}{\sqrt{a_3}}\right)+t_t\Bigg\}
\end{aligned}
$$

where for the case where the satellite altitude is lowered in phase 1,

$$\beta=a_0\left(\sqrt{\frac{\mu}{a_3}}+\Delta\text{V}_{alt}\right)\left(2\sqrt{\frac{\mu}{a_0}}+\sqrt{\frac{\mu}{a_3}}+\Delta\text{V}_{alt}\right)+\mu$$

while for the case in which the satellite altitude is raised in phase 1

$$\beta = a_0 \left(\sqrt{\frac{\mu}{a_3}} - \Delta \mathrm{V}_{alt} \right) \left(2\sqrt{\frac{\mu}{a_0}} + \sqrt{\frac{\mu}{a_3}} - \Delta \mathrm{V}_{alt} \right) + \mu.$$

Appendix B

Full Analytical Equations for Change in Right Ascension of the Ascending Node and Argument of Latitude as Integrated Over Osculating Semi-Major Axis

Right Ascension of the Ascending Node Equations

$$\begin{aligned}\Delta\Omega_1 =&\frac{1}{7560\sqrt{2}A_{prop}J_2R_e^2}\cot(i)\csc^7(i)\left\{\frac{1}{\left(3\gamma-2a_0^2\right)^3}\sqrt{\frac{\mu}{a_0^3}}a_0\sqrt{\frac{\mu\csc^6(i)a_0^3}{\left(2\csc^2(i)a_0^2-3J_2R_e^2\right)^3}}\left[432\gamma(129-236\cos(2i)+171\cos(4i))a_0^6\right.\right.\\
&-64(129-236\cos(2i)+171\cos(4i))a_0^8-2268(57-108\cos(2i)+83\cos(4i))\gamma^2a_0^4+2835(43-84\cos(2i)+73\cos(4i))\gamma^3a_0^2\\
&\left.+102060(1+3\cos(2i))\gamma^4\sin^2(i)\right]\\
&+\frac{1}{\beta\left(\frac{32\mu^2\csc^2(i)a_0^2}{\beta^2}-3J_2R_e^2\right)^3}4\mu\csc^6(i)\sqrt{\frac{\beta^3}{\mu^2a_0^3}}a_0\sqrt{\frac{\mu^4a_0^3}{\beta^3\left(-3\gamma+\frac{32\mu^2a_0^2}{\beta^2}\right)^3}}\left[-\frac{4194304\mu^8(129-236\cos(2i)+171\cos(4i))a_0^8}{\beta^8}\right.\\
&-\frac{580608\mu^4(57-108\cos(2i)+83\cos(4i))a_0^4\gamma^2}{\beta^4}+\frac{45360\mu^2(43-84\cos(2i)+73\cos(4i))a_0^2\gamma^3}{\beta^2}+102060(1+3\cos(2i))\gamma^4\sin^2(i)\\
&\left.\left.+\frac{1769472\gamma\mu^6(129-236\cos(2i)+171\cos(4i))a_0^6}{\beta^6}\right]\right\}\end{aligned}$$

$$\begin{aligned}\Delta\Omega_2 =&-\frac{3\cos(i)J_2R_e^2}{2\left(\frac{4\mu a_0}{\beta}-\frac{3\gamma\beta}{8\mu a_0}\right)^2}\left\{\frac{\sqrt{\mu}\left[-640a_0^2\left(\frac{\mu a_0}{\beta}\right)^{5/2}+96\left(-2+3\sin^2(i)\right)\left(\frac{\mu a_0}{\beta}\right)^{5/2}J_2R_e^2+a_0^{5/2}\left(\frac{320\mu^2a_0^2}{\beta^2}+3\left(2-3\sin^2(i)\right)J_2R_e^2\right)\right]}{640A_{prop}a_0^{5/2}\left(\frac{\mu a_0}{\beta}\right)^{5/2}}\right.\\
&\left.-\frac{\sqrt{\mu}\left[-\frac{320\mu^2a_0^2a_3^{5/2}}{\beta^2}+3\left(-2+3\sin^2(i)\right)a_3^{5/2}J_2R_e^2+32\left(\frac{\mu a_0}{\beta}\right)^{5/2}\left(20a_3^2+3\left(2-3\sin^2(i)\right)J_2R_e^2\right)\right]}{640A_{prop}\left(\frac{\mu a_0}{\beta}\right)^{5/2}a_3^{5/2}}\right\}\end{aligned}$$

$$+t_t\Bigg\}\sqrt{\frac{\mu}{\left(\frac{4\mu a_0}{\beta}-\frac{3\gamma\beta}{8\mu a_0}\right)^3}}\left[1+\frac{3\left(1-\frac{3\sin^2(i)}{2}\right)J_2R_e^2}{2\left(\frac{4\mu a_0}{\beta}-\frac{3\gamma\beta}{8\mu a_0}\right)^2}\right]$$

$$\begin{aligned}\Delta\Omega_3 =& -\frac{1}{7560\sqrt{2}A_{prop}J_2R_e^2}\cot(i)\csc^7(i)\Bigg\{\frac{1}{\left(2\csc^2(i)a_3^2-3J_2R_e^2\right)^3}\csc^6(i)\sqrt{\frac{\mu}{a_3^3}}a_3\sqrt{\frac{\mu a_3^3}{\left(-3\gamma+2a_3^2\right)^3}}\,[432\gamma(129-236\cos(2i)\\ &+171\cos(4i))a_3^6-64(129-236\cos(2i)+171\cos(4i))a_3^8-2268(57-108\cos(2i)+83\cos(4i))a_3^4\gamma^2\\ &+2835(43-84\cos(2i)+73\cos(4i))a_3^2\gamma^3+102060(1+3\cos(2i))\sin^2(i)\gamma^4]\\ &+\frac{1}{\beta\left(3\gamma-\frac{32\mu^2a_0^2}{\beta^2}\right)^3}4\mu\sqrt{\frac{\beta^3}{\mu^2a_0^3}}a_0\sqrt{\frac{\mu^4\csc^6(i)a_0^3}{\beta^3\left(\frac{32\mu^2\csc^2(i)a_0^2}{\beta^2}-3J_2R_e^2\right)^3}}\Bigg[-\frac{4194304\mu^8(129-236\cos(2i)+171\cos(4i))a_0^8}{\beta^8}\\ &-\frac{580608\mu^4(57-108\cos(2i)+83\cos(4i))a_0^4\gamma^2}{\beta^4}+\frac{45360\mu^2(43-84\cos(2i)+73\cos(4i))a_0^2\gamma^3}{\beta^2}\\ &+102060(1+3\cos(2i))\sin^2(i)\gamma^4+\frac{1769472\gamma\mu^6(129-236\cos(2i)+171\cos(4i))a_0^6}{\beta^6}\Bigg]\Bigg\}\end{aligned}$$

$$\begin{aligned}\Omega_{total} =&\frac{1}{7560\sqrt{2}A_{prop}J_2R_e^2}\cot(i)\csc^7(i)\Bigg\{\frac{1}{\left(3\gamma-2a_0^2\right)^3}\sqrt{\frac{\mu}{a_0^3}}a_0\left(102060\gamma^4(1+3\cos(2i))\sin^2(i)\right.\\ &+2835\gamma^3(43-84\cos(2i)+73\cos(4i))a_0^2-2268\gamma^2(57-108\cos(2i)+83\cos(4i))a_0^4+432\gamma(129-236\cos(2i)\\ &\left.+171\cos(4i))a_0^6-64(129-236\cos(2i)+171\cos(4i))a_0^8\right)\sqrt{\frac{\mu\csc^6(i)a_0^3}{\left(2\csc^2(i)a_0^2-3J_2R_e^2\right)^3}}\end{aligned}$$

$$+\frac{1}{\beta\left(\frac{32\mu^2\csc^2(i)a_0^2}{\beta^2}-3J_2R_e^2\right)^3}4\mu\csc^6(i)\sqrt{\frac{\beta^3}{\mu^2a_0^3}}a_0\sqrt{\frac{\mu^4a_0^3}{\beta^3\left(-3\gamma+\frac{32\mu^2a_0^2}{\beta^2}\right)^3}}\left[102060\gamma^4(1+3\cos(2i))\sin^2(i)\right.$$
$$+\frac{45360\gamma^3\mu^2(43-84\cos(2i)+73\cos(4i))a_0^2}{\beta^2}-\frac{580608\gamma^2\mu^4(57-108\cos(2i)+83\cos(4i))a_0^4}{\beta^4}$$
$$\left.+\frac{1769472\gamma\mu^6(129-236\cos(2i)+171\cos(4i))a_0^6}{\beta^6}-\frac{4194304\mu^8(129-236\cos(2i)+171\cos(4i))a_0^8}{\beta^8}\right]\Bigg\}$$
$$-\frac{1}{7560\sqrt{2}A_{prop}J_2R_e^2}\cot(i)\csc^7(i)\left\{\frac{1}{\beta\left(3\gamma-\frac{32\mu^2a_0^2}{\beta^2}\right)^3}4\mu\sqrt{\frac{\beta^3}{\mu^2a_0^3}}a_0\left[102060\gamma^4(1+3\cos(2i))\sin^2(i)\right.\right.$$
$$+\frac{45360\gamma^3\mu^2(43-84\cos(2i)+73\cos(4i))a_0^2}{\beta^2}-\frac{580608\gamma^2\mu^4(57-108\cos(2i)+83\cos(4i))a_0^4}{\beta^4}$$
$$+\frac{1769472\gamma\mu^6(129-236\cos(2i)+171\cos(4i))a_0^6}{\beta^6}$$
$$\left.-\frac{4194304\mu^8(129-236\cos(2i)+171\cos(4i))a_0^8}{\beta^8}\right]\sqrt{\frac{\mu^4\csc^6(i)a_0^3}{\beta^3\left(\frac{32\mu^2\csc^2(i)a_0^2}{\beta^2}-3J_2R_e^2\right)^3}}$$
$$+\frac{1}{\left(2\csc^2(i)a_3^2-3J_2R_e^2\right)^3}\csc^6(i)\sqrt{\frac{\mu}{a_3^3}}a_3\sqrt{\frac{\mu a_3^3}{\left(-3\gamma+2a_3^2\right)^3}}\left[102060\gamma^4(1+3\cos(2i))\sin^2(i)+2835\gamma^3(43-84\cos(2i)\right.$$
$$+73\cos(4i))a_3^2-2268\gamma^2(57-108\cos(2i)+83\cos(4i))a_3^4+432\gamma(129-236\cos(2i)+171\cos(4i))a_3^6-64(129$$
$$\left.-236\cos(2i)+171\cos(4i))a_3^8\right]\Bigg\}-\frac{1}{2\left(-\frac{3\beta\gamma}{8\mu a_0}+\frac{4\mu a_0}{\beta}\right)^2}3\cos(i)\sqrt{\frac{\mu}{\left(-\frac{3\beta\gamma}{8\mu a_0}+\frac{4\mu a_0}{\beta}\right)^3}}J_2R_e^2\left\{1+\right.$$
$$\left.\frac{3\left[1-\frac{3\sin^2(i)}{2}\right]J_2R_e^2}{2\left[-\frac{3\beta\gamma}{8\mu a_0}+\frac{4\mu a_0}{\beta}\right]^2}\right\}\left\{\frac{\sqrt{\mu}\left[-640a_0^2\left(\frac{\mu a_0}{\beta}\right)^{5/2}+96\left(-2+3\sin^2(i)\right)\left(\frac{\mu a_0}{\beta}\right)^{5/2}J_2R_e^2+a_0^{5/2}\left(\frac{320\mu^2a_0^2}{\beta^2}+3\left(2-3\sin^2(i)\right)J_2R_e^2\right)\right]}{640A_{prop}a_0^{5/2}\left(\frac{\mu a_0}{\beta}\right)^{5/2}}\right.$$

$$-\frac{\sqrt{\mu}\left[-\frac{320\mu^2 a_0^2 a_3^{5/2}}{\beta^2}+3\left(-2+3\sin^2(i)\right)a_3^{5/2}J_2R_e^2+32\left(\frac{\mu a_0}{\beta}\right)^{5/2}\left(20a_3^2+3\left(2-3\sin^2(i)\right)J_2R_e^2\right)\right]}{640A_{prop}\left(\frac{\mu a_0}{\beta}\right)^{5/2}a_3^{5/2}}+t_t\Bigg\}+\Omega_0$$

$$\Omega_{ref}=-3\cos(i)\sqrt{\frac{\mu}{\left(-\frac{3\gamma}{2a_{\text{ref}}}+a_{\text{ref}}\right)^3}}J_2R_e^2\left[1+\frac{3\left(1-\frac{3\sin^2(i)}{2}\right)J_2R_e^2}{2\left(-\frac{3\gamma}{2a_{\text{ref}}}+a_{\text{ref}}\right)^2}\right]\frac{t_t}{2\left(-\frac{3\gamma}{2a_{\text{ref}}}+a_{\text{ref}}\right)^2}$$

where

$$\gamma=J_2R_e^2\sin^2(i)$$

and, for the case where the satellite altitude is lowered in phase 1,

$$\beta=a_0\left(\sqrt{\frac{\mu}{a_3}}+\Delta\mathrm{V}_{alt}\right)\left(2\sqrt{\frac{\mu}{a_0}}+\sqrt{\frac{\mu}{a_3}}+\Delta\mathrm{V}_{alt}\right)+\mu$$

while for the case in which the satellite altitude is raised in phase 1

$$\beta=a_0\left(\sqrt{\frac{\mu}{a_3}}-\Delta\mathrm{V}_{alt}\right)\left(2\sqrt{\frac{\mu}{a_0}}+\sqrt{\frac{\mu}{a_3}}-\Delta\mathrm{V}_{alt}\right)+\mu.$$

Argument of Latitude Equations

$$
\begin{aligned}
\Delta u_1 = &- \frac{1}{918540\sqrt{2}A_{prop}\sqrt{\frac{\mu}{a_0^3}}a_0^7 J_2^6 R_e^{12}} \csc^{12}(i) \left[\frac{\mu a_0^3}{\left(-3\gamma+2a_0^2\right)^3}\right]^{\frac{3}{2}} \{18600435(1+3\cos(2i))\sin^{18}(i)J_2^{10}R_e^{20} \\
&+ 229635\sin^{12}(i)a_0^2 J_2^6 R_e^{12}\left[-216\gamma^3+3(1+3\cos(2i))J_2R_e^2\left(-180\gamma^2+3\gamma\kappa\right)\right] \\
&- 2835\sin^6(i)a_0^4 J_2^3 R_e^6\left[3(1+3\cos(2i))J_2R_e^2\left(9\zeta\gamma^2+432\kappa\gamma^3-25920\gamma^4\right)-216\gamma^3\left(144\gamma^2+3\gamma\kappa\right)\right] \\
&+ 2268\sin^4(i)a_0^6 J_2^2 R_e^4\left[3(1+3\cos(2i))J_2R_e^2\left(9\zeta\gamma^2+459\kappa\gamma^3-25920\gamma^4\right)-6\gamma\left(5184\gamma^4+108\gamma^3\kappa+9\gamma^2\zeta\right)\right] \\
&+ 64a_0^{10}\left[3(1+3\cos(2i))J_2R_e^2\left(18\zeta\gamma^2+918\kappa\gamma^3-51435\gamma^4\right)-6\gamma\left(13203\gamma^4+351\gamma^3\kappa+18\gamma^2\zeta\right)\right] \\
&-432\gamma a_0^8\left[-6\gamma\left(10368\gamma^4+351\gamma^3\kappa+18\gamma^2\zeta\right)+3(1+3\cos(2i))J_2R_e^2\left(-51435\gamma^4+918\gamma^3\kappa+18\gamma^2\zeta\right)\right]\}) \\
&+ \frac{1}{3674160\sqrt{2}A_{prop}\mu^7\sqrt{\frac{\beta^3}{\mu^2a_0^3}}a_0^7J_2^6R_e^{12}}\beta^7\csc^{12}(i)\left[\frac{\mu^4a_0^3}{\beta^3\left(-3\gamma+\frac{32\mu^2a_0^2}{\beta^2}\right)^3}\right]^{\frac{3}{2}}\{18600435(1+3\cos(2i))\sin^{18}(i)J_2^{10}R_e^{20} \\
&+ \frac{3674160\mu^2\sin^{12}(i)a_0^2J_2^6R_e^{12}\left[-216\gamma^3+3(1+3\cos(2i))J_2R_e^2\left(-180\gamma^2+3\gamma\kappa\right)\right]}{\beta^2} \\
&- \frac{1}{\beta^4}725760\mu^4\sin^6(i)a_0^4J_2^3R_e^6\left[3(1+3\cos(2i))J_2R_e^2\left(9\zeta\gamma^2+432\kappa\gamma^3-25920\gamma^4\right)-216\gamma^3\left(144\gamma^2+3\gamma\kappa\right)\right] \\
&+ \frac{1}{\beta^6}9289728\mu^6\sin^4(i)a_0^6J_2^2R_e^4\left[3(1+3\cos(2i))J_2R_e^2\left(9\zeta\gamma^2+459\kappa\gamma^3-25920\gamma^4\right)-6\gamma\left(5184\gamma^4+108\gamma^3\kappa+9\gamma^2\zeta\right)\right] \\
&+ \frac{1}{\beta^{10}}67108864\mu^{10}a_0^{10}\left[3(1+3\cos(2i))J_2R_e^2\left(18\zeta\gamma^2+918\kappa\gamma^3-51435\gamma^4\right)-6\gamma\left(13203\gamma^4+351\gamma^3\kappa+18\gamma^2\zeta\right)\right] \\
&- \frac{28311552\gamma\mu^8a_0^8\left[-6\gamma\left(10368\gamma^4+351\gamma^3\kappa+18\gamma^2\zeta\right)+3(1+3\cos(2i))J_2R_e^2\left(-51435\gamma^4+918\gamma^3\kappa+18\gamma^2\zeta\right)\right]}{\beta^8}\Bigg\}
\end{aligned}
$$

$$\Delta u_2 = \left\{ \sqrt{\frac{\mu}{\left(-\frac{3\beta\gamma}{8\mu a_0}+\frac{4\mu a_0}{\beta}\right)^3}}\left[1+\frac{3\left(1-\frac{3\sin^2(i)}{2}\right)J_2R_e^2}{2\left(-\frac{3\beta\gamma}{8\mu a_0}+\frac{4\mu a_0}{\beta}\right)^2}\right] + \frac{3\left(2-\frac{5\sin^2(i)}{2}\right)\sqrt{\frac{\mu}{\left(-\frac{3\beta\gamma}{8\mu a_0}+\frac{4\mu a_0}{\beta}\right)^3}}J_2R_e^2\left(1+\frac{3\left(1-\frac{3\sin^2(i)}{2}\right)J_2R_e^2}{2\left(-\frac{3\beta\gamma}{8\mu a_0}+\frac{4\mu a_0}{\beta}\right)^2}\right)}{2\left(-\frac{3\beta\gamma}{8\mu a_0}+\frac{4\mu a_0}{\beta}\right)^2} \right\} \left\{ -\frac{1}{2A_{prop}}\left[-\frac{9\gamma\sqrt{\mu}}{10a_0^{5/2}} + \frac{2\sqrt{\mu}}{\sqrt{a_0}} + \frac{9\gamma\sqrt{\mu}}{320\left(\frac{\mu a_0}{\beta}\right)^{5/2}} - \frac{\sqrt{\mu}}{\sqrt{\frac{\mu a_0}{\beta}}} + \frac{3\sqrt{\mu}J_2R_e^2}{5a_0^{5/2}} - \frac{3\sqrt{\mu}J_2R_e^2}{160\left(\frac{\mu a_0}{\beta}\right)^{5/2}}\right] + \frac{1}{2A_{prop}}\left[-\frac{9\gamma\sqrt{\mu}}{320\left(\frac{\mu a_0}{\beta}\right)^{5/2}} + \frac{\sqrt{\mu}}{\sqrt{\frac{\mu a_0}{\beta}}} + \frac{9\gamma\sqrt{\mu}}{10a_3^{5/2}} - \frac{2\sqrt{\mu}}{\sqrt{a_3}} + \frac{3\sqrt{\mu}J_2R_e^2}{160\left(\frac{\mu a_0}{\beta}\right)^{5/2}} - \frac{3\sqrt{\mu}J_2R_e^2}{5a_3^{5/2}}\right] + t_t \right\}$$

$$\begin{aligned}
\Delta u_3 = &-\frac{1}{918540\sqrt{2}A_{prop}\sqrt{\frac{\mu}{a_3^3}}a_3^7J_2^6R_e^{12}}\csc^{12}(i)\left[\frac{\mu a_3^3}{\left(-3\gamma+2a_3^2\right)^3}\right]^{\frac{3}{2}}\left\{18600435(1+3\cos(2i))\sin^{18}(i)J_2^{10}R_e^{20}\right.\\
&+229635\sin^{12}(i)a_3^2J_2^6R_e^{12}\left[-216\gamma^3+3(1+3\cos(2i))J_2R_e^2\left(-180\gamma^2+3\gamma\kappa\right)\right]\\
&-2835\sin^6(i)a_3^4J_2^3R_e^6\left[3(1+3\cos(2i))J_2R_e^2\left(9\zeta\gamma^2+432\kappa\gamma^3-25920\gamma^4\right)-216\gamma^3\left(144\gamma^2+3\gamma\kappa\right)\right]\\
&+2268\sin^4(i)a_3^6J_2^2R_e^4\left[3(1+3\cos(2i))J_2R_e^2\left(9\zeta\gamma^2+459\kappa\gamma^3-25920\gamma^4\right)-6\gamma\left(5184\gamma^4+108\gamma^3\kappa+9\gamma^2\zeta\right)\right]\\
&+64a_3^{10}\left(3(1+3\cos(2i))J_2R_e^2\left(18\zeta\gamma^2+918\kappa\gamma^3-51435\gamma^4\right)-6\gamma\left(13203\gamma^4+351\gamma^3\kappa+18\gamma^2\zeta\right)\right)\\
&\left.-432\gamma a_3^8\left[-6\gamma\left(10368\gamma^4+351\gamma^3\kappa+18\gamma^2\zeta\right)+3(1+3\cos(2i))J_2R_e^2\left(-51435\gamma^4+918\gamma^3\kappa+18\gamma^2\zeta\right)\right]\right\}
\end{aligned}$$

$$
\begin{aligned}
&+\frac{1}{3674160\sqrt{2}A_{prop}\mu^7\sqrt{\frac{\beta^3}{\mu^2a_0^3}}a_0^7J_2^6R_e^{12}}\beta^7\csc^{12}(i)\left[\frac{\mu^4a_0^3}{\beta^3\left(-3\gamma+\frac{32\mu^2a_0^2}{\beta^2}\right)^3}\right]^{\frac{3}{2}}\Bigg\{18600435(1+3\cos(2i))\sin^{18}(i)J_2^{10}R_e^{20}\\
&+\frac{1}{\beta^2}3674160\mu^2\sin^{12}(i)a_0^2J_2^6R_e^{12}\left[-216\gamma^3+3(1+3\cos(2i))J_2R_e^2\left(-180\gamma^2+3\gamma\kappa\right)\right]\\
&-\frac{1}{\beta^4}725760\mu^4\sin^6(i)a_0^4J_2^3R_e^6\left[3(1+3\cos(2i))J_2R_e^2\left(9\zeta\gamma^2+432\kappa\gamma^3-25920\gamma^4\right)-216\gamma^3\left(144\gamma^2+3\gamma\kappa\right)\right]\\
&+\frac{1}{\beta^6}9289728\mu^6\sin^4(i)a_0^6J_2^2R_e^4\left[3(1+3\cos(2i))J_2R_e^2\left(9\zeta\gamma^2+459\kappa\gamma^3-25920\gamma^4\right)-6\gamma\left(5184\gamma^4+108\gamma^3\kappa+9\gamma^2\zeta\right)\right]\\
&+\frac{1}{\beta^{10}}67108864\mu^{10}a_0^{10}\left[3(1+3\cos(2i))J_2R_e^2\left(18\zeta\gamma^2+918\kappa\gamma^3-51435\gamma^4\right)-6\gamma\left(13203\gamma^4+351\gamma^3\kappa+18\gamma^2\zeta\right)\right]\\
&-\frac{28311552\gamma\mu^8a_0^8\left[-6\gamma\left(10368\gamma^4+351\gamma^3\kappa+18\gamma^2\zeta\right)+3(1+3\cos(2i))J_2R_e^2\left(-51435\gamma^4+918\gamma^3\kappa+18\gamma^2\zeta\right)\right]}{\beta^8}\Bigg\}
\end{aligned}
$$

$$
\begin{aligned}
u_{total}=&-\frac{1}{918540\sqrt{2}A_{prop}\sqrt{\frac{\mu}{a_0^3}}a_0^7J_2^6R_e^{12}}\csc^{12}(i)\left[\frac{\mu a_0^3}{\left(-3\gamma+2a_0^2\right)^3}\right]^{\frac{3}{2}}\Big\{18600435(1+3\cos(2i))\sin^{18}(i)J_2^{10}R_e^{20}\\
&+229635\sin^{12}(i)a_0^2J_2^6R_e^{12}\left[-216\gamma^3+3\left(-180\gamma^2+3\gamma\kappa\right)(1+3\cos(2i))J_2R_e^2\right]\\
&-2835\sin^6(i)a_0^4J_2^3R_e^6\left[-216\gamma^3\left(144\gamma^2+3\gamma\kappa\right)+3\left(-25920\gamma^4+9\gamma^2\zeta+432\gamma^3\kappa\right)(1+3\cos(2i))J_2R_e^2\right]\\
&+2268\sin^4(i)a_0^6J_2^2R_e^4\left[-6\gamma\left(5184\gamma^4+9\gamma^2\zeta+108\gamma^3\kappa\right)+3\left(-25920\gamma^4+9\gamma^2\zeta+459\gamma^3\kappa\right)(1+3\cos(2i))J_2R_e^2\right]\\
&-432\gamma a_0^8\left[-6\gamma\left(10368\gamma^4+18\gamma^2\zeta+351\gamma^3\kappa\right)+3\left(-51435\gamma^4+18\gamma^2\zeta+918\gamma^3\kappa\right)(1+3\cos(2i))J_2R_e^2\right]\\
&+64a_0^{10}\left[-6\gamma\left(13203\gamma^4+18\gamma^2\zeta+351\gamma^3\kappa\right)+3\left(-51435\gamma^4+18\gamma^2\zeta+918\gamma^3\kappa\right)(1+3\cos(2i))J_2R_e^2\right]\Big\}
\end{aligned}
$$

$$
\begin{aligned}
&+\frac{1}{1837080\sqrt{2}A_{prop}\mu^7\sqrt{\frac{\beta^3}{\mu^2a_0^3}}a_0^7J_2^6R_e^{12}}\beta^7\csc^{12}(i)\left[\frac{\mu^4a_0^3}{\beta^3\left(-3\gamma+\frac{32\mu^2a_0^2}{\beta^2}\right)^3}\right]^{\frac{3}{2}}\Bigg\{18600435(1+3\cos(2i))\sin^{18}(i)J_2^{10}R_e^{20}\\
&+\frac{3674160\mu^2\sin^{12}(i)a_0^2J_2^6R_e^{12}\left(-216\gamma^3+3\left(-180\gamma^2+3\gamma\kappa\right)(1+3\cos(2i))J_2R_e^2\right)}{\beta^2}\\
&-\frac{725760\mu^4\sin^6(i)a_0^4J_2^3R_e^6\left(-216\gamma^3\left(144\gamma^2+3\gamma\kappa\right)+3\left(-25920\gamma^4+9\gamma^2\zeta+432\gamma^3\kappa\right)(1+3\cos(2i))J_2R_e^2\right)}{\beta^4}\\
&+\frac{9289728\mu^6\sin^4(i)a_0^6J_2^2R_e^4\left(-6\gamma\left(5184\gamma^4+9\gamma^2\zeta+108\gamma^3\kappa\right)+3\left(-25920\gamma^4+9\gamma^2\zeta+459\gamma^3\kappa\right)(1+3\cos(2i))J_2R_e^2\right)}{\beta^6}\\
&-\frac{28311552\gamma\mu^8a_0^8\left(-6\gamma\left(10368\gamma^4+18\gamma^2\zeta+351\gamma^3\kappa\right)+3\left(-51435\gamma^4+18\gamma^2\zeta+918\gamma^3\kappa\right)(1+3\cos(2i))J_2R_e^2\right)}{\beta^8}\\
&+\frac{67108864\mu^{10}a_0^{10}\left(-6\gamma\left(13203\gamma^4+18\gamma^2\zeta+351\gamma^3\kappa\right)+3\left(-51435\gamma^4+18\gamma^2\zeta+918\gamma^3\kappa\right)(1+3\cos(2i))J_2R_e^2\right)}{\beta^{10}}\Bigg\}\\
&-\frac{1}{918540\sqrt{2}A_{prop}\sqrt{\frac{\mu}{a_3^3}}a_3^7J_2^6R_e^{12}}\csc^{12}(i)\left[\frac{\mu a_3^3}{\left(-3\gamma+2a_3^2\right)^3}\right]^{\frac{3}{2}}\Big\{18600435(1+3\cos(2i))\sin^{18}(i)J_2^{10}R_e^{20}\\
&+229635\sin^{12}(i)a_3^2J_2^6R_e^{12}\left[-216\gamma^3+3\left(-180\gamma^2+3\gamma\kappa\right)(1+3\cos(2i))J_2R_e^2\right]\\
&-2835\sin^6(i)a_3^4J_2^3R_e^6\left[-216\gamma^3\left(144\gamma^2+3\gamma\kappa\right)+3\left(-25920\gamma^4+9\gamma^2\zeta+432\gamma^3\kappa\right)(1+3\cos(2i))J_2R_e^2\right]\\
&+2268\sin^4(i)a_3^6J_2^2R_e^4\left[-6\gamma\left(5184\gamma^4+9\gamma^2\zeta+108\gamma^3\kappa\right)+3\left(-25920\gamma^4+9\gamma^2\zeta+459\gamma^3\kappa\right)(1+3\cos(2i))J_2R_e^2\right]\\
&-432\gamma a_3^8\left[-6\gamma\left(10368\gamma^4+18\gamma^2\zeta+351\gamma^3\kappa\right)+3\left(-51435\gamma^4+18\gamma^2\zeta+918\gamma^3\kappa\right)(1+3\cos(2i))J_2R_e^2\right]\\
&+64a_3^{10}\left[-6\gamma\left(13203\gamma^4+18\gamma^2\zeta+351\gamma^3\kappa\right)+3\left(-51435\gamma^4+18\gamma^2\zeta+918\gamma^3\kappa\right)(1+3\cos(2i))J_2R_e^2\right]\Big\}\\
&+\left\{\sqrt{\frac{\mu}{\left(-\frac{3\beta\gamma}{8\mu a_0}+\frac{4\mu a_0}{\beta}\right)^3}}\left[1+\frac{3\left(1-\frac{3\sin^2(i)}{2}\right)J_2R_e^2}{2\left(-\frac{3\beta\gamma}{8\mu a_0}+\frac{4\mu a_0}{\beta}\right)^2}\right]\right.
\end{aligned}
$$

$$+\frac{3\left(2-\frac{5\sin^2(i)}{2}\right)\sqrt{\frac{\mu}{\left(-\frac{3\beta\gamma}{8\mu a_0}+\frac{4\mu a_0}{\beta}\right)^3}}J_2R_e^2\left[1+\frac{3\left(1-\frac{3\sin^2(i)}{2}\right)J_2R_e^2}{2\left(-\frac{3\beta\gamma}{8\mu a_0}+\frac{4\mu a_0}{\beta}\right)^2}\right]}{2\left(-\frac{3\beta\gamma}{8\mu a_0}+\frac{4\mu a_0}{\beta}\right)^2}\Bigg\}\Bigg[-\frac{-\frac{9\gamma\sqrt{\mu}}{10a_0^{5/2}}+\frac{2\sqrt{\mu}}{\sqrt{a_0}}+\frac{9\gamma\sqrt{\mu}}{320\left(\frac{\mu a_0}{\beta}\right)^{5/2}}-\frac{\sqrt{\mu}}{\sqrt{\frac{\mu a_0}{\beta}}}+\frac{3\sqrt{\mu}J_2R_e^2}{5a_0^{5/2}}-\frac{3\sqrt{\mu}J_2R_e^2}{160\left(\frac{\mu a_0}{\beta}\right)^{5/2}}}{2A_{prop}}$$

$$+\frac{-\frac{9\gamma\sqrt{\mu}}{320\left(\frac{\mu a_0}{\beta}\right)^{5/2}}+\frac{\sqrt{\mu}}{\sqrt{\frac{\mu a_0}{\beta}}}+\frac{9\gamma\sqrt{\mu}}{10a_3^{5/2}}-\frac{2\sqrt{\mu}}{\sqrt{a_3}}+\frac{3\sqrt{\mu}J_2R_e^2}{160\left(\frac{\mu a_0}{\beta}\right)^{5/2}}-\frac{3\sqrt{\mu}J_2R_e^2}{5a_3^{5/2}}}{2A_{prop}}+t_t\Bigg]$$

$$u_{ref}=\Bigg\{\sqrt{\frac{\mu}{\left(-\frac{3\gamma}{2a_{\text{ref}}}+a_{\text{ref}}\right)^3}}\left[1+\frac{3\left(1-\frac{3\sin^2(i)}{2}\right)J_2R_e^2}{2\left(-\frac{3\gamma}{2a_{\text{ref}}}+a_{\text{ref}}\right)^2}\right]$$
$$+\frac{3}{2\left(-\frac{3\gamma}{2a_{\text{ref}}}+a_{\text{ref}}\right)^2}\left(2-\frac{5\sin^2(i)}{2}\right)\sqrt{\frac{\mu}{\left(-\frac{3\gamma}{2a_{\text{ref}}}+a_{\text{ref}}\right)^3}}J_2R_e^2\left[1+\frac{3\left(1-\frac{3\sin^2(i)}{2}\right)J_2R_e^2}{2\left(-\frac{3\gamma}{2a_{\text{ref}}}+a_{\text{ref}}\right)^2}\right]\Bigg\}t_t$$

where

$$\gamma=J_2R_e^2\sin^2(i)$$

$$\zeta=72J_2^2R_e^4\sin^4(i)+9J_2^2R_e^4\left(7\sin^2(i)-2\right)\left(9\sin^2(i)-4\right)$$

$$\kappa = 3J_2R_e^2\left(7\sin^2(i) - 2\right) + 3J_2R_e^2\left(9\sin^2(i) - 4\right)$$

and, for the case where the satellite altitude is lowered in phase 1,

$$\beta = a_0\left(\sqrt{\frac{\mu}{a_3}} + \Delta \mathrm{V}_{alt}\right)\left(2\sqrt{\frac{\mu}{a_0}} + \sqrt{\frac{\mu}{a_3}} + \Delta \mathrm{V}_{alt}\right) + \mu$$

while for the case in which the satellite altitude is raised in phase 1

$$\beta = a_0\left(\sqrt{\frac{\mu}{a_3}} - \Delta \mathrm{V}_{alt}\right)\left(2\sqrt{\frac{\mu}{a_0}} + \sqrt{\frac{\mu}{a_3}} - \Delta \mathrm{V}_{alt}\right) + \mu.$$

Appendix C

Comparison with Numerical Simulation: Integrating Over Osculating Semi-major Axis

The results produced by applying the general perturbation solution integrated over the osculating semi-major axis to the scenario described in Chapter 4 are here compared to the results produced by numerical simulations. A comparison is made to three numerical simulations, as in Chapter 4; first a comparison is made to the numerical simulation including J_2 perturbations only, secondly a comparison is made with a simulation including J_2 perturbations and atmospheric drag, and finally a comparison is made to a simulation with an 18th order tesseral model and atmospheric drag included.

C.1 Non-manoeuvring Satellite

For a non-manoeuvring satellite (i.e. $\Delta V_{alt} = 0$ m/s) the distance from the sub-satellite point to Los Angeles is shown in Figure C.1 for a 16-day period as calculated by the general perturbation method integrated over the osculating semi-major axis. The horizontal line is drawn at half the swath width, taken to be 100 km, indicating the distance at which the POI will be visible to the satellite, assuming a conical beam. This solution assumes that the satellite maintains a constant altitude over the time considered

by performing atmospheric drag compensation manoeuvres. This was calculated to require 3.22 m/s ΔV_2. The times of each of the target flyovers and the distance of the SSP from the POI at that time as calculated by the general perturbation solution, and each of the numerical simulations, are given in Tables C.1–C.3.

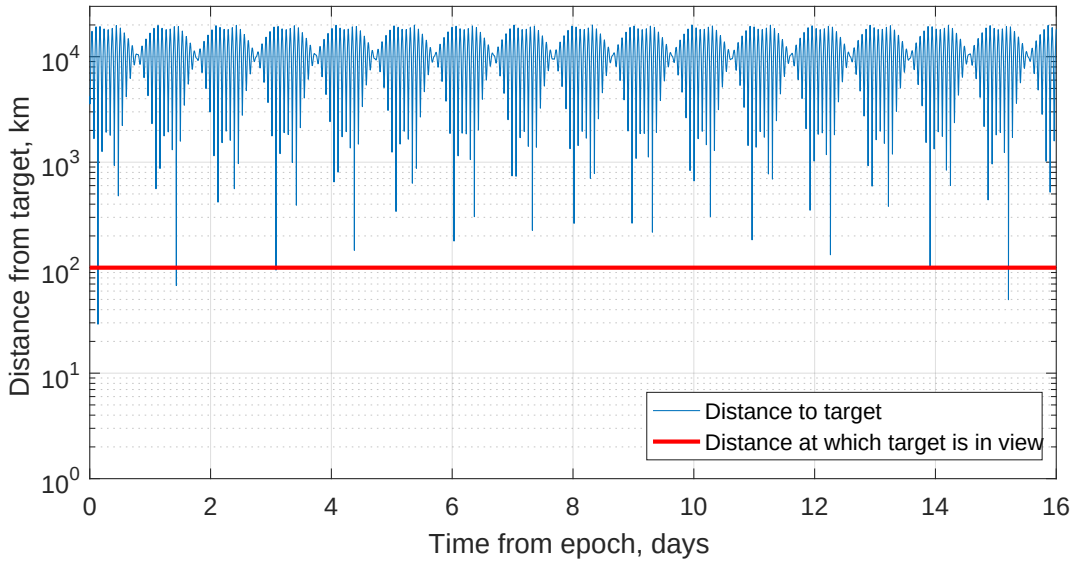

Figure C.1: Distance from sub-satellite point to point of interest plotted as a function of total time for a non-manoeuvring satellite as calculated by the general perturbation method integrated over the osculating semi-major axis.

Considering the results in Tables C.1, C.2 and C.3, the general perturbation solution integrated over the osculating semi-major axis agrees closely with the results produced by the numerical simulations. The greatest difference in flyover time identified between the general perturbation and numerical models is less than 5 sec and the largest difference in distance to target at flyover is approximately 16 km. As was the case using the general perturbation solution integrated over the mean semi-major axis, the general perturbation integrated over the osculating semi-major axis misses a pass at 3.083 days identified by the three numerical solutions, whilst identifying a pass at 13.91 days that is not identified by the three numerical simulations.

Table C.1: Comparison of flyover times for non-manoeuvring satellite calculated by the general perturbation method integrated over the osculating semi-major axis versus numerically including only central body effects to J_2.

	Gen. Perturbation		Numerical		Difference	
Viewing Instance	Time from epoch, days	Distance to target, km	Time from epoch, days	Distance to target, km	Time from epoch, sec	Distance to target, km
1	0.136	20.52	0.136	29.11	4.76	-8.58
2	1.433	55.24	1.433	67.61	-0.47	-12.37
3	—	—	3.083	94.84	—	—
4	13.912	86.98	—	—	—	—
5	15.209	52.84	15.209	49.68	-1.77	3.16

Table C.2: Comparison of flyover times for non-manoeuvring satellite calculated by the general perturbation method integrated over the osculating semi-major axis versus numerically with the inclusion of central body effects to J_2 and atmospheric drag.

	Gen. Perturbation		Numerical		Difference	
Viewing Instance	Time from epoch, days	Distance to target, km	Time from epoch, days	Distance to target, km	Time from epoch, sec	Distance to target, km
1	0.136	20.52	0.136	29.11	4.76	-8.59
2	1.433	55.24	1.433	67.57	-0.48	-12.34
3	—	—	3.083	94.97	—	—
4	13.912	86.98	—	—	—	—
5	15.209	52.84	15.209	47.97	-3.69	4.87

Table C.3: Comparison of flyover times for non-manoeuvring satellite calculated by the general perturbation method integrated over the osculating semi-major axis versus numerically with the inclusion of perturbation due to atmospheric drag and an 18th order tesseral model.

	Gen. Perturbation		Numerical		Difference	
Viewing Instance	Time from epoch, days	Distance to target, km	Time from epoch, days	Distance to target, km	Time from epoch, sec	Distance to target, km
1	0.136	20.52	0.136	10.53	1.47	9.98
2	1.433	55.24	1.433	70.85	1.35	-16.2
3	—	—	3.083	95.93	—	—
4	13.912	86.98	—	—	—	—
5	15.209	52.84	15.209	47.22	3.22	5.61

Figures C.2, C.3, and C.4 show the haversine distance between the sub-satellite points as calculated by the general perturbation solution integrated over the osculating semi-major axis and the three numerical solutions over the same 16-day period as in Figure C.1. These results follow the same trends as when considering the general perturbation solution integrated over the mean semi-major axis as discussed in Chapter 4. The largest maximum difference in the 16-day period is approximately 32 km and the mean difference increases slowly from 14–16 km in all cases.

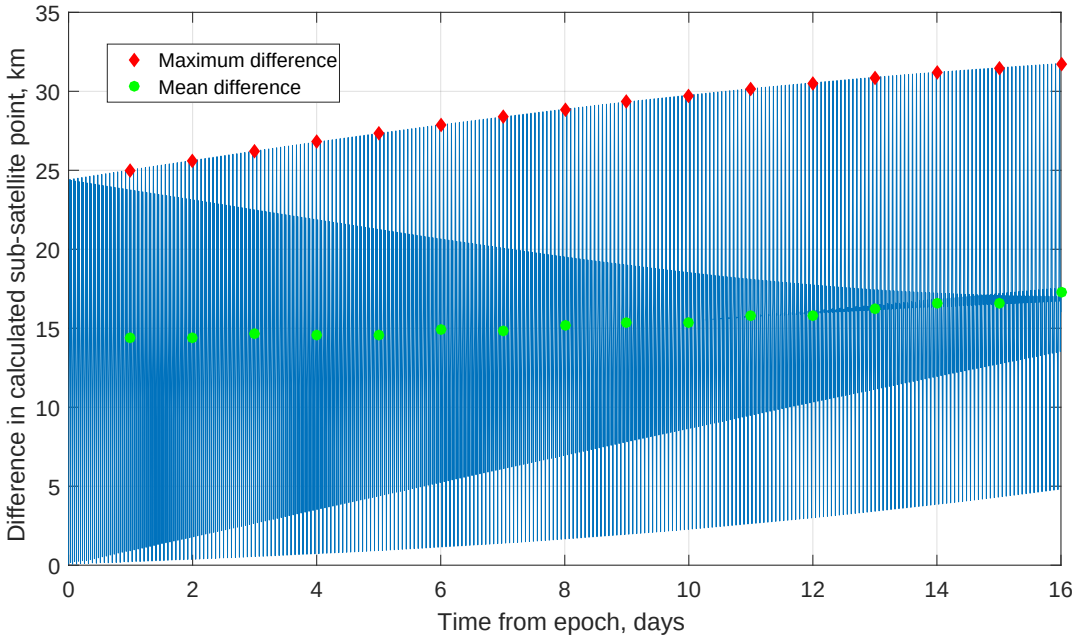

Figure C.2: Haversine distance between sub-satellite points as calculated by the general perturbation solution integrated over the osculating semi-major axis and numerical solution including J_2 for a non-manoeuvring satellite.

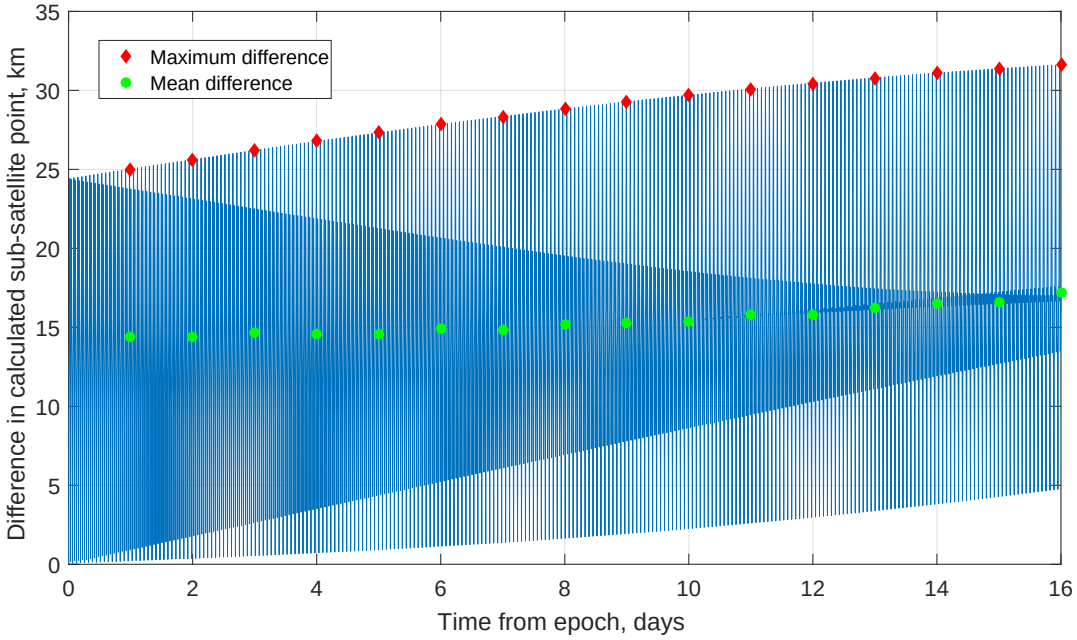

Figure C.3: Haversine distance between sub-satellite points as calculated by the general perturbation solution integrated over the osculating semi-major axis and numerical solution including J_2 and atmospheric drag for a non-manoeuvring satellite.

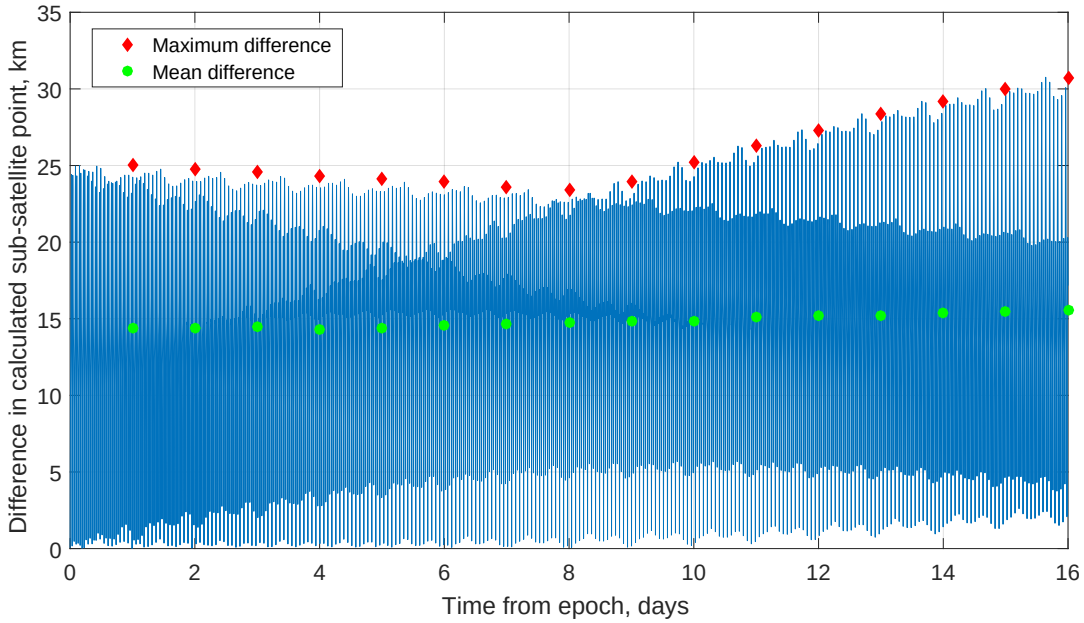

Figure C.4: Haversine distance between sub-satellite points as calculated by the general perturbation solution integrated over the osculating semi-major axis and numerical solution including atmospheric drag and 18th order tesseral model for a non-manoeuvring satellite.

C.2 Manoeuvring Satellite

The general perturbation method integrated over the osculating semi-major axis is now used to calculate the time required to flyover the target when the satellite is manoeuvred using a given ΔV_{alt}. As in Chapter 4, the altitude-lowering manoeuvre will begin 1.433 days from epoch and use 30 m/s ΔV_{alt}. For such a manoeuvre, the general perturbation solution integrated over the osculating semi-major axis identifies three possible manoeuvres in a 13-day period that would end with the satellite in view of the target. These are shown in Table C.4 with the corresponding distance from the SSP to the POI at closest approach. The shortest possible flyover time using 30 m/s is found to be 5.06 days from epoch.

A comparison is then made with the three numerical simulations as described in Chapter 4. The closest pass found by the numerical solution including only J_2 occurs just 1.29 seconds later than predicted by the general perturbation method integrated over the osculating semi-major axis, and the distance from the SSP to the POI at this time is found to be 67.17 km, which is a difference of 13.3 km. The numerical simulation

including atmospheric drag as well as J_2 identifies the closest pass as occurring 37 seconds earlier than predicted by the general perturbation solution integrated over the osculating semi-major axis. The distance from the SSP to the target at this time is found to be 57.67 km, which is a difference of 3.8 km. If atmospheric drag compensation is performed during phase 1 and phase 3 in addition to the coast phases, the predicted flyover occurs just 1.29 seconds after it is predicted by the general perturbation solution integrated over the osculating semi-major axis, at a distance of 67.15 km from the POI, giving a difference of 13.28 km. The numerical simulation with an 18th order tesseral model and atmospheric drag included predicts the closest pass to be almost 39 seconds earlier than predicted by the general perturbation solution integrated over the osculating semi-major axis. The distance from the SSP to the target at this time is found to be 56.34 km; a difference of 2.5 km. If atmospheric drag compensation is performed during the lowering and raising manoeuvres in addition to the coasting phases, the predicted flyover occurs just 0.16 seconds after it is predicted by the general perturbation solution integrated over the osculating semi-major axis, at a distance of 65.98 km from the POI, giving a difference of 12.11 km. These results are summarised in Table C.5.

Table C.4: Flyover times for manoeuvring satellite with 30 m/s ΔV_{alt} calculated by the general perturbation integrated over the osculating semi-major axis.

Possible Flyover Instance	Time from epoch, days	Manoeuvre time, days	Distance from SSP to POI, km
1	5.06	3.62	53.87
2	8.32	6.88	27.20
3	11.94	10.50	59.88

Table C.5: Comparison of flyover times for manoeuvring satellite calculated by the general perturbation method integrated over the osculating semi-major axis versus numerically.

	Time from epoch, days	Distance to target, km	Difference in time, sec	Difference in distance, km
General perturbation method	5.06	53.87	—	—
Numerical: J_2	5.06	67.17	1.29	13.3
Numerical: J_2 and atmospheric drag	5.06	57.67	-36.87	3.8
Numerical: J_2 and atmospheric drag w/ compensation during altitude change	5.06	67.15	1.29	13.28
Numerical: 18th order tesseral and atmospheric drag	5.06	56.34	-38.68	2.5
Numerical: 18th order tesseral and atmospheric drag w/ compensation during altitude change	5.06	65.98	0.16	12.11

Appendix D

Fire Response Target Regions

Figure D.1: Cairngorms National Park region of interest [104].

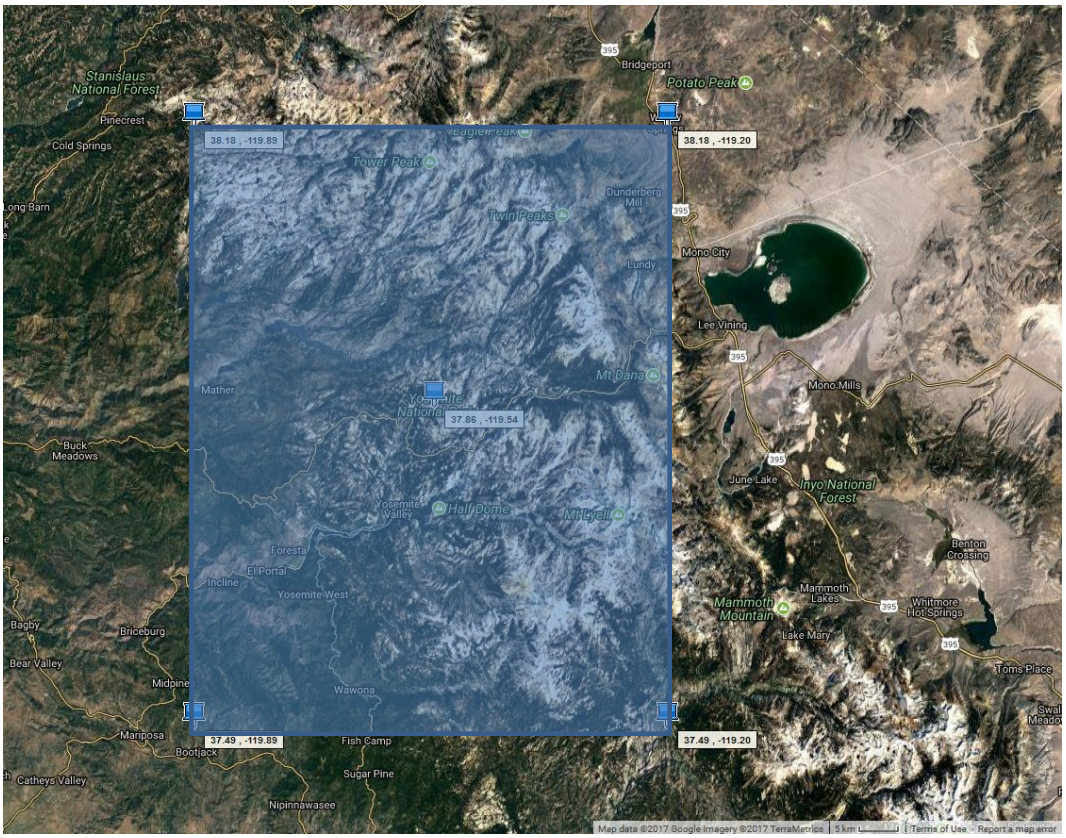

Figure D.2: Yosemite National Park region of interest [104].

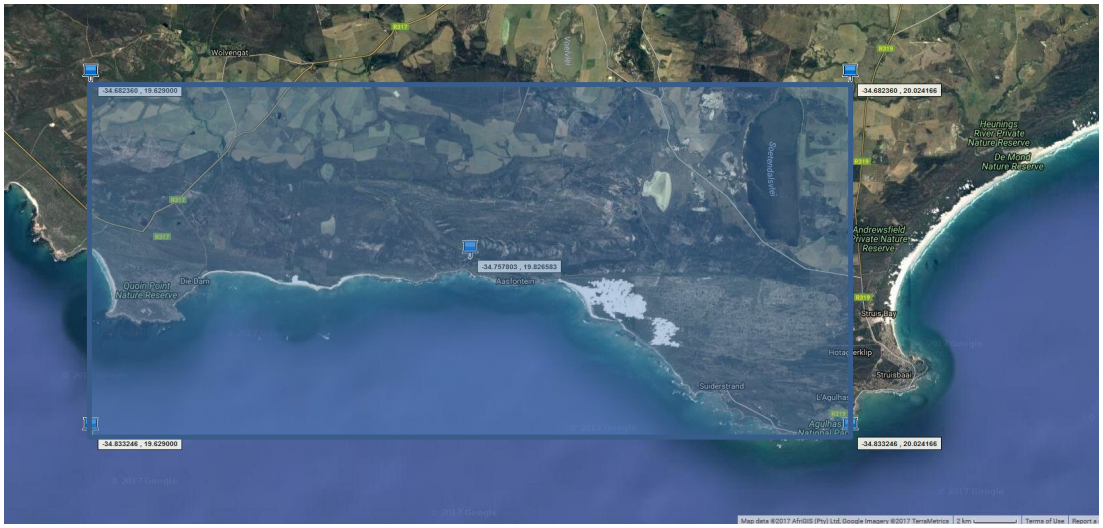

Figure D.3: Agulhas National Park region of interest [104].

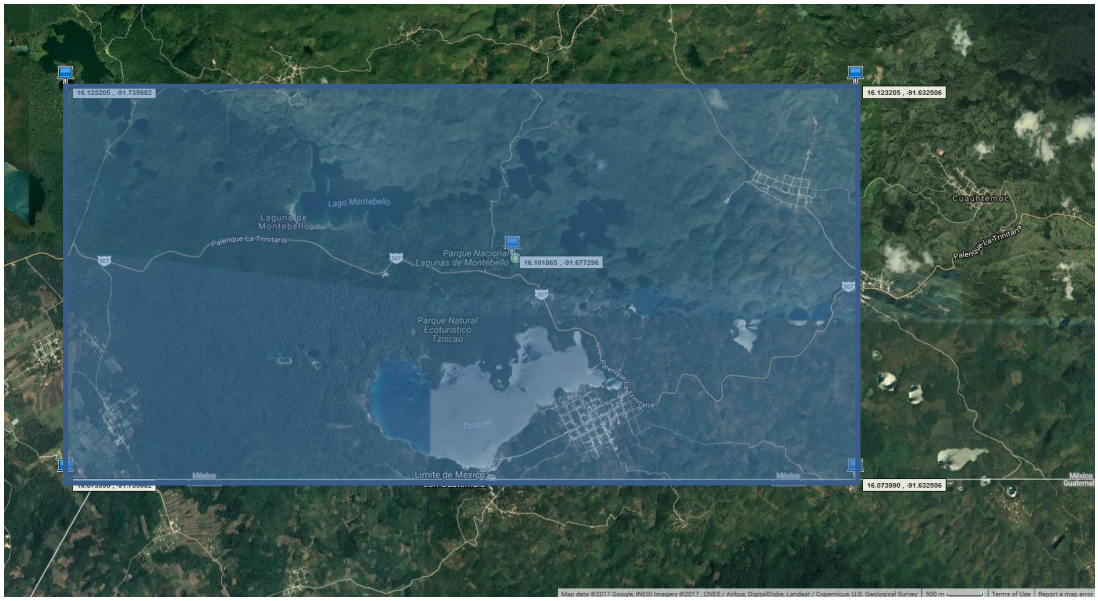

Figure D.4: Lagunas de Montebello National Park region of interest [104].

Appendix E

Utility Plots for Non-Weighted and Weighted Targeting of the Cairngorms

E.1 Non-Weighted

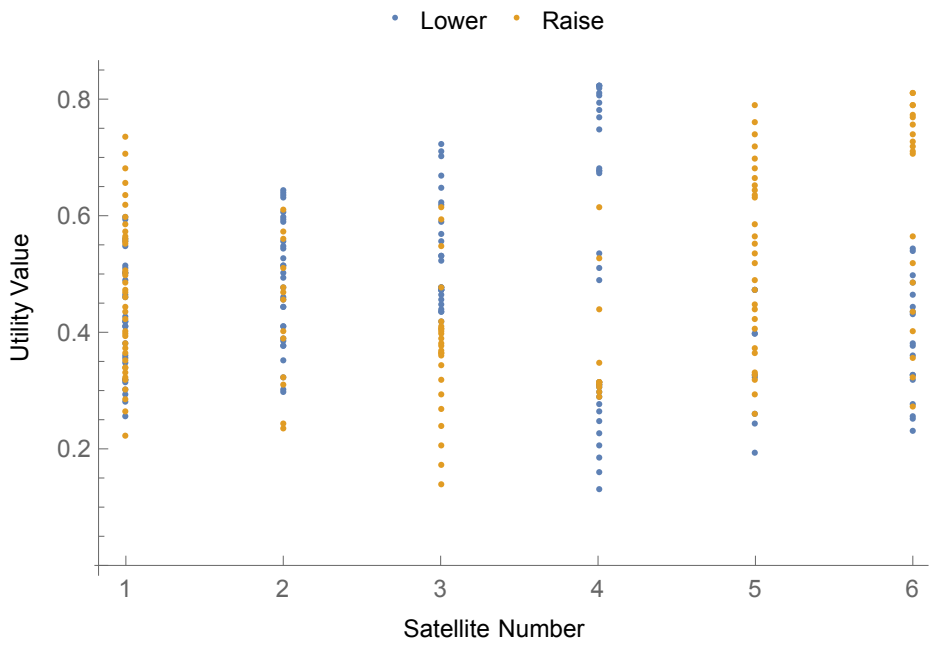

Figure E.1: Utility of manoeuvre versus satellite number for orbit plane 1 for upwards pass over the Cairngorms for the unweighted case. Blue dots are satellite-lowering manoeuvres. Orange dots are satellite-raising manoeuvres.

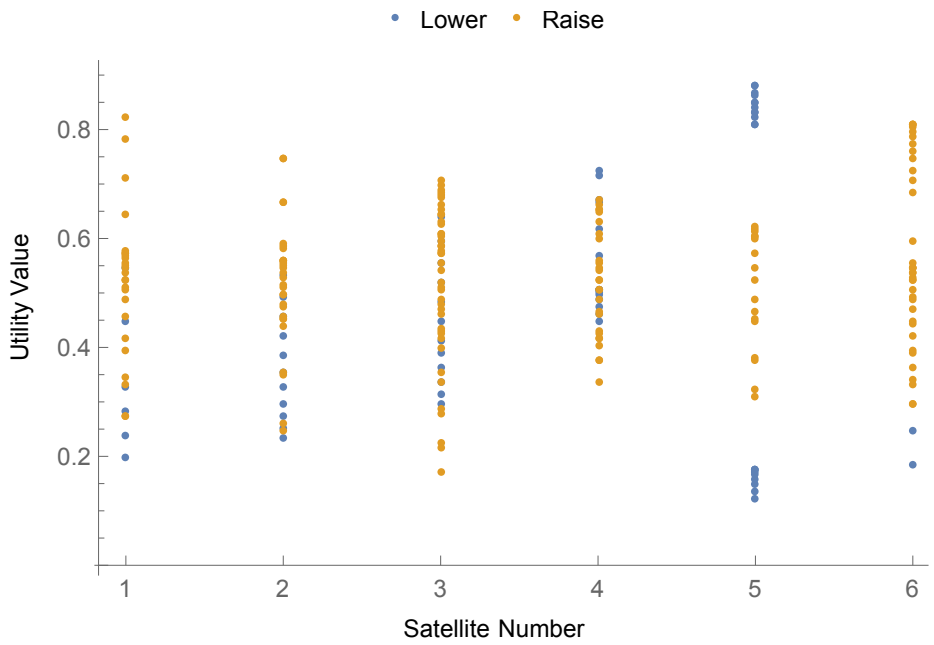

Figure E.2: Utility of manoeuvre versus satellite number for orbit plane 1 for downwards pass over the Cairngorms for the unweighted case. Blue dots are satellite-lowering manoeuvres. Orange dots are satellite-raising manoeuvres.

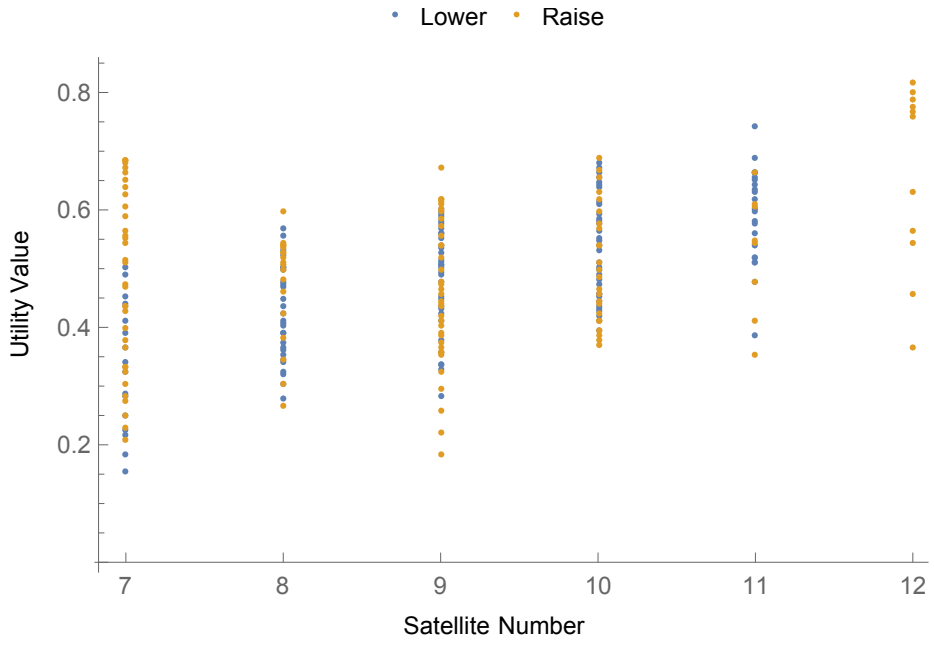

Figure E.3: Utility of manoeuvre versus satellite number for orbit plane 2 for upwards pass over the Cairngorms for the unweighted case. Blue dots are satellite-lowering manoeuvres. Orange dots are satellite-raising manoeuvres.

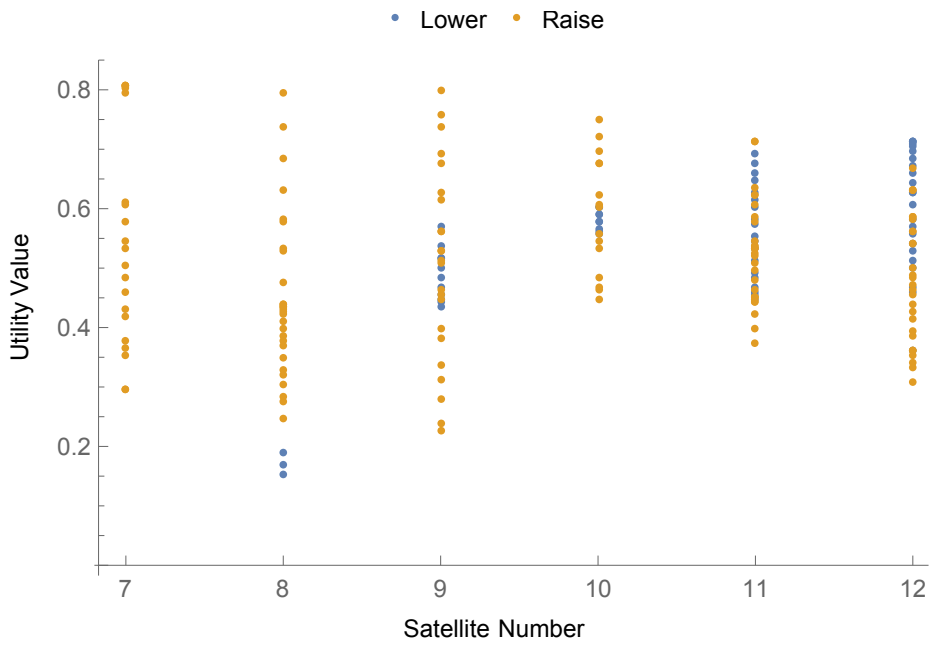

Figure E.4: Utility of manoeuvre versus satellite number for orbit plane 2 for downwards pass over the Cairngorms for the unweighted case. Blue dots are satellite-lowering manoeuvres. Orange dots are satellite-raising manoeuvres.

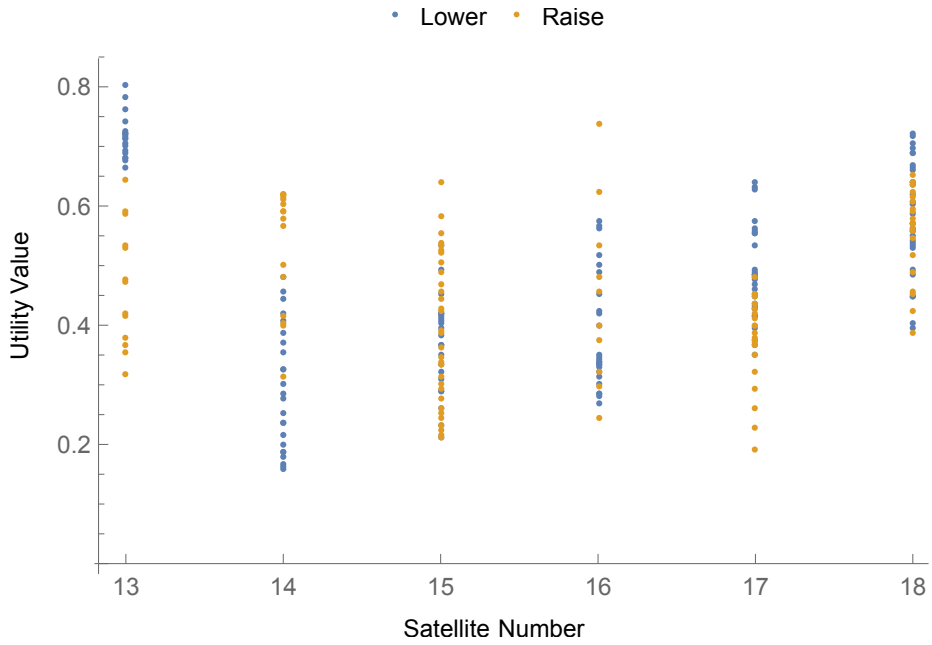

Figure E.5: Utility of manoeuvre versus satellite number for orbit plane 3 for upwards pass over the Cairngorms for the unweighted case. Blue dots are satellite-lowering manoeuvres. Orange dots are satellite-raising manoeuvres.

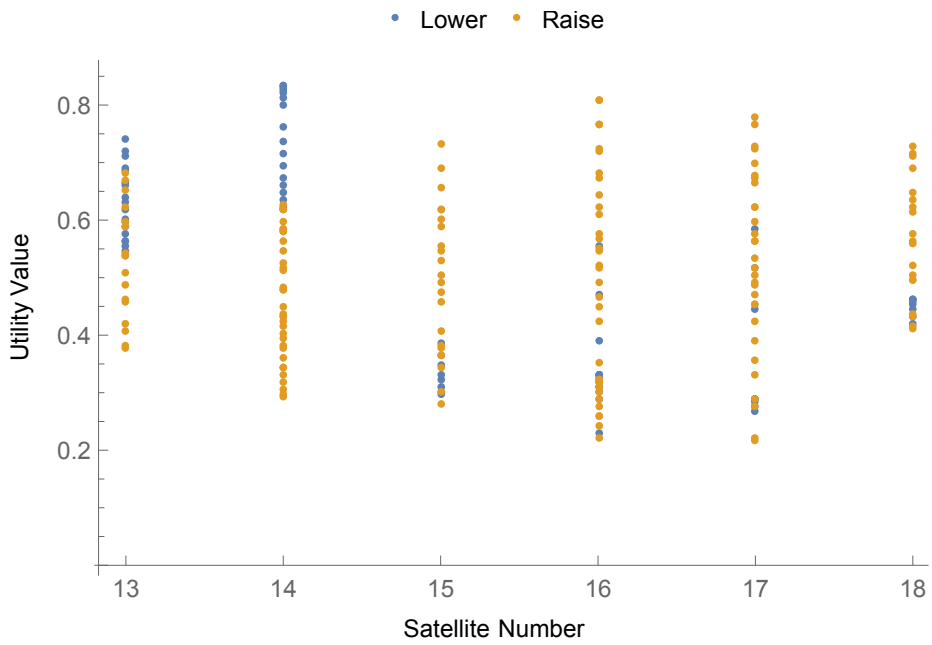

Figure E.6: Utility of manoeuvre versus satellite number for orbit plane 3 for downwards pass over the Cairngorms for the unweighted case. Blue dots are satellite-lowering manoeuvres. Orange dots are satellite-raising manoeuvres.

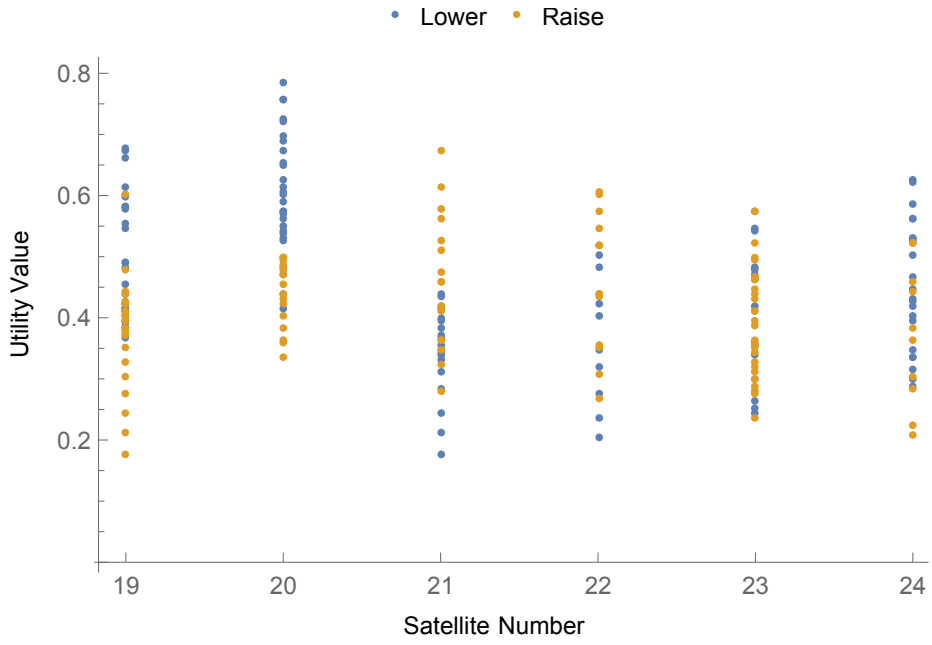

Figure E.7: Utility of manoeuvre versus satellite number for orbit plane 4 for upwards pass over the Cairngorms for the unweighted case. Blue dots are satellite-lowering manoeuvres. Orange dots are satellite-raising manoeuvres.

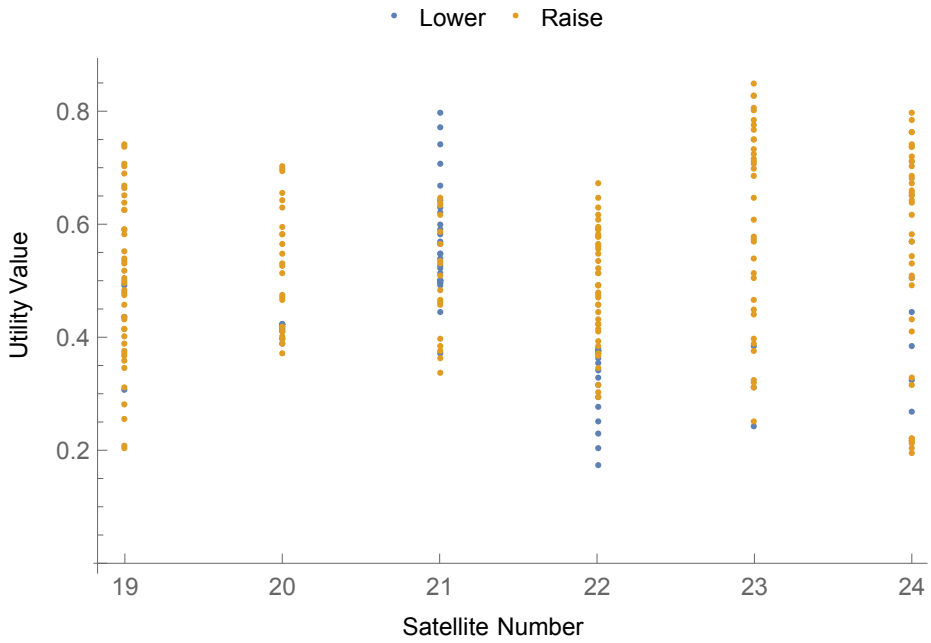

Figure E.8: Utility of manoeuvre versus satellite number for orbit plane 4 for downwards pass over the Cairngorms for the unweighted case. Blue dots are satellite-lowering manoeuvres. Orange dots are satellite-raising manoeuvres.

E.2 Weighted

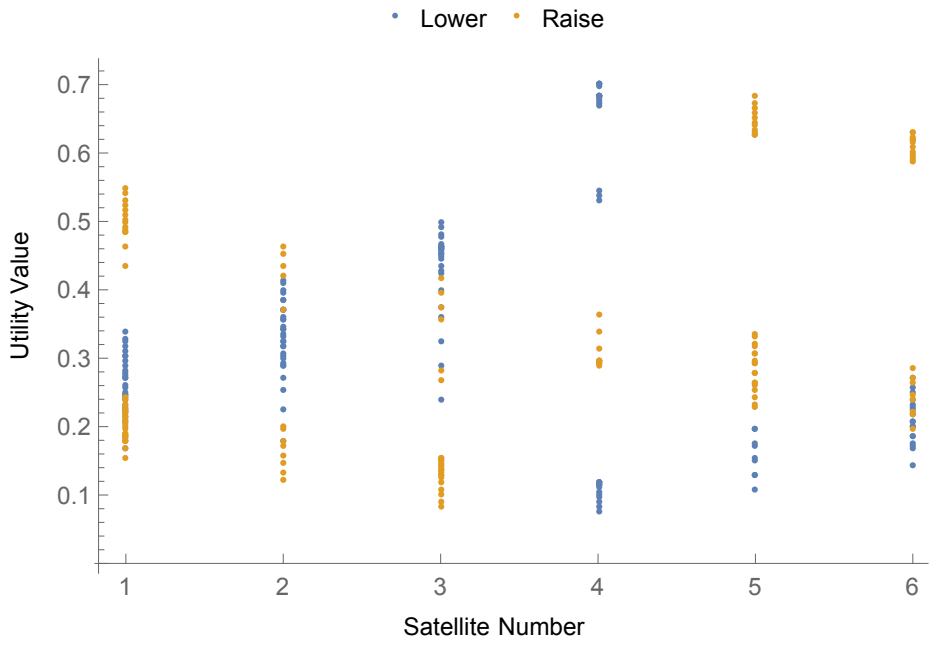

Figure E.9: Utility of manoeuvre versus satellite number for plane 1 for upwards pass over the Cairngorms for the weighted case.Blue dots are satellite-lowering manoeuvres. Orange dots are satellite-raising manoeuvres.

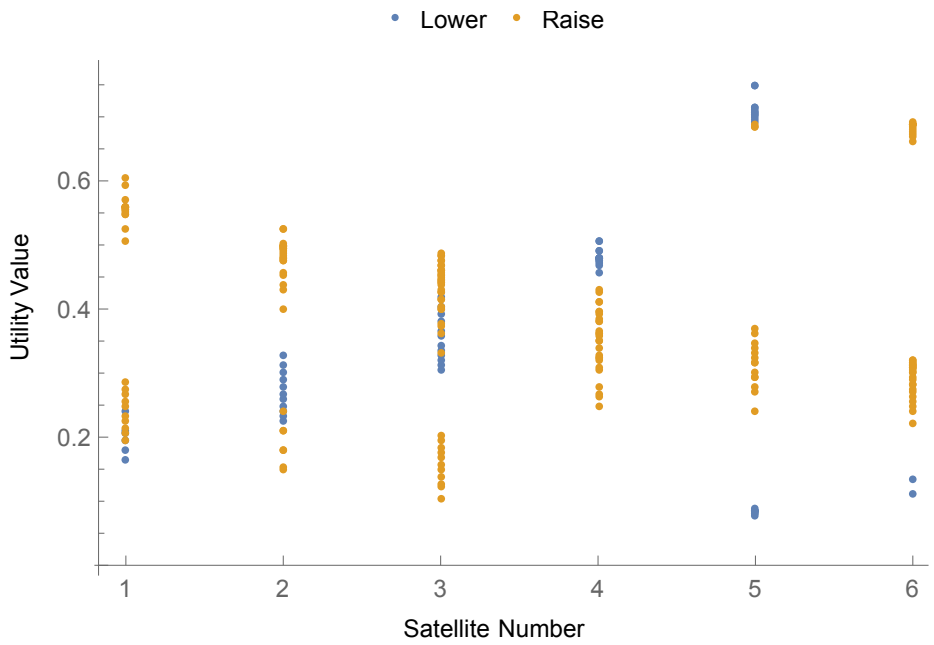

Figure E.10: Utility of manoeuvre versus satellite number for plane 1 for downwards pass over the Cairngorms for the weighted case. Blue dots are satellite-lowering manoeuvres. Orange dots are satellite-raising manoeuvres.

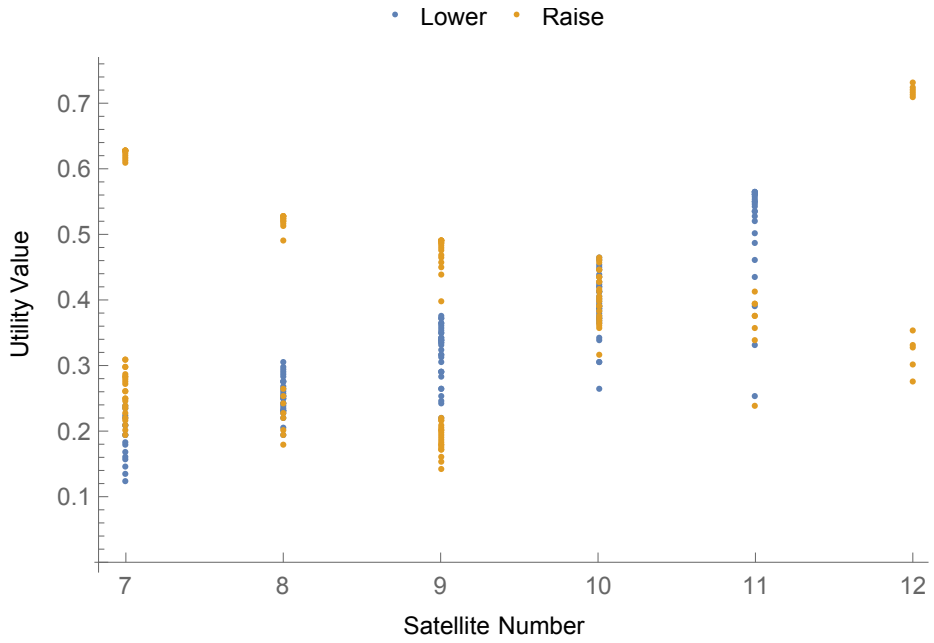

Figure E.11: Utility of manoeuvre versus satellite number for plane 2 for upwards pass over the Cairngorms for the weighted case. Blue dots are satellite-lowering manoeuvres. Orange dots are satellite-raising manoeuvres.

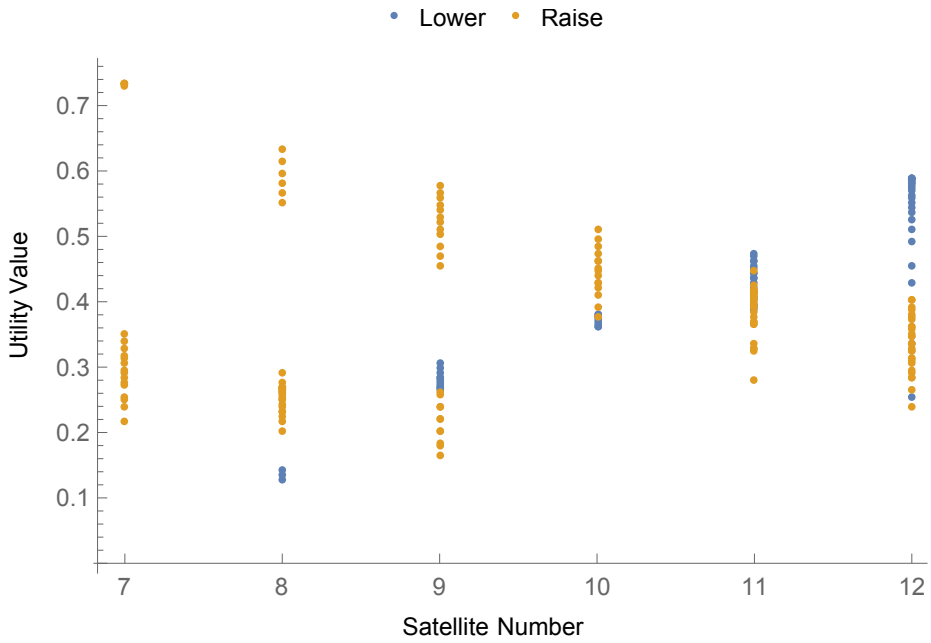

Figure E.12: Utility of manoeuvre versus satellite number for plane 2 for downwards pass over the Cairngorms for the weighted case. Blue dots are satellite-lowering manoeuvres. Orange dots are satellite-raising manoeuvres.

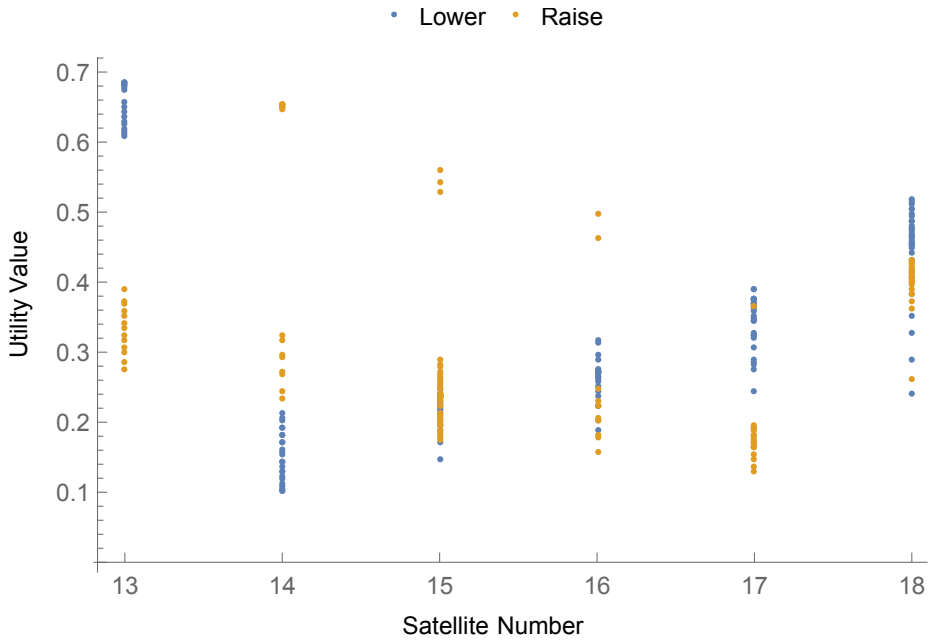

Figure E.13: Utility of manoeuvre versus satellite number for plane 3 for upwards pass over the Cairngorms for the weighted case. Blue dots are satellite-lowering manoeuvres. Orange dots are satellite-raising manoeuvres.

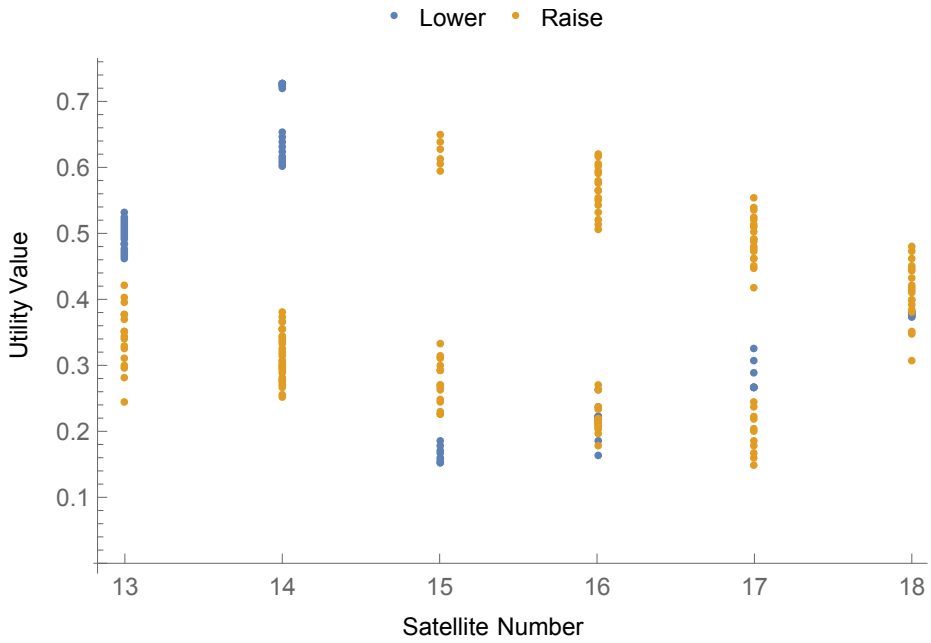

Figure E.14: Utility of manoeuvre versus satellite number for plane 3 for downwards pass over the Cairngorms for the weighted case. Blue dots are satellite-lowering manoeuvres. Orange dots are satellite-raising manoeuvres.

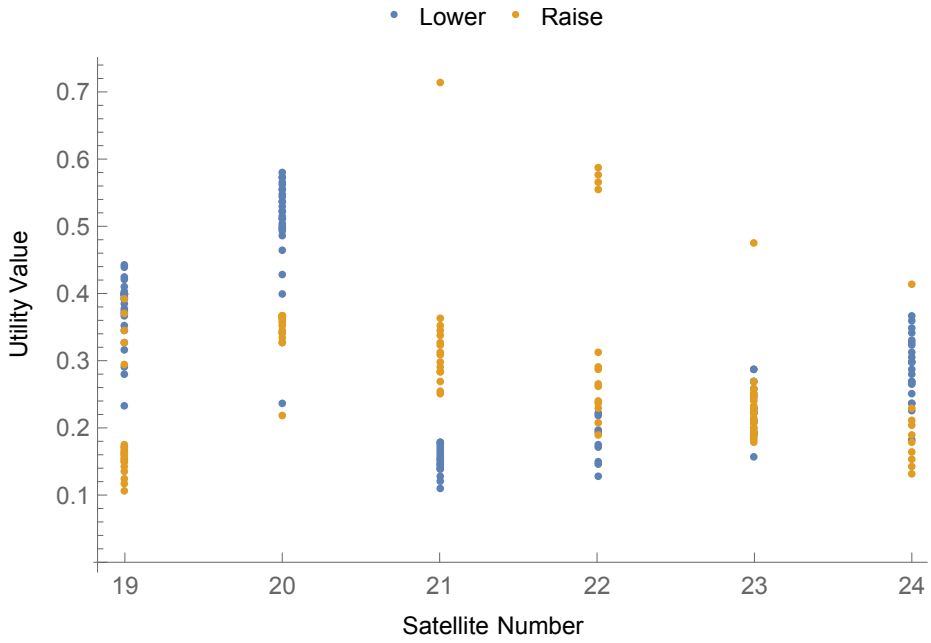

Figure E.15: Utility of manoeuvre versus satellite number for plane 4 for upwards pass over the Cairngorms for the weighted case. Blue dots are satellite-lowering manoeuvres. Orange dots are satellite-raising manoeuvres.

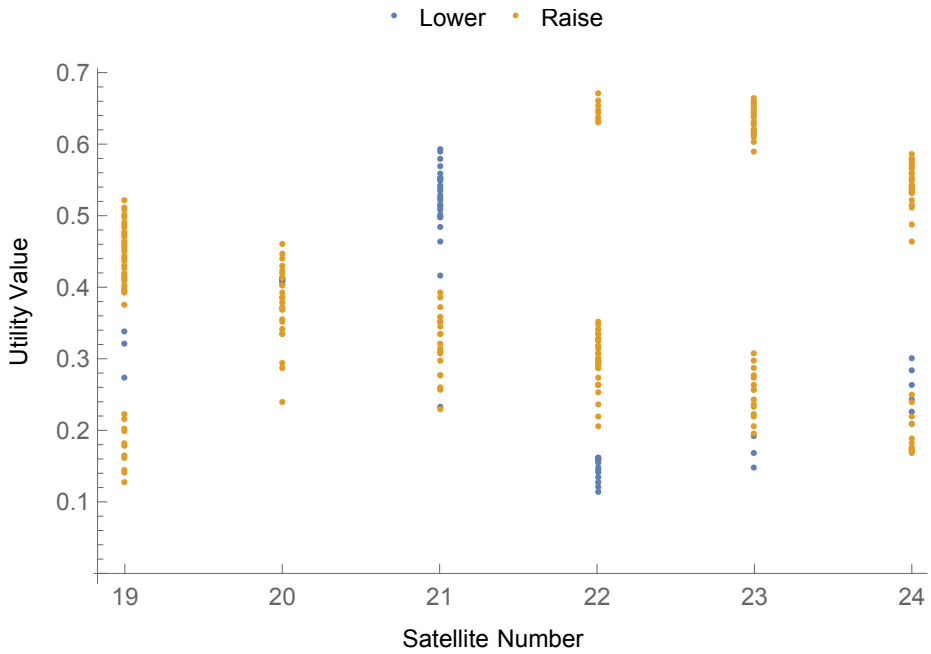

Figure E.16: Utility of manoeuvre versus satellite number for plane 4 for downwards pass over the Cairngorms for the weighted case. Blue dots are satellite-lowering manoeuvres. Orange dots are satellite-raising manoeuvres.

Appendix F

Plots of Numerical Simulation of Manoeuvres to Target the Cairngorms

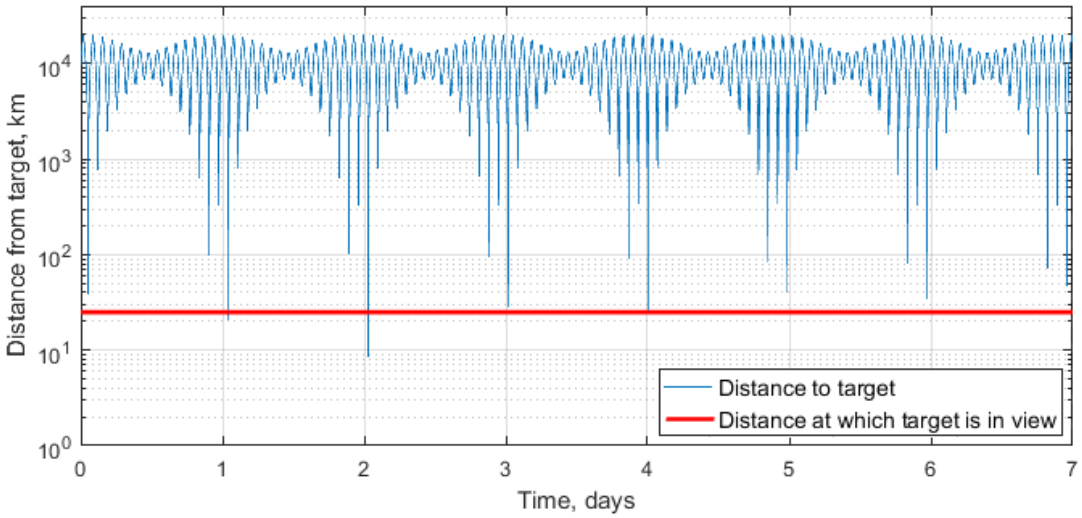

Figure F.1: Distance from sub-satellite point to centre of the Cairgorms plotted as a function of total time for Satellite 4 using numerical solution.

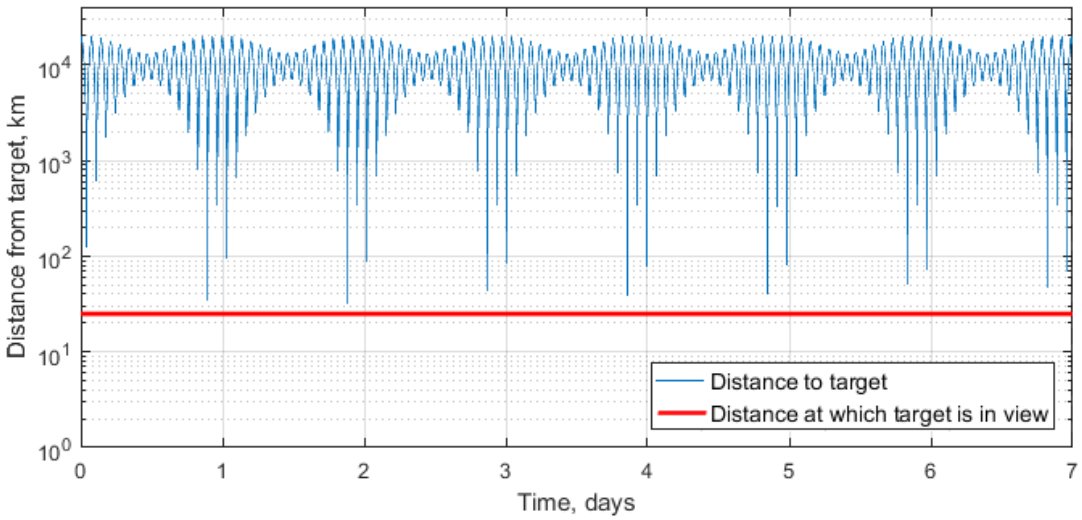

Figure F.2: Distance from sub-satellite point to centre of the Cairgorms plotted as a function of total time for Satellite 5 using numerical solution.

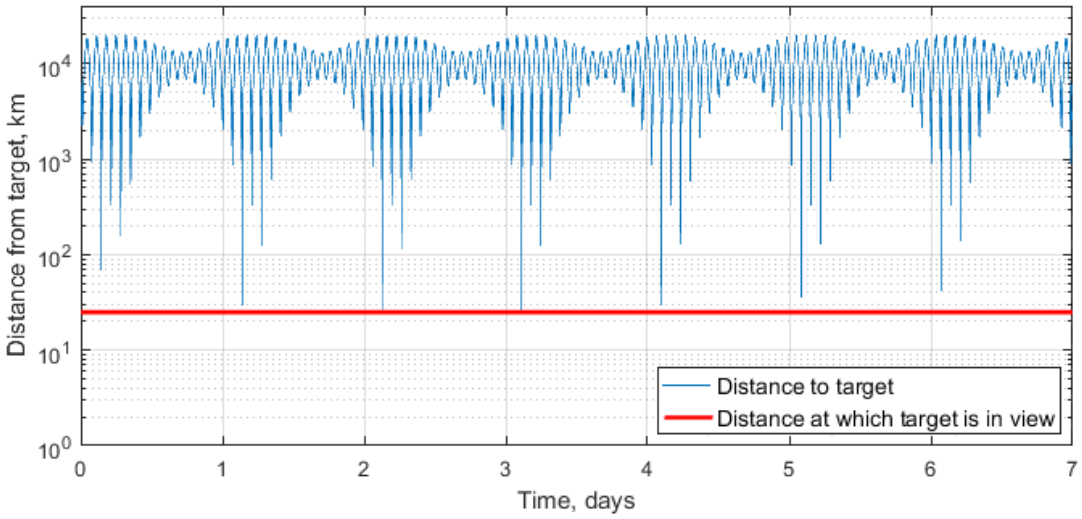

Figure F.3: Distance from sub-satellite point to centre of the Cairgorms plotted as a function of total time for Satellite 7 using numerical solution.

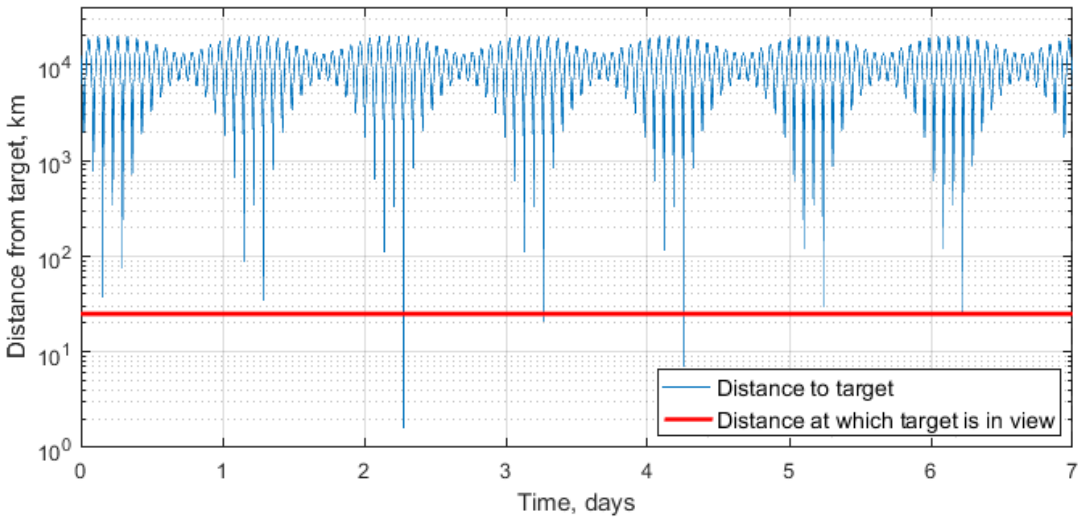

Figure F.4: Distance from sub-satellite point to centre of the Cairgorms plotted as a function of total time for Satellite 12 using numerical solution.

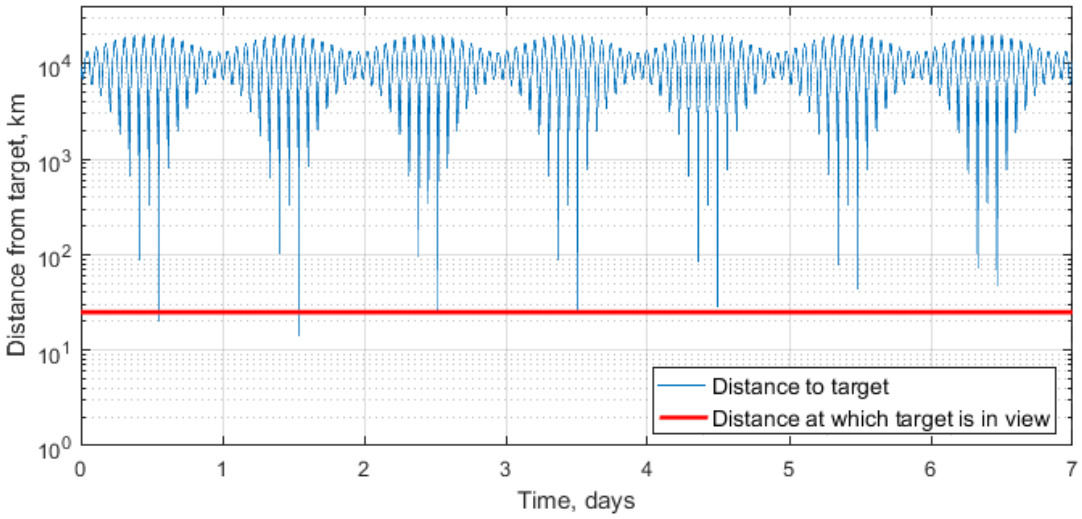

Figure F.5: Distance from sub-satellite point to centre of the Cairgorms plotted as a function of total time for Satellite 13 using numerical solution.

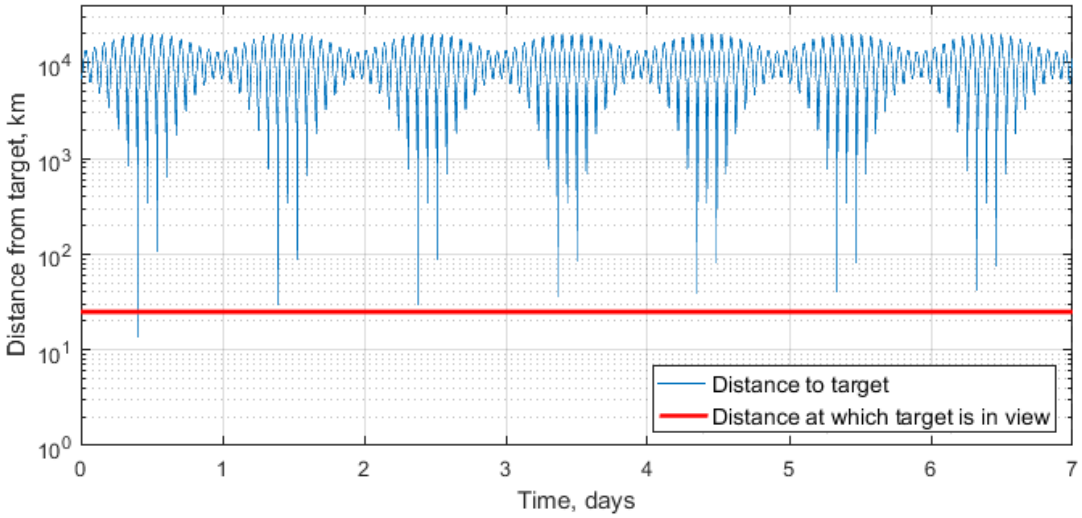

Figure F.6: Distance from sub-satellite point to centre of the Cairgorms plotted as a function of total time for Satellite 14 using numerical solution.

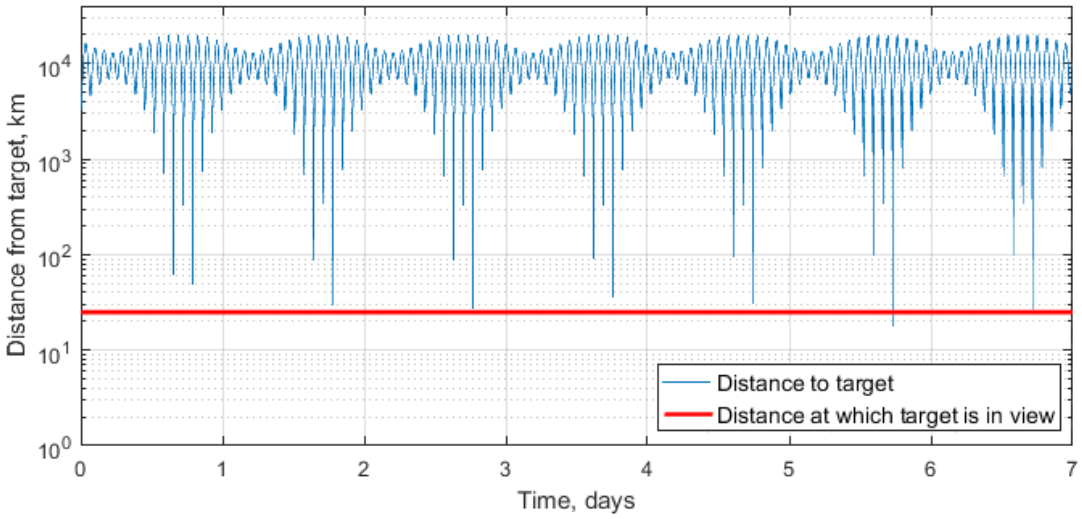

Figure F.7: Distance from sub-satellite point to centre of the Cairgorms plotted as a function of total time for Satellite 21 using numerical solution.

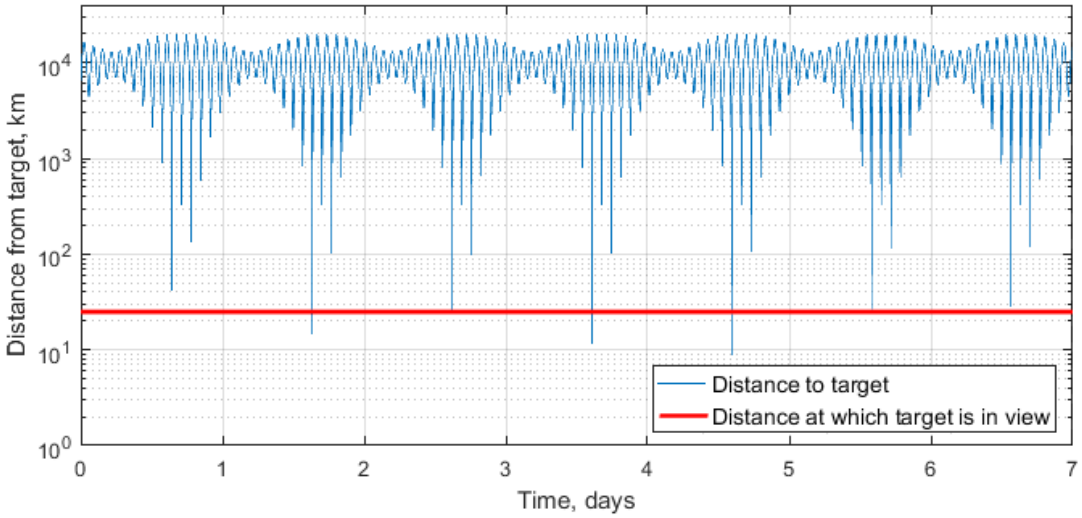

Figure F.8: Distance from sub-satellite point to centre of the Cairgorms plotted as a function of total time for Satellite 22 using numerical solution.

Appendix G

Fire Response Selected Manoeuvre Sequence

Table G.1: Initial positions of fire detection constellation satellites.

		Mean Altitude, km	RAAN, deg	AoL, deg
Orbit Plane 1	Satellite 1	542.857	0	0
	Satellite 2	542.857	0	60
	Satellite 3	542.857	0	120
	Satellite 4	542.857	0	180
	Satellite 5	542.857	0	240
	Satellite 6	542.857	0	300
Orbit Plane 2	Satellite 7	542.857	90	0
	Satellite 8	542.857	90	60
	Satellite 9	542.857	90	120
	Satellite 10	542.857	90	180
	Satellite 11	542.857	90	240
	Satellite 12	542.857	90	300
Orbit Plane 3	Satellite 13	542.857	180	0
	Satellite 14	542.857	180	60
	Satellite 15	542.857	180	120
	Satellite 16	542.857	180	180
	Satellite 17	542.857	180	240
	Satellite 18	542.857	180	300
Orbit Plane 4	Satellite 19	542.857	270	0
	Satellite 20	542.857	270	60
	Satellite 21	542.857	270	120
	Satellite 22	542.857	270	180
	Satellite 23	542.857	270	240
	Satellite 24	542.857	270	300

G.1 Cairngorms National Park

Table G.2: Selected satellite manoeuvres to target the Cairngorms.

		ΔV, m/s	Manoeuvre Time, days	Distance to target, km	Pass type	Manoeuvre Type
Orbit Plane 1	Satellite 4	18.01	2.03	18.80	Downwards	Lower
	Satellite 5	17.01	1.88	9.64	Upwards	Lower
Orbit Plane 2	Satellite 7	19.00	2.13	8.79	Upwards	Raise
	Satellite 12	17.00	2.28	8.07	Downwards	Raise
Orbit Plane 3	Satellite 13	23.01	2.52	13.07	Downwards	Lower
	Satellite 14	21.01	2.38	5.75	Upwards	Lower
Orbit Plane 4	Satellite 21	17.00	1.78	19.92	Downwards	Raise
	Satellite 22	17.02	2.62	18.08	Upwards	Raise

Table G.3: Positions of satellites after manoeuvre to target Cairngorms.

		Mean Altitude, km	RAAN, deg	AoL, deg
Orbit Plane 1	Satellite 1	542.857	350.363	228.300
	Satellite 2	542.857	350.363	288.300
	Satellite 3	542.857	350.363	348.300
	Satellite 4	513.087	350.059	112.888
	Satellite 5	513.087	350.060	172.453
	Satellite 6	542.857	350.363	168.300
Orbit Plane 2	Satellite 7	513.087	80.091	273.386
	Satellite 8	542.857	80.363	288.300
	Satellite 9	542.857	80.363	348.300
	Satellite 10	542.857	80.363	48.300
	Satellite 11	542.857	80.363	108.300
	Satellite 12	513.087	80.098	208.773
Orbit Plane 3	Satellite 13	513.087	170.054	296.403
	Satellite 14	513.087	170.056	354.923
	Satellite 15	542.857	170.363	348.300
	Satellite 16	542.857	170.363	48.300
	Satellite 17	542.857	170.363	108.300
	Satellite 18	542.857	170.363	168.300
Orbit Plane 4	Satellite 19	542.857	260.363	228.300
	Satellite 20	542.857	260.363	288.300
	Satellite 21	513.087	260.069	46.656
	Satellite 22	513.087	260.118	76.245
	Satellite 23	542.857	260.363	108.300
	Satellite 24	542.857	260.363	168.300

Table G.4: Positions of satellites after 7 days in ROM mode targeting Cairngorms.

		Mean Altitude, km	RAAN, deg	AoL, deg
Orbit Plane 1	Satellite 1	542.857	324.127	124.265
	Satellite 2	542.857	324.127	184.265
	Satellite 3	542.857	324.127	244.265
	Satellite 4	513.087	323.424	255.976
	Satellite 5	513.087	323.425	315.541
	Satellite 6	542.857	324.127	64.265
Orbit Plane 2	Satellite 7	513.087	53.456	56.474
	Satellite 8	542.857	54.127	184.265
	Satellite 9	542.857	54.127	244.265
	Satellite 10	542.857	54.127	304.265
	Satellite 11	542.857	54.127	4.265
	Satellite 12	513.087	53.463	351.861
Orbit Plane 3	Satellite 13	513.087	143.419	79.791
	Satellite 14	513.087	143.421	138.011
	Satellite 15	542.857	144.127	244.265
	Satellite 16	542.857	144.127	304.265
	Satellite 17	542.857	144.127	4.265
	Satellite 18	542.857	144.127	64.265
Orbit Plane 4	Satellite 19	542.857	234.127	124.265
	Satellite 20	542.857	234.127	184.265
	Satellite 21	513.087	233.434	189.744
	Satellite 22	513.087	233.483	219.333
	Satellite 23	542.857	234.127	4.265
	Satellite 24	542.857	234.127	64.265

Table G.5: Possible satellite manoeuvres to return to GOM from targeting the Cairngorms. Selected manoeuvres in bold.

		Slot in orbit plane	Manoeuvre Time, days
Orbit Plane 1	Satellite 4	**1**	**2.18**
		2	3.88
	Satellite 5	1	0.49
		2	**2.19**
Orbit Plane 2	Satellite 7	1	12.93
		2	**11.23**
	Satellite 12	**1**	**4.56**
		2	2.86
Orbit Plane 3	Satellite 13	**1**	**12.28**
		2	13.98
	Satellite 14	1	10.62
		2	**12.32**
Orbit Plane 4	Satellite 21	**1**	**2.36**
		2	4.06
	Satellite 22	1	1.52
		2	**3.22**

Table G.6: Positions of satellites after returning to GOM from targeting Cairngorms.

		Mean Altitude, km	RAAN, deg	AoL, deg
Orbit Plane 1	Satellite 1	542.857	277.955	139.261
	Satellite 2	542.857	277.955	199.261
	Satellite 3	542.857	277.955	259.261
	Satellite 4	542.857	277.174	319.261
	Satellite 5	542.857	277.174	19.261
	Satellite 6	542.857	277.955	79.261
Orbit Plane 2	Satellite 7	542.857	6.690	79.261
	Satellite 8	542.857	7.955	199.261
	Satellite 9	542.857	7.955	259.261
	Satellite 10	542.857	7.955	319.261
	Satellite 11	542.857	7.955	19.261
	Satellite 12	542.857	7.077	139.261
Orbit Plane 3	Satellite 13	542.857	96.593	139.261
	Satellite 14	542.857	96.593	199.261
	Satellite 15	542.857	97.955	259.261
	Satellite 16	542.857	97.955	319.261
	Satellite 17	542.857	97.955	19.261
	Satellite 18	542.857	97.955	79.261
Orbit Plane 4	Satellite 19	542.857	187.955	139.261
	Satellite 20	542.857	187.955	199.261
	Satellite 21	542.857	187.174	259.261
	Satellite 22	542.857	187.174	319.261
	Satellite 23	542.857	187.955	19.261
	Satellite 24	542.857	187.955	79.261

G.2 Yosemite National Park

Table G.7: Positions of satellites at detection of fire outbreak in Yosemite.

		Mean Altitude, km	RAAN, deg	AoL, deg
Orbit Plane 1	Satellite 1	542.857	251.719	35.226
	Satellite 2	542.857	251.719	95.226
	Satellite 3	542.857	251.719	155.226
	Satellite 4	542.857	250.938	215.226
	Satellite 5	542.857	250.938	275.226
	Satellite 6	542.857	251.719	335.226
Orbit Plane 2	Satellite 7	542.857	340.454	335.226
	Satellite 8	542.857	341.719	95.226
	Satellite 9	542.857	341.719	155.226
	Satellite 10	542.857	341.719	215.226
	Satellite 11	542.857	341.719	275.226
	Satellite 12	542.857	340.841	35.226
Orbit Plane 3	Satellite 13	542.857	70.357	35.226
	Satellite 14	542.857	70.357	95.226
	Satellite 15	542.857	71.719	155.226
	Satellite 16	542.857	71.719	215.226
	Satellite 17	542.857	71.719	275.226
	Satellite 18	542.857	71.719	335.226
Orbit Plane 4	Satellite 19	542.857	161.719	35.226
	Satellite 20	542.857	161.719	95.226
	Satellite 21	542.857	160.938	155.226
	Satellite 22	542.857	160.938	215.226
	Satellite 23	542.857	161.719	275.226
	Satellite 24	542.857	161.719	335.226

Table G.8: Selected satellite manoeuvres to view Yosemite.

		ΔV, m/s	Manoeuvre Time, days	Distance to target, km	Pass type	Manoeuvre Type
Orbit Plane 1	Satellite 1	25.02	3.11	0.39	Downwards	Lower
	Satellite 2	17.02	2.77	0.68	Upwards	Raise
Orbit Plane 2	Satellite 9	17.01	2.03	18.30	Upwards	Raise
	Satellite 10	33.00	3.36	21.45	Downwards	Raise
Orbit Plane 3	Satellite 16	21.05	3.61	4.70	Downwards	Lower
	Satellite 18	20.04	4.25	2.47	Upwards	Raise
Orbit Plane 4	Satellite 19	19.03	3.51	2.38	Upwards	Raise
	Satellite 20	26.03	4.84	8.28	Downwards	Raise

Table G.9: Positions of satellites after manoeuvre to target Yosemite is completed.

		Mean Altitude, km	RAAN, deg	AoL, deg
Orbit Plane 1	Satellite 1	513.087	233.329	226.818
	Satellite 2	513.087	233.412	235.708
	Satellite 3	542.857	233.575	194.630
	Satellite 4	542.857	232.794	254.630
	Satellite 5	542.857	232.794	314.630
	Satellite 6	542.857	233.575	14.630
Orbit Plane 2	Satellite 7	542.857	322.310	14.630
	Satellite 8	542.857	323.575	134.630
	Satellite 9	513.087	323.369	322.327
	Satellite 10	513.087	323.470	319.199
	Satellite 11	542.857	323.575	314.630
	Satellite 12	542.857	322.697	74.630
Orbit Plane 3	Satellite 13	542.857	52.213	74.630
	Satellite 14	542.857	52.212	134.630
	Satellite 15	542.857	53.575	194.630
	Satellite 16	513.087	53.331	45.692
	Satellite 17	542.857	53.575	314.630
	Satellite 18	513.087	53.510	54.626
Orbit Plane 4	Satellite 19	513.087	143.461	145.357
	Satellite 20	513.087	143.574	134.808
	Satellite 21	542.857	142.794	194.630
	Satellite 22	542.857	142.794	254.630
	Satellite 23	542.857	143.575	314.630
	Satellite 24	542.857	143.575	14.630

Table G.10: Positions of satellites after 7 days in ROM mode targeting Yosemite.

		Mean Altitude, km	RAAN, deg	AoL, deg
Orbit Plane 1	Satellite 1	513.087	206.694	9.906
	Satellite 2	513.087	206.777	18.796
	Satellite 3	542.857	207.339	90.595
	Satellite 4	542.857	206.558	150.595
	Satellite 5	542.857	206.558	210.595
	Satellite 6	542.857	207.339	270.595
Orbit Plane 2	Satellite 7	542.857	296.074	270.595
	Satellite 8	542.857	297.339	30.595
	Satellite 9	513.087	296.734	105.415
	Satellite 10	513.087	296.836	102.287
	Satellite 11	542.857	297.339	210.595
	Satellite 12	542.857	296.461	330.595
Orbit Plane 3	Satellite 13	542.857	25.977	330.595
	Satellite 14	542.857	25.977	30.595
	Satellite 15	542.857	27.339	90.595
	Satellite 16	513.087	26.696	188.780
	Satellite 17	542.857	27.339	210.595
	Satellite 18	513.087	26.875	197.714
Orbit Plane 4	Satellite 19	513.087	116.826	288.445
	Satellite 20	513.087	116.940	277.896
	Satellite 21	542.857	116.558	90.595
	Satellite 22	542.857	116.558	150.595
	Satellite 23	542.857	117.339	210.595
	Satellite 24	542.857	117.339	270.595

G.3 Agulhas National Park

Table G.11: Selected satellite manoeuvres to view Agulhas.

		ΔV, m/s	Manoeuvre Time, days	Distance to target, km	Pass type	Manoeuvre Type
Orbit Plane 1	Satellite 1	14.01	1.88	1.06	Downwards	Raise
	Satellite 6	22.00	2.25	19.72	Upwards	Lower
Orbit Plane 2	Satellite 9	27.05	5.46	3.01	Upwards	Raise
	Satellite 10	15.01	2.13	1.70	Downwards	Raise
Orbit Plane 3	Satellite 15	24.01	2.74	0.14	Upwards	Lower
	Satellite 16	8.04	2.38	0.14	Downwards	Raise
Orbit Plane 4	Satellite 20	8.05	2.62	3.26	Downwards	Raise
	Satellite 24	18.04	3.98	5.25	Upwards	Raise

Table G.12: Possible manoeuvres to return satellites remaining in RGT over Yosemite to GOM for observation of Agulhas. Selected manoeuvres in bold. The italicised solution for Satellite 19 is an invalid solution as the total manoeuvre time would be less than that required to achieve the desired total ΔV and as such is ignored.

		Slot in orbit plane	Manoeuvre Time, days
Orbit Plane 1	Satellite 2	1	11.34
		2	9.64
		3	**7.94**
Orbit Plane 3	Satellite 18	**1**	**7.97**
		2	9.67
		3	13.07
Orbit Plane 4	Satellite 19	**1**	**2.01**
		2	3.71
		3	*0.31*

Table G.13: Positions of satellites after manoeuvring to target Agulhas.

		Mean Altitude, km	RAAN, deg	AoL, deg
Orbit Plane 1	Satellite 1	513.087	176.379	69.504
	Satellite 2	542.857	176.481	66.654
	Satellite 3	542.857	177.450	246.654
	Satellite 4	542.857	176.669	306.654
	Satellite 5	542.857	176.669	6.654
	Satellite 6	513.087	177.038	321.660
Orbit Plane 2	Satellite 7	542.857	266.184	66.654
	Satellite 8	542.857	267.450	186.654
	Satellite 9	513.087	266.584	62.995
	Satellite 10	513.087	266.528	157.399
	Satellite 11	542.857	267.450	6.654
	Satellite 12	542.857	266.572	126.654
Orbit Plane 3	Satellite 13	542.857	356.088	126.654
	Satellite 14	542.857	356.087	186.654
	Satellite 15	513.087	357.031	145.668
	Satellite 16	513.087	356.379	249.250
	Satellite 17	542.857	357.450	6.654
	Satellite 18	542.857	356.577	246.654
Orbit Plane 4	Satellite 19	542.857	86.868	126.654
	Satellite 20	513.087	86.626	336.227
	Satellite 21	542.857	86.669	246.654
	Satellite 22	542.857	86.668	306.654
	Satellite 23	542.857	87.450	6.654
	Satellite 24	513.087	87.182	232.372

Table G.14: Positions of satellites after 7 days in ROM mode targeting Agulhas.

		Mean Altitude, km	RAAN, deg	AoL, deg
Orbit Plane 1	Satellite 1	513.087	149.744	212.592
	Satellite 2	542.857	150.245	322.619
	Satellite 3	542.857	151.214	142.619
	Satellite 4	542.857	150.433	202.619
	Satellite 5	542.857	150.433	262.619
	Satellite 6	513.087	150.403	104.748
Orbit Plane 2	Satellite 7	542.857	239.949	322.619
	Satellite 8	542.857	241.214	82.619
	Satellite 9	513.087	239.949	206.083
	Satellite 10	513.087	239.893	300.487
	Satellite 11	542.857	241.214	262.619
	Satellite 12	542.857	240.336	22.619
Orbit Plane 3	Satellite 13	542.857	329.852	22.619
	Satellite 14	542.857	329.852	82.619
	Satellite 15	513.087	330.396	288.756
	Satellite 16	513.087	329.745	32.338
	Satellite 17	542.857	331.214	262.619
	Satellite 18	542.857	330.342	142.619
Orbit Plane 4	Satellite 19	542.857	60.633	22.619
	Satellite 20	513.087	59.992	119.315
	Satellite 21	542.857	60.433	142.619
	Satellite 22	542.857	60.433	202.619
	Satellite 23	542.857	61.214	262.619
	Satellite 24	513.087	60.547	15.460

Table G.15: Possible satellite manoeuvres to return to GOM after observing Agulhas. Selected manoeuvres in bold.

		Slot in orbit plane	Manoeuvre Time, days
Orbit Plane 1	Satellite 1	1	5.63
		2	**7.33**
	Satellite 6	**1**	**8.68**
		2	10.38
Orbit Plane 2	Satellite 9	**1**	**9.21**
		2	10.91
	Satellite 10	1	6.54
		2	**8.24**
Orbit Plane 3	Satellite 15	1	8.57
		2	**1.77**
	Satellite 16	**1**	**5.64**
		2	9.03
Orbit Plane 4	Satellite 20	1	9.97
		2	**6.57**
	Satellite 24	**1**	**2.71**
		2	9.51

Table G.16: Positions of satellites after returning to GOM from observing Agulhas.

		Mean Altitude, km	RAAN, deg	AoL, deg
Orbit Plane 1	Satellite 1	542.857	114.849	121.335
	Satellite 2	542.857	115.721	1.335
	Satellite 3	542.857	116.690	181.335
	Satellite 4	542.857	115.909	241.335
	Satellite 5	542.857	115.909	301.335
	Satellite 6	542.857	115.430	61.335
Orbit Plane 2	Satellite 7	542.857	205.425	1.335
	Satellite 8	542.857	206.690	121.335
	Satellite 9	542.857	204.946	181.335
	Satellite 10	542.857	204.945	241.335
	Satellite 11	542.857	206.690	301.335
	Satellite 12	542.857	205.812	61.335
Orbit Plane 3	Satellite 13	542.857	295.328	61.335
	Satellite 14	542.857	295.328	121.335
	Satellite 15	542.857	295.818	1.335
	Satellite 16	542.857	294.946	241.335
	Satellite 17	542.857	296.690	301.335
	Satellite 18	542.857	295.818	181.335
Orbit Plane 4	Satellite 19	542.857	26.109	61.335
	Satellite 20	542.857	25.139	1.335
	Satellite 21	542.857	25.909	181.335
	Satellite 22	542.857	25.909	241.335
	Satellite 23	542.857	26.690	301.335
	Satellite 24	542.857	25.915	121.335

G.4 Lagunas de Montebello National Park

Table G.17: Positions of satellites at detection of fire outbreak in Lagunas de Montebello.

		Mean Altitude, km	RAAN, deg	AoL, deg
Orbit Plane 1	Satellite 1	542.857	88.613	17.300
	Satellite 2	542.857	89.485	257.300
	Satellite 3	542.857	90.454	77.300
	Satellite 4	542.857	89.673	137.300
	Satellite 5	542.857	89.674	197.300
	Satellite 6	542.857	89.194	317.300
Orbit Plane 2	Satellite 7	542.857	179.189	257.300
	Satellite 8	542.857	180.454	17.300
	Satellite 9	542.857	178.710	77.300
	Satellite 10	542.857	178.710	137.300
	Satellite 11	542.857	180.454	197.300
	Satellite 12	542.857	179.576	317.300
Orbit Plane 3	Satellite 13	542.857	269.092	317.300
	Satellite 14	542.857	269.092	17.300
	Satellite 15	542.857	269.582	257.300
	Satellite 16	542.857	268.710	137.300
	Satellite 17	542.857	270.454	197.300
	Satellite 18	542.857	269.582	77.300
Orbit Plane 4	Satellite 19	542.857	359.873	317.300
	Satellite 20	542.857	358.904	257.300
	Satellite 21	542.857	359.673	77.300
	Satellite 22	542.857	359.673	137.300
	Satellite 23	542.857	0.454	197.300
	Satellite 24	542.857	359.679	17.300

Table G.18: Selected satellite manoeuvres to view Lagunas de Montebello.

		ΔV, m/s	Manoeuvre Time, days	Distance to target, km	Pass type	Manoeuvre Type
Orbit Plane 1	Satellite 5	23.04	3.48	0.28	Downwards	Lower
	Satellite 6	22.03	3.04	2.32	Upwards	Lower
Orbit Plane 2	Satellite 8	27.02	3.73	3.40	Downwards	Raise
	Satellite 10	32.00	3.29	22.94	Upwards	Raise
Orbit Plane 3	Satellite 17	19.03	3.54	4.89	Upwards	Raise
	Satellite 18	17.02	2.99	1.13	Downwards	Raise
Orbit Plane 4	Satellite 22	17.01	2.25	17.90	Downwards	Raise
	Satellite 23	27.04	3.79	0.71	Upwards	Lower

Table G.19: Positions of satellites after manoeuvre to target Lagunas de Montebello is completed.

		Mean Altitude, km	RAAN, deg	AoL, deg
Orbit Plane 1	Satellite 1	542.857	74.427	74.907
	Satellite 2	542.857	75.299	314.907
	Satellite 3	542.857	76.268	134.907
	Satellite 4	542.857	75.487	194.907
	Satellite 5	513.087	75.300	10.880
	Satellite 6	513.087	74.828	126.827
Orbit Plane 2	Satellite 7	542.857	165.003	314.907
	Satellite 8	513.087	166.248	87.245
	Satellite 9	542.857	164.524	134.907
	Satellite 10	513.087	164.473	226.169
	Satellite 11	542.857	166.268	254.907
	Satellite 12	542.857	165.390	14.907
Orbit Plane 3	Satellite 13	542.857	254.906	14.907
	Satellite 14	542.857	254.906	74.907
	Satellite 15	542.857	255.396	314.907
	Satellite 16	542.857	254.524	194.907
	Satellite 17	513.087	256.216	287.145
	Satellite 18	513.087	255.306	190.661
Orbit Plane 4	Satellite 19	542.857	345.687	14.907
	Satellite 20	542.857	344.717	314.907
	Satellite 21	542.857	345.487	134.907
	Satellite 22	513.087	345.354	277.280
	Satellite 23	513.087	346.068	18.700
	Satellite 24	542.857	345.493	74.907

References

[1] Richelson, J., "The Keyhole satellite program," *The Journal of Strategic Studies*, Vol. 7, No. 2, 1984, pp. 121–153. doi: 10.1080/01402398408437182.

[2] Norris, P., *Spies in the Sky: Surveillance Satellites in War and Peace*, Springer Science & Business Media, 2007.

[3] Bouwmeester, J., and Guo, J., "Survey of worldwide pico-and nanosatellite missions, distributions and subsystem technology," *Acta Astronautica*, Vol. 67, No. 7, 2010, pp. 854–862. doi: 10.1016/j.actaastro.2010.06.004.

[4] Poghosyan, A., and Golkar, A., "CubeSat evolution: Analyzing CubeSat capabilities for conducting science missions," *Progress in Aerospace Sciences*, Vol. 88, 2017, pp. 59–83. doi: 10.1016/j.paerosci.2016.11.002.

[5] Lal, B., de la Rosa Blanco, E., Behrens, J. R., Corbin, B. A., Green, E. K., Picard, A. J., and Balakrishnan, A., "Global trends in small satellites," Technical Report IDA Paper P-8638, Institute for Defense Analyses Science and Technology Policy Institute, July 2017.

[6] Bandyopadhyay, S., Foust, R., Subramanian, G. P., Chung, S.-J., and Hadaegh, F. Y., "Review of formation flying and constellation missions using nanosatellites," *Journal of Spacecraft and Rockets*, Vol. 53, No. 3, 2016, pp. 567–578. doi: 10.2514/1.A33291.

[7] Space Studies Board of the National Academies of Sciences, Engineering, and Medicine, *Achieving Science with CubeSats: Thinking Inside the Box*, National Academies Press, 2016.

[8] Lozano, P. C., Wardle, B. L., Moloney, P., and Rawal, S., "Nanoengineered thrusters for the next giant leap in space exploration," *Materials Research Society Bulletin*, Vol. 40, No. 10, 2015, pp. 842–849. doi: 10.1557/mrs.2015.226.

[9] Hudson, J., Spangelo, S., Hine, A., Kolosa, D., and Lemmer, K., "Mission analysis for CubeSats with micropropulsion," *Journal of Spacecraft and Rockets*, Vol. 53, No. 5, 2016, pp. 836–846. doi: 10.2514/1.A33564.

[10] Lemmer, K., "Propulsion for CubeSats," *Acta Astronautica*, Vol. 134, 2017, pp. 231–243. doi: 10.1016/j.actaastro.2017.01.048.

[11] Leomanni, M., Garulli, A., Giannitrapani, A., and Scortecci, F., "Propulsion options for very low Earth orbit microsatellites," *Acta Astronautica*, Vol. 133, 2017, pp. 444–454. doi: 10.1016/j.actaastro.2016.11.001.

[12] Co, T. C., "Operationally responsive spacecraft using electric propulsion," Ph.D. thesis, Air Force Institute of Technology, 2012.

[13] Co, T. C., Zagaris, C., and Black, J. T., "Responsive satellites through ground track manipulation using existing technology," *Journal of Spacecraft and Rockets*, Vol. 50, No. 1, 2013, pp. 206–216. doi: 10.2514/1.A32263.

[14] Co, T. C., and Black, J. T., "Responsiveness in low orbits using electric propulsion," *Journal of Spacecraft and Rockets*, Vol. 51, No. 3, 2014, pp. 938–945. doi: 10.2514/1.A32405.

[15] Knight, D., "Concept of operations for operationally responsive space," *American Institute of Aeronautics and Astronautics 4th Responsive Space Conference RS4-2006-7003, Los Angeles, California*, 2006.

[16] Wertz, J. R., Van Allen, R. E., and Shelner, C. J., "Aggressive surveillance as a key application area for Responsive Space," *American Institute of Aeronautics and Astronautics 4th Responsive Space Conference RS4-2006-1004, Los Angeles, California*, 2006.

[17] Eves, S., and Cawthorne, A., "Redefining the word "Responsive"in ORS," *American Institute of Aeronautics and Astronautics 7th Responsive Space Conference AIAA-RS7-2009-3007, Los Angeles, California*, 2009.

[18] Eves, S., and Taylor, M., "Thinking at the constellation level," *American Institute of Aeronautics and Astronautics 8th Responsive Space Conference AIAA-RS8-2010-1001, Los Angeles, California*, 2010.

[19] Carrico, J., and Langster, T., "Time critical targeting using responsive tactical satellites," *American Institute of Aeronautics and Astronautics 4th Responsive Space Conference RS4-2006-7005, Los Angeles, California*, 2006.

[20] Battin, R. H., and Vaughan, R. M., "An elegant Lambert algorithm," *Journal of Guidance, Control, and Dynamics*, Vol. 7, No. 6, 1984, pp. 662–670. doi: 10.2514/3.19910.

[21] Prussing, J. E., and Chiu, J.-H., "Optimal multiple-impulse time-fixed rendezvous between circular orbits," *Journal of Guidance, Control, and Dynamics*, Vol. 9, No. 1, 1986, pp. 17–22. doi: 10.2514/3.20060.

[22] Escobal, P. R., *Methods of Orbit Determination*, Wiley, 1965. pp. 187–239.

[23] Bate, R. R., Mueller, D. D., and White, J. E., *Fundamentals of astrodynamics*, Dover Publications, 1971. pp. 227–276.

[24] Woollands, R. M., Bani Younes, A., and Junkins, J. L., "New solutions for the perturbed Lambert problem using regularization and Picard iteration," *Journal of Guidance, Control, and Dynamics*, Vol. 38, No. 9, 2015, pp. 1548–1562. doi: 10.2514/1.G001028.

[25] Wagner, S., Wie, B., and Kaplinger, B., "Computational solutions to Lambert's problem on modern graphics processing units," *Journal of Guidance, Control, and Dynamics*, Vol. 38, No. 7, 2015, pp. 1305–1311. doi: 10.2514/1.G000840.

[26] Wang, X., Yue, X., Dai, H., and Atluri, S. N., "Feedback-accelerated Picard iteration for orbit propagation and Lambert's problem," *Journal of Guidance, Control, and Dynamics*, Vol. 40, No. 10, 2017, pp. 2442–2451. doi: 10.2514/1.G002638.

[27] Bombardelli, C., Gonzalo, J. L., and Roa, J., "Approximate analytical solution of the multiple revolution Lambert's targeting problem," *Journal of Guidance, Control, and Dynamics*, Vol. 41, No. 3, 2018, pp. 792–801. doi: 10.2514/1.G002887.

[28] Racca, G., Marini, A., Stagnaro, L., Van Dooren, J., Di Napoli, L., Foing, B., Lumb, R., Volp, J., Brinkmann, J., Grünagel, R., et al., "SMART-1 mission description and development status," *Planetary and Space Science*, Vol. 50, No. 14-15, 2002, pp. 1323–1337. doi: 10.1016/S0032-0633(02)00123-X.

[29] Betts, J. T., and Erb, S. O., "Optimal low thrust trajectories to the moon," *Society for Industrial and Applied Mathematics Journal on Applied Dynamical Systems*, Vol. 2, No. 2, 2003, pp. 144–170. doi: doi.org/10.1137/S1111111102409080.

[30] Ranieri, C. L., and Ocampo, C. A., "Optimization of roundtrip, time-constrained, finite burn trajectories via an indirect method," *Journal of Guidance, Control, and Dynamics*, Vol. 28, No. 2, 2005, pp. 306–314. doi: 10.2514/1.5540.

[31] Izzo, D., "Lambert's problem for exponential sinusoids," *Journal of Guidance, Control, and Dynamics*, Vol. 29, No. 5, 2006, pp. 1242–1245. doi: 10.2514/1.21796.

[32] Vellutini, E., and Avanzini, G., "Shape-based design of low-thrust trajectories to cislunar Lagrangian point," *Journal of Guidance, Control, and Dynamics*, Vol. 37, No. 4, 2014, pp. 1329–1335. doi: 10.2514/1.G000165.

[33] Petropoulos, A. E., and Longuski, J. M., "Shape-based algorithm for the automated design of low-thrust, gravity assist trajectories," *Journal of Spacecraft and Rockets*, Vol. 41, No. 5, 2004, pp. 787–796. doi: 10.2514/1.13095.

[34] Zuiani, F., Vasile, M., Palmas, A., and Avanzini, G., "Direct transcription of low-thrust trajectories with finite trajectory elements," *Acta Astronautica*, Vol. 72, 2012, pp. 108–120. doi: 10.1016/j.actaastro.2011.09.011.

[35] Avanzini, G., Palmas, A., and Vellutini, E., "Solution of low-thrust Lambert problem with perturbative expansions of equinoctial elements," *Journal of Guidance, Control, and Dynamics*, Vol. 38, No. 9, 2015, pp. 1585–1601. doi: 10.2514/1.G001018.

[36] Gao, Y., "Low-thrust interplanetary transfers, including escape and capture trajectories," *Journal of Guidance, Control, and Dynamics*, Vol. 30, No. 6, 2007, pp. 1814–1818. doi: 10.2514/1.26427.

[37] Gao, Y., and Kluever, C., "Analytic orbital averaging technique for computing tangential-thrust trajectories," *Journal of Guidance, Control, and Dynamics*, Vol. 28, No. 6, 2005, pp. 1320–1323. doi: 10.2514/1.14698.

[38] Kim, H.-D., Jung, O.-C., and Bang, H., "A computational approach to reduce the revisit time using a genetic algorithm," *International Conference on Control, Automation and Systems*, Institute of Electrical and Electronics Engineers, 2007, pp. 184–189.

[39] Chen, Y., Mahalec, V., Chen, Y., He, R., and Liu, X., "Optimal satellite orbit design for prioritized multiple targets with threshold observation time using self-adaptive differential evolution," *Journal of Aerospace Engineering*, Vol. 28, No. 2, 2013, pp. 04014066–1–04014066–9. doi: 10.1061/(ASCE)AS.1943-5525.0000393.

[40] Yao, W., Luo, J., Macdonald, M., Wang, M., and Ma, W., "Improved differential evolution algorithm and its applications to orbit design," *Journal of Guidance, Control, and Dynamics*, Vol. 41, No. 4, 2018, pp. 936–943. doi: 10.2514/1.G003214.

[41] Guelman, M., and Kogan, A., "Electric propulsion for remote sensing from low orbits," *Journal of Guidance, Control, and Dynamics*, Vol. 22, No. 2, 1999, pp. 313–321. doi: 10.2514/2.4380.

[42] Jean, I., and de Lafontaine, I. J., "Autonomous guidance and control of an Earth observation satellite using low thrust," *Advances in the Astronautical Sciences*, Vol. 116, No. 3, 2003, pp. 1829–1844.

[43] Showalter, D. J., and Black, J. T., "Responsive theater maneuvers via particle swarm optimization," *Journal of Spacecraft and Rockets*, Vol. 51, No. 6, 2014, pp. 1976–1985. doi: 10.2514/1.A32989.

[44] Zhu, K.-J., Li, J.-F., and Baoyin, H.-X., "Satellite scheduling considering maximum observation coverage time and minimum orbital transfer fuel cost," *Acta Astronautica*, Vol. 66, No. 1, 2010, pp. 220–229. doi: 10.1016/j.actaastro.2009.05.029.

[45] Zhang, G., Cao, X., and Mortari, D., "Analytical approximate solutions to ground track adjustment for responsive space," *Institute of Electrical and Electronics Engineers Transactions on Aerospace and Electronic Systems*, Vol. 52, No. 3, 2016, pp. 1366–1383. doi: 10.1109/TAES.2016.140644.

[46] Zhang, G., and Sheng, J., "Impulsive ground-track adjustment for assigned final orbit," *Journal of Spacecraft and Rockets*, Vol. 53, No. 4, 2016, pp. 599–609. doi: 10.2514/1.A33447.

[47] Zhang, G., and Cao, X., "Coplanar ground-track adjustment using time difference," *Aerospace Science and Technology*, Vol. 48, 2016, pp. 21–27. doi: 10.1016/j.ast.2015.10.023.

[48] Chaize, M., "Enhancing the economics of satellite constellations via staged deployment and orbital reconfiguration," Ph.D. thesis, Massachusetts Institute of Technology, 2003.

[49] Crisp, N., Smith, K., and Hollingsworth, P., "Launch and deployment of distributed small satellite systems," *Acta Astronautica*, Vol. 114, 2015, pp. 65–78. doi: 10.1016/j.actaastro.2015.04.015.

[50] Fong, C.-J., Huang, C.-Y., Chu, V., Yen, N., Kuo, Y.-H., Liou, Y.-A., and Chi, S., "Mission results from FORMOSAT-3/COSMIC constellation system," *Journal of Spacecraft and Rockets*, Vol. 45, No. 6, 2008, pp. 1293–1302. doi: 10.2514/1.34427.

[51] Fong, C.-J., Shiau, W.-T., Lin, C.-T., Kuo, T.-C., Chu, C.-H., Yang, S.-K., Yen, N. L., Chen, S.-S., Kuo, Y.-H., and Liou, Y.-A., "Constellation deployment for the FORMOSAT-3/COSMIC mission," *Institute of Electrical and Electronics Engineers Transactions on Geoscience and Remote Sensing*, Vol. 46, No. 11, 2008, pp. 3367–3379. doi: 10.1109/TGRS.2008.2005202.

[52] Baranov, A. A., Grishko, D. A., and Mayorova, V. I., "The features of constellations formation and replenishment at near circular orbits in non-central gravity fields," *Acta Astronautica*, Vol. 116, 2015, pp. 307–317. doi: 10.1016/j.actaastro.2015.06.025.

[53] Leppinen, H., "Deploying a single-launch nanosatellite constellation to several orbital planes using drag maneuvers," *Acta Astronautica*, Vol. 121, 2016, pp. 23–28. doi: 10.1016/j.actaastro.2015.12.036.

[54] Foster, C., Mason, J., Vittaldev, V., Leung, L., Beukelaers, V., Stepan, L., and Zimmerman, R., "Constellation phasing with differential drag on Planet Labs satellites," *Journal of Spacecraft and Rockets*, Vol. 55, No. 2, 2018, pp. 473–483. doi: 10.2514/1.A33927.

[55] Davis, J. J., "Constellation reconfiguration: Tools and analysis," Ph.D. thesis, Texas A&M University, 2010.

[56] De Weck, O. L., Scialom, U., and Siddiqi, A., "Optimal reconfiguration of satellite constellations with the auction algorithm," *Acta Astronautica*, Vol. 62, No. 2, 2008, pp. 112–130. doi: 10.1016/j.actaastro.2007.02.008.

[57] Ferringer, M. P., Spencer, D. B., and Reed, P., "Many-objective reconfiguration of operational satellite constellations with the large-cluster epsilon non-dominated sorting genetic algorithm-II," *Congress on Evolutionary Computation*, Institute of Electrical and Electronics Engineers, 2009, pp. 340–349.

[58] Appel, L., Guelman, M., and Mishne, D., "Optimization of satellite constellation reconfiguration maneuvers," *Acta Astronautica*, Vol. 99, 2014, pp. 166–174. doi: 10.1016/j.actaastro.2014.02.016.

[59] Fakoor, M., Bakhtiari, M., and Soleymani, M., "Optimal design of the satellite constellation arrangement reconfiguration process," *Advances in Space Research*, Vol. 58, No. 3, 2016, pp. 372–386. doi: 10.1016/j.asr.2016.04.031.

[60] Mushet, G., and McInnes, C., "Self-organising low Earth orbit constellations for Earth observation," *2nd Conference on Dynamics and Control of Space Systems, IAA-AAS-DyCoSS2-14-01-03*, 2014.

[61] Legge Jr, R. S., "Optimization and valuation of recongurable satellite constellations under uncertainty," Ph.D. thesis, Massachusetts Institute of Technology, 2014.

[62] Paek, S. W., De Weck, O. L., and W., S. M., "Concurrent design optimisation of Earth observation satellites and reconfigurable constellations," *Journal of the British Interplanetary Society*, Vol. 70, 2017, pp. 19–35.

[63] Vallado, D. A., and McClain, W. D., *Fundamentals of Astrodynamics and Applications*, 3rd ed., Microcosm Press & Springer, 2007. pp. 615–633, pp. 642–667.

[64] Macdonald, M., and Badescu, V., *The International Handbook of Space Technology*, Springer, 2014. pp. 75–88.

[65] Cerf, M., "Low-thrust transfer between circular orbits using natural precession," *Journal of Guidance, Control, and Dynamics*, Vol. 39, No. 10, 2016, pp. 2232–2239. doi: 10.2514/1.G001331.

[66] Schaub, H., Vadali, S. R., Junkins, J. L., and Alfriend, K. T., "Spacecraft formation flying control using mean orbit elements," *Journal of the Astronautical Sciences*, Vol. 48, No. 1, 2000, pp. 69–87.

[67] Escobal, P. R., *Methods of Orbit Determination*, Wiley, 1965. pp. 363–371.

[68] Bate, R. R., Mueller, D. D., and White, J. E., *Fundamentals of Astrodynamics*, Dover Publications, 1971. pp. 396–407.

[69] Brouwer, D., "Solution of the problem of artificial satellite theory without drag," *The Astronomical Journal*, Vol. 64, 1959, pp. 378–396.

[70] Schaub, H., and Alfriend, K. T., "J2 invariant relative orbits for spacecraft formations," *Celestial Mechanics and Dynamical Astronomy*, Vol. 79, No. 2, 2001, pp. 77–95. doi: 10.1023/A:1011161811472.

[71] Vallado, D. A., and McClain, W. D., *Fundamentals of Astrodynamics and Applications*, 3rd ed., Microcosm Press & Springer, 2007. pp. 373–389.

[72] Vallado, D. A., and McClain, W. D., *Fundamentals of Astrodynamics and Applications*, 3rd ed., Microcosm Press & Springer, 2007. pp. 549–571.

[73] Kidder, S. Q., and Haar, T. H. V., *Satellite Meteorology: An Introduction*, Gulf Professional Publishing, 1995. pp. 30–41.

[74] Smart, W. M., *Text-book on Spherical Astronomy*, 5th ed., Cambridge University Press, 1962. pp. 1–24.

[75] Geyer, M., "Geometric analysis of an observer on a spherical earth and an aircraft or satellite," Tech. rep., Technical Report, US Department of Transportation-Research and Innovative Technology Administration-John A. Volpe National Transportation Systems Center, 2013. DOT-VNTSC-FAA-13-08, 2013.

[76] Wolfram Research, Inc., *Mathematica, Version 11.3*, Champaign, IL, 2018.

[77] Hutputtanasin, A., and Tooria, A., "CubeSat Design Specification," Technical specification, California Polytechnic State University, 2005.

[78] Rankin, D., Kekez, D. D., Zee, R. E., Pranajaya, F. M., Foisy, D. G., and Beattie, A. M., "The CanX-2 nanosatellite: expanding the science abilities of nanosatellites," *Acta Astronautica*, Vol. 57, No. 2-8, 2005, pp. 167–174. doi: 10.1016/j.actaastro.2005.03.032.

[79] Krejci, D., Mier-Hicks, F., Fucetola, C., Lozano, P., Schouten, A. H., and Martel, F., "Design and characterization of a scalable ion electrospray propulsion system," *30th International Symposium on Space Technology and Science, 34th International Electric Propulsion Conference and 6th Nano-satellite Symposium, IEPC-2015-149/ISTS-2015-b-149*, 2015.

[80] Krejci, D., Mier-Hicks, F., Thomas, R., Haag, T., and Lozano, P., "Emission characteristics of passively fed electrospray microthrusters with propellant reservoirs," *Journal of Spacecraft and Rockets*, Vol. 54, No. 2, 2017, pp. 447–458. doi: 10.2514/1.A33531.

[81] Mier-Hicks, F., and Lozano, P. C., "Electrospray thrusters as precise attitude control actuators for small satellites," *Journal of Guidance, Control, and Dynamics*, Vol. 40, No. 3, 2017, pp. 642–649. doi: 10.2514/1.G000736.

[82] Lozano, P. C., "Less in Space," *American Scientist*, Vol. 104, No. 5, 2016, pp. 270–273.

[83] Walker, M., Ireland, B., and Owens, J., "A set modified equinoctial orbit elements," *Celestial Mechanics*, Vol. 36, No. 4, 1985, pp. 409–419. doi: 10.1007/BF01227493.

[84] MATLAB, *Version (R2016a)*, The MathWorks Inc., Natick, Massachusetts, 2016.

[85] Dormand, J. R., and Prince, P. J., "A family of embedded Runge-Kutta formulae," *Journal of Computational and Applied Mathematics*, Vol. 6, No. 1, 1980, pp. 19–26. doi: 10.1016/0771-050X(80)90013-3.

[86] United States Committee on Extension to the Standard Atmosphere, *U.S. Standard Atmosphere, 1976*, National Oceanic and Atmospheric Administration, 1976.

[87] Castelvi, J., Lancheros, E., Camps, A., and Park, H., "Feasibility of nano-satellites constellations for AIS decoding and fire detection," *Federated Satellite Systems Workshop*, 2016.

[88] "GomSpace and AISTECH Sign a Binding Framework Delivery Agreement for the Supply of 100 Nanosatellite Platforms," `https://gomspace.com/news/gomspace-and-aistech-sign-a-binding-framework.aspx`, 2017. Accessed: 28/10/2017.

[89] Bogosian, J. R., "Image collection optimization in the design and operation of lightweight, low areal-density space telescopes," Ph.D. thesis, Massachusetts Institute of Technology, 2008.

[90] Paek, S. W., "Reconfigurable satellite constellations for geo-spatially adaptive Earth observation missions," Ph.D. thesis, Massachusetts Institute of Technology, 2012.

[91] Carver, S., Comber, L., Fritz, S., McMorran, R., Taylor, S., and Washtell, J., "Wildness study in the Cairngorms National Park," Technical report, University of Leeds, 2008.

[92] Gray, A., and Levy, P., "A review of carbon flux research in UK peatlands in relation to fire and the Cairngorms National Park," Technical report, Natural Environment Research Council Centre for Ecology & Hydrology, July 2009.

[93] "National Park Service visitor use statistics for Yosemite National Park," `https://irma.nps.gov/Stats/Reports/Park/YOSE`, 2017. Accessed: 09/02/2018.

[94] Lutz, J. A., Van Wagtendonk, J. W., Thode, A. E., Miller, J. D., and Franklin, J. F., "Climate, lightning ignitions, and fire severity in Yosemite National Park, California, USA," *International Journal of Wildland Fire*, Vol. 18, No. 7, 2009, pp. 765–774. doi: 10.1071/WF08117.

[95] Kane, V. R., North, M. P., Lutz, J. A., Churchill, D. J., Roberts, S. L., Smith, D. F., McGaughey, R. J., Kane, J. T., and Brooks, M. L., "Assessing fire effects on forest spatial structure using a fusion of Landsat and airborne LiDAR data in Yosemite National Park," *Remote Sensing of Environment*, Vol. 151, 2014, pp. 89–101. doi: 10.1016/j.rse.2013.07.041.

[96] "Agulhas National Park," https://www.sanparks.org/parks/agulhas/, 2018. Accessed: 18/10/2017.

[97] "Agulhas National Park Fire of 2009," https://www.sanparks.org/conservation/scientific_new/cape/data_resources/maps.php, 2018. Accessed: 18/10/2017.

[98] Johnson, K. A., and Nelson, K. C., "Common property and conservation: The potential for effective communal forest management within a national park in Mexico," *Human Ecology*, Vol. 32, No. 6, 2004, pp. 703–733. doi: 10.1007/s10745-004-6833-z.

[99] "The geography of wildfires in Mexico: the disastrous wildfire season of 2011," http://geo-mexico.com/?p=5734, 2012. Accessed: 05/10/2017.

[100] "Lagunas de Montebello: the Montebello Lakes National park in Chiapas," http://geo-mexico.com/?p=14058, 2016. Accessed: 20/10/2017.

[101] Mortari, D., and Wilkins, M. P., "Flower constellation set theory. Part I: Compatibility and phasing," *Institute of Electrical and Electronics Engineers Transactions on Aerospace and Electronic Systems*, Vol. 44, No. 3, 2008, pp. 953–963. doi: 10.1109/TAES.2008.4655355.

[102] Ross, A. M., Hastings, D. E., Warmkessel, J. M., and Diller, N. P., "Multi-attribute tradespace exploration as front end for effective space system design," *Journal of Spacecraft and Rockets*, Vol. 41, No. 1, 2004, pp. 20–28. doi: 10.2514/1.9204.

[103] Lowe, C. J., "Methodologies for the analysis of value from delay-tolerant inter-satellite networking," Ph.D. thesis, University of Strathclyde, 2017.

[104] "Map Data," taken from Google, Terrametrics, and Grid Reference Finder, 2017.

[105] King, J. A., and Beidleman, N. J., "Method and apparatus for deploying a satellite network," US Patent 5,199,672, April 1993.

[106] da Silva Curiel, A., Lambert, M., Liddle, D., Sweeting, S. M., Chu, C.-H. V., Fong, C.-J., and Chang, G.-S., "Introduction to FORMOSAT-7/COSMIC-2 mission," *27th Annual American Institute of Aeronautics and Astronautics and Utah State University Conference on Small Satellites, SSC13-VI-1*, 2013.

[107] Cook, K., Fong, C.-J., Wenkel, M. J., Wilczynski, P., Yen, N., and Chang, G., "FORMOSAT-7/COSMIC-2 GNSS radio occultation constellation mission for global weather monitoring," *Aerospace Conference*, Institute of Electrical and Electronics Engineers, 2013. doi: 10.1109/AERO.2013.6497317.

[108] Sandau, R., "Status and trends of small satellite missions for Earth observation," *Acta Astronautica*, Vol. 66, No. 1-2, 2010, pp. 1–12. doi: 10.1016/j.actaastro.2009.06.008.

[109] Wekerle, T., Pessoa Filho, J. B., Costa, L. E. V. L. d., and Trabasso, L. G., "Status and trends of Smallsats and their launch vehicles — an up-to-date review," *Journal of Aerospace Technology and Management*, Vol. 9, No. 3, 2017, pp. 269–286. doi: 10.5028/jatm.v9i3.853.

[110] "Rocket Lab Ltd: History," `https://www.rocketlabusa.com/about-us/`, 2017. Accessed: 16/02/2018.

[111] "Rocket Lab Ltd: Electron," `https://www.rocketlabusa.com/electron/`, 2017. Accessed: 16/02/2018.

[112] "Rocket Lab Ltd: Launch Cost," `https://www.rocketlabusa.com/book-my-launch/`, 2017. Accessed: 16/02/2018.

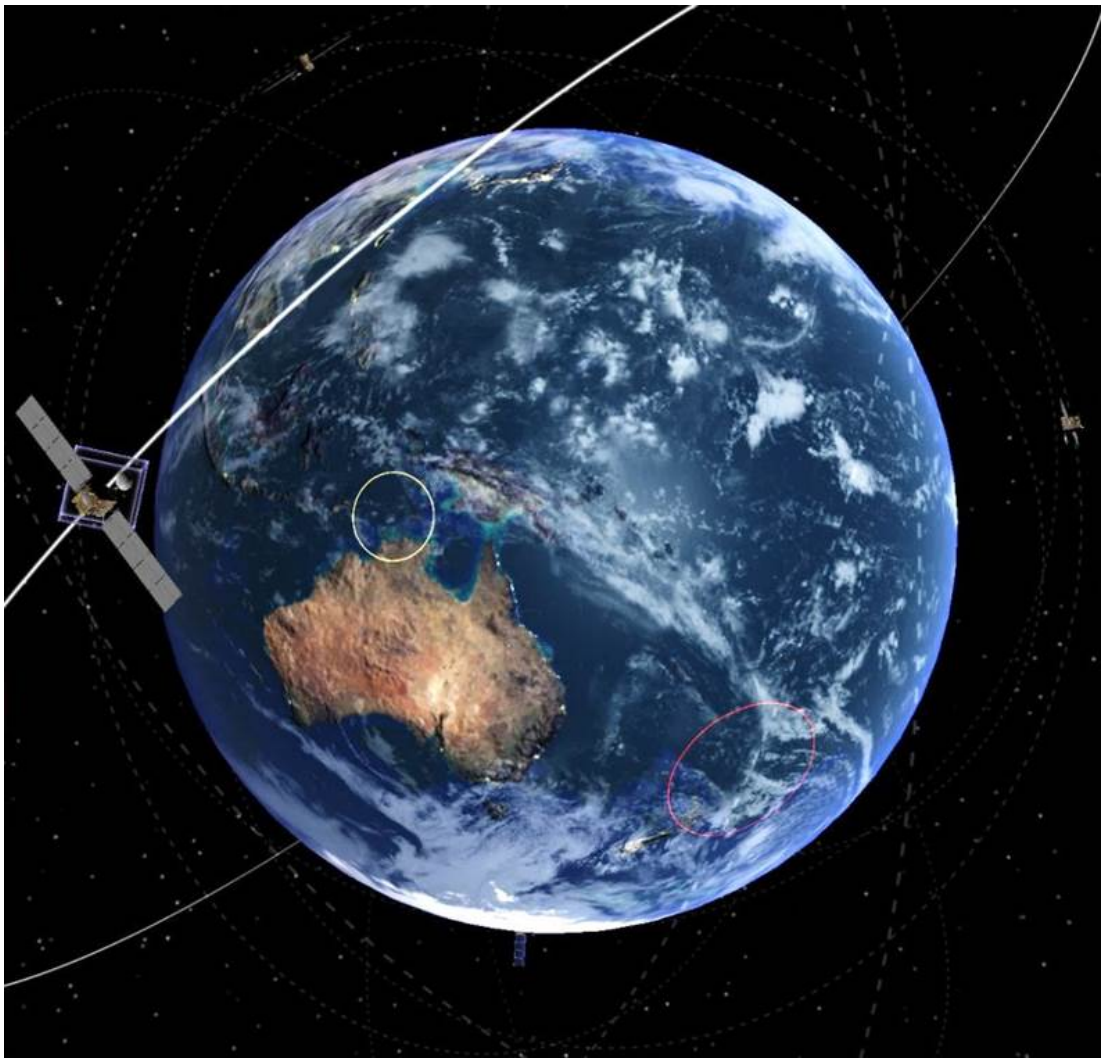

Image taken from a game produced by Glasgow School of Art Digital Design Studio as part of the Space for Art project. The game, based on the work presented in this dissertation, challenges players to manoeuvre satellites and provide targeted coverage to regions of the Earth, without exhausting the available propellant.